Determining Pavement Design Criteria for Recycled Aggregate Base and Large Stone Subbase

MnDOT Project TPF-5(341)
REVISED

Task 5 – Performance Monitoring and Reporting
Task 6 – Instrumentation

April 17, 2020

Prepared by:
Bora Cetin – Principal Investigator
Tuncer B. Edil – Co-Principal Investigator
Haluk Sinan Coban – Graduate Research Assistant

TABLE OF CONTENTS

LIST OF TABLES

LIST OF FIGURES

1. TEST CELLS

A field study was conducted on eleven test cells constructed on the Minnesota Road Research Project (MnROAD) Low Volume Road (LVR), a pavement test facility owned by the Minnesota Department of Transportation (MnDOT). The MnROAD LVR, a two-lane closed loop, is located near westbound I-94, northwest of the Twin Cities, MN [Figure 1.1(a)]. Traffic on the MnROAD LVR was simulated by the MnROAD truck, which was a 5-axle tractor/trailer combination weighing 80 kip (36.3 Mg) (MnDOT 2013a). The MnROAD truck made approximately 70 laps per day, and it was operated in the inside lane (main traffic) only [Figure 1.1(b)]. The outside lane (occasional traffic) was dedicated to installing temperature and moisture sensors to investigate environmental effects.

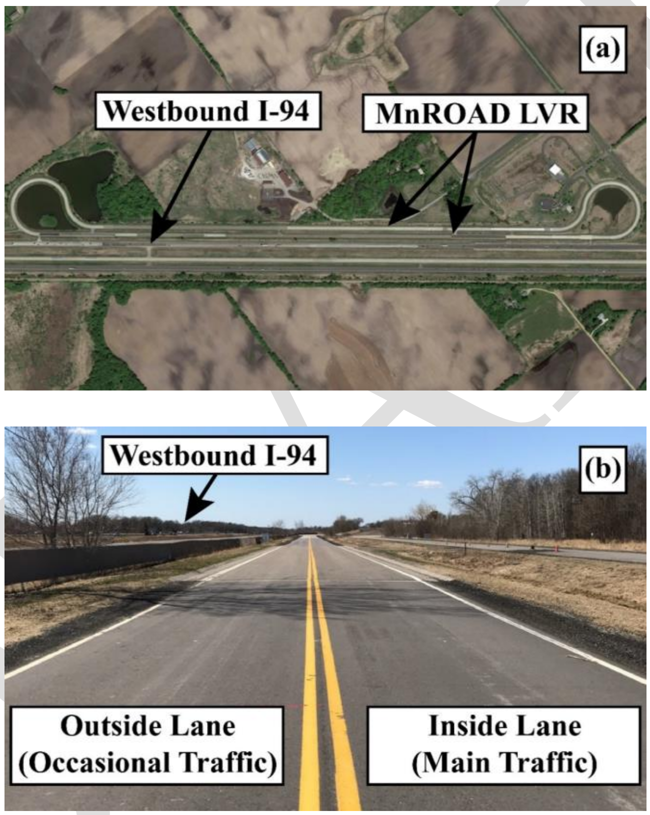

Figure 1.1. (a) Location and (b) traffic lanes of the Minnesota Road Research Project (MnROAD) Low Volume Road (LVR)

Eleven test cells, located on the MnROAD LVR, contained three groups: (1) recycled aggregate base (RAB) group, (2) large stone subbase (LSSB) group, and (3) LSSB with geosynthetics group. A layout of the test cells and their compositions are provided in Figures 1.2(a) and 1.2(b), respectively. More detailed information about the construction of the test cells and the materials used for construction is provided in Task 3 (construction monitoring and reporting), and Task 4 (laboratory testing) reports, respectively.

In the RAB group, cells 185, 186, 188, and 189 were approximately 200 ft (61 m) long [width of each lane was about 12 ft (3.7 m)]. Cells 185 and 186 contained sand subgrade layers, and cells 188 and 189 contained clay loam subgrade layers. Each test cell in this group contained 3.5 in (89 mm) select granular borrow subbase layers overlying the subgrade layers. Over the subbase layers, cells 185, 186, 188, and 189 contained coarse RCA, fine RCA, limestone, and RCA+RAP base layers, respectively. For the surface layer, each test cell contained a 3.5 in (89 mm) asphalt layer [0.5 in (12.5 mm) nominal maximum aggregate size (NMAS) Superpave]

In the LSSB group, cells 127 and 227 were approximately 260 ft (79.2 m) long [width of each lane was about 12 ft (3.7 m)]. Both test cells in this group contained clay loam subgrade layers, 18 in (457 mm) LSSB layers, 6 in (152 mm) class 6 aggregate base layers, and 3.5 in (89 mm) asphalt layers [0.5 in (12.5 mm) NMAS Superpave].

In the LSSB with geosynthetics group, cells 328, 428, 528, and 628 were approximately 110 ft (33.5 m) long, and cell 728 was around 130 ft (39.6 m) long [width of each lane was about 12 ft (3.7 m)]. Each test cell in this group contained a clay loam subgrade layer. On top of the subgrade layers, cells 328, 428, 528, and 628 contained triaxial geogrid (TX), a combination of TX and nonwoven geotextile (GT), a combination of biaxial geogrid (BX) and GT, and BX, respectively [more information about the geosynthetics used is provided in Task 3 (construction monitoring and reporting) report]. Cell 728 did not contain any geosynthetics. Each test cell in this group contained 9 in (229 mm) LSSB layers, 6 in (152 mm) class 5Q aggregate base layers, and 3.5 in (89 mm) asphalt layers [0.5 in (12.5 mm) NMAS Superpave].

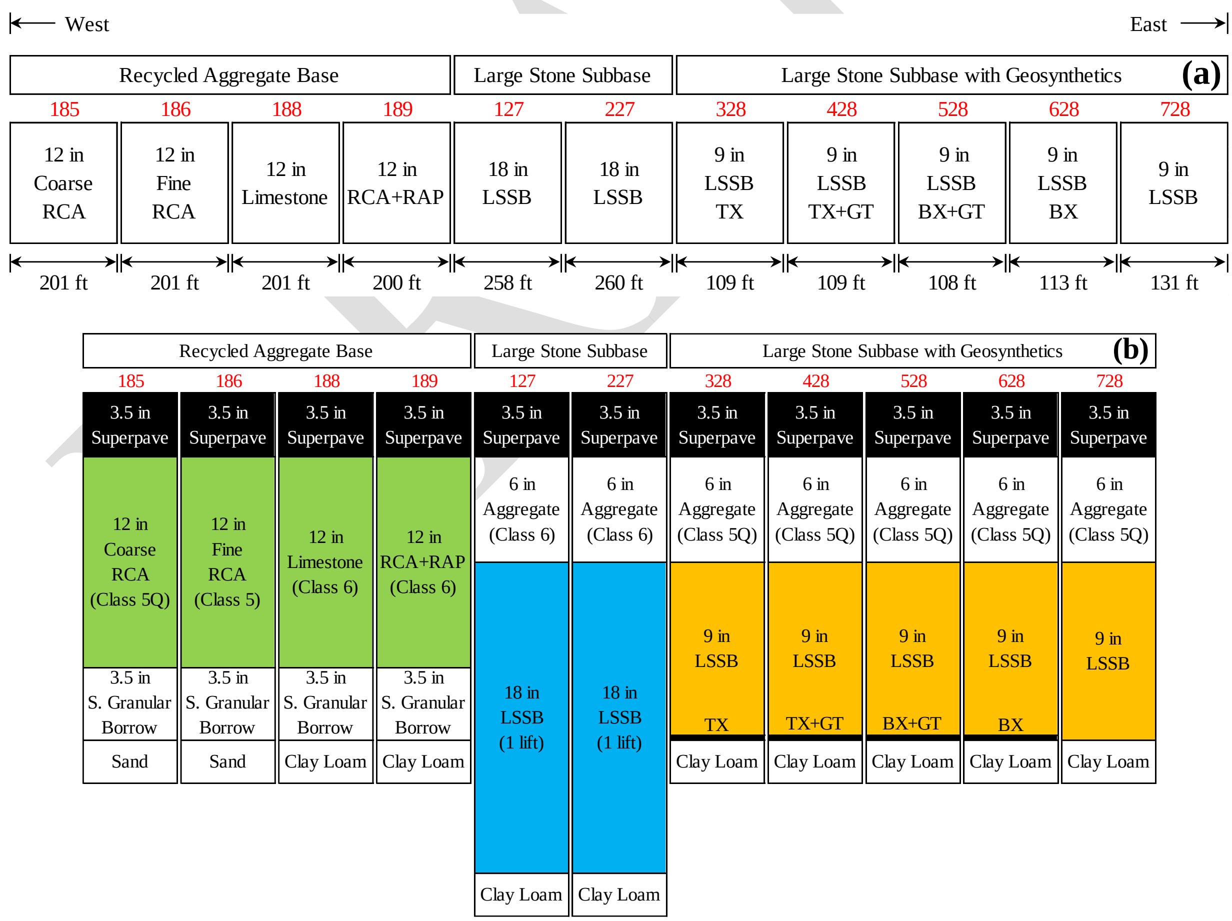

Figure 1.2. (a) Layout and (b) compositions of test cells (not to scale) (s. granular borrow = select granular borrow, TX = triaxial geogrid, GT = geosynthetic, BX = biaxial geogrid)

2. METEOROLOGICAL DATA

Meteorological data was collected by the external weather stations located at the MnROAD LVR test facility (MnDOT 2014a). Table 2.1 shows the list of equipment of which the weather stations contain. Air temperature and precipitation data (average of the two weather stations) during and after construction are provided in Figures 2.1 and 2.2, respectively [detailed information about the construction dates is provided in Task 3 (construction monitoring and reporting) report]. Relative humidity and average wind speed data are also shown in Appendix A.

Between Jul 2017-Apr 2019, the minimum and maximum air temperatures were observed to be -29.6°F (-34.2°C) and 98°F (36.6°C), respectively (Figure 2.1). Air temperature data contained two freezing periods when the temperatures were mainly below 32°F (0°C). The first freezing period was between Nov 2017-Apr 2018, and the second freezing period was between Oct 2018-Apr 2019 (Figure 2.1).

The precipitation data contained two main rainy periods. The first and second rainy periods were between Jul 2017-Nov 2017 and May 2018-Nov 2018, respectively (Figure 2.2). The maximum precipitation was observed to be 0.675 in (17.1 mm) (Figure 2.2).

Table 2.1. MnROAD weather stations (NW = northwest and SE = southeast)

Equipment	NW/SE Weather Stations
Datalogger	Campbell Scientific CR1000s
Temperature/Relative Humidity Sensors	Vaisala probe Model HMP45AC/HMP45C
Wind Monitor Sensors	RM Young Model 05103
Ambient Pressure Sensor	Campbell Scientific CS106 (Vaisla PTB110)
Precipitation Sensor	Tipping bucket - Met One Instruments 380/385
Radiometer	Kipp & Zonen NR Lite 2

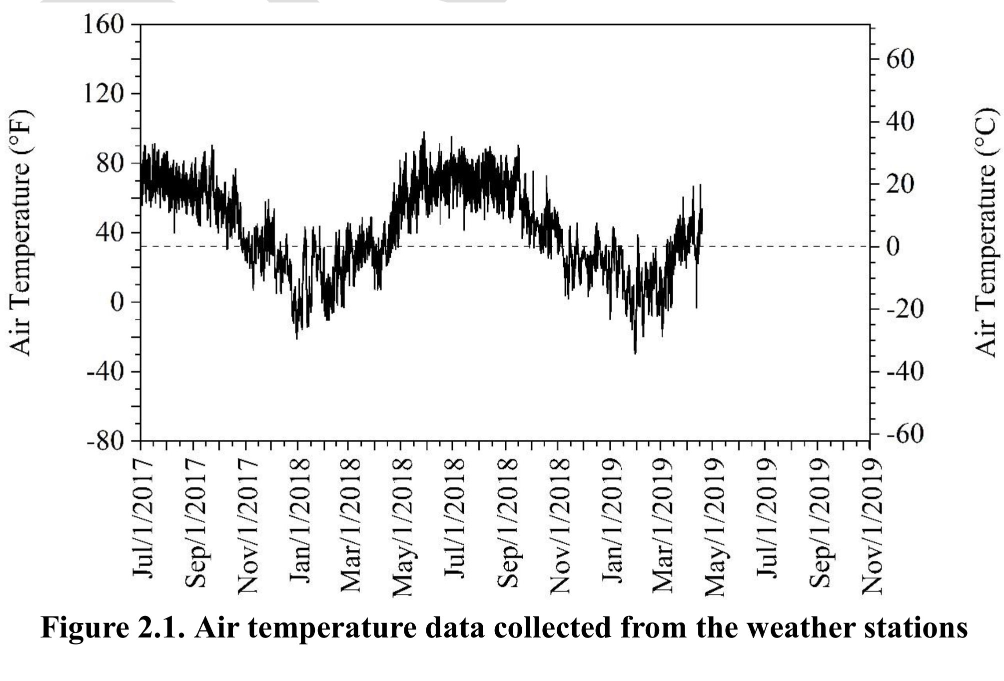

Figure 2.1. Air temperature data collected from the weather stations

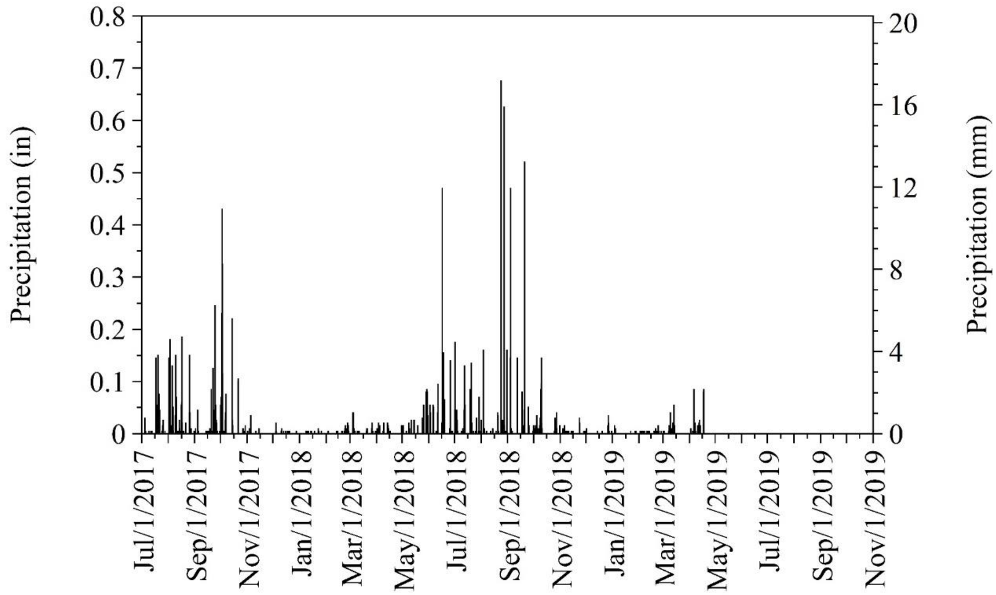

Figure 2.2. Precipitation data collected from the weather stations

3. TEMPERATURE AND MOISTURE MONITORING

3.1. Monitoring Systems

Temperature and moisture measurements at various depths were taken every 15 minutes by thermocouples (TCs) (MnROAD 2014b) (Figure 3.1) and moisture probes (ECs) (Figure 3.2) (MnROAD 2014c), respectively. Detailed information regarding the properties of the thermocouples and moisture probes is provided in Task 3 (construction monitoring and reporting) report. The sensors were installed only in cells 185 (12 in coarse RCA), 186 (12 in fine RCA), 188 (12 in limestone), 189 (12 in RCA+RAP), 127 (18 in LSSB), and 728 (9 in LSSB). The number of sensors installed in those test cells is summarized in Table 3.1. Plan and profile views of the sensor locations are provided in Figures 3.3, 3.4, 3.5, 3.6, 3.7, and 3.8 for cells 185 (12 in coarse RCA), 186 (12 in fine RCA), 188 (12 in limestone), 189 (12 in RCA+RAP), 127 (18 in LSSB), and 728 (9 in LSSB), respectively. Appendix B provides more information about the locations of the sensors.

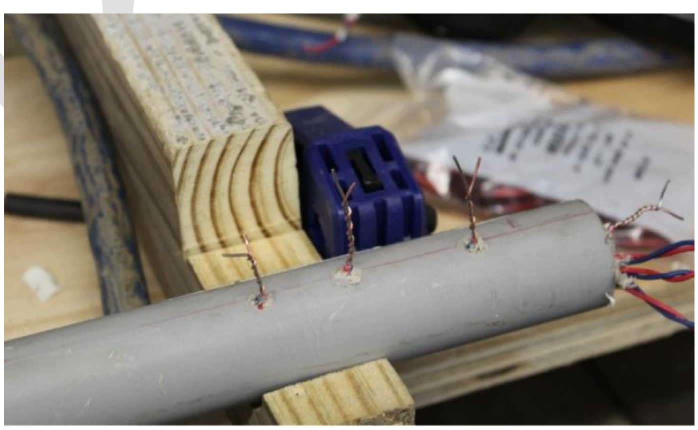

Figure 3.1. Thermocouple array in the PVC pipe (MnDOT 2014b)

Figure 3.2. Decagon 5TE moisture probe (MnDOT 2014c)

Table 3.1. Type and number of sensors installed (Van Deusen et al. 2018)

Cell Number	Cell Description	Number of Environmental Sensors	
		Thermocouple (TC)	Moisture Probe (EC)
185	12 in Coarse RCA	12	4
186	12 in Fine RCA	12	4
188	12 in Limestone	12	4
189	12 in RCA+RAP	12	4
127	18 in LSSB	12	3
728	9 in LSSB	16	4

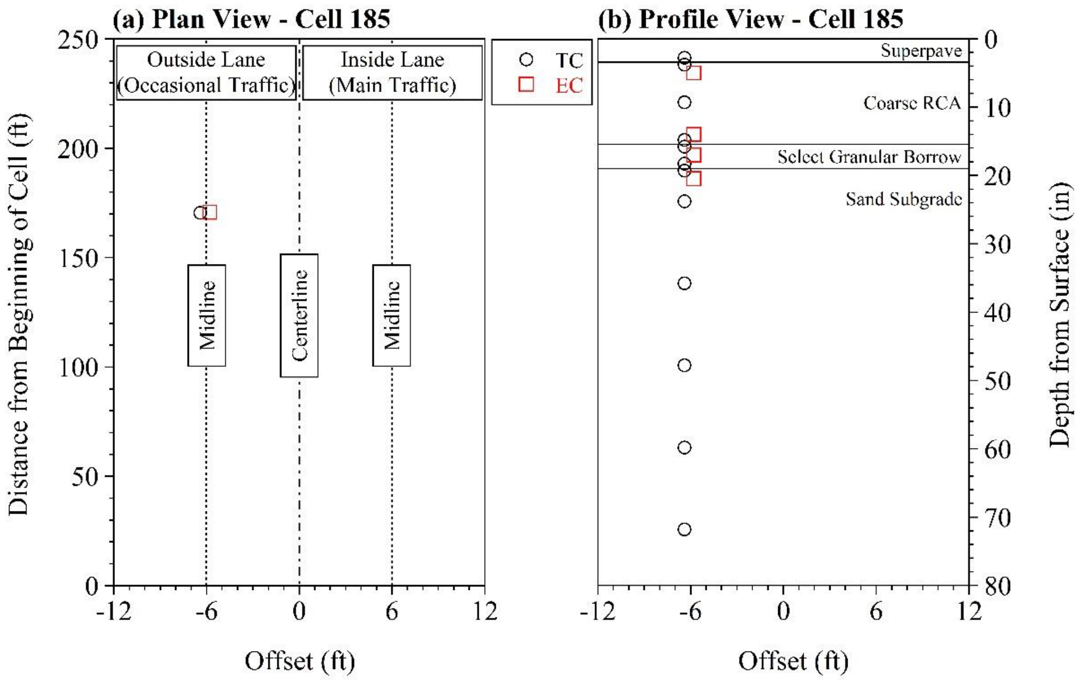

Figure 3.3. (a) Plan and (b) profile view of sensor locations in cell 185 (12 in coarse RCA) (TC = thermocouple, EC = moisture probe)

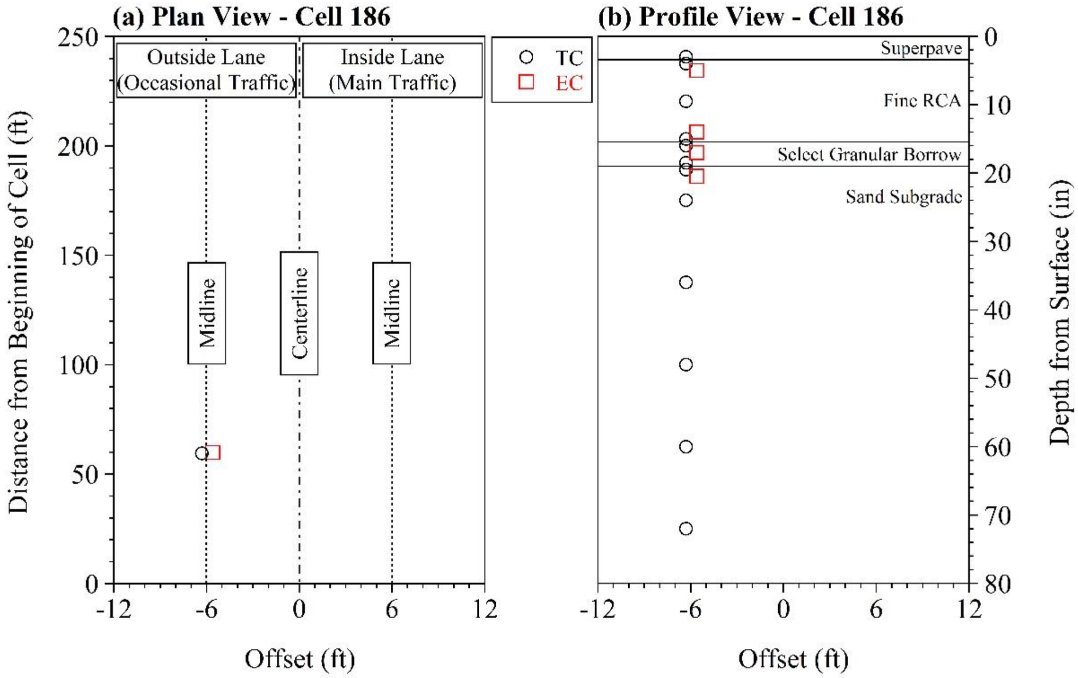

Figure 3.4. (a) Plan and (b) profile view of sensor locations in cell 186 (12 in fine RCA) (TC = thermocouple, EC = moisture probe)

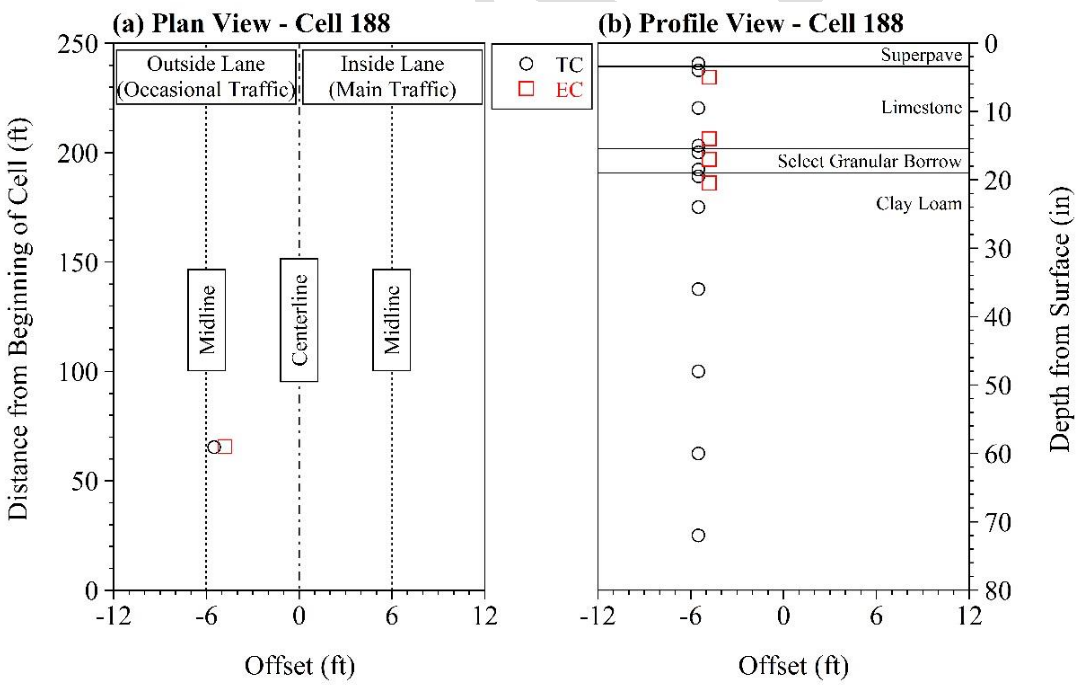

Figure 3.5. (a) Plan and (b) profile view of sensor locations in cell 188 (12 in limestone) (TC = thermocouple, EC = moisture probe)

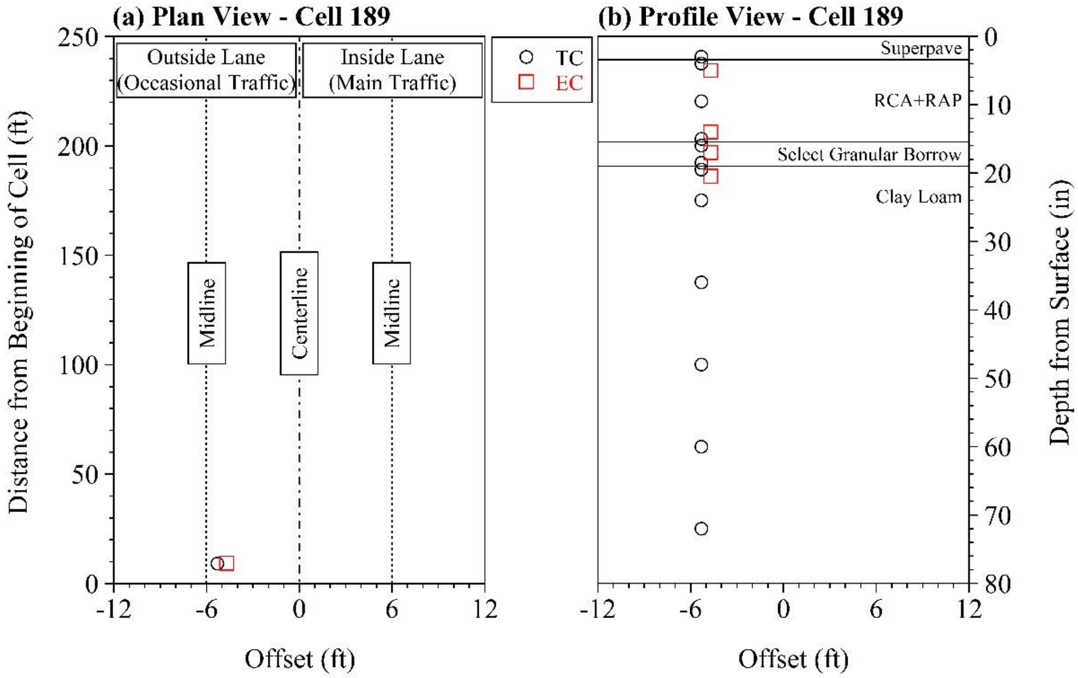

Figure 3.6. (a) Plan and (b) profile view of sensor locations in cell 189 (12 in RCA+RAP) (TC = thermocouple, EC = moisture probe)

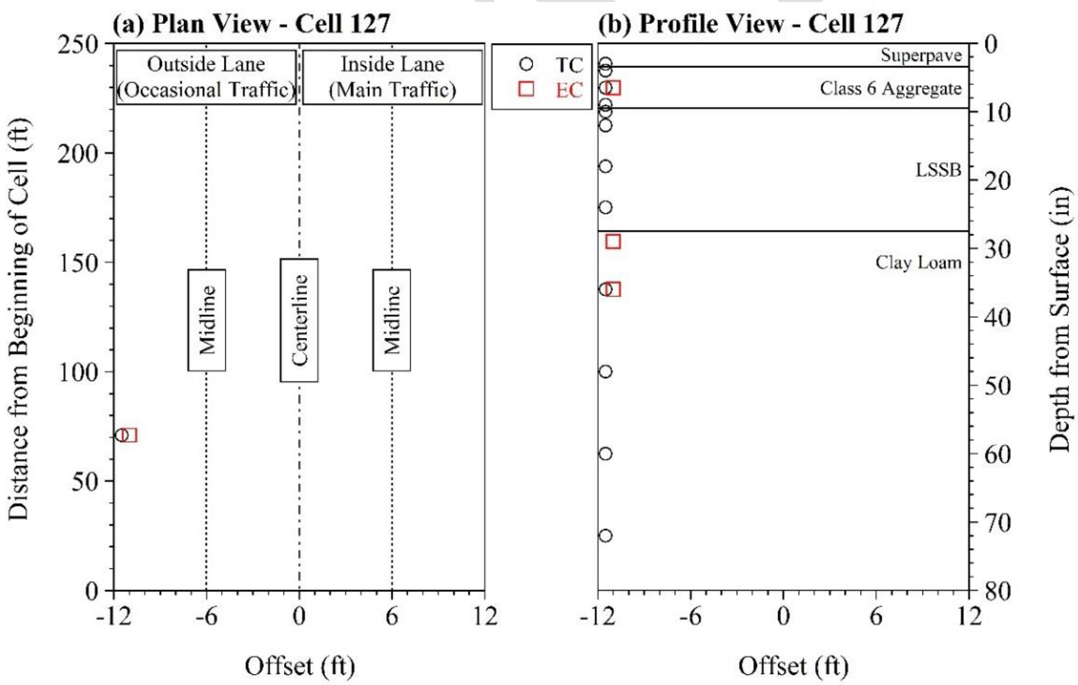

Figure 3.7. (a) Plan and (b) profile view of sensor locations in cell 127 (18 in LSSB) (TC = thermocouple, EC = moisture probe)

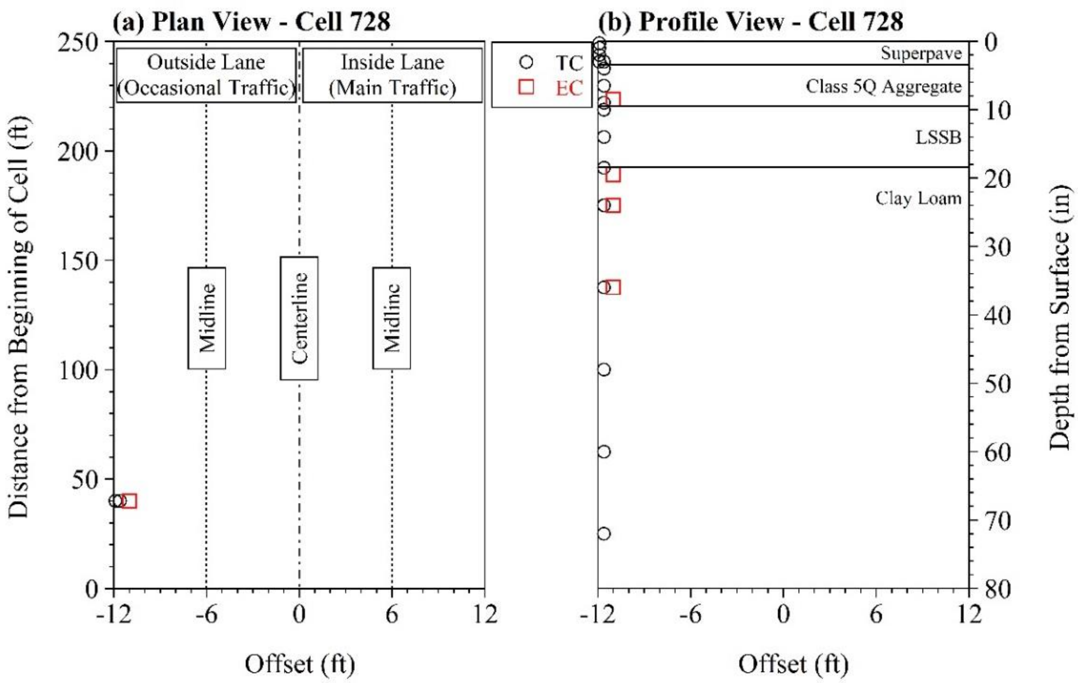

Figure 3.8. (a) Plan and (b) profile view of sensor locations in cell 728 (9 in LSSB) (TC = thermocouple, EC = moisture probe)

3.2. Temperature Profiles of the Select Test Cells

In general, the temperature of an asphalt pavement surface is prone to be different from air temperature. The difference is related to the composition, thermal properties, color, and texture of the asphalt material (Guan 2011). Light-colored materials have a higher albedo and can reflect more light than dark-colored materials. On the contrary, dark-colored materials tend to absorb heat and show lower albedo (Sailor 1995; Guan 2011). Since asphalt materials have a dark color (asphalt layer's color may fade depending on the age of the material), they are prone to absorb a high heat load and exhibit higher temperatures than air temperature (Guan 2011). Relatively rougher surfaces have more surface areas than smoother surfaces; therefore, materials having rougher surface properties can absorb more heat (Doulos et al. 2004). Briefly, asphalt surface layers are expected to be warmer than air under daylight. In addition, asphalt surface layers are expected to release the heat slowly over the night, which allows them to be warmer than air during night times (Buyantuyev and Wu 2010).

To compare the differences between air temperature and asphalt temperature at the test cells, the shallowest thermocouple [the one located at 0.3 in (7.6 mm) depth in the asphalt layer in cell 728 (9 in LSSB)] was selected. As expected, relatively higher temperature values were observed in the asphalt layer compared to air temperature (Figure 3.9).

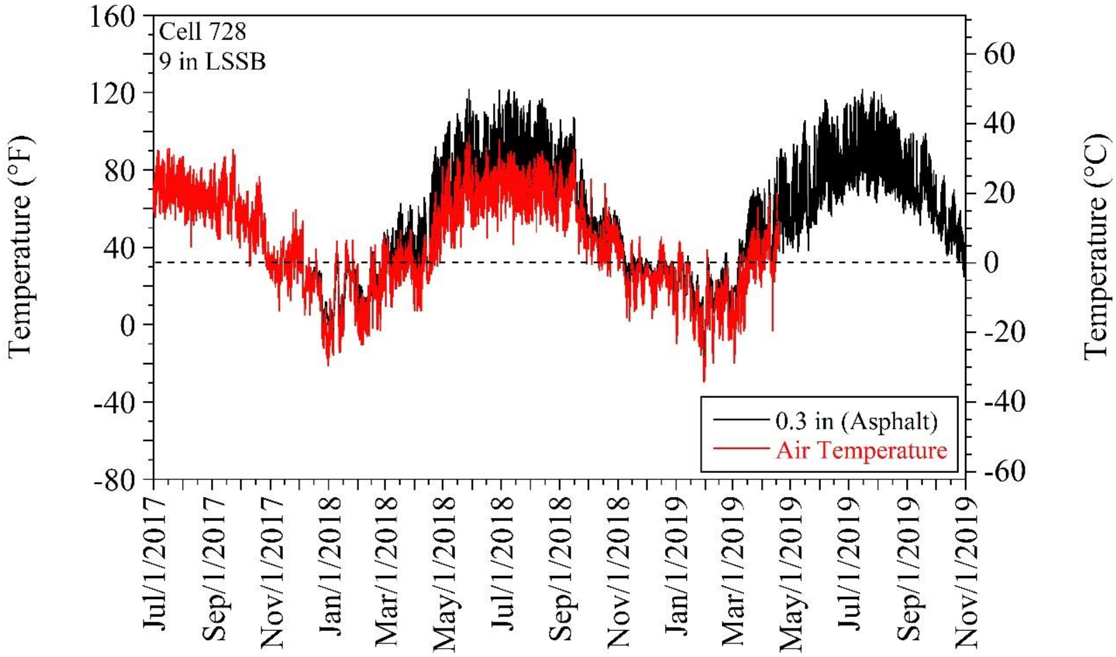

Figure 3.9. Differences between asphalt temperature and air temperature in cell 728 (9 in LSSB)

In the one-dimensional conduction heat transfer theory, the analytical solution to determine the soil temperature at a specific depth (z) and time (t) is shown in Equation (1) (Horton et al. 1983). In the given theory, the amplitude (A) decreases as soil depth increases, and the sinusoidal-like temperature curve shifts to the right as soil depth increases due to the phase constant (Figure 3.10) (Genc 2019). Time is required for heat transfer from higher elevations (closer to the surface) to lower elevations (deeper levels).

$$T(z,t) = \overline{T} + Ae^{-z\sqrt{\frac{\omega}{2\alpha}}} \sin\left(\omega t - z\sqrt{\frac{\omega}{2\alpha}} + C_4\right) \tag{1}$$

where; $\overline{T}$ is the average soil temperature, A is the surface amplitude of temperature, ω is the radial frequency $\left(\frac{2\pi}{p}\right)$, p is the period, and α is the thermal diffusivity, and C_4 is the phase constant.

Temperature readings taken from cells 185 (12 in coarse RCA), 186 (12 in fine RCA), 188 (12 in limestone), 189 (12 in RCA+RAP), 127 (18 in LSSB), and 728 (9 in LSSB) are provided in Figures 3.11, 3.12, 3.13, 3.14, 3.15, and 3.16, respectively. As the depth increased, the amplitude of the soil temperature curves decreased, and the curves shifted to the right. In addition, the temperature readings exhibited relatively higher fluctuations at the depths closer to the surface. On the other hand, the temperature readings became more stable and showed relatively lower fluctuations with depth over time. Thermocouple readings, taken from the asphalt layer in cell 728 (9 in LSSB) (at between 0.3-3 in depth), are provided in Appendix C.

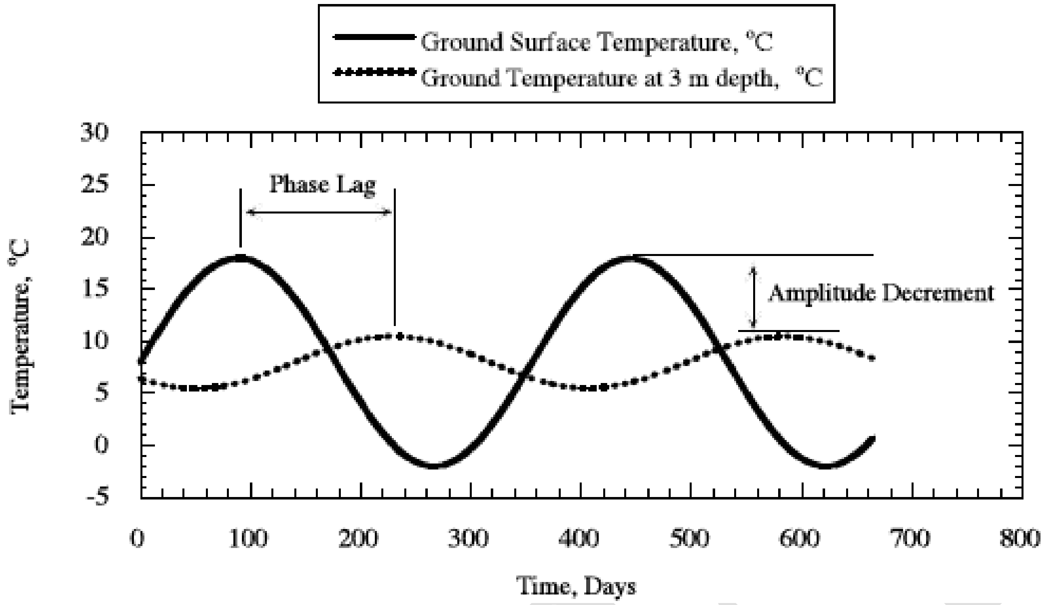

Figure 3.10. Effect of depth on the soil temperature curves (Hanson et al. 2000)

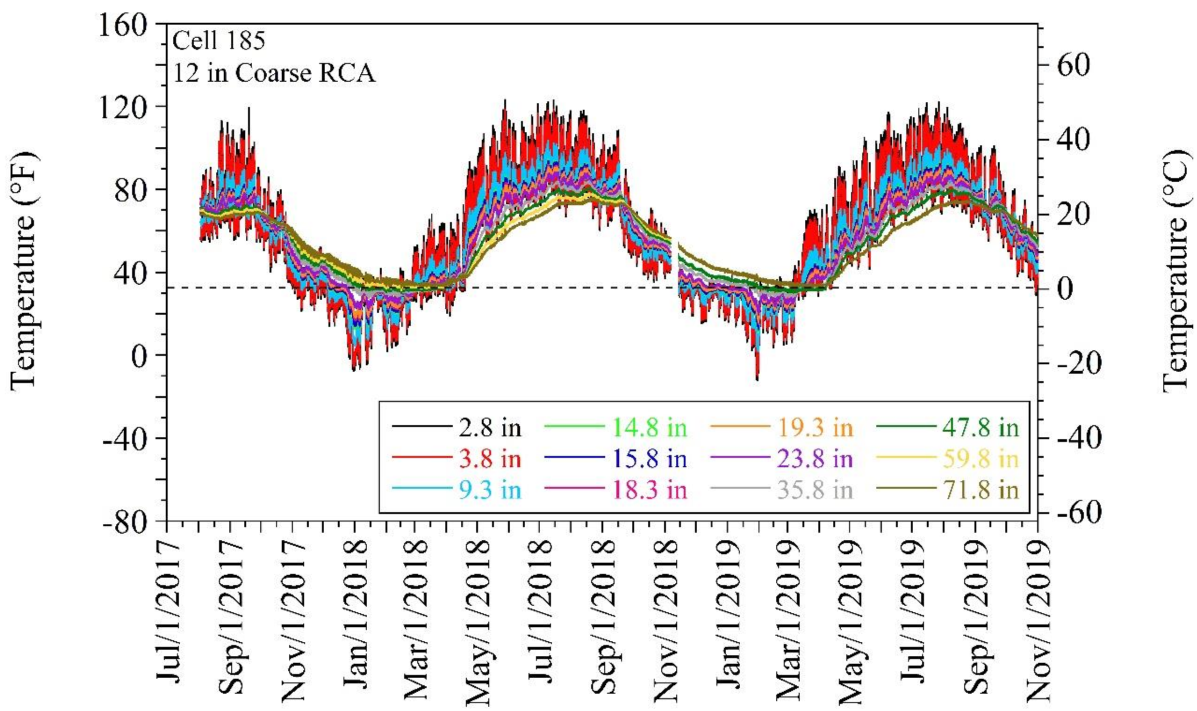

Figure 3.11. Temperature readings taken from cell 185 (12 in coarse RCA)

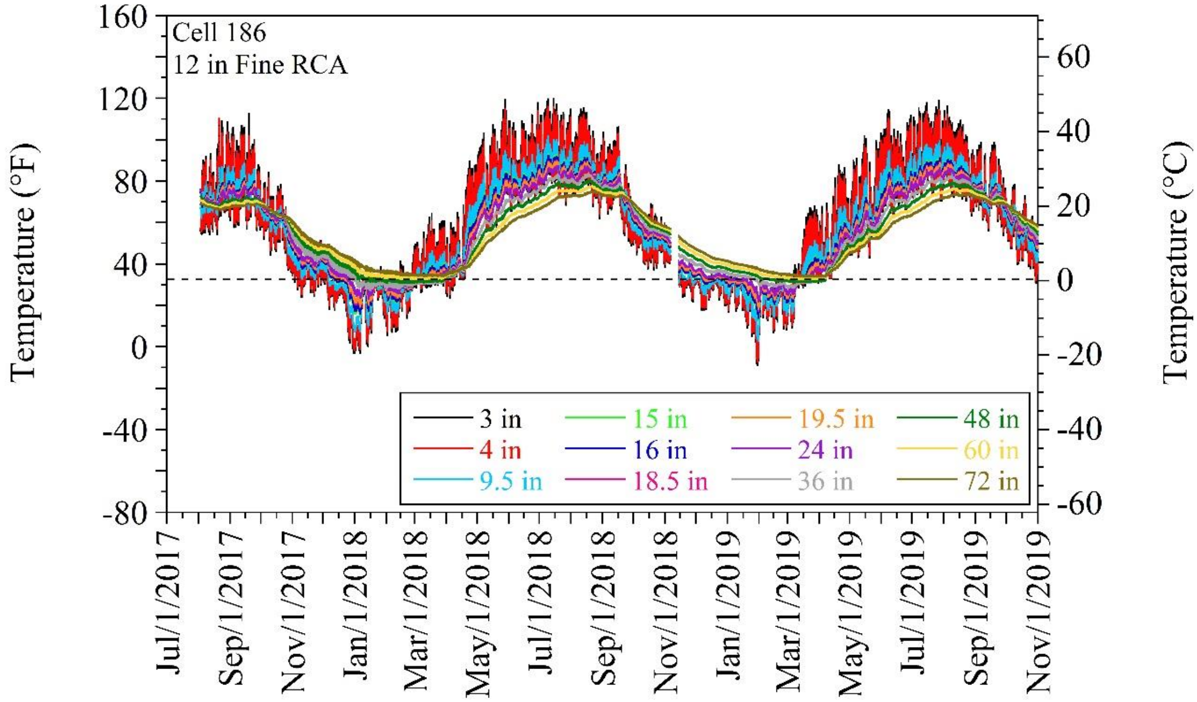

Figure 3.12. Temperature readings taken from cell 186 (12 in fine RCA)

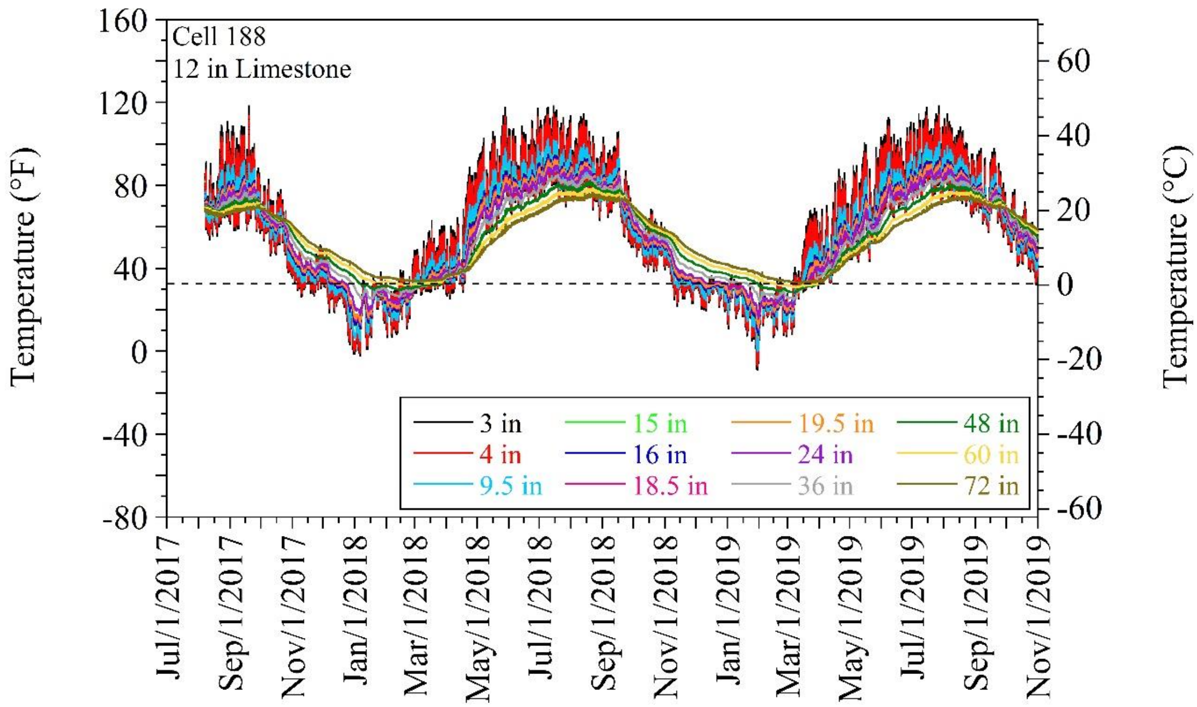

Figure 3.13. Temperature readings taken from cell 188 (12 in limestone)

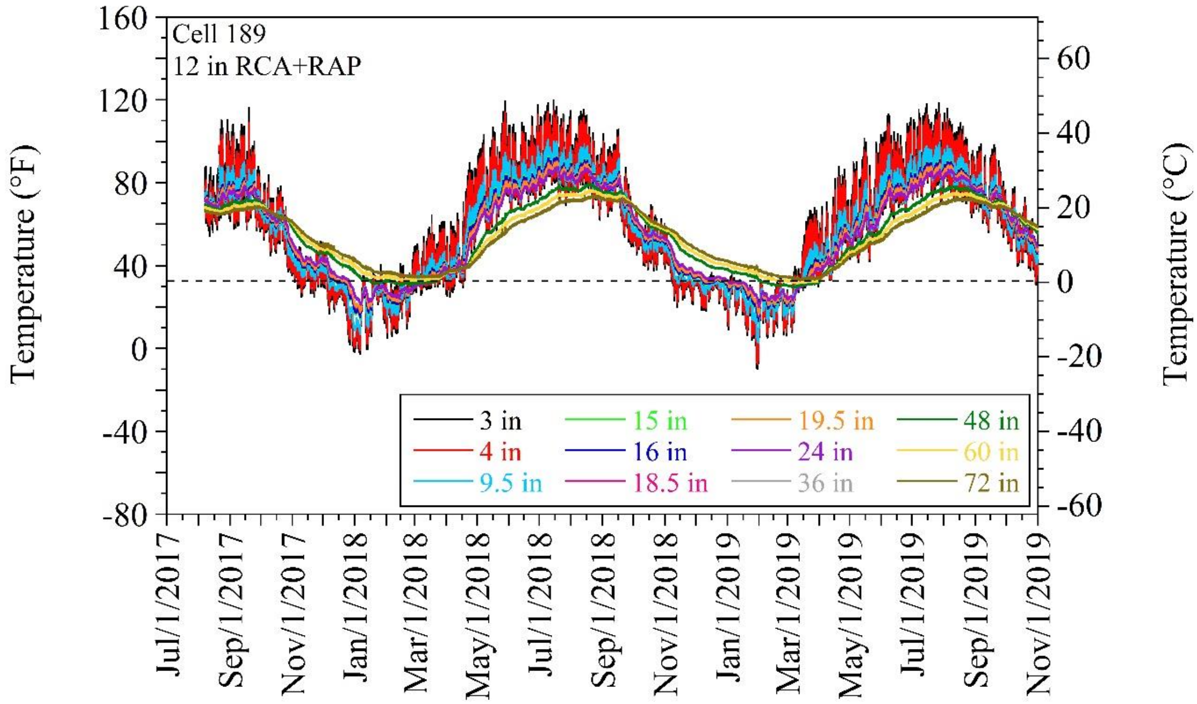

Figure 3.14. Temperature readings taken from cell 189 (12 in RCA+RAP)

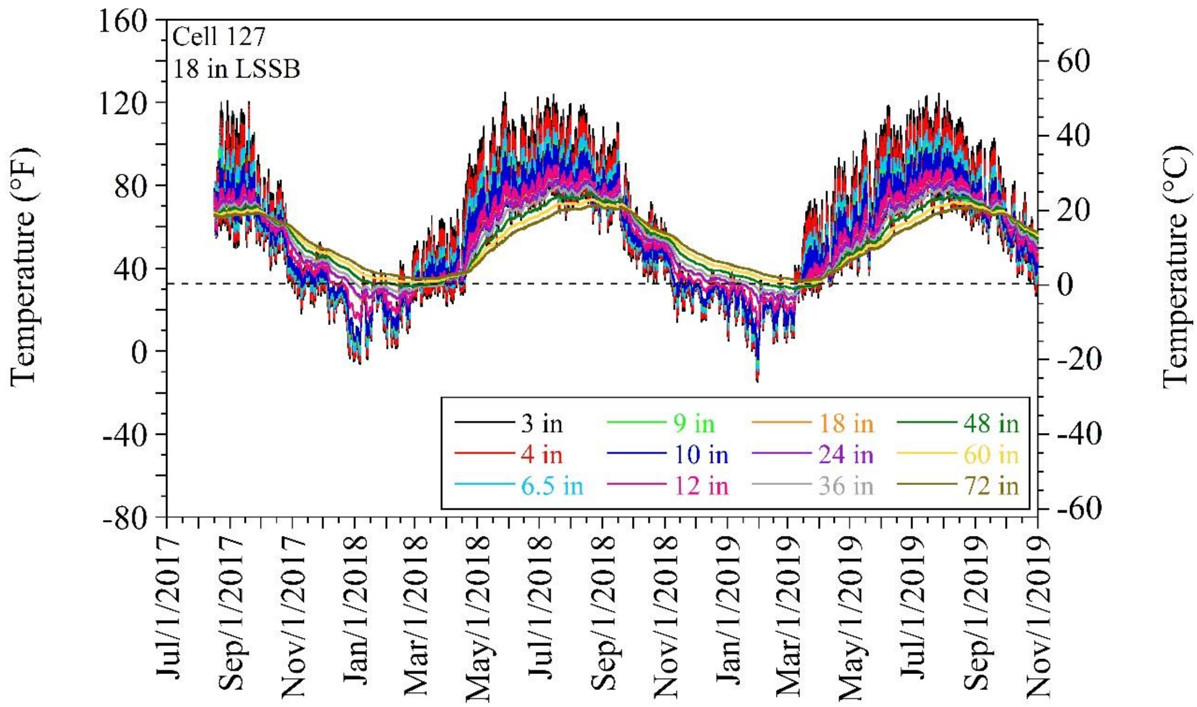

Figure 3.15. Temperature readings taken from cell 127 (18 in LSSB)

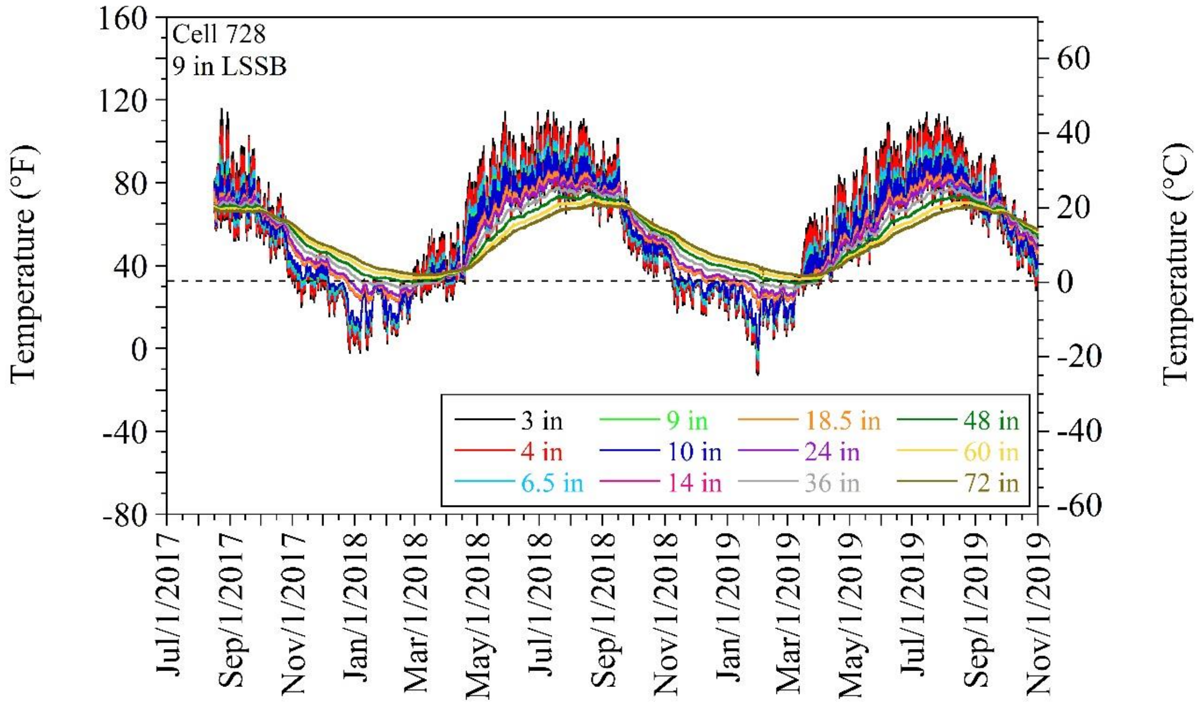

Figure 3.16. Temperature readings taken from cell 728 (9 in LSSB)

3.3. Volumetric Water Content (VWC) Profiles of the Select Test Cells

Moisture probes embedded in the test cells used the differences between dielectric constants of different soil phases to estimate volumetric water content (VWC) in the soil matrix. While air and dry soil have dielectric constants of about 1 and 4-16, respectively, the dielectric constant of liquid water is about 80 (Wraith and Or 1999; Bittelli 2011; Hallikainen et al. 1985). Therefore, soil medium with higher liquid water content has a higher dielectric constant.

When liquid water starts to freeze and transform to ice, its dielectric constant (about 80) begins to reduce, which also reduces the dielectric constant of the soil medium. Therefore, freezing events can be detected by observing sudden reductions in the VWC values over time. When the soil is fully frozen, its dielectric constant is expected to stay constant since there will be no change in the liquid water content under fully frozen conditions. Following the freezing and fully frozen conditions, thawing events can be determined from sudden increases in the VWC values over time. It is expected that the data obtained by the moisture probes to be compatible with the data collected by the thermocouples and demonstrate the freezing and thawing periods properly (Genc 2019).

Decagon's recommended calibration procedure was followed by the MnROAD staff to develop material-specific calibration equations for various base and subgrade materials to convert the collected raw data into VWC (MnDOT 2013b). The developed calibration equations and the properties of the materials used are provided in Appendix D.

Two-year VWC values for cells 185 (12 in coarse RCA), 186 (12 in fine RCA), 188 (12 in limestone), 189 (12 in RCA+RAP), 127 (18 in LSSB), and 728 (9 in LSSB) are provided in Figures 3.17, 3.18, 3.19, 3.20, 3.21, and 3.22, respectively [degree of saturation (DOS) values are provided in Appendix D]. The VWC values of the materials at the optimum moisture content (OMC) and maximum dry density (MDD) (determined by modified Proctor testing) are summarized in Table 3.2. Nuclear density gauge (NDG) readings, taken from the outside lanes of the test cells during construction (detailed information on construction monitoring and reporting is provided in Task 3 report), were converted to the VWC values, and the results are provided as box plots in Figure 3.23 and briefly summarized in Table 3.2. In addition, relative dry density and moisture content values of the base and subgrade layers in the outside lanes of cells 185 (12 in coarse RCA), 186 (12 in fine RCA), 188 (12 in limestone), 189 (12 in RCA+RAP), 127 (18 in LSSB), and 728 (9 in LSSB) (calculated based on the NDG measurements and laboratory OMC and MDD of the materials) are summarized in Figures 3.24 and 3.25, respectively. Overall, the results showed that the VWC values calculated from the NDG data collected from the outside lanes during construction were lower than the VWC values of the materials calculated based on laboratory compaction data at OMC and MDD (Table 3.2). In addition, it was observed that the base layers in the outside lanes of the test cells were compacted at the dry side of OMC (Figure 3.24). Therefore, the relative dry density values of the base layers were lower than 100% (Figure 3.25).

For cell 185 (12 in coarse RCA), continuous readings could not be taken from any of the pavement layers due to the malfunctioning of the moisture probes embedded in the test cell (Figure 3.17). For the 12 in coarse RCA base layer, the median VWC values recorded by the moisture probes on Aug/3/2017 [0.09 and 0.05 for the sensors at 5 and 14 in depths, respectively (Figure 3.17)] were lower than the VWC value of coarse RCA at OMC and MDD [0.20 (Table 3.2)] and the VWC values observed by NDG during construction on Aug/1/2017 [between 0.12 and 0.15 (Table 3.2)]. For the select granular borrow subbase layer, the median VWC value recorded by the moisture probe on Aug/3/2017 [0.06 for the sensor at 17 in depth (Figure 3.17)] was lower than the VWC values of select granular borrow at OMC and MDD [0.12 (Table 3.2)]. For the sand subgrade layer, the median VWC value recorded by the moisture probe on Aug/3/2017 [0.07 for the sensor at 20.5 in depth (Figure 3.17)] was lower than the VWC values of sand subgrade at OMC and MDD [0.12 (Table 3.2)] and comparable with the VWC values observed by NDG during construction on Jul/21/2017 [between 0.07 and 0.13 (Table 3.2)]. The data collected from cell 185 (12 in coarse RCA) between Aug 2017-Oct 2017 showed that the coarse RCA base layer (sensors were at 5 and 14 in depths) contained relatively higher VWC than the select granular borrow subbase (sensor was at 17 in depth) and sand subgrade layers (sensor was at 20.5 in depth) (Figure 3.17).

For cell 186 (12 in fine RCA), no continuous VWC readings were able to be taken from the select granular borrow subbase (sensor was at 17 in depth) and the bottom of the fine RCA base layer (sensor was at 14 in depth). Also, the sensor embedded at 20.5 in depth (in the sand subgrade) exhibited highly fluctuated data, which could be the indication of malfunctioning of that sensor, too. For the 12 in fine RCA base layer, the median VWC values recorded by the moisture probes on Aug/3/2017 [0.11 for both of the sensors at 5 and 14 in depths (Figure 3.18)] were lower than the VWC values of fine RCA at OMC and MDD [0.22 (Table 3.2)] and the VWC values observed by NDG during construction on Aug/1/2017 [between 0.13 and 0.17 (Table 3.2)]. For the select granular borrow subbase layer, the median VWC value recorded by the moisture probe on Aug/3/2017 [0.05 for the sensor at 17 in depth (Figure 3.18)] was lower than the VWC value of select granular borrow at OMC and MDD [0.12 (Table 3.2)]. For the sand subgrade layer, the median VWC value recorded by the moisture probe on Aug/3/2017 [0.06 for the sensor at 20.5 in depth (Figure 3.18)] was lower than the VWC value of sand subgrade at OMC and MDD [0.12 (Table 3.2)]. For the top of the fine RCA base layer (sensor was at 5 in depth), the VWC values reacted to freezing (decrease in the values) and thawing (increase in the values) between Nov 2017-Apr 2018 and Nov 2018-Apr 2019. Other times when no freezing or thawing occurred, the VWC values reacted to precipitation (Figure 2.2). During precipitation (Jul 2017-Nov 2017 and May 2018-Oct 2019) (Figure 2.2), slight increases in the VWC values were observed.

For cell 188 (12 in limestone), continuous readings were taken from the pavement sublayers. For the 12 in limestone base layer, the median VWC values recorded by the moisture probes on Aug/7/2017 [0.02 and 0.03 for the sensors at 5 and 14 in, respectively (Figure 3.19)] were lower than the VWC value of limestone at OMC and MDD [0.14 (Table 3.2)] and the VWC values observed by NDG during construction on Aug/1/2017 [between 0.09 and 0.11 (Table 3.2)]. For the select granular borrow subbase layer, the median VWC value recorded by the moisture probe on Aug/7/2017 [0.05 for the sensor at 17 in depth (Figure 3.19)] was lower than the VWC value of select granular borrow at OMC and MDD [0.12 (Table 3.2)]. For the clay loam subgrade layer, the median VWC value recorded by the moisture probe on Aug/7/2017 [0.07 for the sensor at 20.5 in depth (Figure 3.19)] was lower than the VWC value of clay loam at OMC and MDD [0.20 (Table 3.2)] and comparable with the VWC values observed by NDG during construction on Jul/25/2017 [between 0.04 and 0.15 (Table 3.2)]. For the top and bottom of the limestone base layer (sensors were at 5 and 14 in depths, respectively), similar VWC values were observed, and these values were lower than those observed in the select granular borrow subbase (sensor was at 17 in depth) and clay loam subgrade layers (sensor was at 20.5 in depth). The VWC values of the select granular borrow subbase (sensor was at 17 in depth) were slightly lower than those of the clay loam subgrade (sensor was at 20.5 in depth) (the difference was more considerable between freezing and thawing events). The sensor data showed that the VWC values reacted to freezing and thawing between Nov 2017-Apr 2018 and Nov 2018-Apr 2019.

For cell 189 (12 in RCA+RAP), continuous readings were taken from the pavement sublayers. For the 12 in RCA+RAP base layer, the median VWC values recorded by the moisture probes on Aug/7/2017 [0.07 and 0.04 for the sensors at 5 and 14 in, respectively (Figure 3.20)] were lower than the VWC value of RCA+RAP at OMC and MDD [0.20 (Table 3.2)] and the VWC values observed by NDG during construction on Aug/1/2017 [between 0.09 and 0.14 (Table 3.2)]. For the select granular borrow subbase layer, the median VWC value recorded by the moisture probe on Aug/7/2017 [0.10 for the sensor at 17 in depth (Figure 3.20)] was lower than the VWC value of select granular borrow at OMC and MDD [0.12 (Table 3.2)]. For the clay loam subgrade layer, the median VWC value recorded by the moisture probe on Aug/7/2017 [0.11 for the sensor at 20.5 in depth (Figure 3.20)] was lower than the VWC value of clay loam at OMC and MDD [0.20 (Table 3.2)] and comparable with the VWC values observed by NDG during construction on Jul/25/2017 [between 0.06 and 0.13 (Table 3.2)]. Unlike the trend observed in the limestone base layer in cell 188 (12 in limestone), the bottom of the RCA+RAP base layer (sensor was at 14 in depth) exhibited lower VWC values than the top of the same layer (sensor was at 5 in depth). Overall, the VWC values of the RCA+RAP base layer (sensors were at 5 in and 14 in depths) were lower than those of the select granular borrow subbase (sensor was at 17 in depth) and clay loam subgrade layers (sensor was at 20.5 in depth). The select granular borrow subbase layer (sensor was at 17 in depth) exhibited lower VWC values than the clay loam subgrade layer (sensor was at 20.5 in depth). The sensor data showed that the VWC values reacted to freezing and thawing between Nov 2017-Apr 2018 and Nov 2018-Apr 2019. During late spring, summer, and fall seasons (Jul 2017-Nov 2017 and May 2018-Oct 2019), slight increases in the VWC values were observed due to precipitation (Figure 2.2).

For cell 127 (18 in LSSB), continuous readings were taken from the pavement sublayers. For the 6 in class 6 aggregate base layer, the median VWC value recorded by the moisture probe on Aug/28/2017 [0.08 for the sensor at 6.5 in depth (Figure 3.21)] was lower than the VWC value of class 6 aggregate at OMC and MDD [0.17 (Table 3.2)] and the VWC values observed by NDG during construction on Aug/21/2017 [between 0.10 and 0.11 (Table 3.2)]. For the clay loam subgrade layer, the median VWC values recorded by the moisture probes on Aug/16/2017 [0.29 and 0.27 for the sensors at 29 and 36 in depths, respectively (Figure 3.21)] was higher than the VWC value of clay loam at OMC and MDD [0.20 (Table 3.2)]. The middle of the class 6 aggregate base layer (sensor was at 6.5 in depth) exhibited considerably lower VWC values than the clay loam subgrade layer (sensors were at 29 and 36 in depths). This could indicate that the drainage provided by the 18 in LSSB layer was efficient. The sensor at a higher elevation (at 29 in depth) in the clay loam subgrade layer exhibited slightly higher VWC values than the sensor at a lower elevation (at 36 in depth) in the same layer. All of the sensor readings at this cell reacted to freezing and thawing between Nov 2017-Apr 2018 and Nov 2018-Apr 2019. In addition, rainy periods (Jul 2017-Nov 2017 and May 2018-Oct 2019) (Figure 2.2) caused slight increases in the VWC values of the clay loam subgrade (sensors were at 29 and 36 in depths). On the other hand, the middle of the class 6 aggregate base layer (sensor was at 6.5 in depth) did not exhibit such an increase due to precipitation. This could also indicate the presence of an effective drainage system due to the 18 in LSSB layer.

For cell 728 (9 in LSSB), continuous readings were taken from the pavement sublayers. For the 6 in class 5Q aggregate base layer, the median VWC value recorded by the moisture probe on Aug/21/2017 [0.11 for the sensor at 8.5 in depth (Figure 3.22)] was lower than the VWC value of class 5Q aggregate at OMC and MDD [0.20 (Table 3.2)] and the VWC values observed by NDG during construction on Aug/21/2017 [between 0.15 and 0.16 (Table 3.2)]. For the clay loam subgrade layer, the median VWC values recorded by the moisture probes on Aug/16/2017 [0.20, 0.16, and 0.24 for the sensors at 19.5, 24, and 36 in depths, respectively (Figure 3.22)] were lower than, equal to, or higher than the VWC value of clay loam at OMC and MDD [0.20 (Table 3.2)]. The bottom of the class 5Q aggregate base layer (sensor was at 8.5 in depth) exhibited considerably lower VWC values than the clay loam subgrade layer (sensors were at 19.5, 24, and 36 in depths). Similar to cell 127 (18 in LSSB), this result could indicate that effective drainage was provided by the 9 in LSSB layer in cell 728. Different VWC values were observed at different elevations in the clay loam subgrade (sensors were at 19.5, 24, and 36 in depths). While the top of the clay loam subgrade (sensor was at 19.5 in depth) exhibited lower VWC values than the lower subgrade levels, the VWC values were higher at 24 in depth (from the surface) in the subgrade layer. Similar to the other cells, all of the sensor readings in cell 728 (9 in LSSB) reacted to freezing and thawing between Nov 2017-Apr 2018 and Nov 2018-Apr 2019. In addition, precipitation events caused slight increases in the VWC values of the subgrade layer during the rainy periods [Jul 2017-Nov 2017 and May 2018-Nov 2018] (Figure 2.2). No considerable change in the VWC was observed in the bottom of the class 5Q aggregate base layer, possibly due to the good drainage properties of the 9 in LSSB layer.

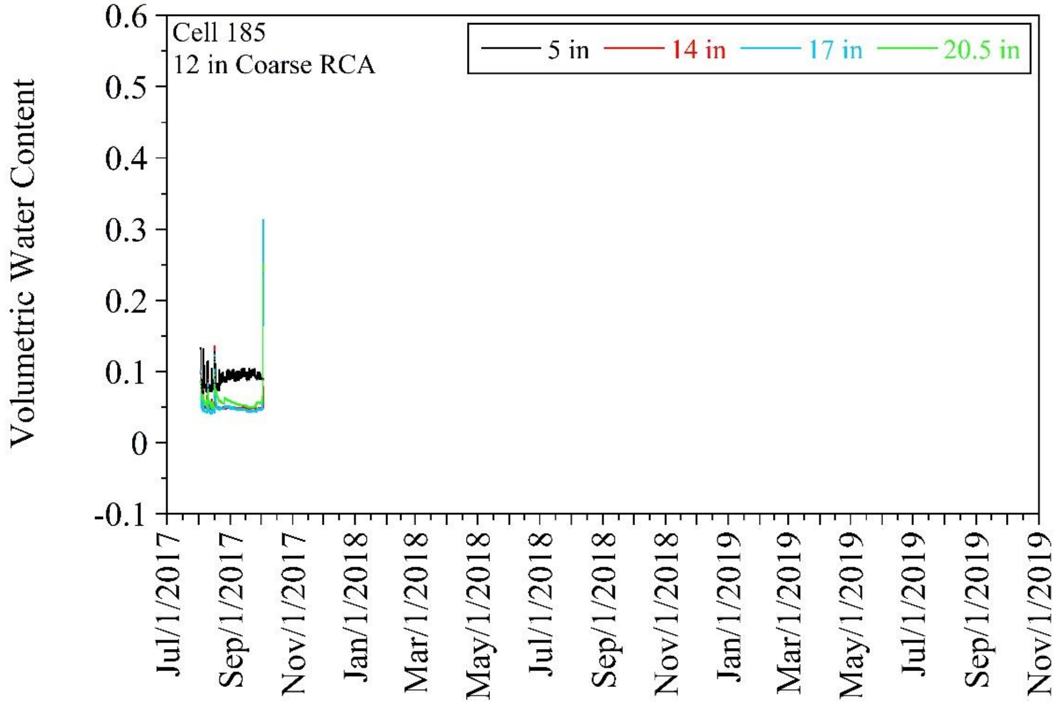

Figure 3.17. Volumetric water content (VWC) data taken from cell 185 (12 in Coarse RCA)

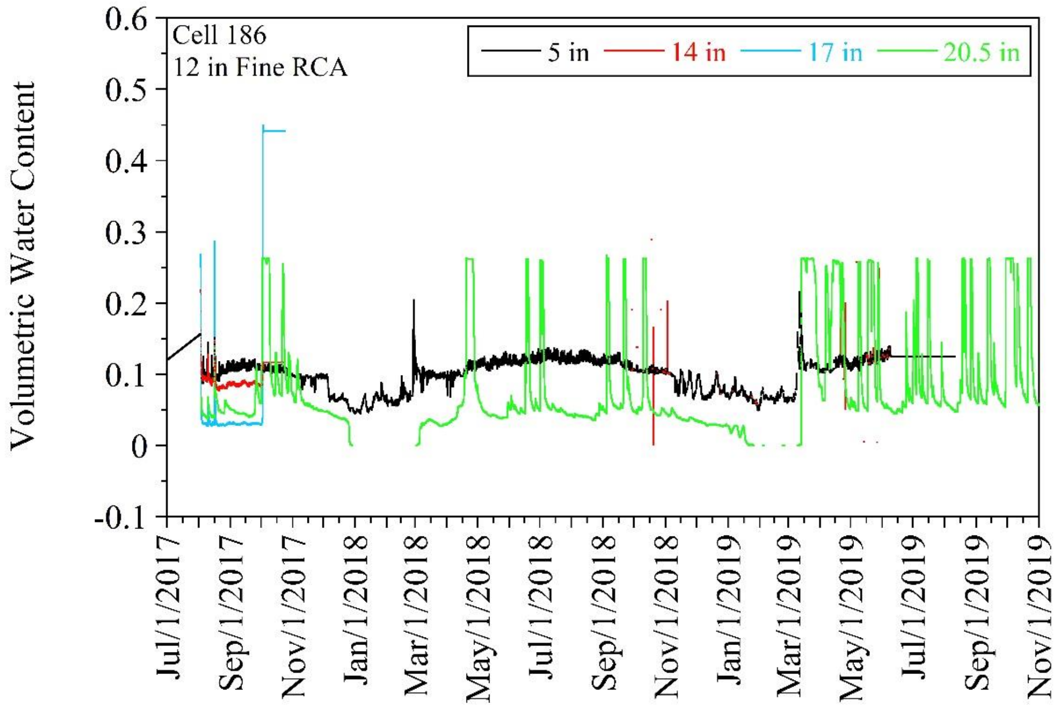

Figure 3.18. Volumetric water content (VWC) data taken from cell 186 (12 in Fine RCA)

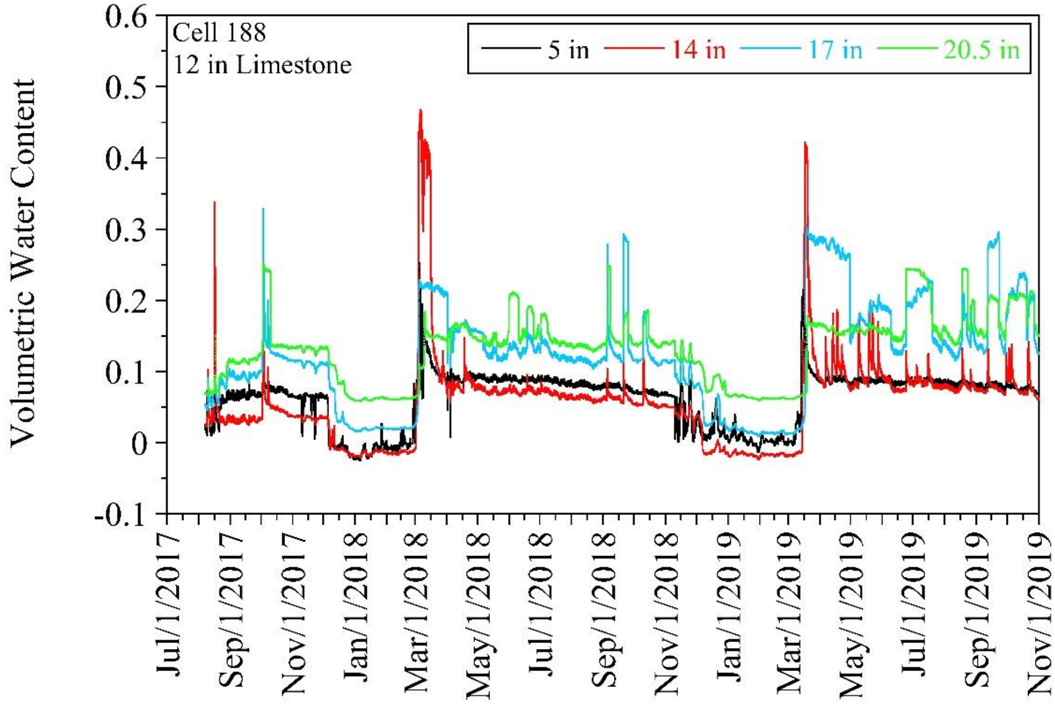

Figure 3.19. Volumetric water content (VWC) data taken from cell 188 (12 in Limestone)

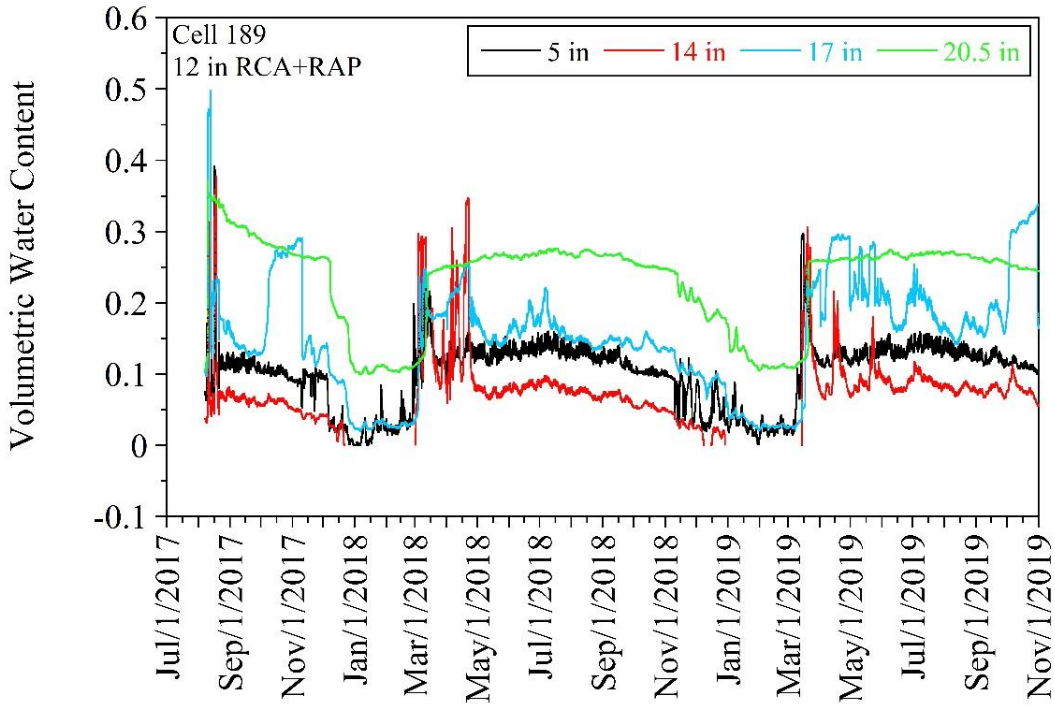

Figure 3.20. Volumetric water content (VWC) data taken from cell 189 (12 in RCA+RAP)

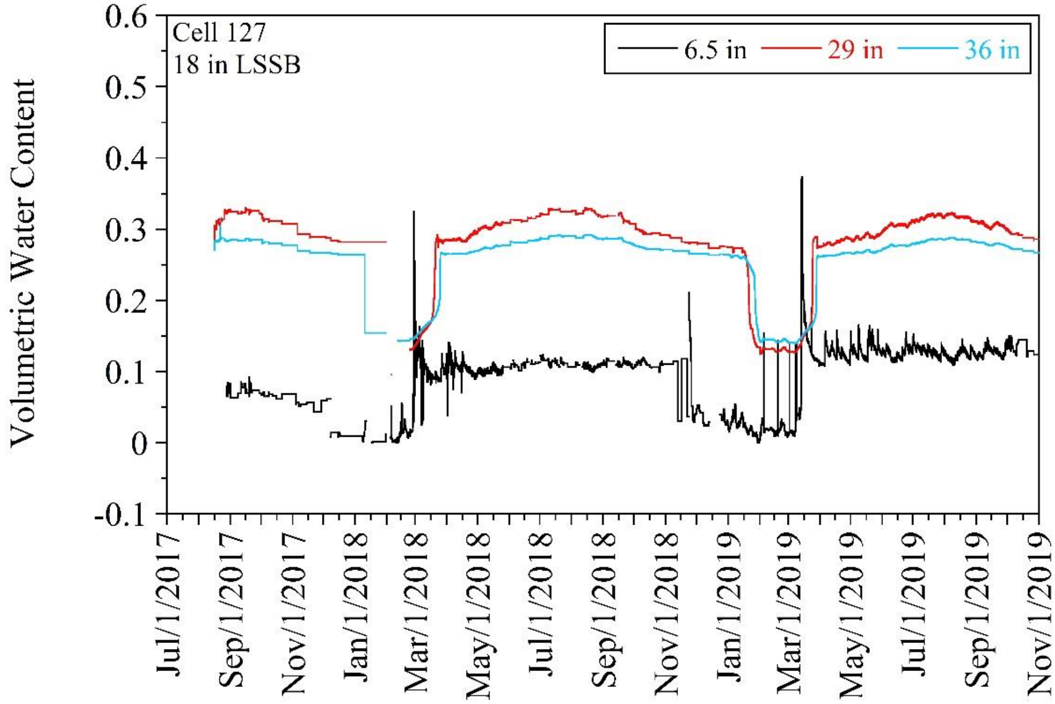

Figure 3.21. Volumetric water content (VWC) data taken from cell 127 (18 in LSSB)

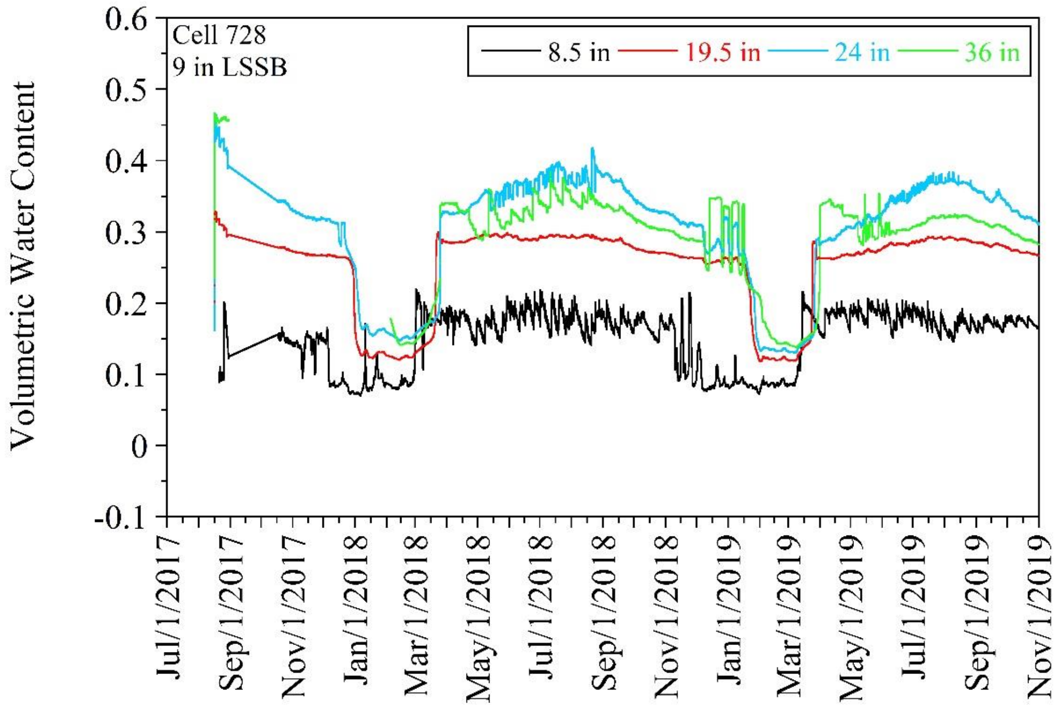

Figure 3.22. Volumetric water content (VWC) data taken from cell 728 (9 in LSSB)

Table 3.2. Volumetric water content (VWC) values of the materials calculated based on laboratory compaction data at optimum moisture content (OMC) and maximum dry density (MDD) and VWC values calculated from nuclear density gauge (NDG) data taken from the outside lanes of the test cells during construction

Material	VWC at OMC and MDD	VWC Taken by NDG During Construction
Sand Subgrade	0.12	0.07 - 0.13 (cell 185)
Clay Loam	0.20	0.04 - 0.15 (cell 188) 0.06 - 0.13 (cell 189)
Select Granular Borrow	0.12	NA
LSSB	NA	NA
Coarse RCA	0.20	0.12 - 0.15 (cell 185)
Fine RCA	0.22	0.13 - 0.17 (cell 186)
Limestone	0.14	0.09 - 0.11 (cell 188)
RCA+RAP	0.20	0.09 - 0.14 (cell 189)
Class 6 Aggregate	0.17	0.10 - 0.11 (cell 127)
Class 5Q Aggregate	0.20	0.15 - 0.16 (cell 728)

NA = not available.

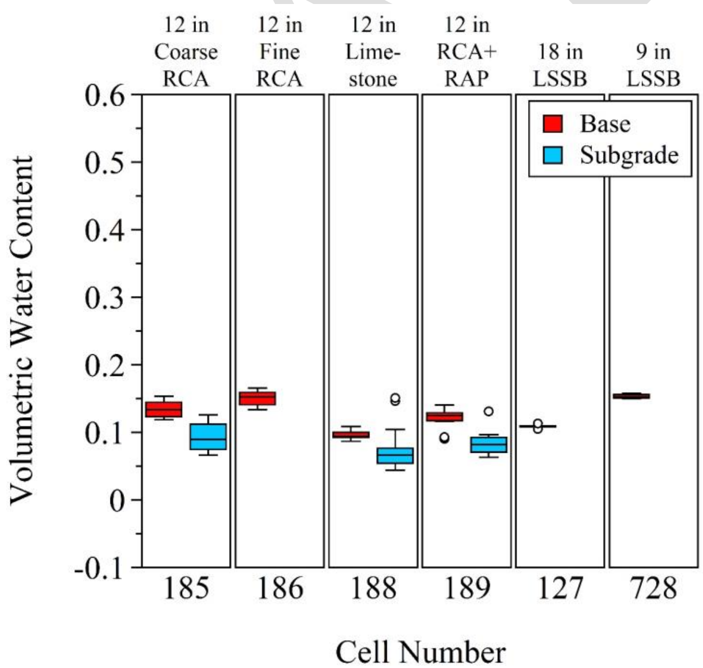

Figure 3.23. Volumetric water content (VWC) data calculated from nuclear density gauge (NDG) data taken from the outside lanes of the test cells during construction

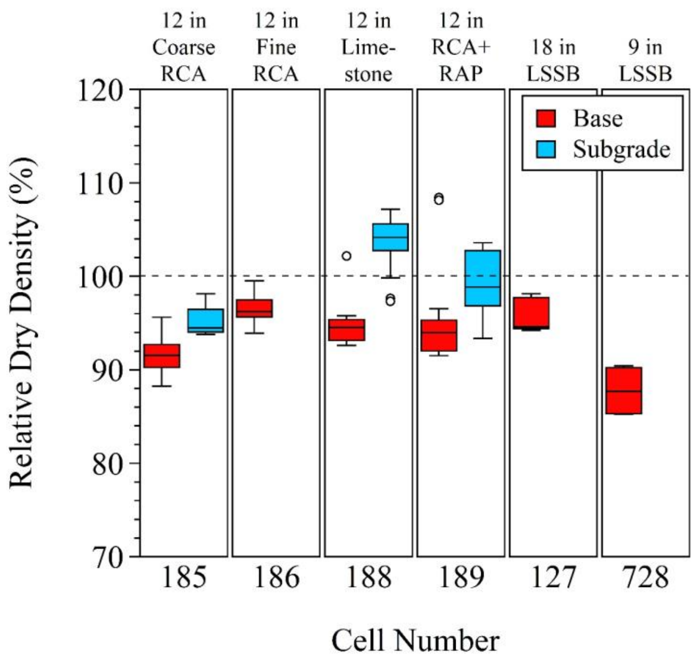

Figure 3.24. Relative dry density of the base and subgrade layers in the outside lanes of cells 185 (12 in coarse RCA), 186 (12 in fine RCA), 188 (12 in limestone), 189 (12 in RCA+RAP), 127 (18 in LSSB), and 728 (9 in LSSB)

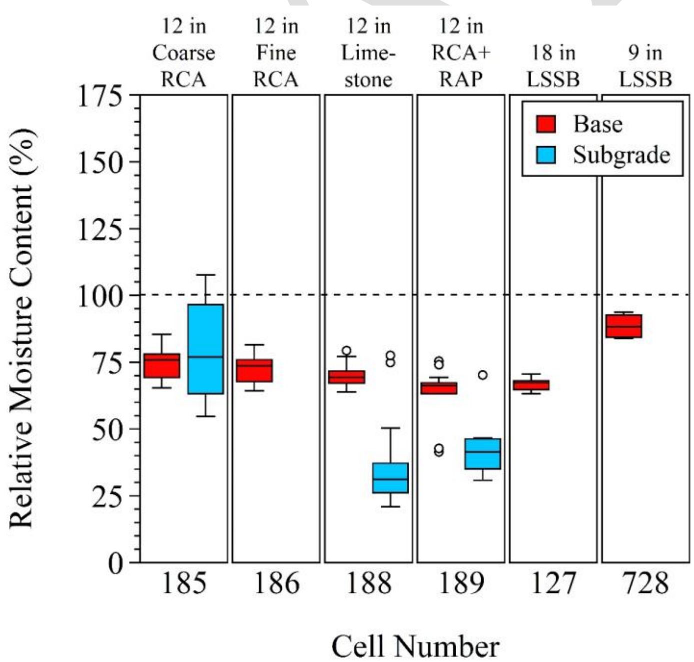

Figure 3.25. Relative moisture content of the base and subgrade layers in the outside lanes of cells 185 (12 in coarse RCA), 186 (12 in fine RCA), 188 (12 in limestone), 189 (12 in RCA+RAP), 127 (18 in LSSB), and 728 (9 in LSSB)

3.4. Annual Frost Penetration Depths

Water in soil/aggregate voids is expected to exhibit a freezing point that is lower than 32°F (0°C) (freezing-point depression) due to the presence of solutes (minerals, other chemicals, etc.). Rosa et al. (2016) and Edil et al. (2017) reported different freezing point temperatures for different soils and aggregates. According to Edil et al. (2017), while the freezing point of water in natural aggregate [Class 5 (MnDOT 2018)] was -5.2°C (22.6°F), it was -10°C (14°F) for RAP materials. However, many studies considered the freezing point of soil/aggregate water to be 0°C (Genc 2019). Since there was no sensor installed in the test cells that could determine the impurity of the soil/aggregate water, 0°C was selected to be the freezing point of water in this research.

0°C isotherm points were selected from the temperature profiles [Figures 3.11, 3.12, 3.13, 3.14, 3.15, and 3.16 for cells 185 (12 in coarse RCA), 186 (12 in fine RCA), 188 (12 in limestone), 189 (12 in RCA+RAP), 127 (18 in LSSB), and 728 (9 in LSSB), respectively] (Andersland and Ladanyi 2004; Zhang 2016; Li 2017) to determine the frost penetration depth of each test cell over time. A group of 0°C isotherm points generated a 0°C isotherm region, and the inner area of such a region represented the frozen zones (Zhang 2016). The deepest 0°C isotherm points were used to determine the maximum frost penetration depth. An example of the determination of the maximum frost penetration depth and freezing and thawing periods is provided in Figure 3.26.

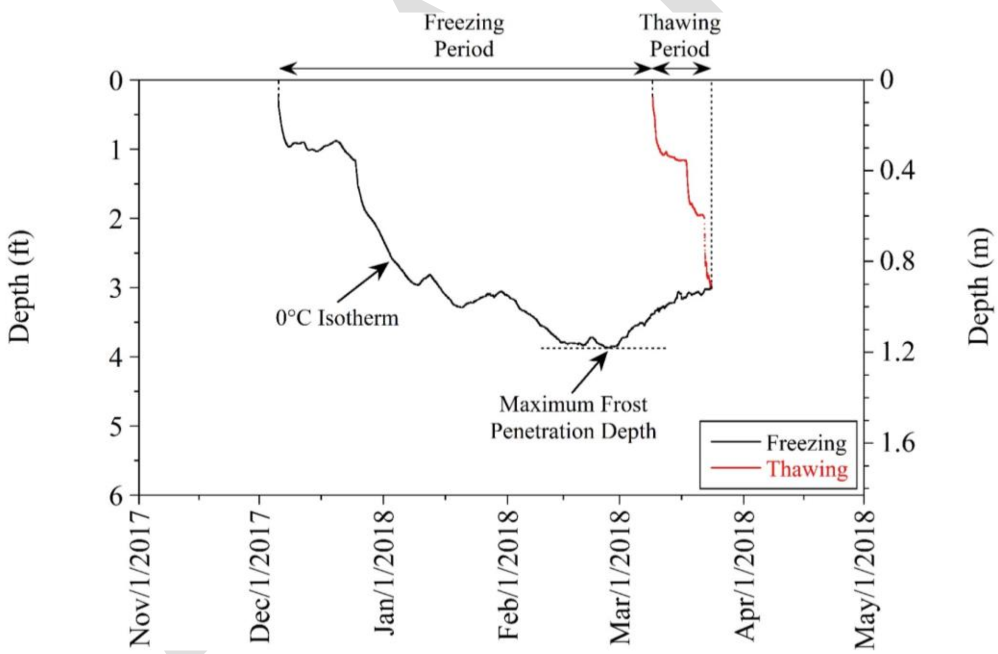

Figure 3.26. Maximum frost penetration depth and freezing and thawing periods

Two-year frost penetration depths determined for cells 185 (12 in coarse RCA), 186 (12 in fine RCA), 188 (12 in limestone), 189 (12 in RCA+RAP), 127 (18 in LSSB), and 728 (9 in LSSB) are provided in Figures 3.27, 3.28, 3.29, 3.30, 3.31, and 3.32, respectively. Summaries of the maximum frost penetration depths and the freezing and thawing periods for the monitored test cells [cells 185 (12 in coarse RCA), 186 (12 in fine RCA), 188 (12 in limestone), 189 (12 in RCA+RAP), 127 (18 in LSSB), and 728 (9 in LSSB)] are provided in Tables 3.3 and 3.4, respectively.

In the 2017-2018 winter, the shallowest maximum frost penetration depth was 3.87 ft (1.18 m), and it was observed in cell 728 (9 in LSSB). In the same winter, the deepest maximum penetration depth was 4.9 ft (1.49 m), and it was observed in cell 188 (12 in limestone). For cells 185 (12 in coarse RCA), 186 (12 in fine RCA), 189 (12 in RCA+RAP), and 127 (18 in LSSB), the maximum frost penetration depths were 4.44 ft (1.35 m), 4.24 ft (1.29 m), 4.47 ft (1.36 m), and 4.29 ft (1.31 m), respectively, in the 2017-2018 winter. In the 2018-2019 winter, all of the observed frost penetration depths were deeper than those observed in the 2017-2018 winter [the difference between the maximum frost penetration depths in these winters were between 0.15-0.62 ft (0.05-0.19 m)]. In the 2018-2019 winter, the shallowest maximum frost penetration depth was 4.17 ft (1.27 m), and it was observed in cell 728 (9 in LSSB). In the same winter, the deepest maximum frost penetration depth was 5.52 ft (1.68 m), and it was observed in cell 188 (12 in limestone). The maximum frost penetration depths of cells 185 (12 in coarse RCA), 186 (12 in fine RCA), 189 (12 in RCA+RAP), and 127 (18 in LSSB) in the 2018-2019 winter were 4.75 ft (1.45m), 4.39 ft (1.34 m), 5.09 ft (1.55 m), and 4.81 ft (1.47 m), respectively.

In 2017-2018, the freezing periods were between 83 and 94 days. For cells 185 (12 in coarse RCA), 186 (12 in fine RCA), 188 (12 in limestone), 189 (12 in RCA+RAP), 127 (18 in LSSB), and 728 (9 in LSSB), the freezing periods were 83, 84, 84, 84, 84, and 94 days, respectively. In the same year, the thawing periods were much shorter than the freezing periods, and they were between 15 and 28 days. For cells 185 (12 in coarse RCA), 186 (12 in fine RCA), 188 (12 in limestone), 189 (12 in RCA+RAP), 127 (18 in LSSB), and 728 (9 in LSSB), the thawing periods were 25, 28, 18, 16, 28, and 15 days, respectively. In 2018-2019, the freezing periods were between 116 and 124 days, and the effect of the 2018-2019 winter was expected to be higher than the 2017-2018 winter. For cells 185 (12 in coarse RCA), 186 (12 in fine RCA), 188 (12 in limestone), 189 (12 in RCA+RAP), 127 (18 in LSSB), and 728 (9 in LSSB), the freezing periods were 116, 116, 121, 120, 121, and 124 days, respectively. Similar to 2017-2018, the thawing periods (between 17 and 27 days) in 2018-2019 were much shorter than the freezing periods (between 116 and 124 days). While it was determined that the 2018-2019 winter was much longer than the 2017-2018 winter, no significant differences were observed between the two years in terms of the thawing periods. This indicates that the thawing periods of the base and subbase layers do not change significantly with a difference within different seasonal changes in the weather.

It was speculated that the difference in the maximum frost penetration depths and the freezing and thawing periods for different test cells can be related to the thermal properties (thermal conductivity, heat capacity, and thermal diffusivity) of each material used in the test cells. Laboratory tests to determine the thermal properties of each material will be conducted later on to explain these results properly, even though it was not within the scope of this study. In addition, the thermal diffusivity of each material will be calculated from the field observations (Figures 3.11 – 3.16). More detailed information regarding this will be provided in the final report.

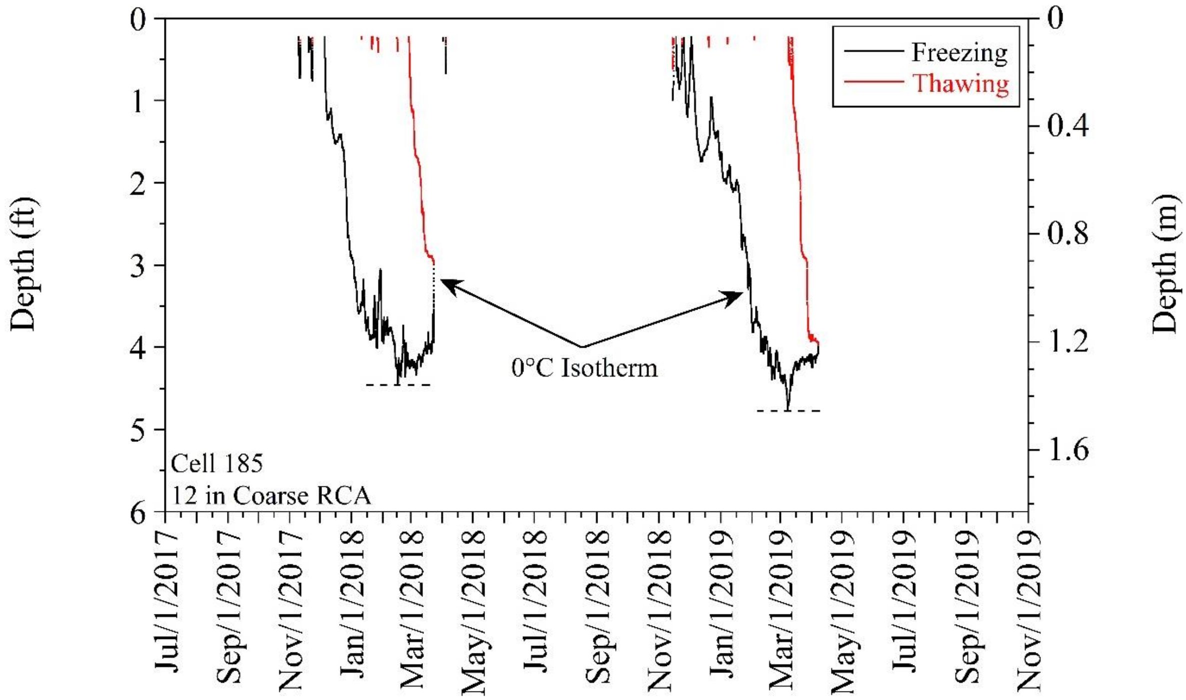

Figure 3.27. Two-year frost penetration depths in cell 185 (12 in Coarse RCA)

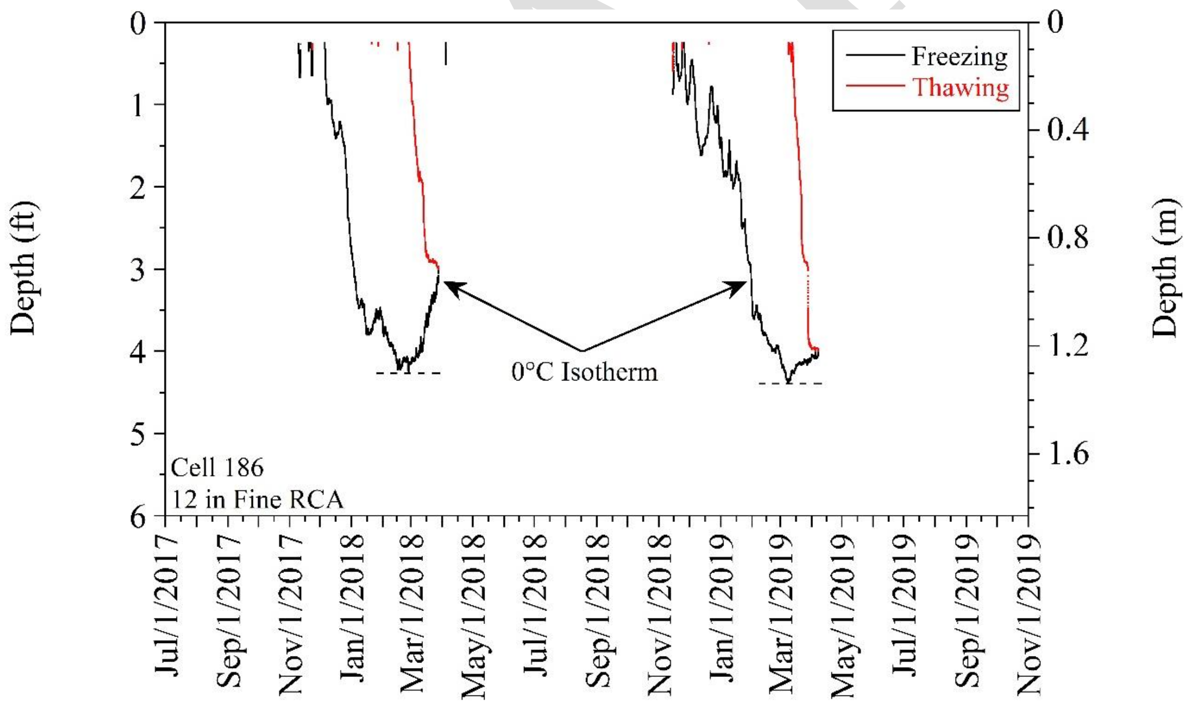

Figure 3.28. Two-year frost penetration depths in cell 186 (12 in Fine RCA)

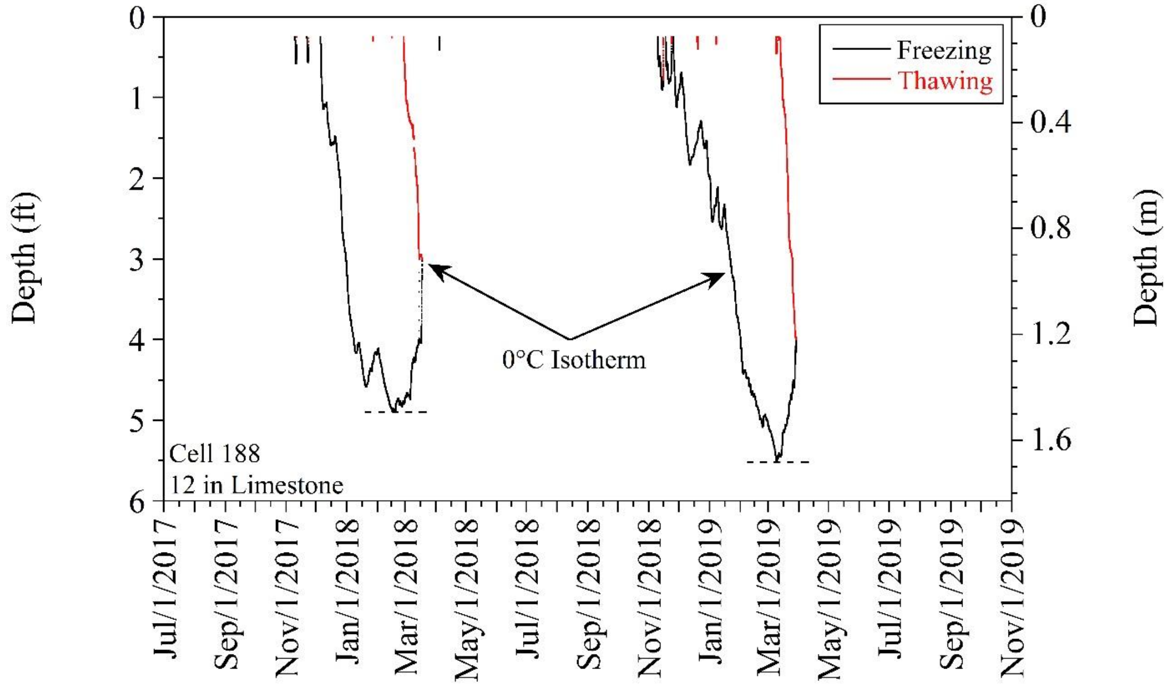

Figure 3.29. Two-year frost penetration depths in cell 188 (12 in Limestone)

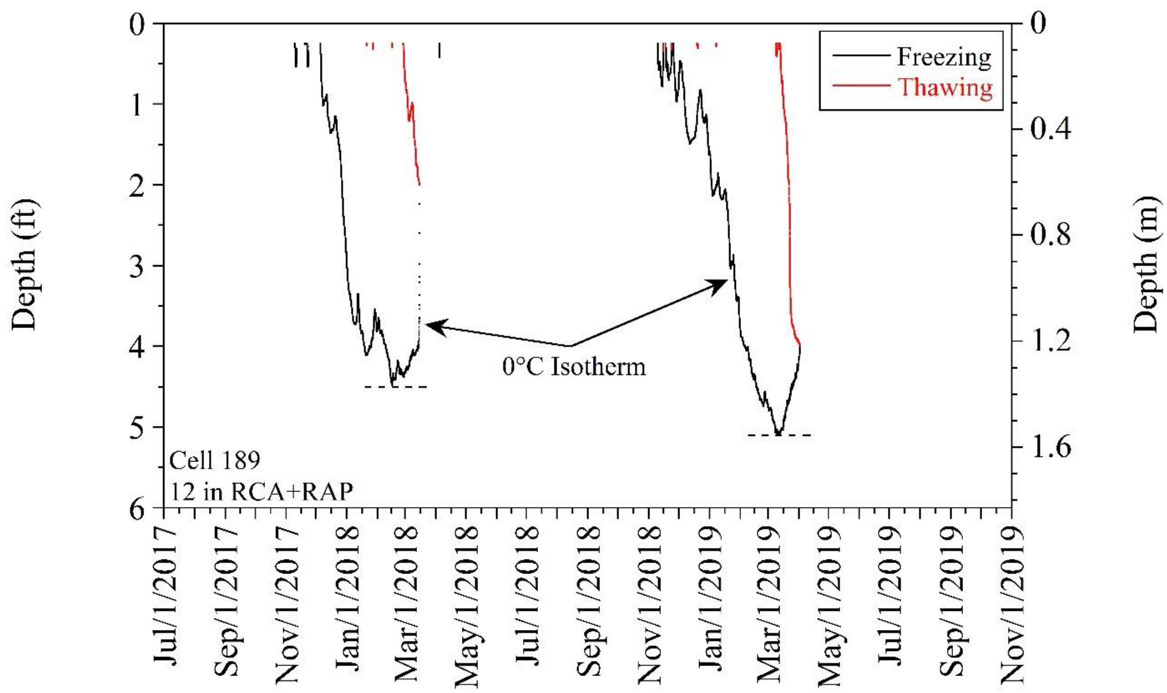

Figure 3.30. Two-year frost penetration depths in cell 189 (12 in RCA+RAP)

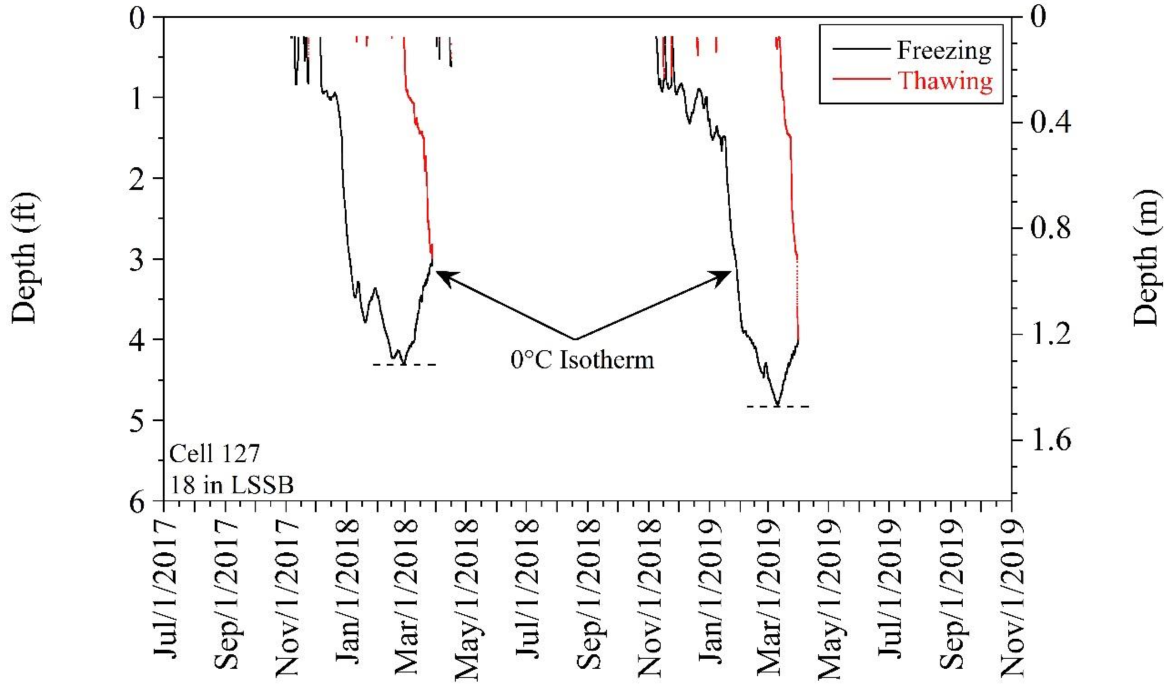

Figure 3.31. Two-year frost penetration depths in cell 127 (18 in LSSB)

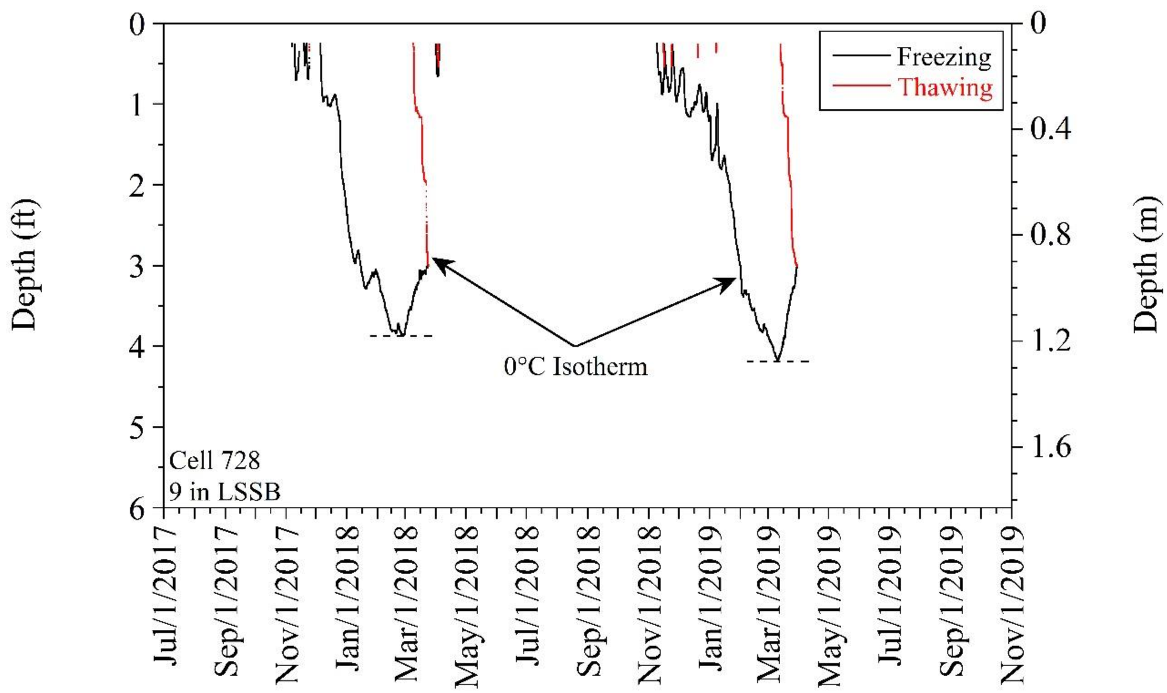

Figure 3.32. Two-year frost penetration depths in cell 728 (9 in LSSB)

Table 3.3. Two-year maximum frost penetration depths

Cell Number	Cell Description	2017-2018 Maximum Frost Penetration Depth		2018-2019 Maximum Frost Penetration Depth	
		(ft)	(m)	(ft)	(m)
185	12 in Coarse RCA	4.44	1.35	4.75	1.45
186	12 in Fine RCA	4.24	1.29	4.39	1.34
188	12 in Limestone	4.9	1.49	5.52	1.68
189	12 in RCA+RAP	4.47	1.36	5.09	1.55
127	18 in LSSB	4.29	1.31	4.81	1.47
728	9 in LSSB	3.87	1.18	4.17	1.27

Table 3.4. Two-year freezing and thawing periods

Cell Number	Cell Description	2017-2018		2018-2019	
		Freezing Duration (days)	Thawing Duration (days)	Freezing Duration (days)	Thawing Duration (days)
185	12 in Coarse RCA	83	25	116	27
186	12 in Fine RCA	84	28	116	27
188	12 in Limestone	84	18	121	18
189	12 in RCA+RAP	84	16	120	23
127	18 in LSSB	84	28	121	22
728	9 in LSSB	94	15	124	17

4. FALLING WEIGHT DEFLECTOMETER (FWD) TESTS

4.1. Test Method and Data Analysis

Falling weight deflectometer (FWD) tests were performed to measure maximum deflection and FWD elastic modulus (E_{FWD}) values throughout the test cells. A trailer-mounted FWD device with a plate (rigid) diameter of 11.8 in (300 mm) was used (Figure 4.1). Nine geophones were placed at the center of the loading plate and distances of 8 in (203.2 mm), 12 in (304.8 mm), 18 in (457.2 mm), 24 in (609.6 mm), 36 in (914.4 mm), 48 in (1219.2 mm), 60 in (1524 mm), and 72 in (1828.8 mm) from the center of the loading plate. Three different loads were applied [the first, second, and third loads were normalized to 6,000 lb (26.7 kN), 9,000 (40 kN), and 12,000 lb (53.4 kN), respectively]. The influence depth of each load ranged from 11.8 to 17.7 in (300 to 450 mm) (1 to 1.5 times the plate diameter) (Mooney et al. 2010; Vennapusa et al. 2012). Two analyses were performed for the determination of the E_{FWD} values: (1) composite analysis, and (2) layered analysis (Figure 4.2).

Figure 4.1. Trailer-mounted Dynatest Model 8002 FWD device

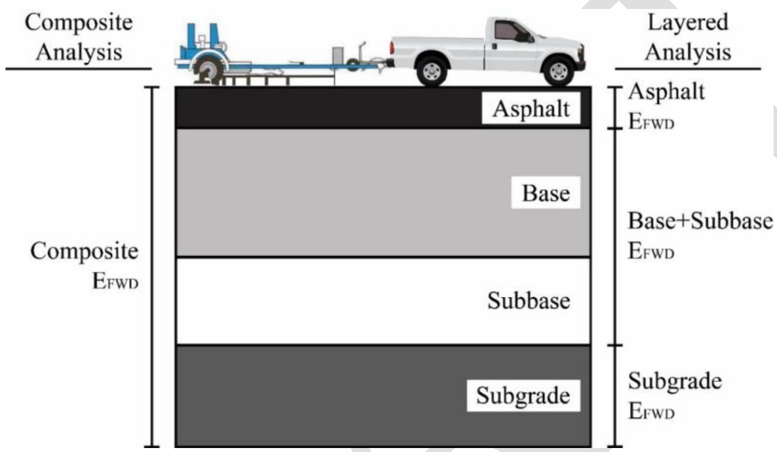

Figure 4.2. Composite and layered FWD analysis

For the composite analysis (Figure 4.2), only the deflections under the loading plate (maximum deflections) were considered. Boussinesq elastic half-space equation, shown in Equation (2), was used to determine the composite E_{FWD} values for the entire pavement structure (Figure 4.2) (Vennapusa and White 2009; Li et al. 2019).

$$\text{Composite } E_{FWD} = \frac{(1 - v^2)\sigma_0 r}{d_0} f \tag{2}$$

where; composite E_{FWD} is the composite FWD elastic modulus (MPa), v is the Poisson's ratio (assumed to be 0.35), σ_0 is the applied stress (MPa), r is the radius of the loading plate (mm), d_0 is the average deflection (mm), and f is the shape factor [assumed to be 8/3 (a rigid plate on a granular material) (Vennapusa and White 2009)].

For the layered analysis (Figure 4.2), deflection basins (recorded by the geophones) were considered. The MODULUS 7.0 program, which was developed at the Texas A&M Transportation Institute (TTI) based on linear-elastic theory, was used for back-calculation (Edil et al. 2012). This program is mainly for flexible pavements and uses the database method to determine the layered E_{FWD} values (William 1999; Baladi et al. 2011).

Per Newcomb et al. (1995), the water table at the MnROAD test facility is relatively shallow and must be considered for back-calculation. Under dynamic loads, such as those applied during FWD testing, there is no time for pore water pressure to dissipate. Therefore, the pore water pressure increases suddenly under dynamic loads and withstands the loads. As a result, saturated soils tend to exhibit higher stiffness under dynamic loads. To be able to consider a shallow water table for back-calculation, the thickness of the unsaturated zone (between the subgrade layer surface and water table) must be determined. To do so, the depth-to-bedrock analysis must be performed (Rohde et al. 1992). By using the depth-to-bedrock analysis, not only the presence of bedrock but also the depth of the water table can be estimated (Liu and Scullion 2001; Chatti et al. 2017). If the subgrade layer is assumed as semi-infinite and the location of the water table is ignored, higher-than-actual subgrade layer stiffness can be observed. In addition, incorrect back-calculation for the upper layers (asphalt, base, and subbase layers) can be made by selecting a semi-infinite subgrade layer in case the water table is shallow (Newcomb et al. 1995). In addition, the subgrade/bedrock modular ratio of 100 is recommended for the depth-to-bedrock analysis. However, since the case in this study was the presence of a shallow water table rather than bedrock, a ratio of 5 was used for back-calculation as recommended by Liu and Scullion (2001). For the subgrade layers, Poisson's ratio (υ) was considered to be 0.40. The base and subbase layers were combined and considered as a single layer (base+subbase layer). The total design thickness of the base+subbase layer (base layer thickness + subbase layer thickness) was entered manually (υ was considered to be 0.35). For the asphalt layers, the design thickness [3.5 in (89 mm)] was entered manually into the program (υ was considered to be 0.30).

4.2. Falling Weight Deflectometer (FWD) Test Results Under Different Loads

Maximum Deflection

Regardless of the test location and date (detailed information about the effects of the test location and the date on the FWD test results will be provided in sections 4.3 and 4.4, respectively), higher maximum deflections were observed under higher loads for each test cell as expected. Figure 4.3 is an example that shows the two-year maximum deflection data for the inside lane (main traffic) – OWP of cell 188 (12 in limestone) under each load. All of the maximum deflection graphs for each test cell and test location are provided in Appendix E.

Composite E_{FWD}

Regardless of the test location and date, the composite E_{FWD} values calculated for 6,000 lb (26.7 kN) load were slightly lower than or similar to those calculated for 9,000 lb (40 kN) and 12,000 lb (53.4 kN) loads. The composite E_{FWD} values calculated for 9,000 lb (40 kN) and 12,000 lb (53.4 kN) loads were similar. Figure 4.4 is an example that shows the two-year composite E_{FWD} data for the inside lane (main traffic) – OWP of cell 188 (12 in limestone) under each load. All other graphs for the composite E_{FWD} of each test cell and test location are provided in Appendix F.

Asphalt and Base+Subbase E_{FWD}

Regardless of the test location and date, the asphalt and base+subbase E_{FWD} values determined for 6,000 lb (26.7 kN) load were slightly lower than or similar to those determined for 9,000 lb (40 kN) and 12,000 lb (53.4 kN) loads (similar to the trend observed for the composite E_{FWD}). Again, similar to the composite E_{FWD} values, the asphalt and base+subbase E_{FWD} values determined for 9,000 lb (40 kN) and 12,000 lb (53.4 kN) loads were similar to each other overall. Figure 4.5 is an example that shows the two-year asphalt E_{FWD} data for the inside lane (main traffic) – OWP of cell 188 (12 in limestone) under each load. Figure 4.6 is an example that shows the two-year base+subbase E_{FWD} data for the same location of the same test cell under each load. All of the asphalt and base+subbase E_{FWD} graphs for each test cell and test location are provided in Appendices G and H, respectively.

Subgrade E_{FWD}

Regardless of the test location and date, all of the loads yielded similar subgrade E_{FWD} values. Figure 4.7 is an example that shows the two-year subgrade E_{FWD} data for the inside lane (main traffic) – OWP of cell 188 (12 in limestone) under each load. All of the subgrade E_{FWD} graphs for each test cell and test location are provided in Appendix I.

By considering the effects of different loads on the FWD test results and several other studies (Baladi et al. 2011; Edil et al. 2012; Bilodeau et al. 2014; Becker 2016; Zhang 2017), only the FWD test results under 9,000 lb (40 kN) [one-half equivalent single axle load (ESAL)] will be discussed in the following sections.

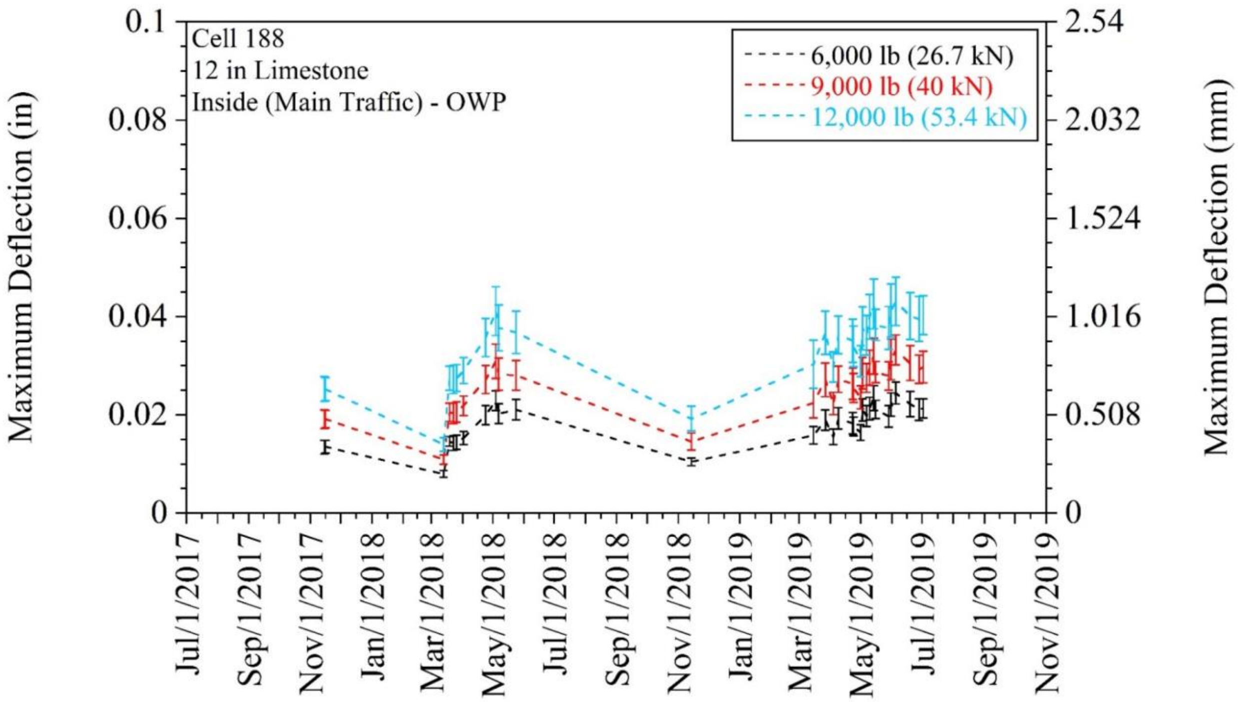

Figure 4.3. Maximum deflections for the inside lane (main traffic) – outer wheel path (OWP) of cell 188 (12 in limestone) under different loads (error bars represent one standard deviation of the data)

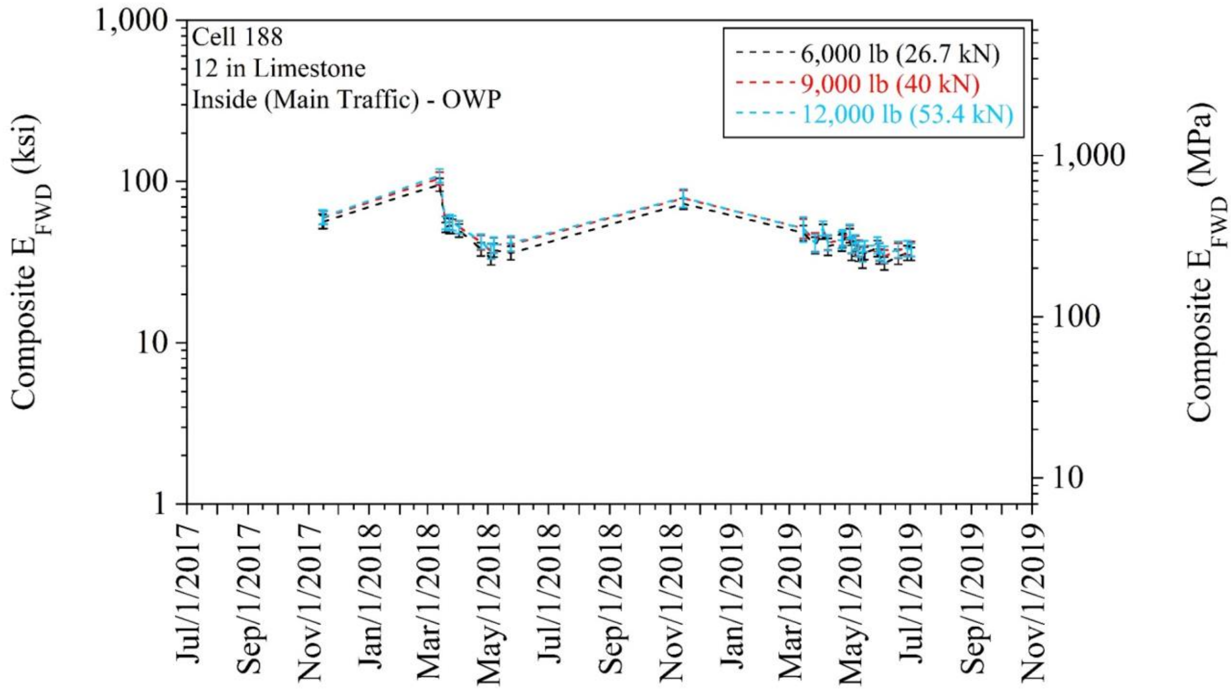

Figure 4.4. Composite E_{FWD} for the inside lane (main traffic) – outer wheel path (OWP) of cell 188 (12 in limestone) under different loads (error bars represent one standard deviation of the data)

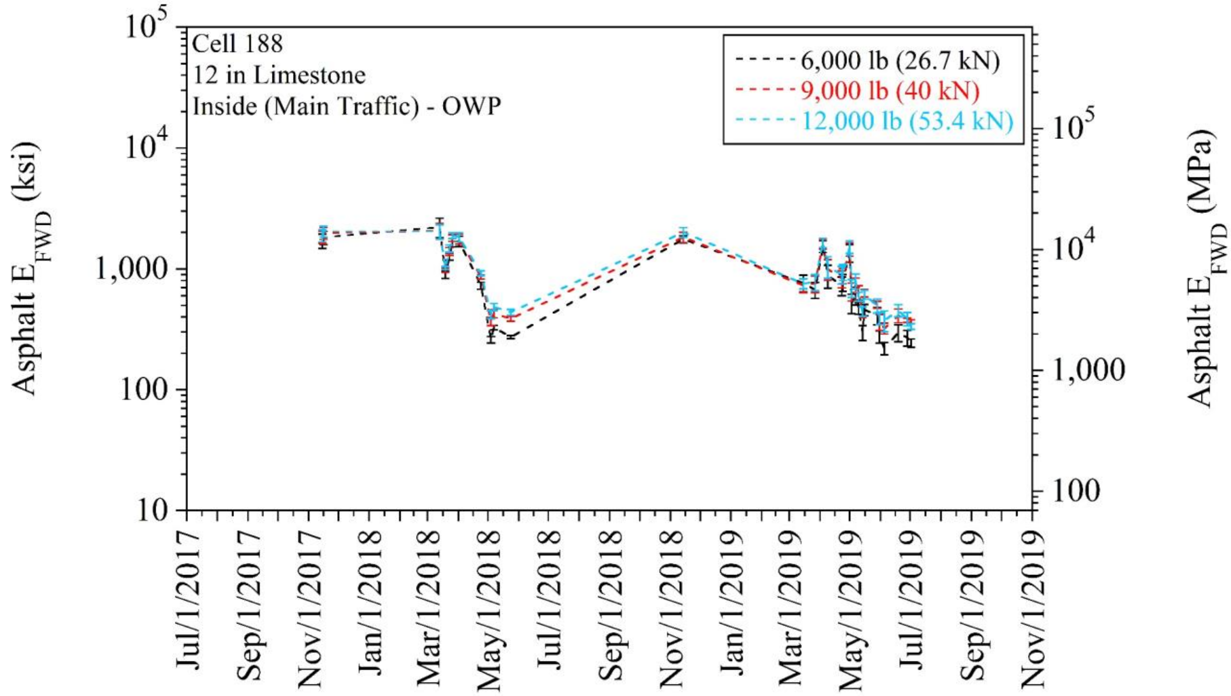

Figure 4.5. Asphalt E_{FWD} for the inside lane (main traffic) – outer wheel path (OWP) of cell 188 (12 in limestone) under different loads (error bars represent one standard deviation of the data)

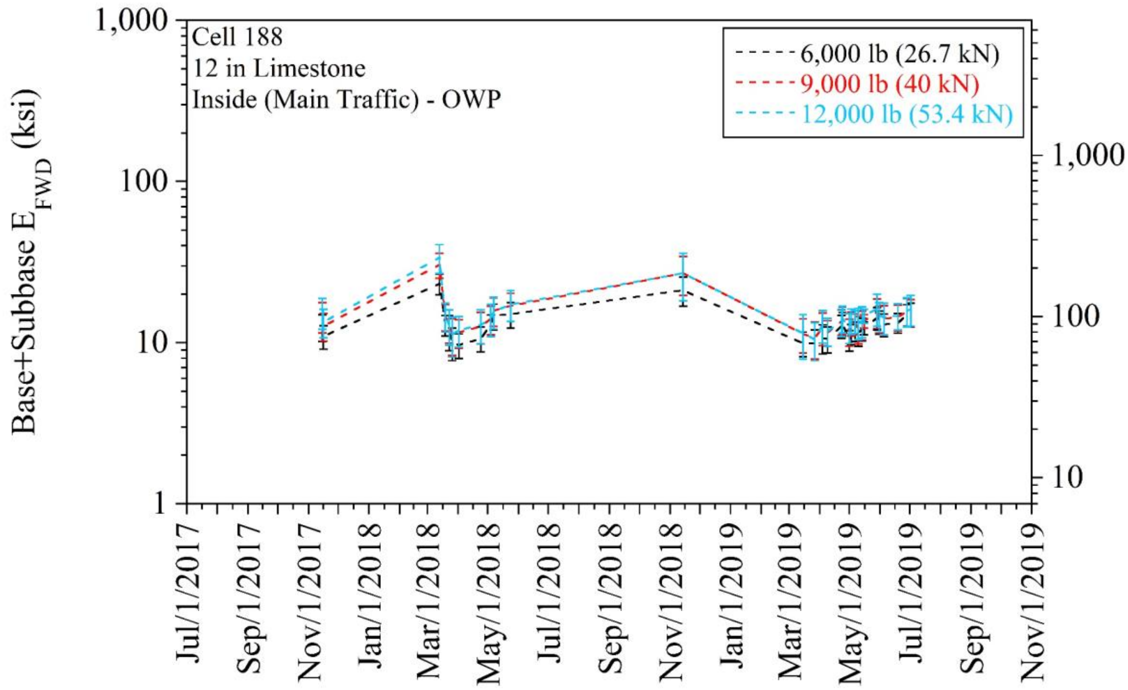

Figure 4.6. Base+subbase E_{FWD} for the inside lane (main traffic) – outer wheel path (OWP) of cell 188 (12 in limestone) under different loads (error bars represent one standard deviation of the data)

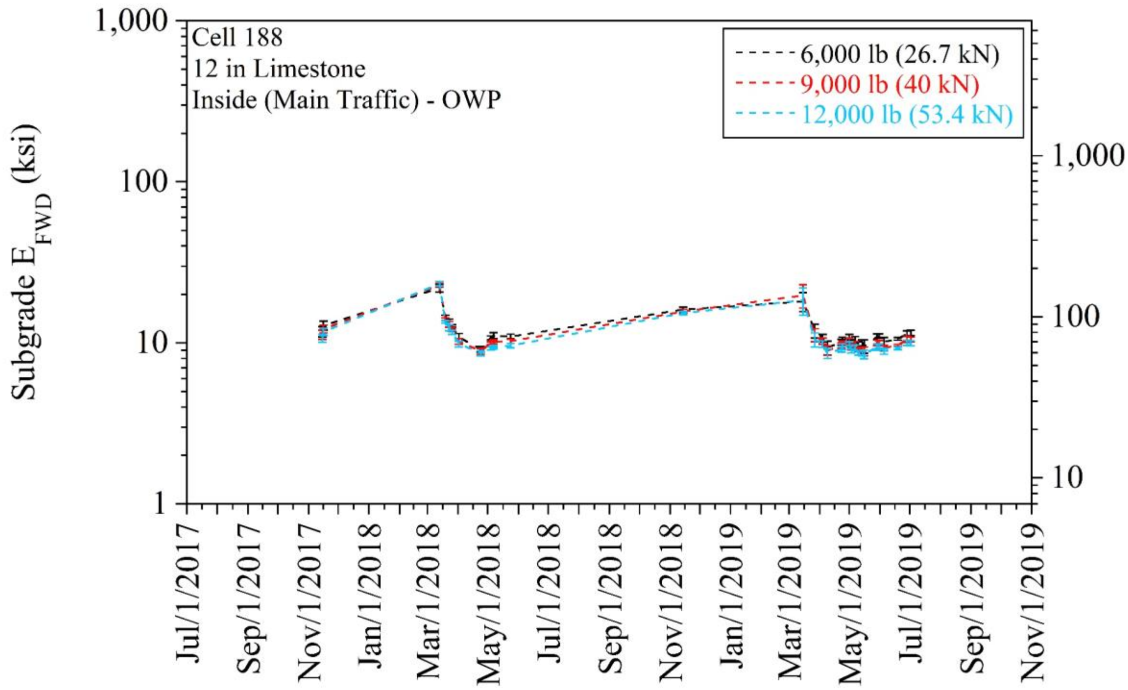

Figure 4.7. Subgrade E_{FWD} for the inside lane (main traffic) – outer wheel path (OWP) of cell 188 (12 in limestone) under different loads (error bars represent one standard deviation of the data)

4.3. Falling Weight Deflectometer (FWD) Test Results at Different Test Locations

Maximum deflection

Regardless of the date (detailed information about the effects of the date on the FWD test results will be provided in section 4.4), the outside lane (occasional traffic) – OWP yielded relatively higher maximum deflections than the other locations [outside lane (occasional traffic) – MID, inside lane (main traffic) – OWP, and inside lane (main traffic) – MID] under 9,000 lb (40 kN) load. The maximum deflections observed in the outside lane (occasional traffic) – MID were higher than or similar to those observed in the inside lane (main traffic). Overall, it was concluded that the maximum deflections observed in the inside lane (main traffic) were lower than those observed in the outside lane (occasional traffic). Furthermore, since the inside lane (main traffic) was subjected to more traffic [provided by the MnROAD truck weighing 80 kip (36.3 Mg)] than the outside lane (occasional traffic), the inside lane (main traffic) experienced a greater degree of compaction over time. Thus, the further compaction of the pavement sublayers for the inside lane (main traffic) yielded denser material matrices, which improved the overall stiffness of the materials (Edil et al. 2012). In particular, the inside lane (main traffic) – OWP was expected to exhibit lower maximum deflections than the inside lane (main traffic) – MID since the weight of the MnROAD truck [80 kip (36.3 Mg)] directly impacted the inside lane (main traffic) – OWP. However, in this study, this trend could not be observed clearly. Figure 4.8 is an example that shows the two-year maximum deflection data for each test location of cell 227 (18 in LSSB). All of the maximum deflection graphs for each test cell are provided in Appendix J.

Composite E_{FWD}

Regardless of the date, the trends observed in the composite E_{FWD} values were exactly compatible with those observed in the maximum deflections under 9,000 lb (40 kN) load. Higher maximum deflections yielded lower composite E_{FWD} values, and lower maximum deflections yielded higher composite E_{FWD} values consistently. This was because the composite E_{FWD} values were inversely proportional to the maximum deflections under the same load [9,000 lb (40 kN)] based on Equation (2). Overall, the outside lane (occasional traffic) – OWP exhibited relatively lower composite E_{FWD} values than those measured at other locations. The composite E_{FWD} values calculated for the outside lane (occasional traffic) – MID were lower than or similar to those calculated for the inside lane (main traffic). In general, the inside lane (main traffic) yielded higher composite E_{FWD} values than the outside lane (occasional traffic) due to the aforementioned further compaction. Just like the observations made for the maximum deflections, no clear trend was observed between the inside lane (main traffic) – OWP and the inside lane – MID. Figure 4.9 is an example that shows the two-year composite E_{FWD} data for each test location of cell 227 (18 in LSSB). All of the composite E_{FWD} graphs for each test cell are provided in Appendix K.

Asphalt and Base+Subbase E_{FWD}

Regardless of the date, the trends observed in the asphalt and base+subbase E_{FWD} values were similar to those observed in the composite E_{FWD} values under 9,000 lb (40 kN) load. Figure 4.10 is an example that shows the two-year asphalt E_{FWD} data for each test location of cell 227 (18 in LSSB). Figure 4.11 is an example that shows the two-year base+subbase E_{FWD} data for each test location of the same test cell. All of the asphalt E_{FWD} and base+subbase E_{FWD} graphs for each test cell are provided in Appendices L and M, respectively.

Subgrade E_{FWD}

Regardless of the date, no significant differences were observed in the subgrade E_{FWD} values for different test locations of each test cell under 9,000 lb (40 kN) load. Figure 4.12 is an example that shows the two-year subgrade E_{FWD} data for each test location of cell 227 (18 in LSSB). All of the subgrade E_{FWD} graphs for each test cell are provided in Appendix N.

Since the traffic load provided by the MnROAD truck [80 kip (36.3 Mg)] directly applied to the inside lane (main traffic) – OWP of each test cell, the FWD test results in the long-term will be discussed only for that specific test location [under 9,000 lb (40 kN) load (the reason for the selection of that load was explained previously)] in the following sections.

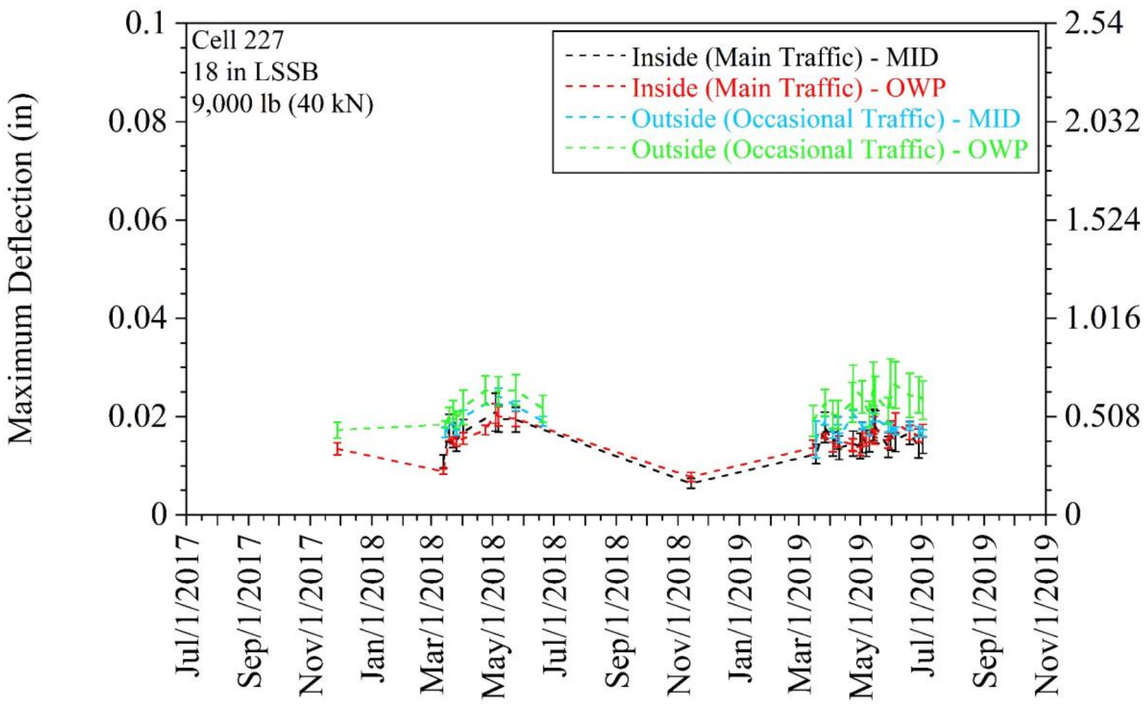

Figure 4.8. Maximum deflections for cell 227 (18 in LSSB) under 9,000 lb (40 kN) load (error bars represent one standard deviation of the data)

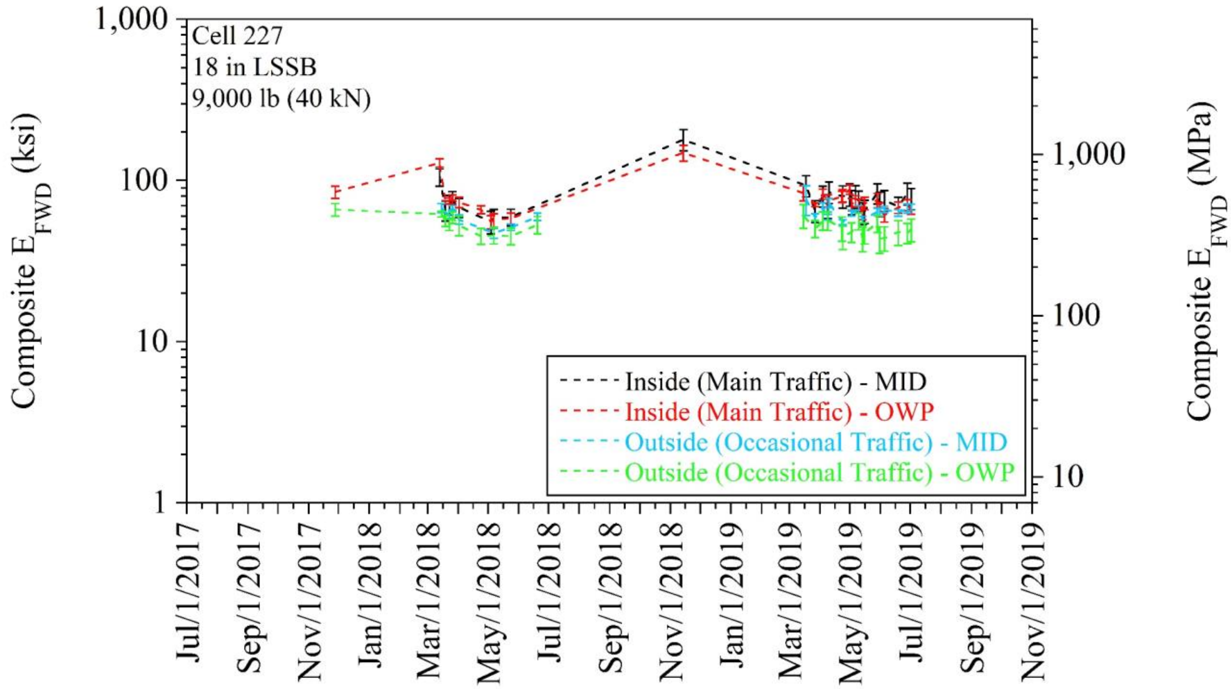

Figure 4.9. Composite E_{FWD} for cell 227 (18 in LSSB) under 9,000 lb (40 kN) load (error bars represent one standard deviation of the data)

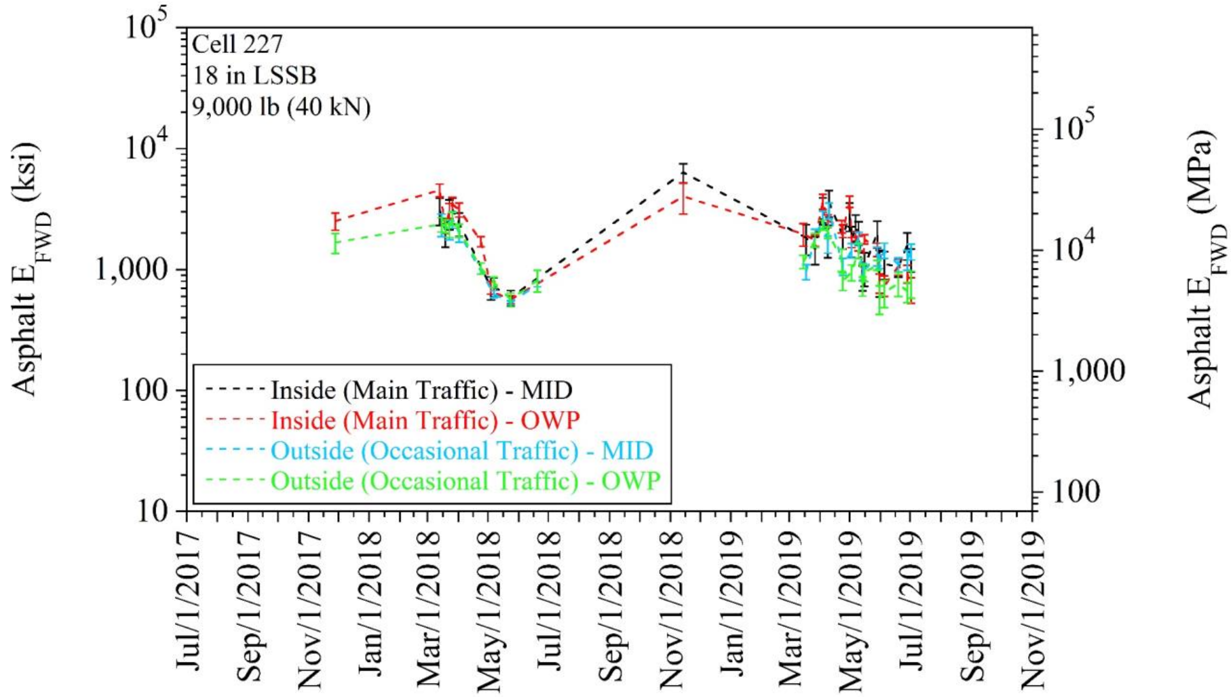

Figure 4.10. Asphalt E_{FWD} for cell 227 (18 in LSSB) under 9,000 lb (40 kN) load (error bars represent one standard deviation of the data)

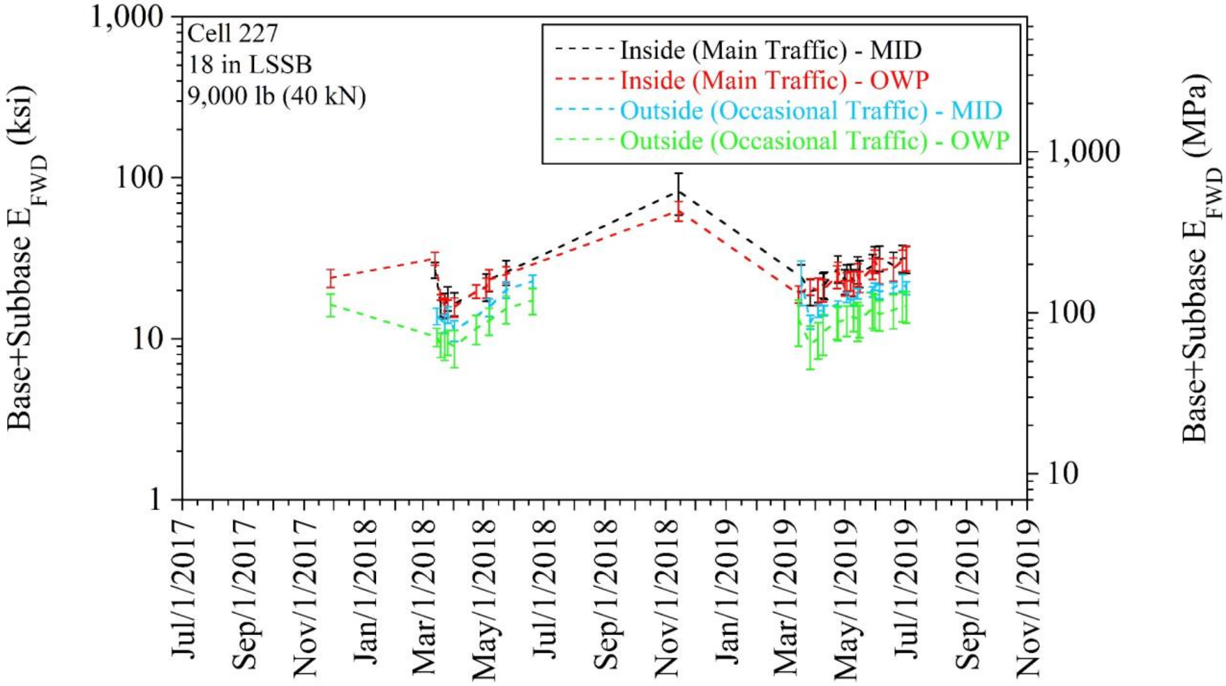

Figure 4.11. Base+subbase E_{FWD} for cell 227 (18 in LSSB) under 9,000 lb (40 kN) load (error bars represent one standard deviation of the data)

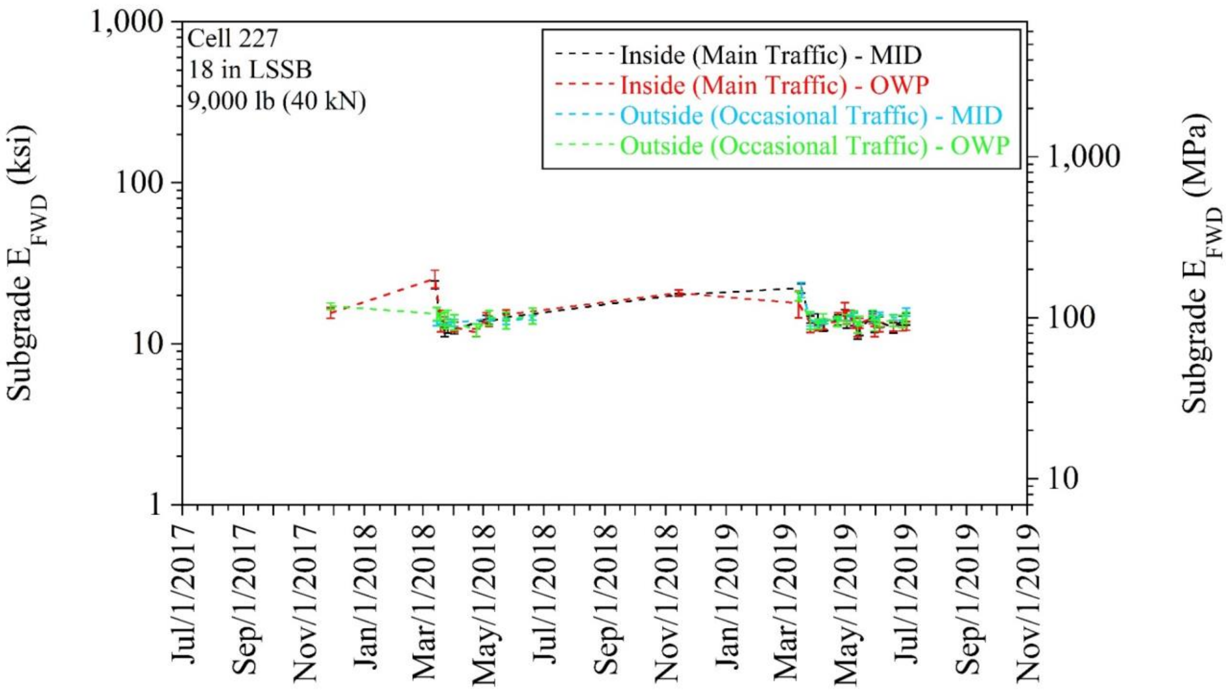

Figure 4.12. Subgrade E_{FWD} for cell 227 (18 in LSSB) under 9,000 lb (40 kN) load (error bars represent one standard deviation of the data)

4.4. Effects of the Freeze-Thaw (F-T) Cycles and Temperature Changes on the Falling Weight Deflectometer (FWD) Test Results

The engineering properties of pavement foundation systems can change considerably in the long term due to seasonal variations in weather conditions (Rosa et al. 2016). In cold regions, pavement structures experience several freeze-thaw (F-T) cycles. During the freezing period, water freezes and turns into ice with an increase (around 10%) in its volume. Frozen soils or aggregates are expected to exhibit higher stiffness than unfrozen soils; therefore, the stiffness of pavement systems increases during the freezing period. During the thawing period, ice melts with a reduction in its volume and it leaves a relatively more porous structure in the soil or aggregate matrix. In addition, expansion of the water molecules during freezing generates internal pressures in the soil or aggregate matrix. Thus, it may deteriorate soil or aggregate particles. During the thawing period, the fines content of the soils or aggregates may increase due to the deterioration of coarser particles. Such an increase in the fines content may yield an increase in the water absorption capacity of the soils or aggregates due to an increase in the specific surface area of the soil or aggregate (Edil et al. 2012; Rosa et al. 2017). Higher fines content and water absorption capacity may cause further detrimental effects during another freezing period as more water may turn into ice.

The long-term performances of the test cells are summarized in Figures 4.13, 4.14, 4.15, 4.16, and 4.17 for the maximum deflection, composite E_{FWD}, asphalt E_{FWD}, base+subbase E_{FWD}, and subgrade E_{FWD}, respectively [the results shown are only for the inside lane (main traffic) – OWP of each test cell under 9,000 lb (40 kN) load]. For the comparisons, the FWD test results obtained in Nov 2017 (before the first freezing period), Mar 2018 (in the first thawing period), Mar 2019 (in the second thawing period), and Jul 2019 (the latest test date) were selected.

4.4.1. Falling Weight Deflectometer (FWD) Test Results Before the First Freezing Period

Maximum Deflection

In Nov 2017 (before the first freezing period) (Figure 4.13), cells 186 (12 in fine RCA), 127 (18 in LSSB), and 227 (18 in LSSB) yielded lower maximum deflections than the other cells. Cell 185 (12 in coarse RCA) exhibited higher maximum deflections than cells 186 (12 in fine RCA), 127 (18 in LSSB), and 227 (18 in LSSB) and lower maximum deflections than cell 189 (12 in RCA+RAP). Cells 188 (12 in limestone), 328 (9 in LSSB – TX), and 728 (9 in LSSB) exhibited higher deflections than cell 189 (12 in RCA+RAP). Cells 428 (9 in LSSB – TX+GT), 528 (9 in LSSB – BX+GT), and 628 (9 in LSSB – BX) yielded higher deflections than the other test cells.

Composite E_{FWD}

In Nov 2017 (before the first freezing period) (Figure 4.14), the trends observed in the composite E_{FWD} values were exactly compatible with those observed in the maximum deflections. Higher maximum deflections yielded lower composite E_{FWD} values. On the contrary, lower maximum deflections yielded higher composite E_{FWD} values. This was due to the inversely proportional relationship of composite E_{FWD} with the maximum deflections under the same load [9,000 lb (40 kN)] based on Equation (2).

Asphalt E_{FWD}

In Nov 2017 (before the first freezing period) (Figure 4.15), cells 188 (12 in limestone), 189 (12 in RCA+RAP), 328 (9 in LSSB – TX), 428 (9 in LSSB – TX+GT), 528 (9 in LSSB – BX+GT), and 628 (9 in LSSB – BX) yielded similar asphalt E_{FWD} values which were lower than those of the other cells. Cells 185 (12 in coarse RCA) and 728 (9 in LSSB) exhibited intermediate asphalt E_{FWD} values. Cells 186 (12 in fine RCA), 127 (18 in LSSB), and 227 (18 in LSSB) provided higher asphalt E_{FWD} values than the other cells [cell 127 (18 in LSSB) yielded the highest asphalt E_{FWD} values]. Asphalt E_{FWD} values exhibited relatively higher standard deviations, possibly due to the temperature-dependency of the asphalt material. The stiffness of asphalt material is inversely proportional to the air temperature due to viscosity (Edil et al. 2012). At higher temperatures, the viscosity of the asphalt material decreases and this reduces the asphalt stiffness (Edil et al. 2012). On the other hand, the viscosity of the asphalt material increases at lower temperatures which increases the asphalt stiffness (Edil et al. 2012). It is very well known that even the test time on the same day (early in the morning, in the afternoon, etc.) can affect the asphalt stiffness significantly.

Base+Subbase E_{FWD}

In Nov 2017 (before the first freezing period) (Figure 4.16), the coarse RCA and fine RCA base+subbase layers [cells 185 (12 in coarse RCA) and 186 (12 in fine RCA), respectively] exhibited higher E_{FWD} values than the limestone and RCA+RAP base+subbase layers [cells 188 (12 in limestone) and 189 (12 in RCA+RAP)]. This was attributed to the cementation of unhydrated cement of the coarse RCA and fine RCA materials. In addition, higher E_{FWD} values were also attributed to rougher surfaces of the coarse RCA and fine RCA materials due to cement mortar (Kuo et al. 2002; Edil et al. 2012). In fact, the fine RCA base+subbase layer [cell 186 (12 in fine RCA)] yielded higher E_{FWD} values than the coarse RCA base+subbase layer [cells 185 (12 in coarse RCA)]. It was speculated that the unhydrated cement content of the fine RCA material was higher than that of the coarse RCA material due to its higher fines content (ACPA 2009). The RCA+RAP base+subbase layer [cell 189 (12 in RCA+RAP)] showed lower E_{FWD} values than the coarse RCA and fine RCA base+subbase layers [cells 185 (12 in coarse RCA) and 186 (12 in fine RCA), respectively]. Because of the hydrophobicity of RAP, lower absorption would be expected for the RCA+RAP material compared to the RCA materials (Edil et al. 2012; Rahardjo et al. 2010). Therefore, it was speculated that the RAP particles in the RCA+RAP material reduced the amount of water that could be in contact with the RCA particles for cementation. In the literature, RCA and RAP materials tend to exhibit higher stiffness than virgin aggregates (VAs) (Edil et al. 2012; Stolle et al. 2014; Rosa et al. 2017). Since the limestone material was a VA, the limestone base+subbase layer exhibited lower E_{FWD} values than the coarse RCA, fine RCA, and RCA+RAP base+subbase layers [cells 185 (12 in coarse RCA), 186 (12 in fine RCA), and 189 (12 in RCA+RAP), respectively]. In Task 4 (laboratory testing) report, it was determined that the class 5Q aggregate was similar to the coarse RCA material and the class 6 aggregate was similar to the RCA+RAP material. Therefore, the base layers constructed with the class 5Q aggregate [cells 328 (9 in LSSB – TX), 428 (9 in LSSB – TX+GT), 528 (9 in LSSB – BX+GT), 628 (9 in LSSB – BX), and 728 (9 in LSSB)] were expected to show greater stiffness than those constructed with the class 6 aggregate [cells 127 (18 in LSSB) and 227 (18 in LSSB)] due to cementation and rougher surface. However, in this study, the class 6 aggregate base+subbase layers [cells 127 (18 in LSSB) and 227 (18 in LSSB)] exhibited higher E_{FWD} values than the class 5Q aggregate base+subbase layers [cells 328 (9 in LSSB – TX), 428 (9 in LSSB – TX+GT), 528 (9 in LSSB – BX+GT), 628 (9 in LSSB –

BX), and 728 (9 in LSSB)]. For flexible pavements, higher stiffness is expected for thicker layers as a result of an improvement in the load distribution with an increase in the layer thickness (Tanyu et al. 2003). Therefore, it was concluded that 18 in LSSB layers [cells 127 (18 in LSSB) and 227 (18 in LSSB)] performed considerably better than 9 in LSSB layers [cells 328 (9 in LSSB – TX), 428 (9 in LSSB – TX+GT), 528 (9 in LSSB – BX+GT), 628 (9 in LSSB – BX), and 728 (9 in LSSB)] due to their higher thickness.

Subgrade E_{FWD}

In Nov 2017 (before the first freezing period) (Figure 4.17), the sand subgrade layers in cells 185 (12 in coarse RCA) and 186 (12 in fine RCA) provided higher E_{FWD} values than the clay loam subgrade layers in cells 188 (12 in limestone) and 189 (12 in RCA+RAP). The coarser materials were prone to exhibit higher E_{FWD} values than the finer materials because of the interlocking between coarser particles (Lekarp et al. 200; Cunningham et al. 2013). The clay loam subgrade layers in cells 127 (18 in LSSB) and 227 (18 in LSSB) exhibited higher E_{FWD} values than the clay loam subgrade layers in cells 328 (9 in LSSB – TX), 428 (9 in LSSB – TX+GT), 528 (9 in LSSB – BX+GT), 628 (9 in LSSB – BX), and 728 (9 in LSSB). Higher stiffness is expected for thicker layers as a result of an improvement in the load distribution with an increase in the layer thickness due to the strain effect (Tanyu et al. 2003). Therefore, it was speculated that the subgrade improvement provided by using 18 in LSSB layers in cells 127 (18 in LSSB) and 227 (18 in LSSB) was more effective than using 9 in LSSB layers [cells 328 (9 in LSSB – TX), 428 (9 in LSSB – TX+GT), 528 (9 in LSSB – BX+GT), 628 (9 in LSSB – BX), and 728 (9 in LSSB)].

4.4.2. Falling Weight Deflectometer (FWD) Test Results in the First Thawing Period

Maximum Deflection

In Mar 2018 (in the first thawing period) (Figure 4.13), cells 186 (12 in fine RCA), 328 (9 in LSSB – TX), 428 (9 in LSSB – TX+GT), 528 (9 in LSSB – BX+GT), and 628 (9 in LSSB – BX) yielded slightly lower maximum deflections compared to those observed in Nov 2017 (before the first freezing period). Cells 185 (12 in coarse RCA) and 728 (9 in LSSB) exhibited slightly higher maximum deflections in Mar 2018 (in the first thawing period) compared to those observed in Nov 2017 (before the first freezing period), possibly indicating that those cells were not as durable as cells 186 (12 in fine RCA), 328 (9 in LSSB – TX), 428 (9 in LSSB – TX+GT), 528 (9 in LSSB – BX+GT), and 628 (9 in LSSB – BX) against the first F-T period. For cells 188 (12 in limestone), 189 (12 in RCA+RAP), 127 (18 in LSSB), and 227 (18 in LSSB), higher maximum deflections were observed in Mar 2018 (in the first thawing period) compared to those observed in Nov 2017 (before the freezing period of 2017-2018), indicating that these cells were not as durable as the other test cells against the first F-T period.

Composite E_{FWD}

In Mar 2018 (in the first thawing period) (Figure 4.14), the trends observed in the composite E_{FWD} values [relative to those observed in Nov 2017 (before the first freezing period)] were exactly compatible with those observed in the maximum deflections [relative to those observed in Nov 2017 (before the first freezing period)]. Higher maximum deflections yielded lower composite E_{FWD} values. On the contrary, lower maximum deflections yielded higher composite E_{FWD} values. This was due to the inversely proportional relationship of composite E_{FWD} with the maximum deflections under the same load [9,000 lb (40 kN)] based on Equation (2).

Asphalt E_{FWD}

In Mar 2018 (in the first thawing period) (Figure 4.15), lower asphalt E_{FWD} values were observed in all the test cells (except cell 728) compared to those observed in Nov 2017 (before the first freezing period). This was possibly due to the softening of the asphalt layers at relatively higher temperatures in Mar 2018 (in the first thawing period) compared to those in Nov 2017 (before the first freezing period).

Base+Subbase E_{FWD}

In Mar 2018 (in the first thawing period) (Figure 4.16), considerably higher E_{FWD} values were observed in the coarse RCA and fine RCA base+subbase layers [cells 185 (12 in coarse RCA) and 186 (12 in fine RCA), respectively] compared to those observed in Nov 2017 (before the first freezing period). For those cells, it was speculated that the cementation of coarse RCA and fine RCA materials overcame the negative effects of the first F-T period. More traffic loads were transferred to the coarse RCA and fine RCA base+subbase layers [cells 185 (12 in coarse RCA) and 186 (12 in fine RCA), respectively] due to the softening of the asphalt layers. Aggregates generally show a stress-hardening behavior due to the reorientation of the particles into a denser state under higher loads (Ceylan et al. 2009; White et al. 2018). However, aggregates can exhibit decreasing stiffness values after reaching the breakpoint stress due to the presence of underlying softer or wetter subgrade conditions (White et al. 2018). Therefore, it was also speculated that the coarse RCA and fine RCA base+subbase layers [cells 185 (12 in coarse RCA) and 186 (12 in fine RCA), respectively] exhibited stress-hardening behavior since they were on the sand subgrade layers (Ceylan et al. 2009; White et al. 2018). On the contrary, the limestone and RCA+RAP base+subbase layers [cells 188 (12 in limestone) and 189 (12 in RCA+RAP), respectively] did not show higher E_{FWD} values in Mar 2018 (in the first thawing period) compared to those observed in Nov 2017 (before the first freezing period). Limestone in the base layer of cell 188 (12 in limestone) was a virgin aggregate and did not contain any RCA and no cementation occurred. For the RCA+RAP material in the base layer of cell 189 (12 in RCA+RAP), the activity of the cementation of RCA was possibly low due to the presence of hydrophobic RAP material. For cells 127 (18 in LSSB) and 227 (18 in LSSB), the class 6 aggregate base+subbase layers exhibited lower E_{FWD} values in Mar 2018 (in the first thawing period) compared to those observed in Nov 2017 (before the first freezing period). As mentioned previously, the class 6 aggregate was similar to the RCA+RAP material. Therefore, it was speculated that the RCA material in the class 6 aggregate matrix exhibited a lower rate of cementation compared to the coarse RCA and fine RCA materials. In addition, the class 6 aggregate base+subbase layers [cells 127 (18 in LSSB) and 227 (18 in LSSB)] may have shown stress-softening behavior after the breakpoint stress under the relatively softer asphalt layers. The class 5Q aggregate base+subbase layers in cells 328 (9 in LSSB – TX), 428 (9 in LSSB – TX+GT), 528 (9 in LSSB – BX+GT), and 628 (9 in LSSB – BX) did not exhibit considerable changes in Mar 2018 (in the first thawing period) compared to those observed in Nov 2017 (before the first freezing period). However, for the class 5Q aggregate base+subbase layer in cell 728 (9 in LSSB), slightly lower E_{FWD} values were observed in Mar 2018 (in the first thawing) compared to those observed in Nov 2017 (before the first freezing period). Overall, it was speculated that the cementation of the class 5Q aggregate (as mentioned previously, the class 5Q aggregate was similar to the coarse RCA material) and effective drainage provided by 9 in LSSB layer neutralized the negative effects of the first F-T period. In addition, it was observed that the use of geosynthetics in cells 328 (9 in LSSB – TX), 428 (9 in LSSB – TX+GT), 528 (9 in LSSB – BX+GT), and 628 (9 in LSSB – BX) contributed to the durability of the test cells against freezing and thawing. It was speculated that the use of geosynthetics reduced the stresses acting on the clay loam subgrade layers by improving the distribution of the loads coming from the class 5Q aggregate base+subbase layers and this improved the stiffness (fine-grained materials are expected to show stress-softening behavior; therefore, a decrease in the stress applied to fine-grained subgrade layers tends to cause an improvement in the stiffness of such subgrade layers) and durability of the clay loam subgrade layers. Improved stiffness and durability of the clay loam subgrade layers are expected to improve the durability of the pavement sublayers overlying the subgrade layers.

Subgrade E_{FWD}

In Mar 2018 (in the first thawing period) (Figure 4.17), the sand subgrade layers in cells 185 (12 in coarse RCA) and 186 (12 in fine RCA) and the clay loam layers in cells 188 (12 in limestone) and 189 (12 in RCA+RAP) yielded higher E_{FWD} values compared to those observed in Nov 2017 (before the first freezing period). The clay loam subgrade layers in cells 127 (18 in LSSB) and 227 (18 in LSSB) exhibited lower E_{FWD} values than those observed in Nov 2017 (before the first freezing period). The clay loam subgrade layers of cells 328 (9 in LSSB – TX), 428 (9 in LSSB – TX+GT), and 728 (9 in LSSB) did not exhibit significant differences in the E_{FWD} values in Mar 2018 (in the first thawing period) compared to those observed in Nov 2017 (before the first freezing period). On the other hand, the clay loam subgrade layers of cells 528 (9 in LSSB – BX+GT) and 628 (9 in LSSB – BX) yielded higher E_{FWD} values in Mar 2018 (in the first thawing period) compared to those observed in Nov 2017 (before the first freezing period). Explaining the behaviors of subgrade layers is considerably complex because none of the pavement layers could be considered by itself with the tests conducted in this study. Observing lower or higher subgrade stiffness due to freezing and thawing could be due to several factors. One of these reasons could be the actual softening or hardening of the subgrade layer under loading conditions. The other reason could be the softening or hardening of base+subbase layer. When a base+subbase layer softens, it tends to transmit more load to the subgrade layer. Fine-grained soils tend to exhibit stress-softening behavior. When a fine-grained subgrade layer receives higher loads from the base+subbase layer, the subgrade layer tends to exhibit lower stiffness. On the other hand, when the fine-grained subgrade layer receives fewer loads from the base+subbase layer due to the stiffening of the base+subbase layer, the subgrade layer is prone to exhibit higher stiffness.

4.4.3. Falling Weight Deflectometer (FWD) Test Results in the Second Thawing Period

Maximum Deflection

In Mar 2019 (in the second thawing period) (Figure 4.13) (the VWC values determined for the second thawing period are summarized in Appendix O), overall, all of the test cells [except cell 127 (18 in LSSB)] exhibited higher maximum deflections than those observed in Mar 2018 (in the first thawing period). The increases in the maximum deflections from Mar 2018 (in the first thawing period) to Mar 2019 (in the second thawing period) were higher for cells 185 (12 in coarse RCA), 186 (12 in fine RCA), 188 (12 in limestone), and 189 (12 in RCA+RAP), possibly indicating that those test cells were not as durable as the other test cells against the second F-T period. For cell 227 (18 in LSSB), the maximum deflections observed in Mar 2019 (in the second thawing period) were only slightly higher (almost equal) than those observed in Mar 2018 (in the first thawing period). Therefore, it was concluded that cells 127 (18 in LSSB) and 227 (18 in LSSB) were more durable than the other cells against the second F-T period. It was speculated that the main contributors to the observed performance of cells 127 (18 in LSSB) and 227 (18 in LSSB) were effective drainage and relatively higher thickness of the 18 in LSSB layers (compared to other subbase layers). Higher stiffness is expected for thicker layers as a result of an improvement in the load distribution with an increase in the layer thickness due to the strain effect (Tanyu et al. 2003).

Composite E_{FWD}

In Mar 2019 (in the second thawing period) (Figure 4.14), the trends observed in the composite E_{FWD} values [relative to those observed in Mar 2018 (in the first thawing period)] were exactly compatible with those observed in the maximum deflections [relative to those observed in Mar 2018 (in the first thawing period)]. Higher maximum deflections yielded lower composite E_{FWD} values. On the contrary, lower maximum deflections yielded higher composite E_{FWD} values. This was due to the inversely proportional relationship of composite E_{FWD} with the maximum deflections under the same load [9,000 lb (40 kN)] based on Equation (2).

Asphalt E_{FWD}

In Mar 2019 (in the second thawing period) (Figure 4.15), lower asphalt E_{FWD} values were observed in all the test cells compared to those observed in Mar 2018 (in the first thawing period). This result was possibly due to the softening of the asphalt layers at relatively higher temperatures in Mar 2019 (in the second thawing period) compared to Mar 2018 (in the first thawing).

Base+Subbase E_{FWD}

In Mar 2019 (in the second thawing period) (Figure 4.16), the coarse RCA, fine RCA, limestone, and RCA+RAP base+subbase layers in cells 185 (12 in coarse RCA), 186 (12 in fine RCA), 188 (12 in limestone), and 189 (12 in RCA+RAP), respectively, yielded lower E_{FWD} values than those observed in Mar 2018 (in the first thawing period). It was speculated that no more cementation of the coarse RCA and fine RCA materials continued in the second thawing period. Therefore, the coarse RCA and fine RCA base+subbase layers [cells 185 (12 in coarse RCA) and 186 (12 in fine RCA), respectively] experienced a reduction in stiffness during the second F-T period. However, the E_{FWD} values of the coarse RCA and fine RCA base+subbase layers [cells 185 (12 in coarse RCA) and 186 (12 in fine RCA), respectively] were still higher than those observed for the limestone and RCA+RAP base+subbase layers [cells 188 (12 in limestone) and 189 (12 in RCA+RAP), respectively] in Mar 2019 (in the second thawing period). In Mar 2019 (in the second thawing period), the E_{FWD} values of the class 6 aggregate base+subbase layers [cells 127 (18 in LSSB) and 227 (18 in LSSB)] and the class 5Q aggregate base+subbase layers [cells 328 (9 in LSSB – TX), 428 (9 in LSSB – TX+GT), 528 (9 in LSSB – BX+GT), 628 (9 in LSSB – BX), and 728 (9 in LSSB)] were higher than or similar to those observed in Mar 2018 (in the first thawing period). While the class 6 aggregate base+subbase layers [cells 127 (18 in LSSB) and 227 (18 in LSSB)] were not durable against the first F-T period, they were more durable against the second F-T period compare to the first F-T period. In general, the most drastic decreases in the stiffness of soils/aggregates are observed after the first F-T cycle, and the soils/aggregates become more stable as F-T cycles continue over time (Coban 2017). It was speculated that such a mechanism was observed in the class 6 aggregate base+subbase layers [cells 127 (18 in LSSB) and 227 (18 in LSSB)]. In addition, it was speculated that 18 in LSSB layers in cells 127 (18 in LSSB) and 227 (18 in LSSB) provided durability against F-T cycles in the long-term due to effective drainage and better load distribution due to relatively higher thickness of the 18 in LSSB layers (compared to other subbase layers) (Tanyu et al. 2003). The class 5Q aggregate base+subbase layers in cells 328 (9 in LSSB – TX), 428 (9 in LSSB – TX+GT), 528 (9 in LSSB – BX+GT), 628 (9 in LSSB – BX), and 728 (9 in LSSB) were also durable against the second F-T period (those layers were also durable against the first F-T period).

Subgrade E_{FWD}

In Mar 2019 (in the second thawing period) (Figure 4.17), no consistent trends in the E_{FWD} values were observed. While the sand subgrade layer in cell 185 (12 in coarse RCA) exhibited similar E_{FWD} values in Mar 2019 (in the second thawing period) compared to those observed in Mar 2018 (in the first thawing period), the sand subgrade layer in cell 186 (12 in fine RCA) yielded higher E_{FWD} values in Mar 2019 (in the second thawing period) compared to those observed in Mar 2018 (in the first thawing period). While the clay loam subgrade layer in cell 188 (12 in limestone) exhibited lower E_{FWD} values in Mar 2019 (in the second thawing period) compared to those observed in Mar 2018 (in the first thawing period), the clay loam subgrade layer in cell 189 (12 in RCA+RAP) yielded higher E_{FWD} values in Mar 2019 (in the second thawing period) compared to those observed in Mar 2018 (in the first thawing period). The clay loam subgrade layers in cells 328 (9 in LSSB – TX), 428 (9 in LSSB – TX+GT), 528 (9 in LSSB – BX+GT), 628 (9 in LSSB – BX), and 728 (9 in LSSB) exhibited relatively similar results in Mar 2019 (in the second thawing period) compared to those observed in Mar 2018 (in the first thawing period).

4.4.4. Falling Weight Deflectometer (FWD) Test Results After the Second Thawing Period

Maximum Deflection

In Jul 2019 (after the second thawing period) (Figure 4.13), cells 185 (12 in coarse RCA), 186 (12 in fine RCA), and 189 (12 in RCA+RAP) exhibited lower maximum deflections than those observed in Mar 2019 (in the second thawing period). On the other hand, cells 188 (12 in limestone), 127 (18 in LSSB), 227 (18 in LSSB), 328 (9 in LSSB – TX), 428 (9 in LSSB – TX+GT), 528 (9 in LSSB – BX+GT), 628 (9 in LSSB – BX), and 728 (9 in LSSB) exhibited higher maximum deflections in Jul 2019 (after the second thawing) than those observed in Mar 2019 (in the second thawing period). The increases in the maximum deflections from Mar 2019 (in the second thawing period) to Jul 2019 (after the second thawing period) were higher for cells 328 (9 in LSSB – TX), 428 (9 in LSSB – TX+GT), 528 (9 in LSSB – BX+GT), 628 (9 in LSSB – BX), and 728 (9 in LSSB).

Composite E_{FWD}

In Jul 2019 (after the second thawing period) (Figure 4.14), the trends observed in the composite E_{FWD} values [relative to those observed in Mar 2019 (in the second thawing period)] were exactly compatible with those observed in the maximum deflections [relative to those observed in Mar 2019 (in the second thawing period)]. Higher maximum deflections yielded lower composite E_{FWD} values. On the contrary, lower maximum deflections yielded higher composite E_{FWD} values. This was due to the inversely proportional relationship of composite E_{FWD} with the maximum deflections under the same load [9,000 lb (40 kN)] based on Equation (2).

Asphalt E_{FWD}

In Jul 2019 (after the second thawing period) (Figure 4.15), considerably lower asphalt E_{FWD} values were observed in all of the test cells compared to those observed in Mar 2019 (in the second thawing period). This was possibly due to the softening of the asphalt layers at relatively higher temperatures in Jul 2019 (after the second thawing period) compared to those observed in Mar 2019 (in the second thawing period).

Base+Subbase E_{FWD}

In Jul 2019 (after the second thawing period) (Figure 4.16), all of the base+subbase layers exhibited higher E_{FWD} values than those observed in Mar 2019 (in the second thawing period). The increases in the E_{FWD} values were considerably higher for the coarse RCA and fine RCA base+subbase layers [cells 185 (12 in coarse RCA) and 186 (12 in fine RCA), respectively)]. As the asphalt layers became softer at higher temperatures, more traffic loads were transferred to the coarse RCA and fine RCA base+subbase layers [cells 185 (12 in coarse RCA) and 186 (12 in fine RCA), respectively)], and higher E_{FWD} values were observed in both base+subbase layers due to their stress-hardening behavior. In particular, the fine RCA base+subbase layer [cell 186 (12 in fine RCA)] exhibited higher E_{FWD} values than the coarse RCA base+subbase layer [cell 185 (12 in coarse RCA)]. As seen in Figure 4.15, the asphalt E_{FWD} values of cell 186 (12 in fine RCA) were lower than those of cell 185 (12 in coarse RCA). The fine RCA base+subbase layer [cell 186 (12 in fine RCA)] experienced greater traffic loads than the coarse RCA base+subbase layer [cell 185 (12 in coarse RCA)]. The fine RCA base+subbase layer [cell 186 (12 in fine RCA) exhibited higher E_{FWD} values than the coarse RCA base+subbase layer [cell 185 (coarse RCA)] due to the stress-hardening behavior. For all of the other base+subbase layers, it was speculated that the base+subbase layers densified and became stiffer over time due to the traffic provided by the MnROAD truck [80 kip (36.3 Mg)].

Subgrade E_{FWD}

In Jul 2019 (after the second thawing period) (Figure 4.17), overall, the E_{FWD} values of the subgrade layers were lower than or similar to those observed in Mar 2019 (in the second thawing period). The most considerable difference was observed in the sand subgrade layer in cell 186 (12 in fine RCA). The sand subgrade layer in cell 186 (12 in fine RCA) exhibited considerably lower E_{FWD} in Jul 2019 (after the second thawing period) than those observed in Mar 2019 (in the second thawing period).

In conclusion, according to the results observed from Nov 2017 (before the first freezing period) to Jul 2019 (after the second thawing period), cells 185 (12 in coarse RCA) and 186 (12 in fine RCA), constructed over sand subgrade layers, performed considerably better than the other cells. After approximately two years, cells 185 (12 in coarse RCA) and 186 (12 in fine RCA) exhibited lower maximum deflections and higher composite E_{FWD} values. In fact, cell 186 (12 in fine RCA) performed better than cell 185 (12 in coarse RCA) as it exhibited relatively lower maximum deflections and higher composite E_{FWD} values compared to cell 185 (12 in coarse RCA). This could indicate that the fine RCA material would be a better option to construct aggregate base layers than the coarse RCA material. After approximately two years, cell 189 (12 in RCA+RAP) exhibited lower maximum deflections and higher composite E_{FWD} values than cell 188 (12 in limestone) (both test cells were constructed over clay loam subgrade layers). Overall, these results indicate that the sand subgrade layers in cells 185 (12 in coarse RCA) and 186 (12 in fine RCA) performed better than the clay loam subgrade layers in cells 188 (12 in limestone) and 189 (12 in RCA+RAP). In addition, the following material selection can be recommended for building aggregate base layers from the most preferred to least preferred, based on the FWD test results: (1) fine RCA, (2) coarse RCA, (3) RCA+RAP, and (4) limestone. Lastly, cells 127 (18 in LSSB) and 227 (18 in LSSB) exhibited lower deflections and higher composite E_{FWD} values than cells 328 (9 in LSSB – TX), 428 (9 in LSSB – TX+GT), 528 (9 in LSSB – BX+GT), 628 (9 in LSSB – BX), and 728 (9 in LSSB) and it could be indicated that thicker LSSB layers should be built in pavement foundation systems. In brief, having strong and well-performing base, subbase, and subgrade layers is essential for overall pavement performance. From the results obtained from this field study, it can be concluded that constructing fine RCA base, sufficiently thick LSSB, and sand subgrade layers together would maximize the overall pavement performance.

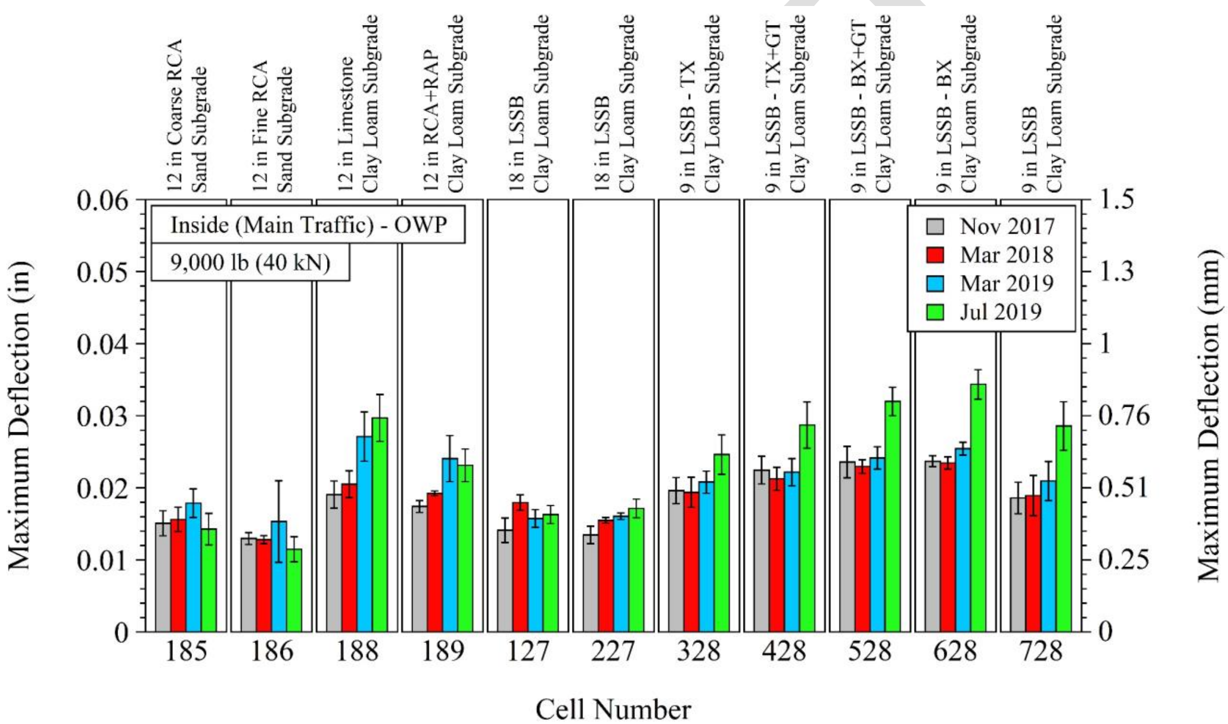

Figure 4.13. Summary of the maximum deflections of the test cells under 9,000 lb (40 kN) load (error bars represent one standard deviation of the data)

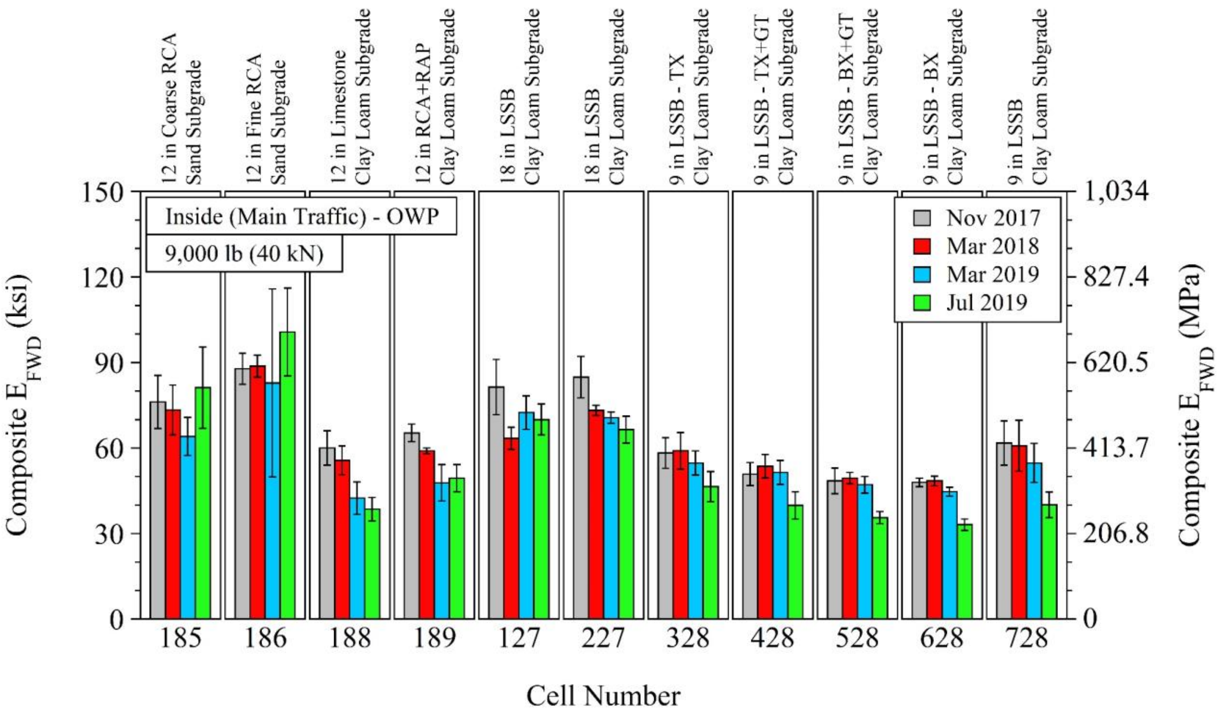

Figure 4.14. Summary of the subgrade E_{FWD} of the test cells under 9,000 lb (40 kN) load (error bars represent one standard deviation of the data)

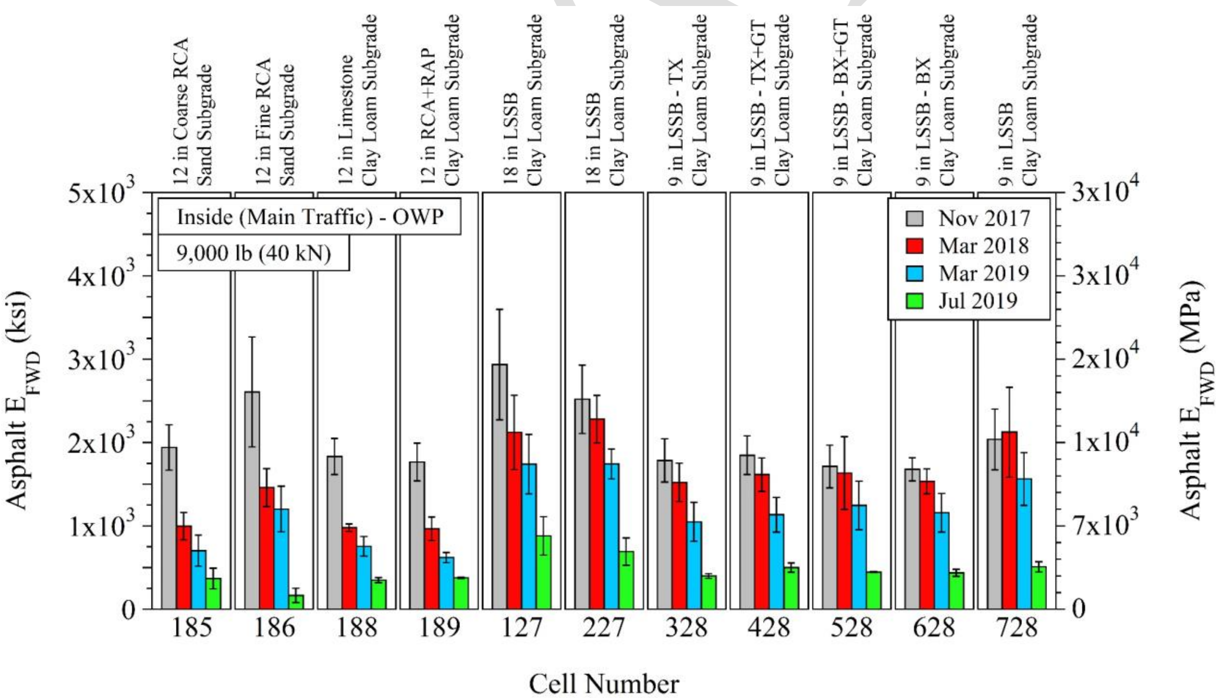

Figure 4.15. Summary of the asphalt E_{FWD} of the test cells under 9,000 lb (40 kN) load (error bars represent one standard deviation of the data)

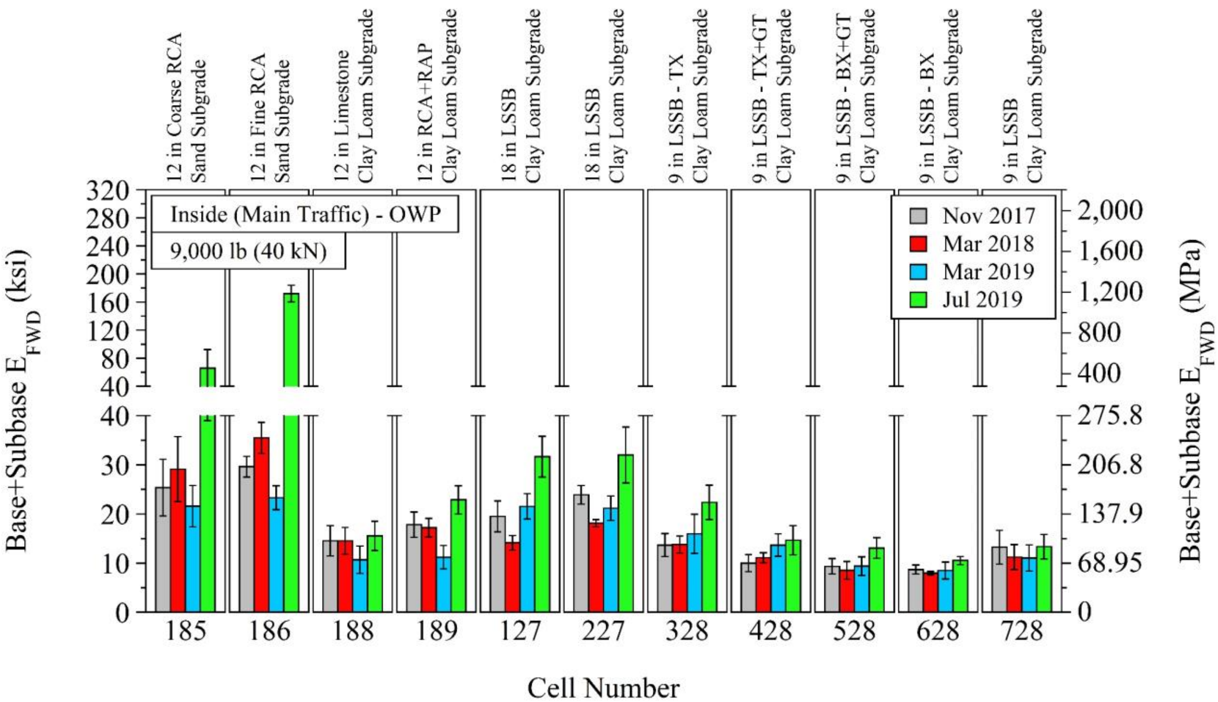

Figure 4.16. Summary of the base+subbase EFWD of the test cells under 9,000 lb (40 kN) load (error bars represent one standard deviation of the data)

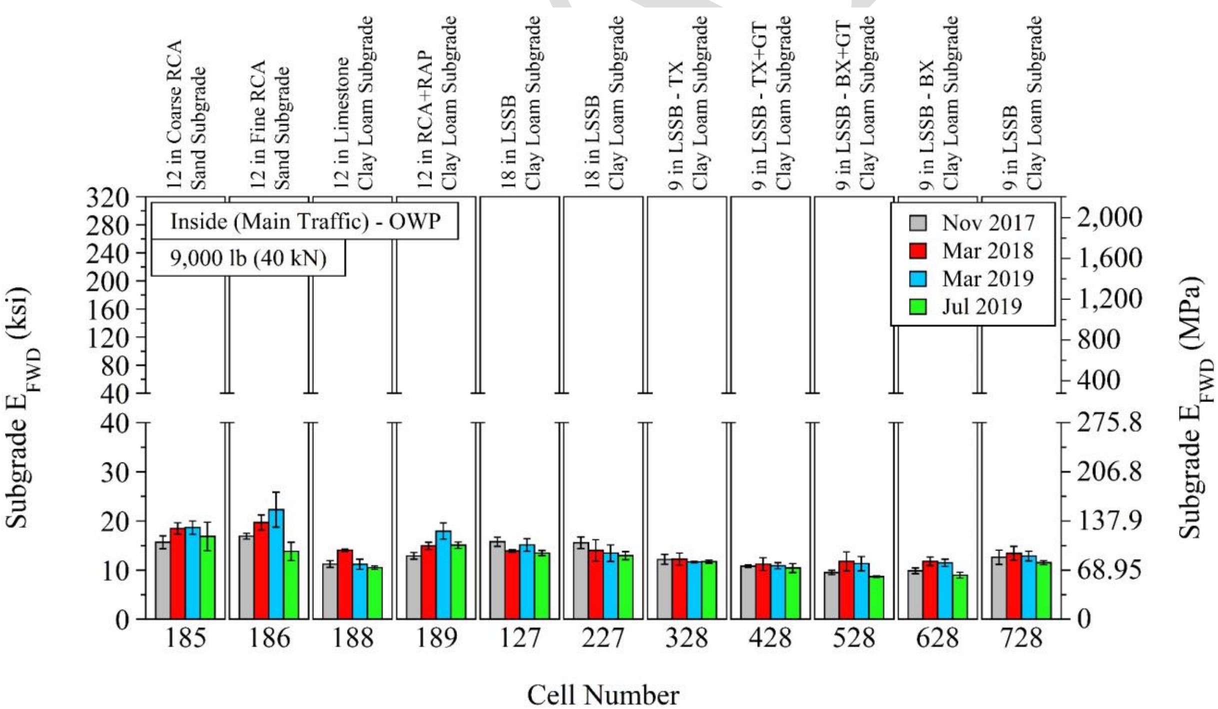

Figure 4.17. Summary of the subgrade EFWD of the test cells under 9,000 lb (40 kN) load (error bars represent one standard deviation of the data)

5. FROST HEAVE AND THAW SETTLEMENT MEASUREMENTS

During the freezing period, water freezes and turns into ice with an increase (around 10%) in its volume, and this event causes frost heave in the pavement structure. On the contrary, during the thawing period, ice melts with a reduction in its volume and this event causes thaw settlement in the pavement structure. Seasonal frost heave and thaw settlement can cause pavement distresses that decrease the long-term performance and the service life of pavements.

Several stations were selected for each test cell and five test points were marked on each station before taking elevation measurements. The same points were tested at different dates. Figure 5.1 is an example that shows the locations of the test points for two stations in cell 185 (12 in coarse RCA). Leveling readings were taken from the five test points on each station and elevation profiles were plotted. Figure 5.2 is an example that shows the elevation profiles of one station in cell 185 (12 in coarse RCA) at different dates. Elevation profiles for all of the test cells are provided in Appendix P. The elevation changes due to frost heave and thaw settlement were evaluated from the elevation profiles (no statistical analysis was performed in this report). In Figure 5.3, the elevation measurements taken on Dec/4/2017 (the early stage of the first freezing period) were considered as zero (reference elevation), and the relative elevation measurements taken on Dec/18/2017 (the later stage of the first freezing period compared to the date of Dec/4/2017) and Mar/21/2018 (the final stage of the first thawing period or after fully thawing) are summarized and evaluated visually.

On Dec/18/2017 (the later stage of the first freezing period compared to the date of Dec/4/2017), no considerable frost heave was observed in cells 185 (12 in coarse RCA), 189 (12 in RCA+RAP), 127 (18 in LSSB), 227 (18 in LSSB), 428 (9 in LSSB – TX+GT), 528 (9 in LSSB – BX+GT), 628 (9 in LSSB – BX), and 728 (9 in LSSB) (Figure 5.3). On the other hand, cells 186 (12 in fine RCA), 188 (12 in limestone), and 328 (9 in LSSB – TX) exhibited relatively more considerable frost heave (Figure 5.3). These differences could be related to the amount of water available for freezing. The freezing of a higher amount of water can cause greater frost heave than the freezing of a less amount of water. In addition, due to different thermal properties of the base, subbase, and subgrade materials, the materials in the test cells could have different freezing levels.

On Mar/21/2018 (the final stage of the first thawing period or after thawing), the greatest thaw settlements were observed in cells 185 (12 in coarse RCA) and 186 (12 in fine RCA) (Figure 5.3), and this could be related to the water absorption capacities of coarse RCA and fine RCA materials. In Task 4 (laboratory testing) report, it was determined that the water absorptions of coarse RCA and fine RCA materials were higher than those of the other materials. For cells 185 (12 in coarse RCA) and 186 (12 in fine RCA), it was speculated that the thawing of higher amounts of water in the coarse RCA and fine RCA base layers yielded greater thaw settlements. Cell 188 (12 in limestone) yielded less thaw settlement than cell 189 (12 in RCA+RAP) (Figure 5.3). In Task 4 (laboratory testing) report, it was determined that water absorption of limestone was lower than that of RCA+RAP material. Therefore, it was speculated that the limestone base layer [cell 188 (12 in limestone)] yielded less thaw settlement than the RCA+RAP base layer [cell 189 (RCA+RAP)] due to the thawing of fewer amounts of water. Although the thaw settlements of cells 127 (18 in LSSB) and 227 (18 in LSSB) were expected to be lower due to good drainage properties of 18 in LSSB layers, considerable thaw settlements were observed in those test cells

(Figure 5.3). The lowest thaw settlements were observed in cells 428 (9 in LSSB – TX+GT), 528 (9 in LSSB – BX+GT), 628 (9 in LSSB – BX), and 728 (9 in LSSB) (Figure 5.3). For cell 328 (9 in LSSB – TX), the elevations recorded on Mar/21/2018 (the final stage of the first thawing period or after fully thawing) were higher than those recorded on Dec/18/2017 (the later stage of the first freezing period compared to the date of Dec/4/2017) (Figure 5.3). This result was attributed to an experimental error. Overall, it was speculated that the effective drainage provided by 9 in LSSB layers decreased frost heave and thaw settlement.

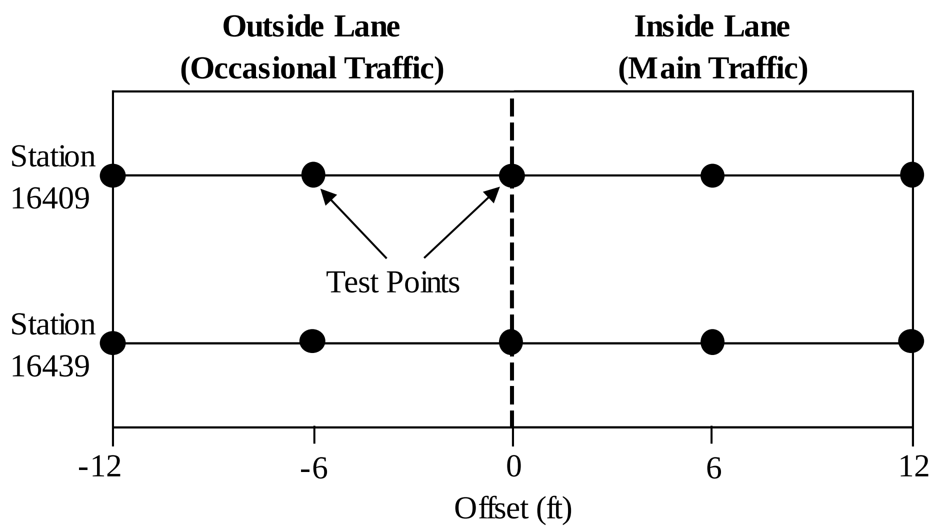

Figure 5.1. Locations of the test points for two stations in cell 185 (12 in coarse RCA)

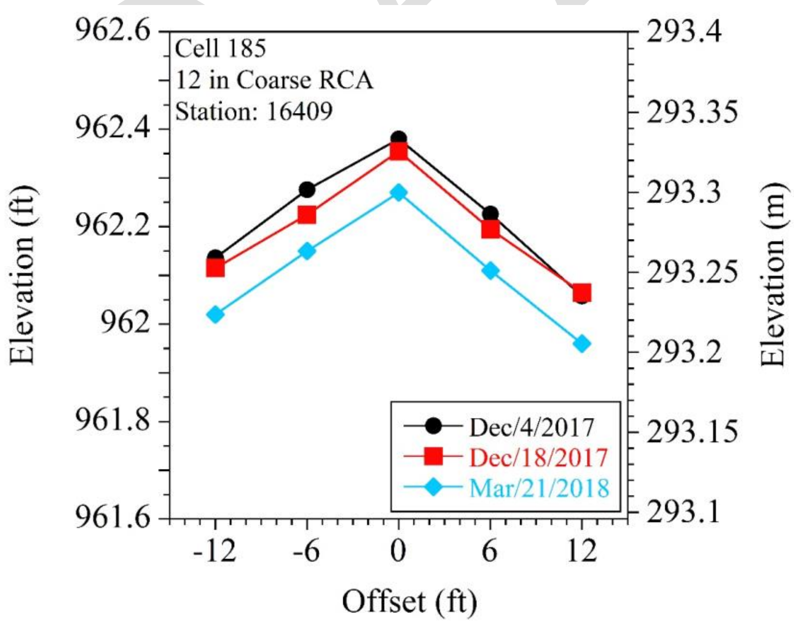

Figure 5.2. Elevation profiles of one station in cell 185 (12 in coarse RCA) at different dates

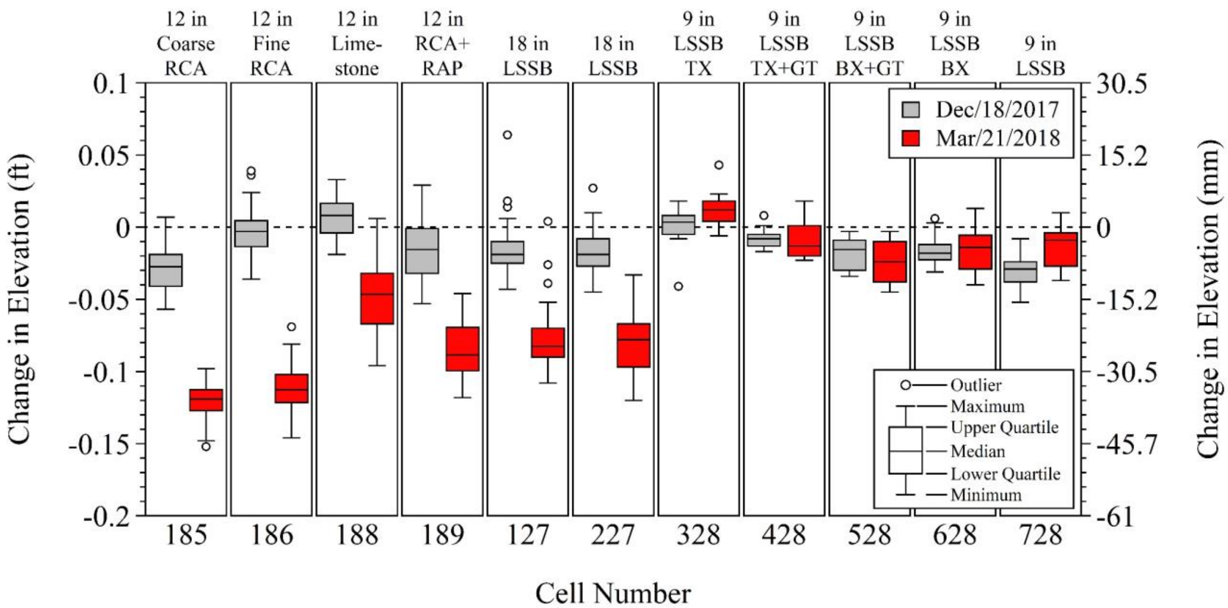

Figure 5.3. Summary of the changes in the elevations of the test cells

6. RUTTING MEASUREMENTS

Rutting measurements were taken by using an automated laser profile system (ALPS) (MnDOT 2003; MnDOT 2009a) for each lane at 50 ft intervals (Figure 6.1). For the ALPS measurements, the ALPS beam [the length of the beam was 12 ft 10 in (3.9 m)] was centered on the lane by locating it between two previously marked paint marks. The beam was stationary while testing was conducted, and 616 data points were collected for each test. Since the width of each lane was 12 ft (3.7 m), which was 10 in (25.4 cm) shorter than the beam length [12 ft 10 in (3.9 m)], 5 in (12.7 cm) from the other lane and 5 in (12.7 cm) from the shoulder were also captured during testing. The ALPS data was then analyzed by using a macro in Excel that generated a digital pavement lane profile for each test and smoothed the data by using a 16-point moving average. The readings were adjusted to eliminate extreme outlying data points by the macro, and straight edges were simulated for the inside wheel path (IWP) and OWP of the generated pavement profile (Figure 6.2). Then, the maximum rut depths were determined by taking the differences between the simulated straight edges and the smoothed digital pavement profiles.

Figure 6.1. Automated laser profile system (ALPS) (MnDOT 2003)

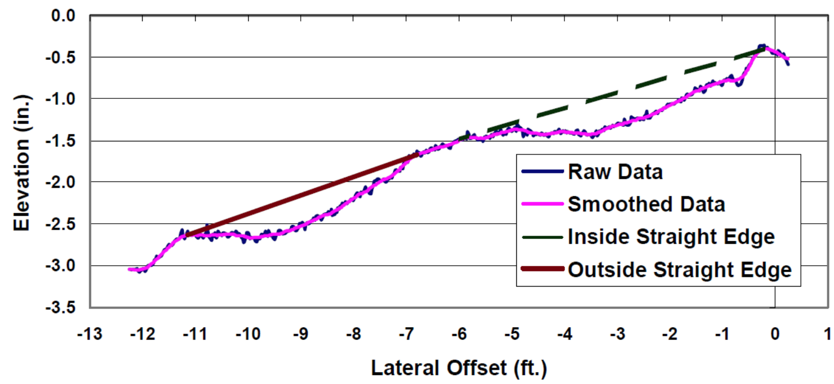

Figure 6.2. Automated laser profile system (ALPS) rutting data (MnDOT 2003)

It was observed in several test results that the macro was not able to simulate straight edges on the IWP or OWP. In addition, the digital separation of the IWP and OWP could not be made for several test cells due to relatively higher rut depths throughout the lane. Therefore, the rut depths are not summarized separately for the IWP and OWP of one lane hereinafter to overcome such problems. The rut depths are summarized simply for the inside lane (main traffic) and outside lane (occasional traffic).

For each test cell, the rut depths observed in the inside lane (main traffic) were higher than those observed in the outside lane (occasional traffic). Since the inside lane (main traffic) was subjected to more traffic [provided by the MnROAD truck weighing 80 kip (36.3 Mg)] than the outside lane (occasional traffic), it was expected to observe higher rutting in the inside lane (main traffic). It was also concluded that the rut depths became more stable as time progressed. Figure 6.3 is an example that shows the rut depth measurements for cell 428 (9 in LSSB – TX+GT). All of the rut depth measurements for the test cells are provided in Appendix R.

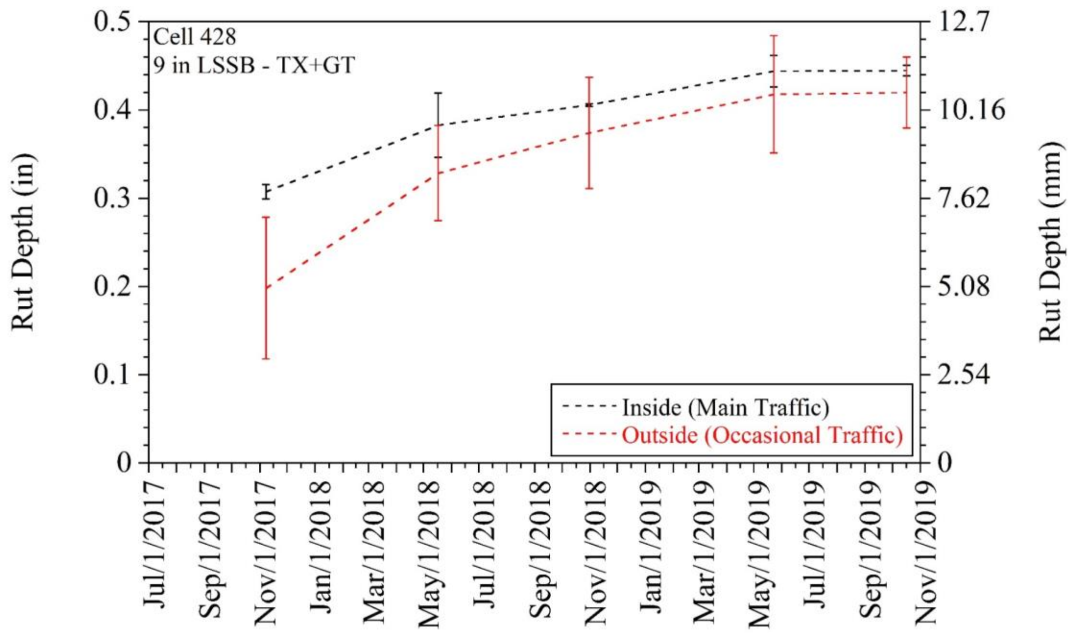

Figure 6.3. Rut depth measurements for cell 428 (9 in LSSB – TX+GT) (error bars represent one standard deviation of the data)

A summary of the rut depths observed in the inside lane (main traffic) of the test cells is provided in Figure 6.4. Overall, cells 328 (9 in LSSB – TX), 428 (9 in LSSB – TX+GT), 528 (9 in LSSB – BX+GT), and 628 (9 in LSSB – BX) exhibited higher rut depths than the other cells. It was speculated that 9 in LSSB layers could not be compacted properly due to the nature of the large stones and relatively lower thickness of 9 in LSSB layers compared to 18 in LSSB layers in cells 127 (18 in LSSB) and 227 (18 in LSSB). In addition, the class 5Q aggregate base layers in cells 328 (9 in LSSB – TX), 428 (9 in LSSB – TX+GT), 528 (9 in LSSB – BX+GT), and 628 (9 in LSSB – BX) was not compacted adequately. In fact, cells 328 (9 in LSSB – TX) and 628 (9 in LSSB BX) exhibited lower rut depths than cells 428 (9 in LSSB – TX+GT) and 528 (9 in LSSB – BX+GT). As determined in Task 3 (construction monitoring and reporting) report, lower in-situ dry density values were observed for the class 5Q aggregate base layers in cells 428 (9 in LSSB – TX+GT) and 528 (9 in LSSB – BX+GT) compared to those observed in cells 328 (9 in LSSB – TX) and 628 (9 in LSSB – BX). Thus, it resulted in higher rutting values for cells 428 (9 in LSSB – TX+GT) and 528 (9 in LSSB – BX+GT) [compared to cells 328 (9 in LSSB – TX) and 628 (9 in LSSB – BX)]. The lowest rut depths were observed in cell 728 (9 in LSSB). Cells 185 (12 in coarse RCA), 186 (12 in fine RCA), 127 (18 in LSSB), and 227 (18 in LSSB) exhibited similar rut depths which were lower than those observed in cells 188 (12 in limestone) and 189 (12 in RCA+RAP). Cell 188 (12 in limestone) exhibited higher rut depths than cell 189 (12 in RCA+RAP).

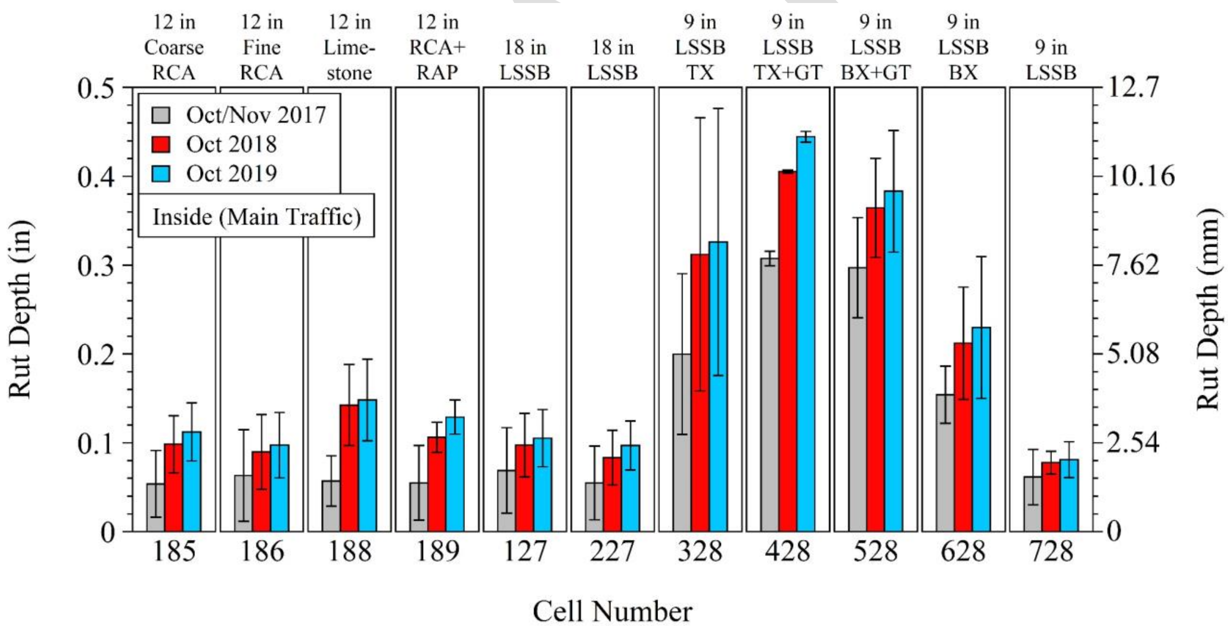

Figure 6.4. Summary of the rut depth measurements for the test cells (error bars represent one standard deviation of the data)

7. INTERNATIONAL ROUGHNESS INDEX (IRI) MEASUREMENTS

The international roughness index (IRI) is a standard measure of pavement smoothness and ride quality (Akkari and Izevbekhai 2012). The IRI measurements were taken by a lightweight internal surface analyzer (LISA) profiler mounted on a utility vehicle (Figure 7.1) (MnDOT 2009b). The LISA profiler measured the amount of vertical rise over a horizontal distance [tire pressure = 10 psi (69 kPa)] [vehicle speed = 10-12 mph (16-19 kmh)] (MnDOT 2009). The profiler contained two laser sources on the two sides of the vehicle. One of the lasers took continuous profile measurements over a 4 in path. The second laser measured three discrete profiles across the 4 in path. The IRI was calculated from the data obtained by the lasers (Akkari and Izevbekhai 2012).

The FHWA describes condition criteria for different IRI values (Table 7.1). While the IRI values lower than 2.68 m/km (169.8 in/mile) are acceptable for the ride quality, the values greater than 2.68 m/km (169.8 in/mile) are considered unacceptable. Overall, by considering all of the test cells, no consistent trends were observed between different test locations [inside (main traffic) – IWP, inside (main traffic) – OWP, outside (occasional traffic) – IWP, and outside (occasional traffic (OWP)]. Although some fluctuations were observed over time, the general trend was that the IRI values increased over time. Figure 7.2 is an example that shows the IRI measurements for cell 227 (18 in LSSB). All of the IRI measurements for each test cell are provided in Appendix S.

Figure 7.1. Lightweight inertial surface analyzer (LISA) profiler (MnDOT 2009)

Table 7.1. FHWA international roughness index (IRI) condition criteria (Elbheiry et al. 2011)

Condition Term	IRI	Ride Quality
Very Good	< 0.95 m/km	Acceptable 0 – 2.68 m/km
Good	0.95 – 1.49 m/km	
Fair	1.50 – 1.88 m/km	
Poor	1.89 – 2.68 m/km	
Very Poor	> 2.68 m/km	Unacceptable

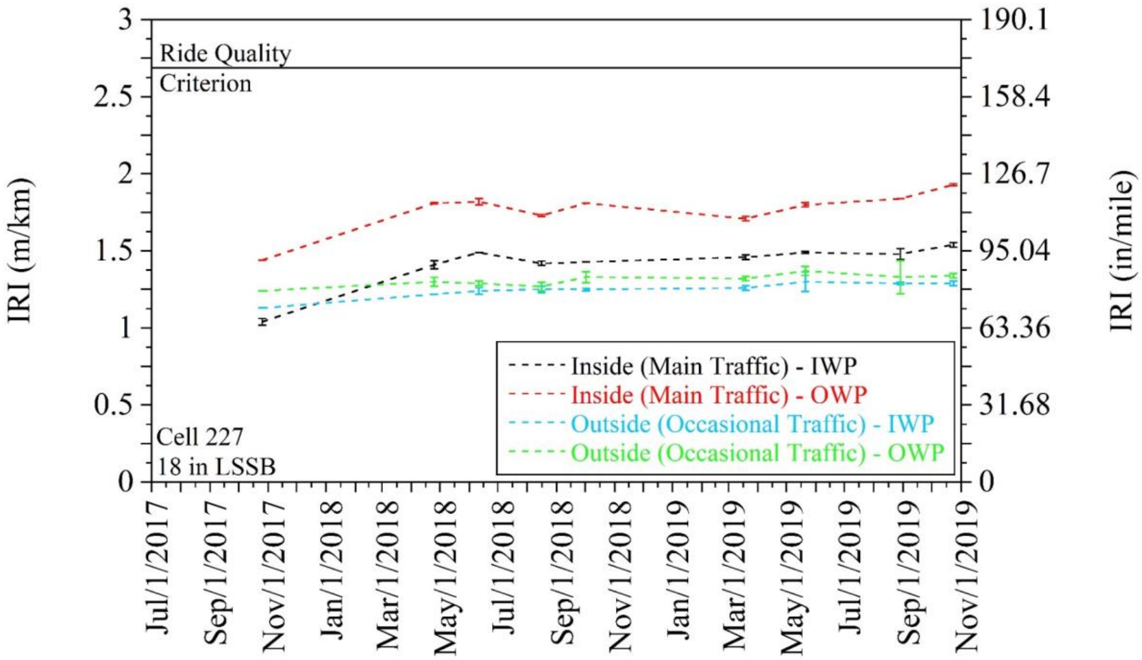

Figure 7.2. IRI measurements for cell 227 (18 in LSSB) (error bars represent one standard deviation of the data)

A summary of the IRI measurements for the inside lane (main traffic) – OWP of the test cells is provided in Figure 7.3. Appendix T shows the IRI measurements for the inside lane (main traffic) – OWP of the test cells. Cells 628 (9 in LSSB – BX) and 728 (9 in LSSB) exhibited higher IRI values than the other cells. Cells 127 (18 in LSSB), 227 (18 in LSSB), 328 (9 in LSSB – TX), and 428 (9 in LSSB – TX+GT) yielded higher IRI values than cells 185 (12 in coarse RCA), 186 (12 in fine RCA), 188 (12 in limestone), 189 (12 in RCA+RAP), and 528 (9 in LSSB – BX+GT). The lower IRI values were observed in cells 186 (12 in fine RCA) and 189 (12 in RCA+RAP).

Overall, except cell 728 (9 in LSSB), all other IRI values were lower than 2.68 m/km (169.8 in/mile) (Figure 7.3), which indicated that the ride quality was acceptable throughout all the test cells except cell 728 (9 in LSSB) according to the FHWA (Table 7.1). For cell 728 (9 in LSSB), while the initial IRI values were lower than 2.68 m/km (169.8 in/mile) in Oct 2017, the values slightly exceeded that criterion over time, which indicated that the ride quality was unacceptable.

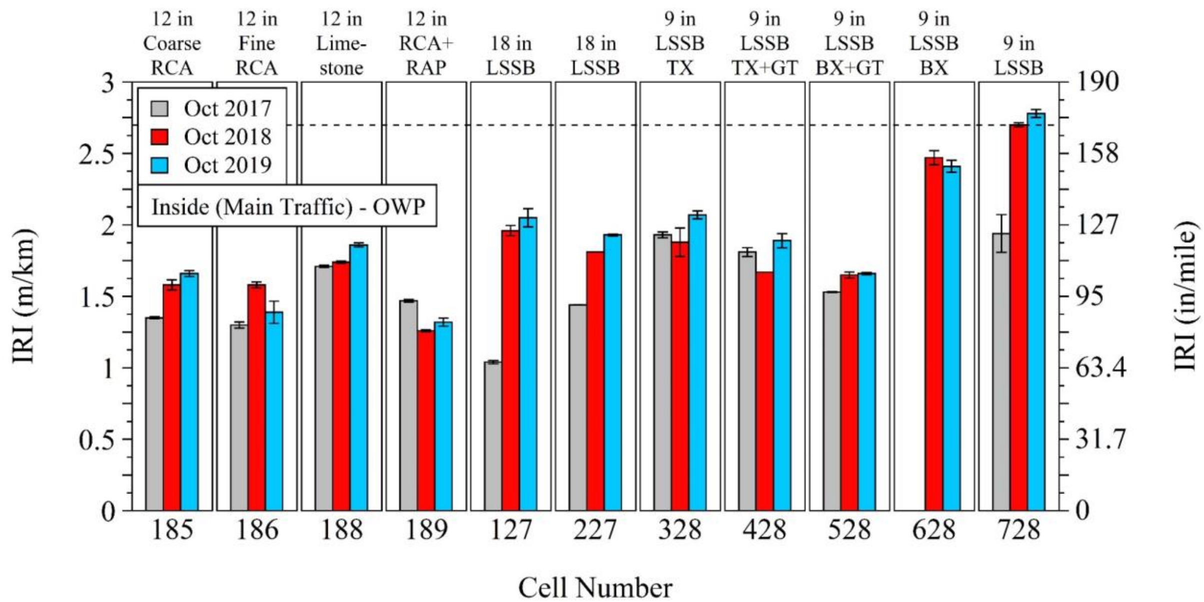

Figure 7.3. Summary of the international roughness index (IRI) measurements for the inside lane (main traffic) – outer wheel path (OWP)

8. PAVEMENT DISTRESSES

Pavement distress surveys were performed by the MnROAD Operations staff to monitor the field performance of the test cells. The data collected included the distress type, extent or amount of distress, and the severity of the distress. For the evaluation, a modified distress identification manual for the long-term pavement performance program (LTTP) was used (Miller and Bellinger 2014). The visible failure mechanisms were marked on the maps (Figure 8.1) and then entered into an Excel spreadsheet.

Table 8.1 summarizes the pavement distress types for flexible pavements as described in the distress identification manual for the LTTP (Miller and Bellinger 2014). Among all the distress types, only transverse cracking (cracks that are predominantly perpendicular to the pavement centerline), longitudinal cracking (cracks predominantly parallel to pavement centerline), and raveling (wearing away of the pavement surface caused by the dislodging of aggregate particles and loss of asphalt binder) were observed in the test cells (Table 8.1). The severity levels for transverse cracking and longitudinal cracking were determined to be low (a crack with a mean width ≤ 6 mm). In addition, the severity level for raveling was determined as low to medium.

Figures 8.2 and 8.3 summarize the transverse cracking on the inside lane (main traffic) and outside lane (occasional traffic) of the test cells, respectively. The lengths were reported as the number of the unit squares shown in Figure 8.1. For both lanes, transverse cracking was only observed in cells 189 (12 in RCA+RAP), 227 (18 in LSSB), 328 (9 in LSSB – TX), 528 (9 in LSSB – BX+GT), and 728 (9 in LSSB).

Figure 8.4 summarizes the longitudinal cracking on the inside lane (main traffic) of the test cells. All the cracks were observed on the inside lane (main traffic) only, and the locations of the cracks were right by the centerline (non-wheel path). Longitudinal cracking was only observed on the inside lane (main traffic) of cells 328 (9 in LSSB – TX), 528 (9 in LSSB – BX+GT), 728 (9 in LSSB). While the shortest longitudinal cracking (total length) was observed in cells 328 (9 in LSSB – TX), the longest cracking (total length) was observed in cell 528 (9 in LSSB – BX+GT).

Since raveling is related to the quality and the long-term performance of the asphalt material only, no discussion was included in the context of the report. However, survey results for raveling can be seen in Appendix U.

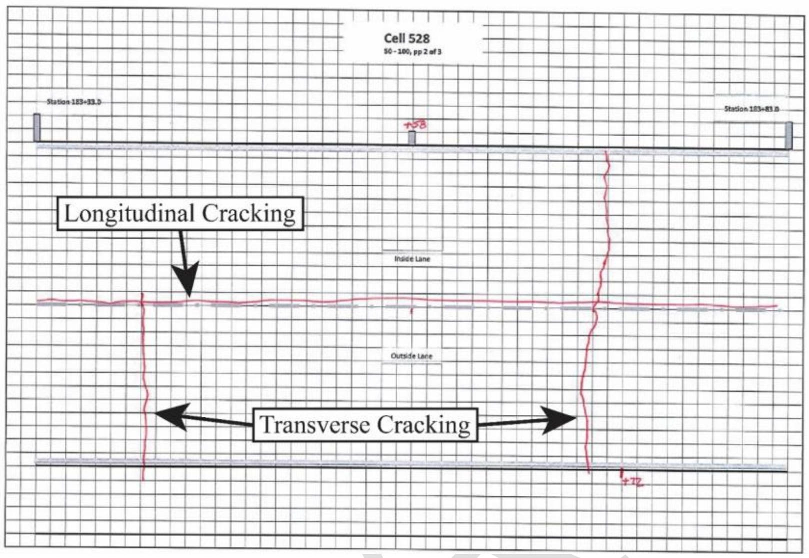

Figure 8.1. Pavement distress map for cell 528 (9 in LSSB – BX+GT)

Table 8.1. List of flexible pavement distresses (NA = not available)

Distress Category	Distress Type	Observed	Severity
Cracking	Fatigue Cracking	No	NA
	Block Cracking	No	NA
	Edge Cracking	No	NA
	Longitudinal Cracking	Yes	Low
	Reflection Cracking at Joints	No	NA
	Transverse Cracking	Yes	Low
Patching and Potholes	Patch/Patch Deterioration	No	NA
	Potholes	No	NA
Surface Deformation	Rutting	See Section 6	NA
	Shoving	No	NA
Surface Defects	Bleeding	No	NA
	Polished Aggregate	No	NA
	Raveling	Yes	Low/Moderate
Miscellaneous Distresses	Lane-to-Shoulder Dropoff	No	NA
	Water Bleeding and Pumping	No	NA

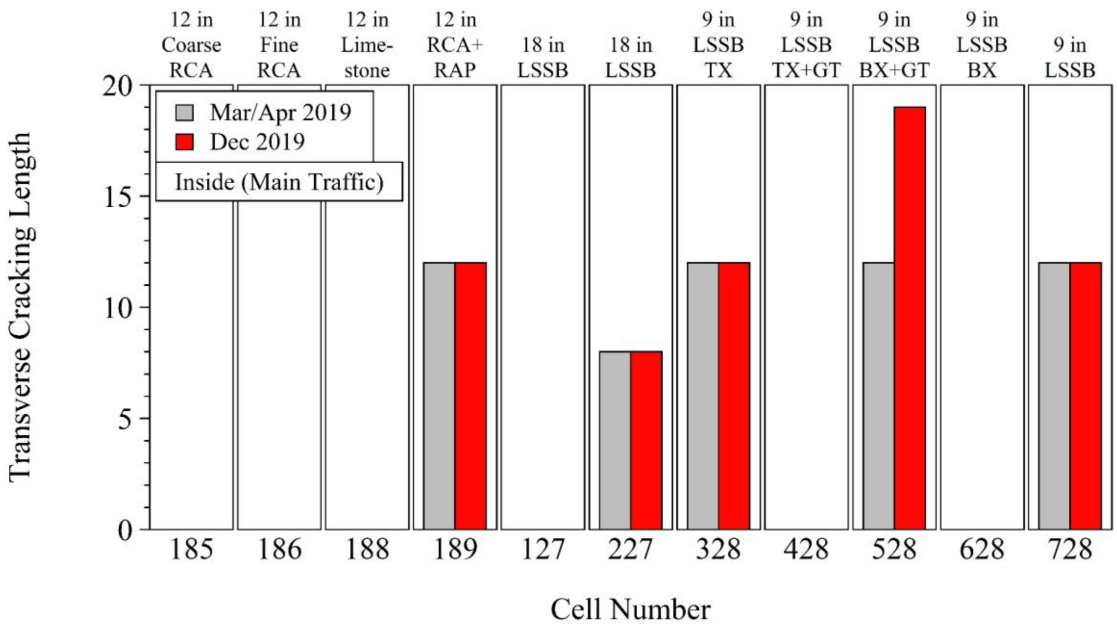

Figure 8.2. Summary of the transverse cracking lengths on the inside lane (main traffic) of the test cells (lengths are number of unit squares shown in the distress maps)

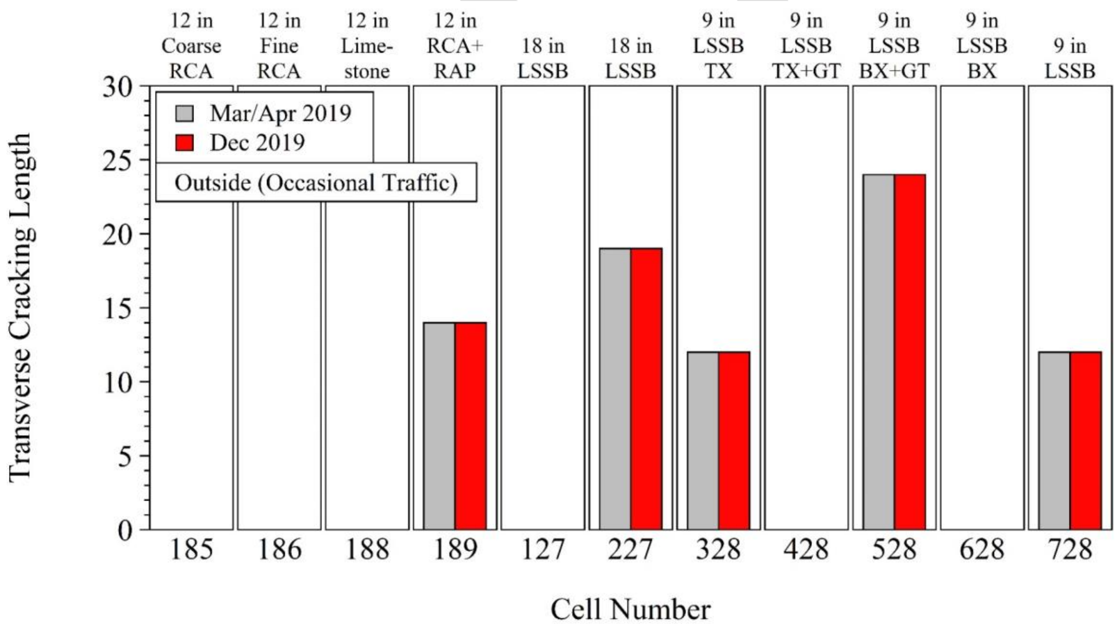

Figure 8.3. Summary of the transverse cracking lengths on the outside lane (occasional traffic) of the test cells (lengths are number of unit squares shown in the distress maps)

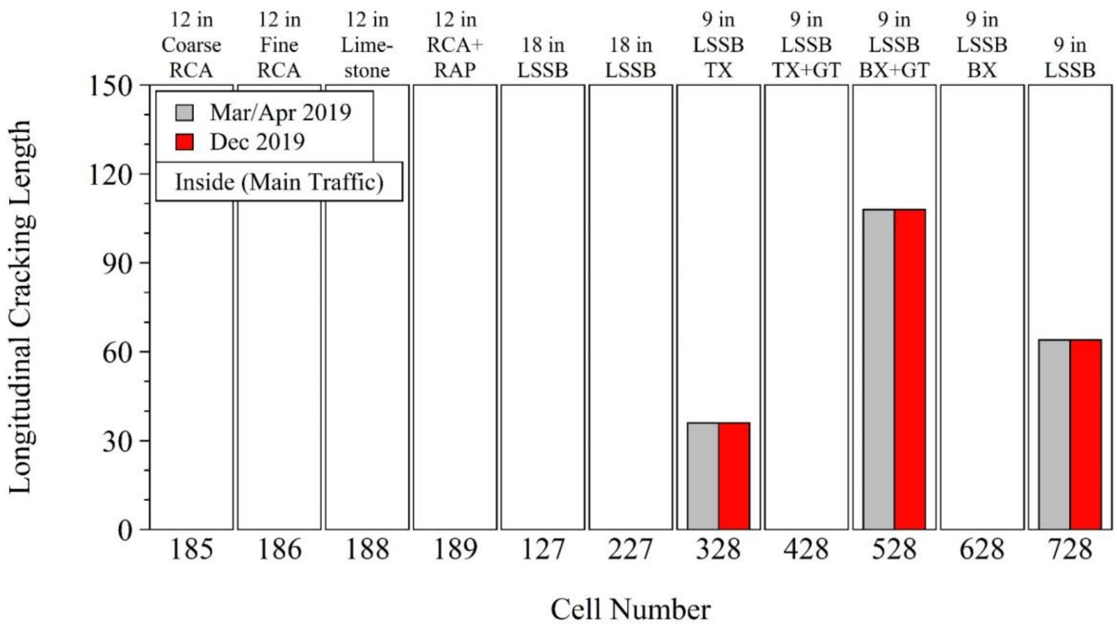

Figure 8.4. Summary of the longitudinal cracking lengths of the test cells (lengths are number of unit squares shown in the distress maps)

9. CONCLUSIONS

- Moisture probe readings were compatible with thermocouple readings and both sensors readings demonstrated the freezing and thawing periods properly. In addition, the VWC values slightly increased due to precipitation in the rainy periods. However, the class 6 aggregate [cell 127 (18 in LSSB)] and the class 5Q aggregate [cell 728 (9 in LSSB)] base layers did not exhibit such an increase in the rainy periods. This could indicate that a good drainage system was provided by the LSSB layers in cell 127 (18 in LSSB) and cell 728 (9 in LSSB).
- Different maximum frost penetration depths and freezing and thawing periods were observed for each test cell. It was speculated that such parameters were affected by the thermal property of each material used in the test cells.

- For the FWD tests, regardless of the test location and date, higher maximum deflections were observed under higher loads for each test cell as expected. The composite, asphalt, and base+subbase E_{FWD} values determined for 6,000 lb (26.7 kN) load were slightly lower than or similar to those calculated for 9,000 lb (40 kN) and 12,000 lb (53.4 kN) loads. The composite, asphalt, and base+subbase E_{FWD} values calculated for 9,000 lb (40 kN) and 12,000 lb (53.4 kN) loads were similar. All of the loads yielded similar subgrade E_{FWD} values.

- For the FWD tests, regardless of the date, the outside lane (occasional traffic) – OWP yielded relatively higher maximum deflections than the other locations under 9,000 lb (40 kN) load. The maximum deflections observed in the outside lane (occasional traffic) – MID were higher than or similar to those observed in the inside lane (main traffic). Overall, it was concluded that the maximum deflections observed in the inside lane (main traffic) were lower than those observed in the outside lane (occasional traffic). The trends observed in the composite E_{FWD} values were exactly compatible with those observed in the maximum deflections under 9,000 lb (40 kN) load. The trends observed in the asphalt and base+subbase E_{FWD} values were similar to those observed in the composite E_{FWD} values under 9,000 lb (40 kN) load. No significant differences were observed in the subgrade E_{FWD} values for different test locations of each test cell under 9,000 lb (40 kN) load.

- For the FWD tests, according to the two-year test results, cells 185 (12 in coarse RCA) and 186 (12 in fine RCA), constructed over sand subgrade layers, performed considerably better (lower maximum deflections and higher composite E_{FWD} values) than the other cells. In fact, cell 186 (12 in fine RCA) performed better than cell 185 (12 in coarse RCA). This could indicate that the fine RCA material would be a better option to construct aggregate base layers than the coarse RCA material. After approximately two years, cell 189 (12 in RCA+RAP) performed better than cell 188 (12 in limestone) (both test cells were constructed over clay loam subgrade layers). This could indicate that the RCA+RAP material would be a better option to construct aggregate base layers than the limestone material. Overall, the sand subgrade layers in cells 185 (12 in coarse RCA) and 186 (12 in fine RCA) performed better than the clay loam subgrade layers in cells 188 (12 in limestone) and 189 (12 in RCA+RAP). Lastly, after approximately two years, cells 127 (18 in LSSB) and 227 (18 in LSSB) performed better than cells 328 (9 in LSSB – TX), 428 (9 in LSSB – TX+GT), 528 (9 in LSSB – BX+GT), 628 (9 in LSSB – BX), and 728 (9 in LSSB). This could indicate that constructing 18 in LSSB layers would be a better option than constructing 9 in LSSB layers. Overall, it can be concluded that constructing fine RCA base, sufficiently thick LSSB, and sand subgrade layers together would maximize the overall pavement performance.

- No considerable frost heave was observed in cells 185 (12 in coarse RCA), 189 (12 in RCA+RAP), 127 (18 in LSSB), 227 (18 in LSSB), 428 (9 in LSSB – TX+GT), 528 (9 in LSSB – BX+GT), 628 (9 in LSSB – BX), and 728 (9 in LSSB). On the other hand, cells 186 (12 in fine RCA), 188 (12 in limestone), and 328 (9 in LSSB – TX) exhibited relatively more considerable frost heave. It was speculated that the amount of water available for freezing and each road material's thermal property resulted in such differences.

- The greatest thaw settlements were observed in cells 185 (12 in coarse RCA) and 186 (12 in fine RCA), and this could be related to the water absorption capacities of coarse RCA and fine RCA materials. Cell 188 (12 in limestone) yielded less thaw settlement than cell 189 (12 in RCA+RAP), possibly because of lower water absorption of limestone. Although the thaw settlements of cells 127 (18 in LSSB) and 227 (18 in LSSB) were expected to be lower due to good drainage properties of 18 in LSSB layers, considerable thaw settlements were observed in those test cells. The lowest thaw settlements were observed in cells 428 (9 in LSSB – TX+GT), 528 (9 in LSSB – BX+GT), 628 (9 in LSSB – BX), and 728 (9 in LSSB), and it was speculated that the effective drainage provided by 9 in LSSB layers decreased frost heave and thaw settlement.

- Cells 185 (12 in coarse RCA), 186 (12 in fine RCA), 127 (18 in LSSB), and 227 (18 in LSSB) exhibited less rutting than cells 188 (12 in limestone) and 189 (12 in RCA+RAP). Cell 188 (12 in limestone) exhibited more rutting than cell 189 (12 in RCA+RAP). Cells 328 (9 in LSSB – TX), 428 (9 in LSSB – TX+GT), 528 (9 in LSSB BX+GT), and 628 (9 in LSSB – BX) yielded more rutting than the other cells. It was speculated that 9 in LSSB layers could not be compacted properly due to the nature of the large stones and relatively lower thickness of 9 in LSSB layers compared to 18 in LSSB layers in cells 127 (18 in LSSB) and 227 (18 in LSSB). In addition, the class 5Q aggregate base layers in cells 328 (9 in LSSB – TX), 428 (9 in LSSB – TX+GT), 528 (9 in LSSB – BX+GT), and 628 (9 in LSSB – BX) was not be compacted adequately. In fact, cells 328 (9 in LSSB – TX) and 628 (9 in LSSB BX) exhibited less rut depths than cells 428 (9 in LSSB – TX+GT) and 528 (9 in LSSB – BX+GT). As determined in Task 3 (construction monitoring and reporting) report, lower in-situ dry density values were observed for the class 5Q aggregate base layers in cells 428 (9 in LSSB – TX+GT) and 528 (9 in LSSB – BX+GT) compared to those observed in cells 328 (9 in LSSB – TX) and 628 (9 in LSSB – BX). Thus, it resulted in higher rutting values for cells 428 (9 in LSSB – TX+GT) and 528 (9 in LSSB – BX+GT) [compared to cells 328 (9 in LSSB – TX) and 628 (9 in LSSB – BX)]. The lowest rut depths were observed in cell 728 (9 in LSSB).

- Except cell 728 (9 in LSSB), all other test cells exhibited IRI values lower than 2.68 m/km (169.8 in/mile), indicating that the ride quality was acceptable throughout all the test cells except cell 728 (9 in LSSB). For cell 728 (9 in LSSB), while the initial IRI values were lower than 2.68 m/km (169.8 in/mile), the values slightly exceeded that criterion over time, which indicated that the ride quality was unacceptable. Cells 628 (9 in LSSB – BX) and 728 (9 in LSSB) exhibited higher IRI values than the other cells. Cells 127 (18 in LSSB), 227 (18 in LSSB), 328 (9 in LSSB – TX), and 428 (9 in LSSB – TX+GT) yielded higher IRI values than cells 185 (12 in coarse RCA), 186 (12 in fine RCA), 188 (12 in limestone), 189 (12 in RCA+RAP), and 528 (9 in LSSB – BX+GT). The lower IRI values were observed in cells 186 (12 in fine RCA) and 189 (12 in RCA+RAP).

- For both the inside lane (main traffic) and outside lane (occasional traffic), transverse cracking was only observed in cells 189 (12 in RCA+RAP), 227 (18 in LSSB), 328 (9 in LSSB – TX), 528 (9 in LSSB – BX+GT), and 728 (9 in LSSB). Longitudinal cracking was observed on the inside lane (main traffic) only, and the locations of the cracks were right by the centerline (non-wheel path). Longitudinal cracking was only observed on the inside lane (main traffic) of cells 328 (9 in LSSB – TX), 528 (9 in LSSB – BX+GT), 728 (9 in LSSB). While the shortest longitudinal cracking (total length) was observed in cells 328 (9 in LSSB – TX), the longest cracking (total length) was observed in cell 528 (9 in LSSB – BX+GT).

10. DISCUSSION & RECOMMENDATION

- Aggregates generally show a stress-hardening behavior due to the reorientation of the particles into a denser state under higher loads. However, aggregates can exhibit decreasing stiffness values after reaching the breakpoint stress due to the presence of underlying softer or wetter subgrade conditions. Stress-hardening and stress-softening behavior of each road material, as well as stresses at layer interfaces (asphalt/base and base+subbase/subgrade), should be investigated to better understand the performances of the pavement layers and the interactions between the pavement layers in the long-term.

- For the RAB group, the FWD results showed that RCA-included base layers performed superior to those built with limestone. Results showed that fine RCA performed the best followed by the coarse RCA and RCA+RAP while limestone performed the lowest within the test cells that were not built with LSSB. These results indicate that the following material selection can be recommended for building aggregate base layers from the most preferred to least preferred, based on the FWD test results: (1) Fine RCA, (2) Coarse RCA, (3) RCA+RAP, and (4) limestone.

- On the other hand, road materials containing RCA may attract more water due to higher absorption capacity and hydrophilicity. An increase in the water-holding capacity of aggregate base layers constructed with RCA materials may decrease the freeze-thaw (F-T) durability and cause considerable frost heave and thaw settlement. Current results showed that frost heave could not be monitored clearly, possibly due to measurement errors or operating different levelling equipment on different dates. On the other hand, thaw settlements could be observed overall. Pavement systems built with RCA materials showed higher affinity to thaw settlement overall. The amount of water available for freezing and each road material's thermal property should be well known to better understand the frost heave and thaw settlement mechanisms.

- The thickness of the LSSB layers should be sufficient enough to provide good subgrade improvement, drainage, and structural support and the results of this study showed that 18 in thick LSSB performed better than that of 9 in thick LSSB sections. It should also be noted that the FWD test may not be appropriate to evaluate the impact of geosynthetics in the LSSB system and heavy weight deflectometer (HWD) tests should be conducted in the future studies on the LSSB sections.

- Large stones having higher coefficient of uniformity (C_u) values may be used to construct LSSB layers to overcome particle reorientation during compaction and to provide a more stable foundation to effectively compact the pavement layers overlying LSSB layers. By doing so, rutting may be minimized.

- While LSSB layers are expected to show good drainage properties, conditions that could lower the permeability of the LSSB layers (e.g. contamination by the subgrade soil) should be investigated. The placement of geocomposite layers in the LSSB layers (preferably in the middle of the layers) should be investigated to improve the lateral drainage.

- The thermal property of each road material should be investigated to understand the different maximum frost penetration depths and freezing and thawing periods observed for each test cell.

11. REFERENCES

Akkari, A., & Izevbekhai, B. (2012). *Composite Pavements and Exposed Aggregate Texturing at MnROAD: Cells 70, 71, and 72, Construction Report and Early Performance Evaluation* (No. MN/RC 2012-29). Minnesota Department of Transportation, Research Services Section.

American Concrete Pavement Association (ACPA), (2009). Recycling concrete pavements, http://wikipave.org/index.php?title=Recycling_Concrete_Pavements

Andersland, O. B., & Ladanyi, B., (2004). Frozen Ground Engineering. The American Society for Civil Engineers.

Baladi, G., Thottempudi, A., & Dawson, T. A. (2011). Backcalculation of Unbound Granular Layer Moduli (No. RC-1548).
Becker, P. J. (2016). The Central Iowa Expo site pavement foundation stabilization and paving project: an investigation into the influence of pavement foundation stiffness on pavement design, construction, and performance.
Bilodeau, J. P., Doré, G., & Perier, L. (2014). Falling weight deflectometer analysis of flexible pavement structure built with geotextile drainage layers. *Canadian Journal of Civil Engineering*, *41*(6), 540-549.
Bittelli, M. (2011). Measuring soil water content: A review. *HortTechnology*, *21*(3), 293-300.
Buyantuyev, A., & Wu, J. (2010). Urban heat islands and landscape heterogeneity: linking spatiotemporal variations in surface temperatures to land-cover and socioeconomic patterns. *Landscape ecology*, *25*(1), 17-33.
Ceylan, H., Gopalakrishnan, K., & Kim, S. (2009). MEPDG work plan task no. 5: Characterization of unbound materials (soils/aggregates) for mechanistic-empirical pavement design guide.
Chatti, K., Kutay, M. E., Lajnef, N., Zaabar, I., Varma, S., & Lee, H. S. (2017). Enhanced Analysis of Falling Weight Deflectometer Data for Use with Mechanistic-Empirical Flexible Pavement Design and Analysis and Recommendations for Improvements to Falling Weight Deflectometers (No. FHWA-HRT-15-063). Turner-Fairbank Highway Research Center.
Cunningham, C. N., Evans, T. M., & Tayebali, A. A. (2013). Gradation effects on the mechanical response of crushed stone aggregate. *International Journal of Pavement Engineering*, *14*(3), 231-241.
Doulos, L., Santamouris, M., & Livada, I. (2004). Passive cooling of outdoor urban spaces. The role of materials. *Solar energy*, *77*(2), 231-249.
Edil, T. B., Cetin, B., & Soleimanbeigi, A. (2018). Laboratory and field performance of recycled aggregate base in a seasonally cold region. *Sciences in Cold and Arid Regions*, *9*(3), 183-191.
Edil, T. B., Tinjum, J. M., & Benson, C. H. (2012). Recycled Unbound Materials. Report No. 2012-35. Minnesota Department of Transportation. St. Paul, MN.
Elbheiry, M. R., Kandil, K. A., & Kotb, A. S. (2011). *Investigation of factors affecting pavement roughness* (Doctoral dissertation, Arab Academy for Science and Technology and Maritime Transport).
Genc, D. (2019). Development, installation and preliminary data collection of an environmental sensor system for freeze–thaw monitoring under granular-surfaced roadways.
Guan, K. K. (2011). Surface and ambient air temperatures associated with different ground material: a case study at the University of California, Berkeley. *Environmental Science*, *196*, 1-14.
Hallikainen, M. T., Ulaby, F. T., Dobson, M. C., El-Rayes, M. A., & Wu, L. K. (1985). Microwave dielectric behavior of wet soil-part 1: Empirical models and experimental observations. *IEEE Transactions on Geoscience and Remote Sensing*, (1), 25-34.
Hanson, J. L., Edil, T. B., & Yesiller, N. (2000). Thermal properties of high water content materials. In *Geotechnics of High Water Content Materials*. ASTM International.
Horton, R., Wierenga, P. J., & Nielsen, D. R. (1983). Evaluation of Methods for Determining the Apparent Thermal Diffusivity of Soil Near the Surface 1. *Soil Science Society of America Journal*, *47*(1), 25-32.

Kuo, S. S., Mahgoub, H., & Nazef, A. (2002). Investigation of recycled concrete made with limestone aggregate for a base course in flexible pavement. Transportation Research Record: Journal of the Transportation Research Board, (1787), 99-108.

Lekarp, F., Isacsson, U., & Dawson, A. (2000). State of the art. II: Permanent strain response of unbound aggregates. *Journal of transportation engineering*, *126*(1), 76-83.

Li, C., Ashlock, J. C., White, D. J., & Vennapusa, P. K. (2019). Mechanistic-based comparisons of stabilised base and granular surface layers of low-volume roads. *International Journal of Pavement Engineering*, *20*(1), 112-124.

Li, C., Vennapusa, P. K., Ashlock, J., & White, D. J. (2017). Mechanistic-based comparisons for freeze-thaw performance of stabilized unpaved roads. *Cold Regions Science and Technology*, *141*, 97-108.

Liu, W., & Scullion, T. (2001). MODULUS 6.0 for windows: User's manual (No. FHWA/TX-05/0-1869-2). Texas Transportation Institute, Texas A&M University System.

Miller, J. S., & Bellinger, W. Y. (2003). *Distress identification manual for the long-term pavement performance program* (No. FHWA-RD-03-031). United States. Federal Highway Administration. Office of Infrastructure Research and Development.

MnDOT (2003). MnROAD Automated Laser Profile System "ALPS", http://dotapp7.dot.state.mn.us/research/pdf/2003MRRDOC005.pdf

MnDOT (2009a). Rutting – ALPS, http://www.dot.state.mn.us/mnroad/data/pdfs/alps.pdf

MnDOT (2009b). Lightweight Internal Surface Analyzer – MnROAD Ride Measurement, http://www.dot.state.mn.us/mnroad/data/pdfs/lisa.pdf

MnDOT (2013a). MnROAD Semi Tractor Trailer, https://www.dot.state.mn.us/mnroad/data/pdfs/MnROADSemiDescriptions(March%202013).pdf

MnDOT (2013b). Moisture Sensing Documentation, http://www.dot.mn.gov/mnroad/pdfs/Moisture%20Sensing%20at%20MnROAD(working%20document).pdf

MnDOT (2014a). MnROAD Weather Stations, https://www.dot.state.mn.us/mnroad/pdfs/MnROADWeather2014.pdf

MnDOT (2014b). Building Temperature Sensing Arrays (Thermocouple Trees), http://mndot.org/mnroad/data/pdfs/envsense/BuildingTemperatureSensors.pdf

MnDOT (2014c). Moisture Content – EW (EC, ET), https://www.dot.state.mn.us/mnroad/data/pdfs/envsense/Base_Moisture_EC.pdf

MnDOT (2018). Standard Specifications for Construction (2018 Edition). Minnesota Department of Transportation, St. Paul, MN.

Mooney, M. A. (2010). *Intelligent soil compaction systems* (Vol. 676). Transportation Research Board.

Newcomb, D. E., Van Deusen, D. A., Jiang, Y., & Mahoney, J. P. (1995). Considerations of Saturated Soil Conditions in Backcalculation of Pavement Layer Moduli. Transportation Research Record, (1473)

Rahardjo, H., Vilayvong, K., & Leong, E. C. (2010). Water characteristic curves of recycled materials. Geotechnical Testing Journal, 34(1), 89-96.

Rohde, G. T., Smith, R. E., & Scullion, T. (1992). Pavement deflection analysis on sections where the subgrade vary in stiffness with depth. In International Conference on Asphalt Pavements, 7th, 1992, Nottingham, United Kingdom (Vol. 3).

Rosa, M. G., Cetin, B., Edil, T. B., & Benson, C. H. (2016). Development of a test procedure for freeze-thaw durability of geomaterials stabilized with fly ash. *Geotechnical Testing Journal*, *39*(6), 938-953.

Rosa, M., Cetin, B., Edil, T.B., & Benson, C.H. (2017), "Freeze-Thaw Performance of Fly Ash-Stabilized Materials and Recycled Pavement Materials. Journal of Materials in Civil Engineering, 2017. 29(6): 04017015.

Sailor, D. J. (1995). Simulated urban climate response to modifications in surface albedo and vegetative cover. *Journal of applied meteorology*, *34*(7), 1694-1704.

Stolle, D. F., Guo, P., & Emery, J. J. (2014). Mechanical properties of reclaimed asphalt pavement—natural aggregate blends for granular base. Canadian Journal of Civil Engineering, 41(6), 493-499.

Tanyu, B. F., Kim, W. H., Edil, T. B., & Benson, C. H. (2003). Comparison of laboratory resilient modulus with back-calculated elastic moduli from large-scale model experiments and FWD tests on granular materials. In *Resilient modulus testing for pavement components*. ASTM International.

Van Deusen, D., Burnham, T., Dai, S., Geib, J., Hanson, C., Izevbekhai, B., Johnson, E., Palek, L., Siekmeier, J., Vrtis, M., & Worel, B. (2018). Report on 2017 MnROAD Construction Activities. Report MN/RC 2018-16. Minnesota Department of Transportation, St. Paul, MN.

Vennapusa, P. K. R., White, D. J., Siekmeier, J., & Embacher, R. A. (2012). In situ mechanistic characterisations of granular pavement foundation layers. *International Journal of Pavement Engineering*, *13*(1), 52-67.

Vennapusa, P. K., & White, D. J. (2009). Comparison of light weight deflectometer measurements for pavement foundation materials. Geotechnical Testing Journal, 32(3), 1-13.

White, D. J., Vennapusa, P. K., Becker, P., Rodriguez, J., Zhang, Y., & White, C. (2018). *Central Iowa Expo Pavement Test Sections: Pavement and Foundation Construction Testing and Performance Monitoring* (No. IHRB Project TR-671).

William, G. W. (1999). Backcalculation of pavement layers moduli using 3D nonlinear explicit finite element analysis (Doctoral dissertation, West Virginia University Libraries).

Wraith, J. M., & Or, D. (1999). Temperature effects on soil bulk dielectric permittivity measured by time domain reflectometry: Experimental evidence and hypothesis development. *Water Resources Research*, *35*(2), 361-369.

Zhang, Y. (2016). Assessing Seasonal Performance, Stiffness, and Support Conditions of Pavement Foundations.

APPENDIX A. RELATIVE HUMIDITY AND AVERAGE WIND SPEED DATA

Relative humidity (results are the average of the data collected from the two weather stations):

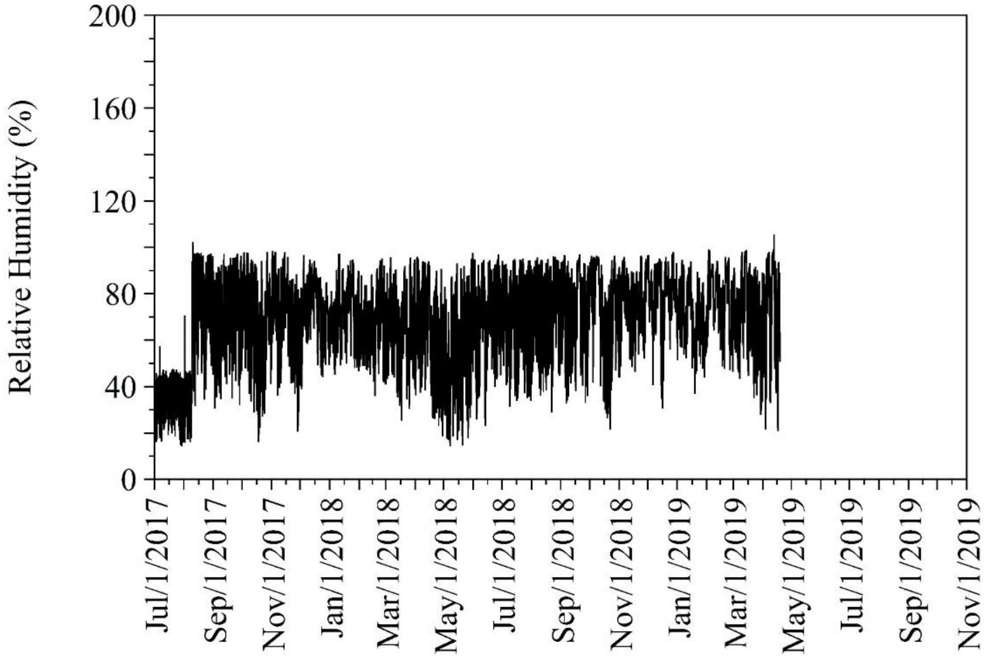

Average wind speed (results are the average of the data collected from the two weather stations):

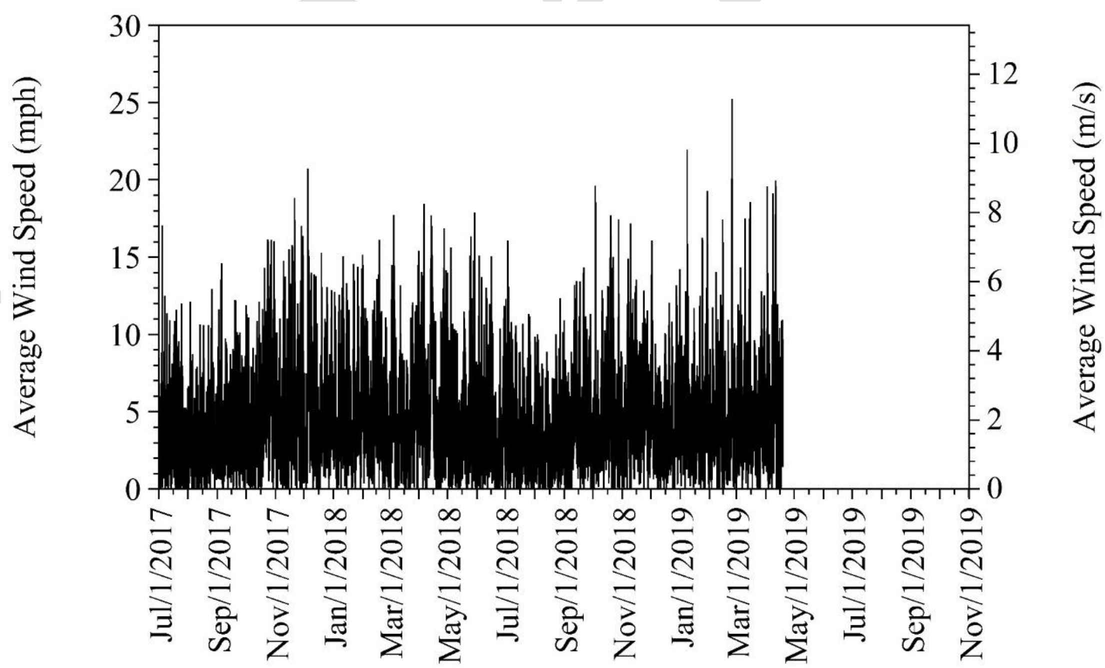

APPENDIX B. LOCATIONS OF THE EMBEDDED SENSORS

Cell Number	Cell Description	Sensor	Number	Station	Offset (ft)	Depth from Surface (in)
185	12 in Coarse RCA	Thermocouple (TC)	1	16538.51	-6.4	2.8
			2	16538.51	-6.4	3.8
			3	16538.51	-6.4	9.3
			4	16538.51	-6.4	14.8
			5	16538.51	-6.4	15.8
			6	16538.51	-6.4	18.3
			7	16538.51	-6.4	19.3
			8	16538.51	-6.4	23.8
			9	16538.51	-6.4	35.8
			10	16538.51	-6.4	47.8
			11	16538.51	-6.4	59.8
			12	16538.51	-6.4	71.8
		Moisture Probe (EC)	1	16538.81	-5.8	5
			2	16538.81	-5.8	14
			3	16538.81	-5.8	17
			4	16538.81	-5.8	20.5
186	12 in Fine RCA	Thermocouple (TC)	1	16678.52	-6.3	3
			2	16678.52	-6.3	4
			3	16678.52	-6.3	9.5
			4	16678.52	-6.3	15
			5	16678.52	-6.3	16
			6	16678.52	-6.3	18.5
			7	16678.52	-6.3	19.5
			8	16678.52	-6.3	24
			9	16678.52	-6.3	36
			10	16678.52	-6.3	48
			11	16678.52	-6.3	60
			12	16678.52	-6.3	72
		Moisture Probe (EC)	1	16678.91	-5.6	5
			2	16678.91	-5.6	14
			3	16678.91	-5.6	17
			4	16678.91	-5.6	20.5

Cell Number	Cell Description	Sensor	Number	Station	Offset (ft)	Depth from Surface (in)
188	12 in Limestone	Thermocouple (TC)	1	17111.5	-5.5	3
			2	17111.5	-5.5	4
			3	17111.5	-5.5	9.5
			4	17111.5	-5.5	15
			5	17111.5	-5.5	16
			6	17111.5	-5.5	18.5
			7	17111.5	-5.5	19.5
			8	17111.5	-5.5	24
			9	17111.5	-5.5	36
			10	17111.5	-5.5	48
			11	17111.5	-5.5	60
			12	17111.5	-5.5	72
		Moisture Probe (EC)	1	17111.8	-4.8	5
			2	17111.8	-4.8	14
			3	17111.8	-4.8	17
			4	17111.8	-4.8	20.5
189	12 in RCA+RAP	Thermocouple (TC)	1	17306.1	-5.3	3
			2	17306.1	-5.3	4
			3	17306.1	-5.3	9.5
			4	17306.1	-5.3	15
			5	17306.1	-5.3	16
			6	17306.1	-5.3	18.5
			7	17306.1	-5.3	19.5
			8	17306.1	-5.3	24
			9	17306.1	-5.3	36
			10	17306.1	-5.3	48
			11	17306.1	-5.3	60
			12	17306.1	-5.3	72
		Moisture Probe (EC)	1	17306.2	-4.7	5
			2	17306.2	-4.7	14
			3	17306.2	-4.7	17
			4	17306.2	-4.7	20.5

Cell Number	Cell Description	Sensor	Number	Station	Offset (ft)	Depth from Surface (in)
127	18 in LSSB	Thermocouple (TC)	1	17569	-11.5	3
			2	17569	-11.5	4
			3	17569	-11.5	6.5
			4	17569	-11.5	9
			5	17569	-11.5	10
			6	17569	-11.5	12
			7	17569	-11.5	18
			8	17569	-11.5	24
			9	17569	-11.5	36
			10	17569	-11.5	48
			11	17569	-11.5	60
			12	17569	-11.5	72
		Moisture Probe (EC)	1	17569	-11	6.5
			2	17569	-11	29
			3	17569	-11	36
728	9 in LSSB	Thermocouple (TC)	1	18544.1	-11.6	3
			2	18544.1	-11.6	4
			3	18544.1	-11.6	6.5
			4	18544.1	-11.6	9
			5	18544.1	-11.6	10
			6	18544.1	-11.6	14
			7	18544.1	-11.6	18.5
			8	18544.1	-11.6	24
			9	18544.1	-11.6	36
			10	18544.1	-11.6	48
			11	18544.1	-11.6	60
			12	18544.1	-11.6	72
			13	18544.1	-11.9	0.3
			14	18544.1	-11.9	1
			15	18544.1	-11.9	2
			16	18544.1	-11.9	3
		Moisture Probe (EC)	1	18544	-11	8.5
			2	18544	-11	19.5
			3	18544	-11	24
			4	18544	-11	36

APPENDIX C. CHANGE IN TEMPERATURE FOR THE ASPHALT LAYER IN CELL 728 (9 IN LSSB)

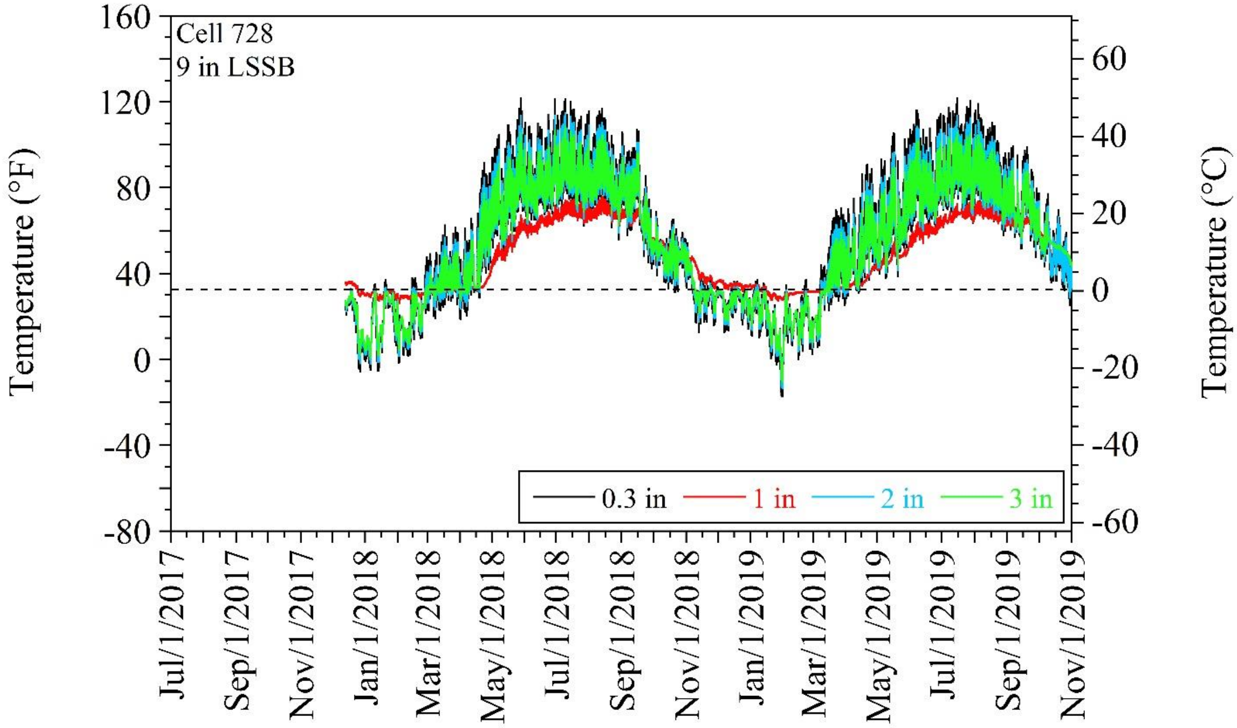

APPENDIX D. CALIBRATION EQUATIONS TO ESTIMATE VOLUMETRIC WATER CONTENT (VWC) AND THE DEGREE OF SATURATION (DOS) VALUES

Calibration equations (MnDOT 2013b):

MnROAD Model	Sensor	MnROAD Material	Calibration Equation
EW	TE	Generic (2006)	VWC= 0.00109 RAW - 0.629
		Sand	VWC= 0.0009 RAW - 0.4929
		Clay	VWC = 0.0009 RAW - 0.4693
		Select Granular	VWC = 0.0011 RAW - 0.6615
		Class-3	VWC = 0.0009 RAW - 0.5149
		Class-4	VWC = 0.0008 RAW - 0.4120
		Class-5	VWC = 0.0007 RAW - 0.3524
		Class-6	VWC = 0.0011 RAW - 0.6787
	5TE	Generic (2008)	VWC = 0.00109 RAW - 0.629
		Sand	VWC = 0.0004 RAW - 0.0780
		Clay	VWC = 0.0003 RAW - 0.0021
		Select Granular	VWC = 0.0005 RAW - 0.0908
		Class-3	VWC = 0.0004 RAW - 0.0481
		Class-4	VWC = 0.0004 RAW - 0.0520
		Class-5	VWC = 0.0003 RAW - 0.0239
		Class-6	VWC = 0.0006 RAW - 0.1438
		Class-7 (Reclaimed HMA)	VWC = 0.0006 RAW – 0.1358

Gradations of the materials (MnDOT 2013):

	MnROAD Unbound Base Materials												Sub-grade Materials	
	Select Granular		Class-3 Special		Class-4		Class-5		Class-6		Class-7 Special		Clay	Sand
Sieves Size (Passing)	Spec	Field	Spec	Field	Spec	Field	Spec	Field	Spec	Field	Spec	Field	Field	Field
2”	100	100		100		100		100		100		100	100	100
1”	100	100		99.3		100		100		100		99	100	100
3/4”	Well graded	99		97.5		99		97		97.3		96	99	98
3/8”		88		93.9		92		81		72.4		68	95	96
4		74	35-100	84.7	35-100	82	30-80	70	35-70	49.6	15-45	46	90	86
10		60	20-100	72.9	20-100	66	20-65	59	20-55	31.5	10-30	26	84	
20		39				44		42				13	78	
40		24	5-50	31.3	5-35	26	10-35	24	10-30	14.6	5-25	7	69	39
60		16				15		15				5	61	
100		12		13.3		11		10		8.9		4	52	8
200	<12	8.9	5-10	8.8	4-10	8.7	3-10	7.6	3-7	6.1	<12	2.5	43	4.6

Maximum density and optimum moisture content values of the materials (MnDOT 2013):

Material	Density (PCF)	Optimum Moisture (%) Gravimetric
Silty-Clay Subgrade	106.7	16.8
Silty-Clay Subgrade	127.4	9.5
Sand Subgrade	115.8	7.4
Sand Subgrade	121	10.1
Select Granular Base	131.4	7.3
Select Granular Base	132.3	8.2
Class 3 Base	129	8.9
Class 3 Base	127	9.8
Class 4 Base	127	9.6
Class 4 Base	124.5	10.7
Class 5 Base	132	7.2
Class 5 Base	131.2	7.5
Class 6 Base	128.7	6.8
Class 7 (RAP + Cl-4)	106.5	18.1

Degree of Saturation (DOS) Values

The following equation was used to calculate the degree of saturation (DOS). The median dry unit weight (γ_{dry}) values of the materials were determined from the nuclear density gauge (NDG) measurements taken from the outside lanes of the test cells during construction. The specific gravity (G_s) values of the materials were taken from Task 4 (laboratory testing) report. To calculate the moisture content (gravimetric) of the materials (ω), the VWC values were divided by γ_{dry} (γ_{water} = 1 g/cm^3). Overall, it was concluded that slight increases in the DOS values were observed due to precipitation in the rainy periods.

$$\text{DOS (\%)} = \frac{\gamma_{dry} * G_s * \omega}{\gamma_{water} * G_s - \gamma_{dry}} * 100$$

Cell 185 (12 in coarse RCA)

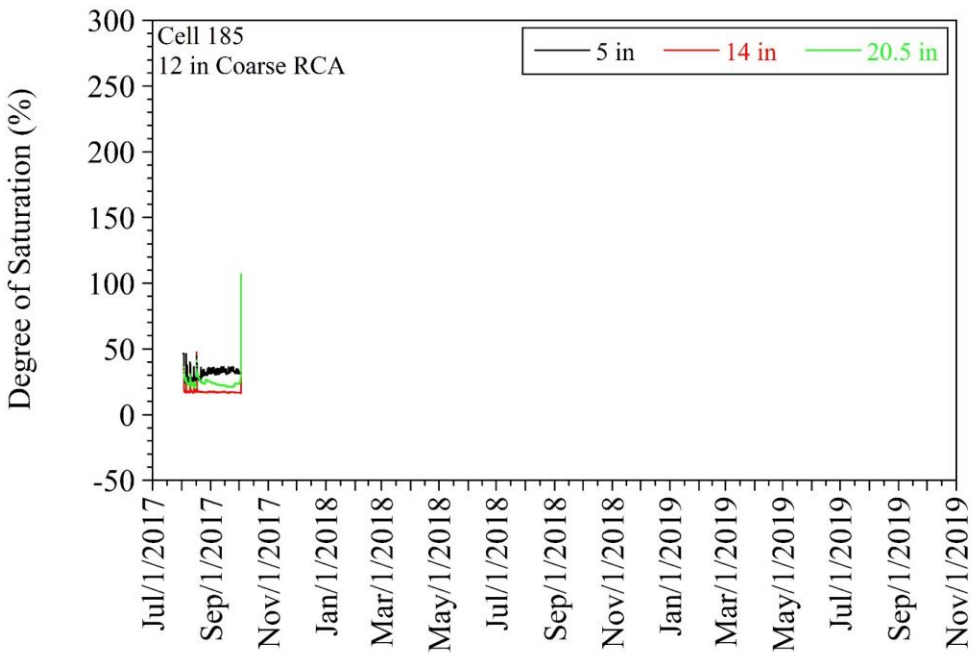

Cell 186 (12 in fine RCA)

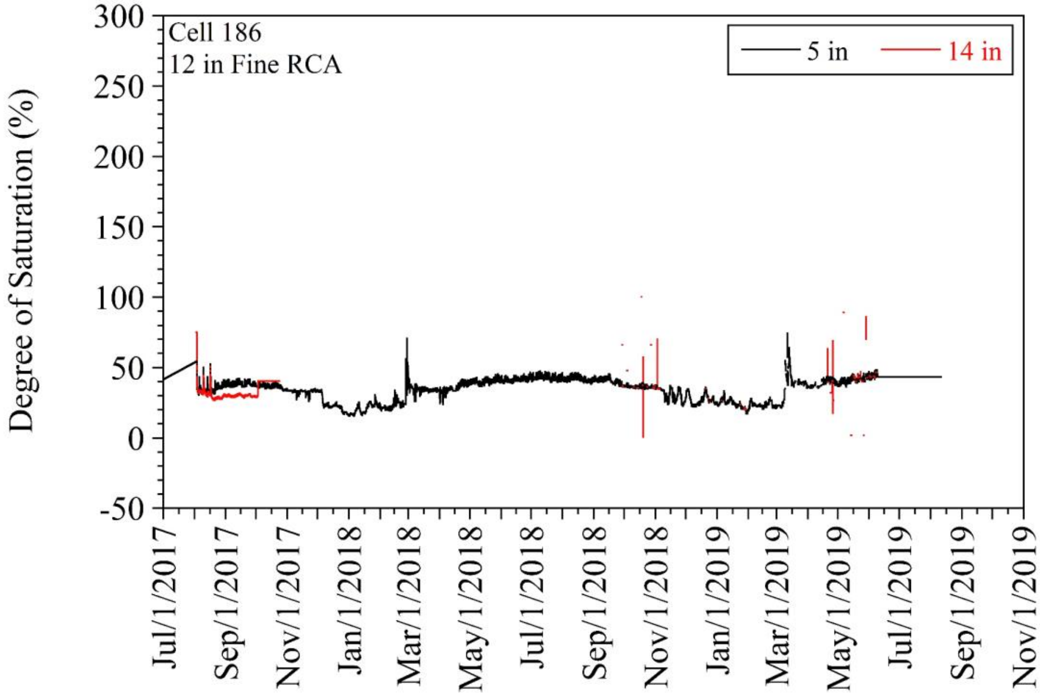

Cell 188 (12 in limestone)

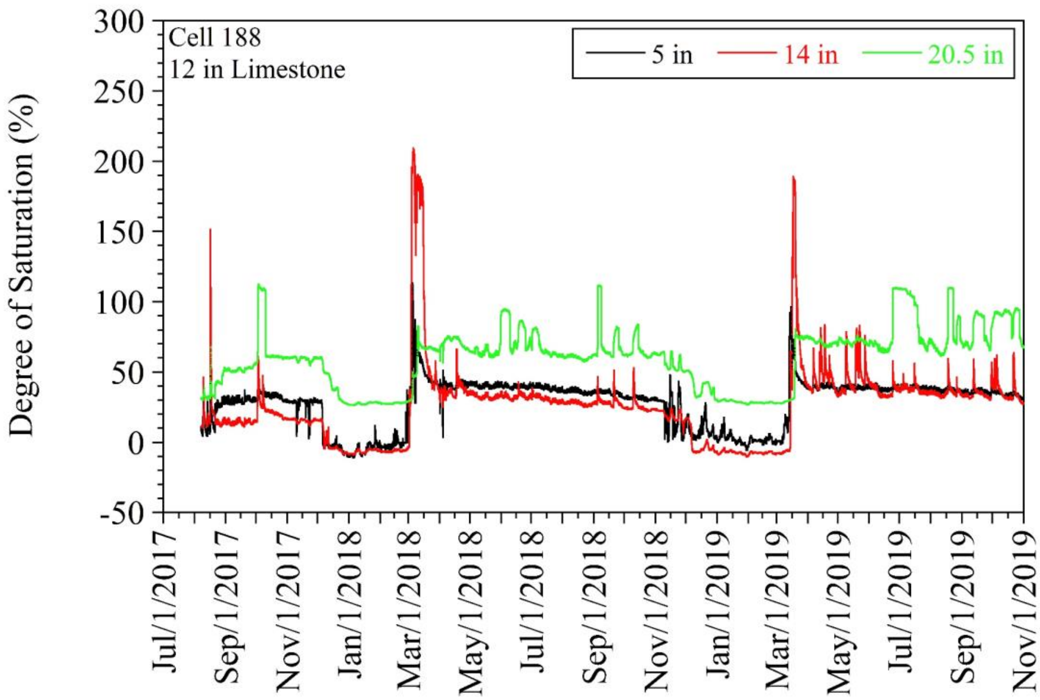

Cell 189 (12 in RCA+RAP)

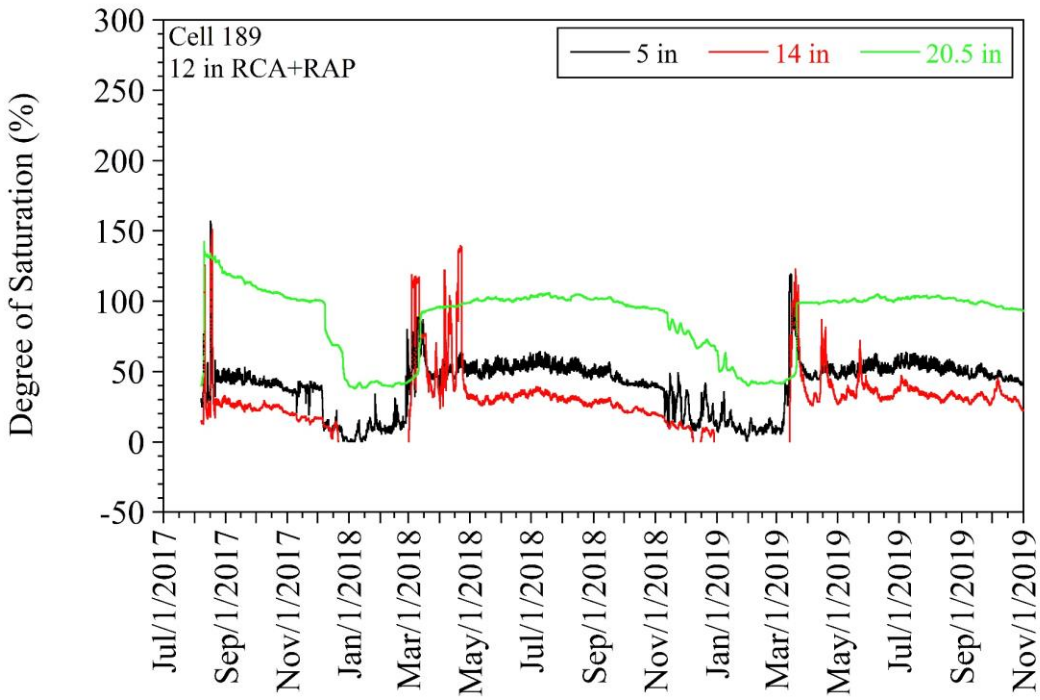

Cell 127 (18 in LSSB)

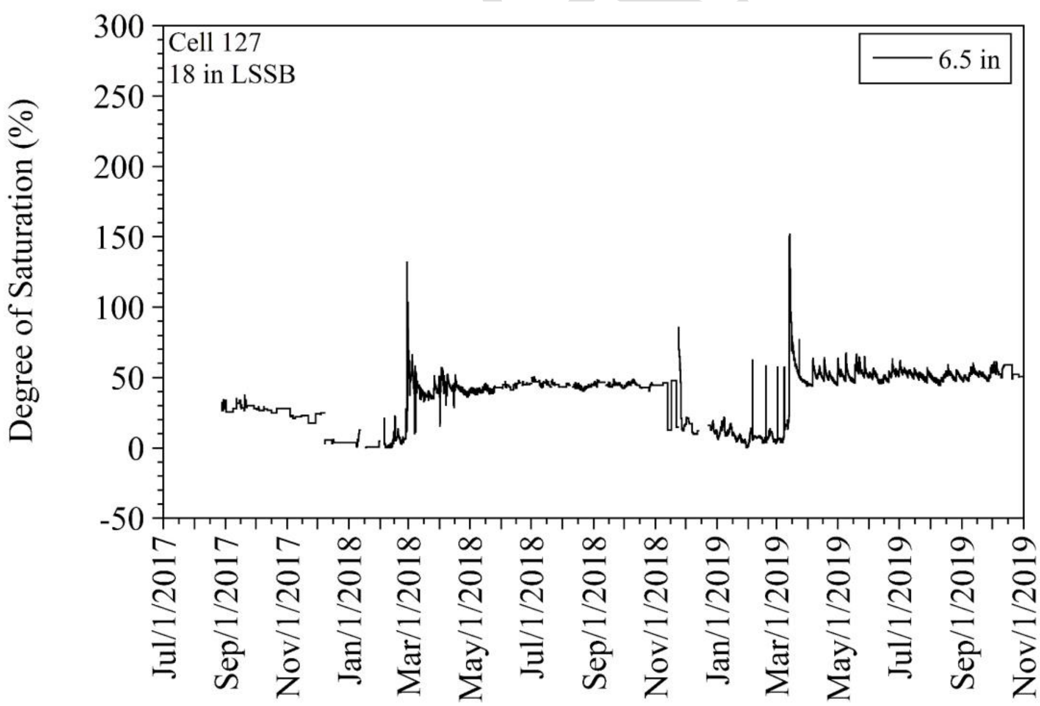

Cell 728 (9 in LSSB)

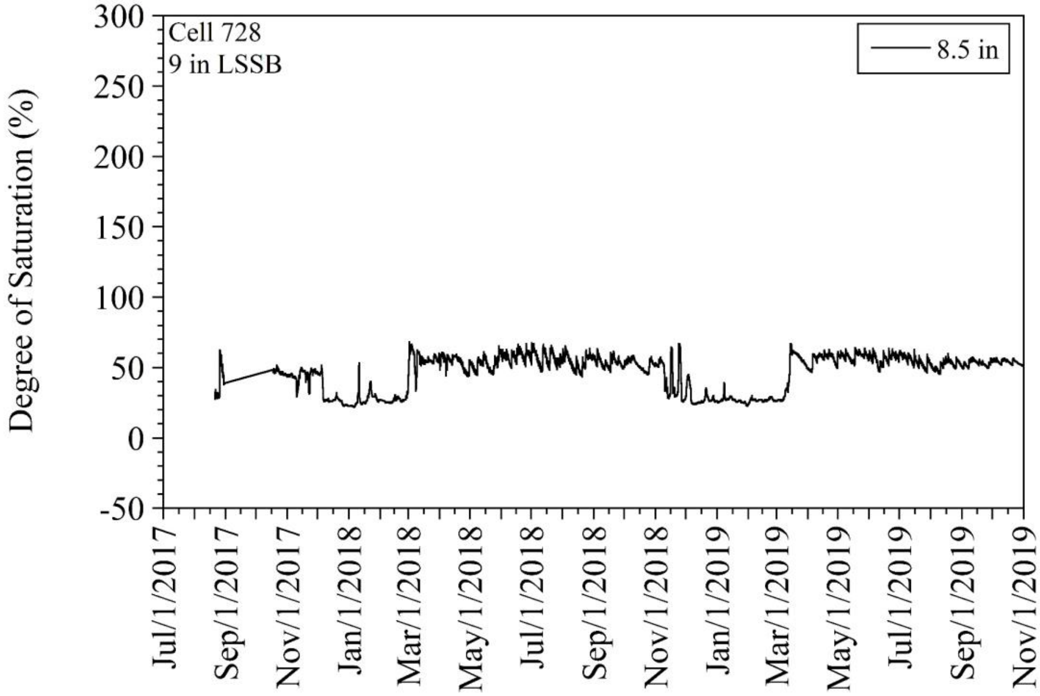

APPENDIX E. MAXIMUM DEFLECTION VALUES AT 6,000 LB (26.7 KN), 9,000 LB (40 KN), AND 12,000 LB (53.4 KN) FOR EACH CELL

Cell 185 (12 in coarse RCA) – maximum deflection (error bars represent one standard deviation of the data):

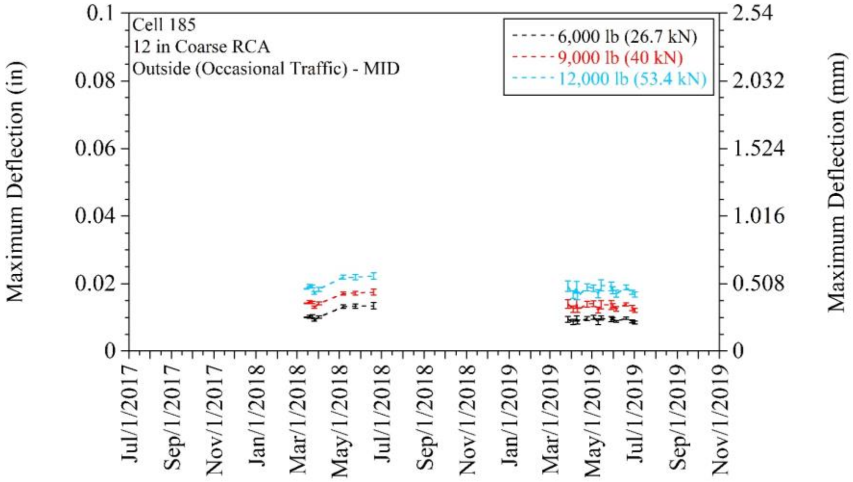

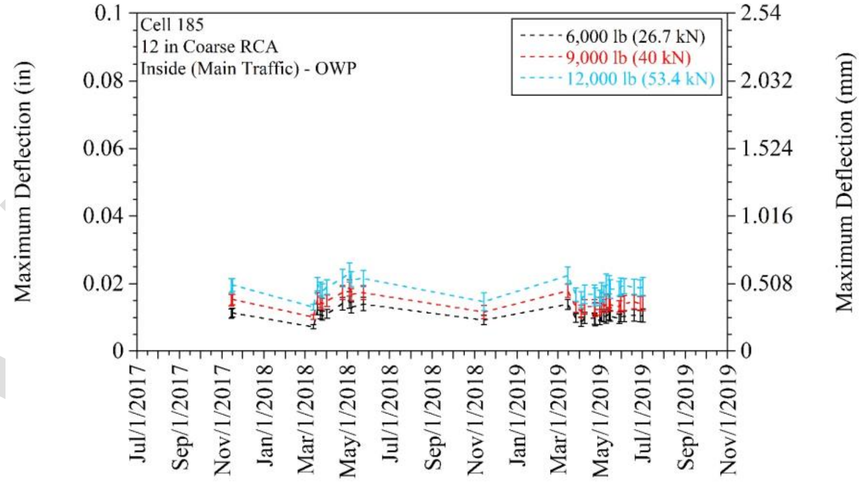

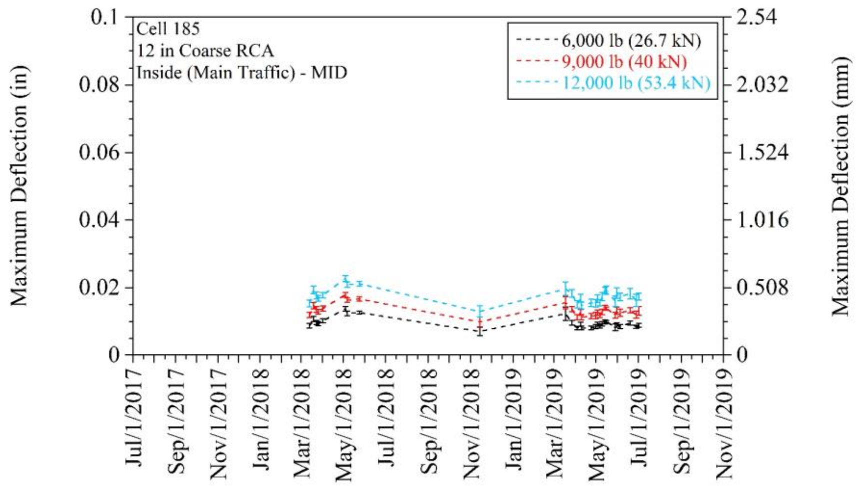

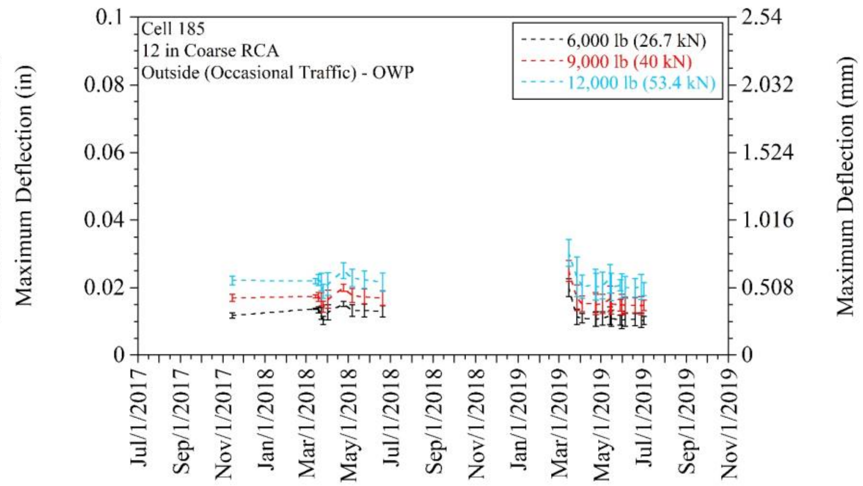

Cell 186 (12 in fine RCA) – maximum deflection (error bars represent one standard deviation of the data):

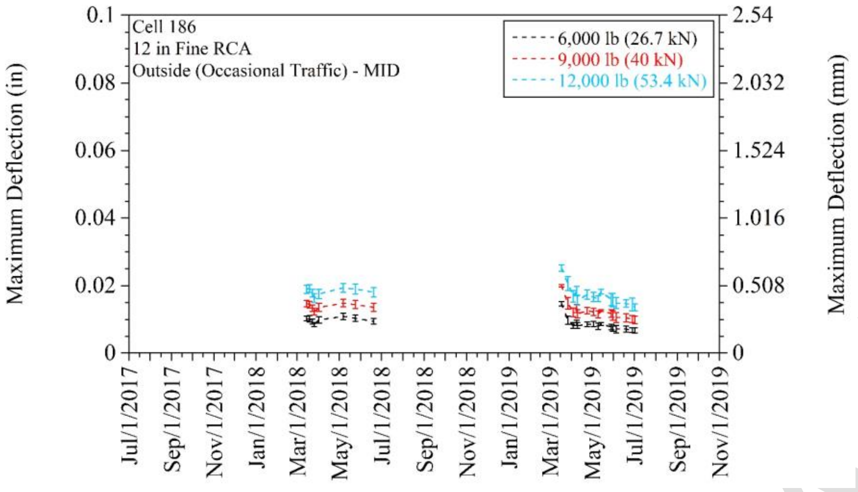

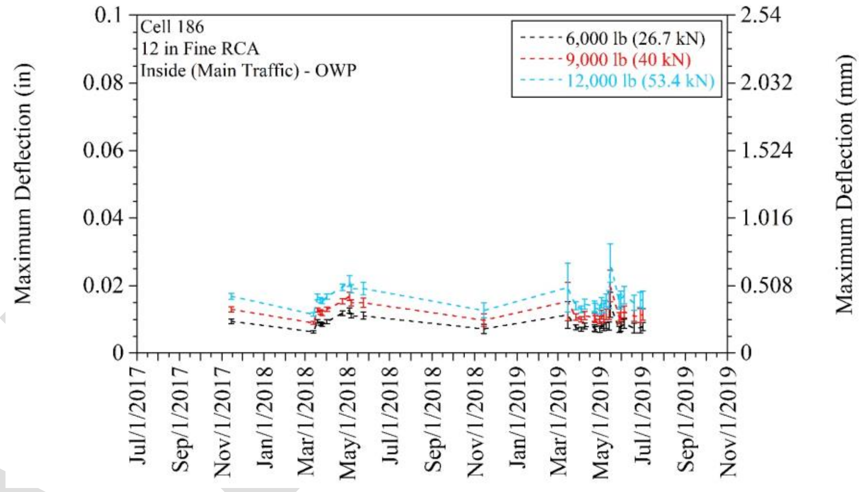

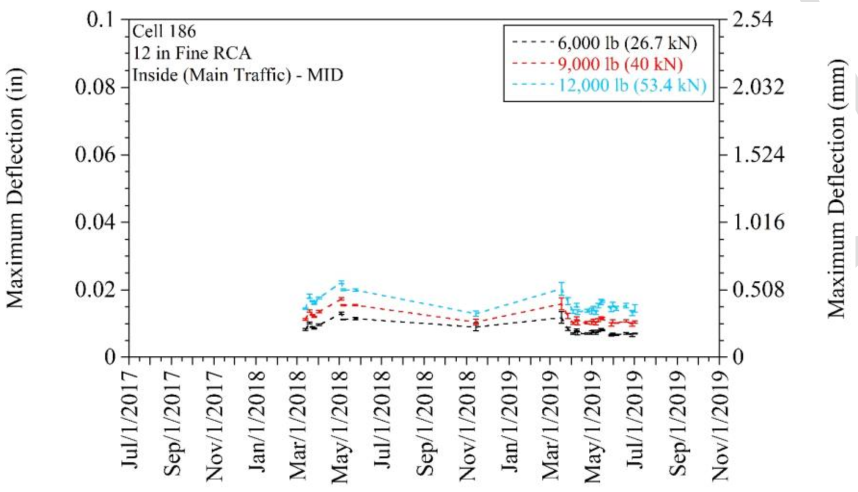

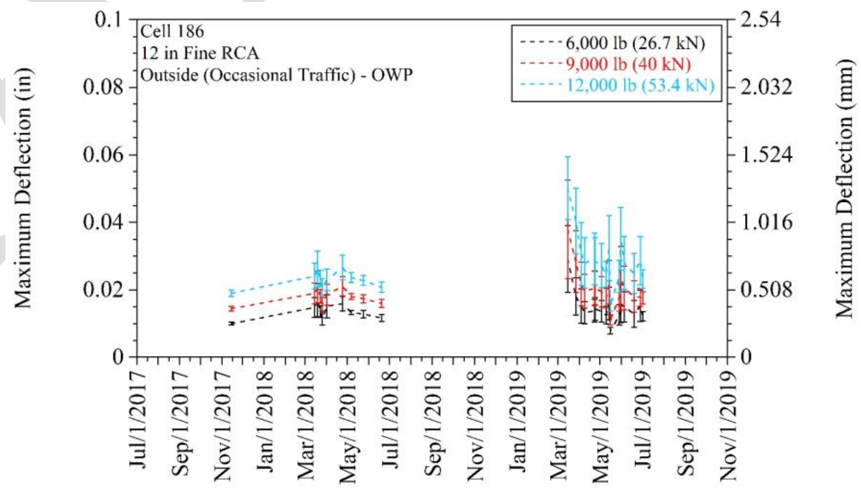

Cell 188 (12 in limestone) – maximum deflection (error bars represent one standard deviation of the data):

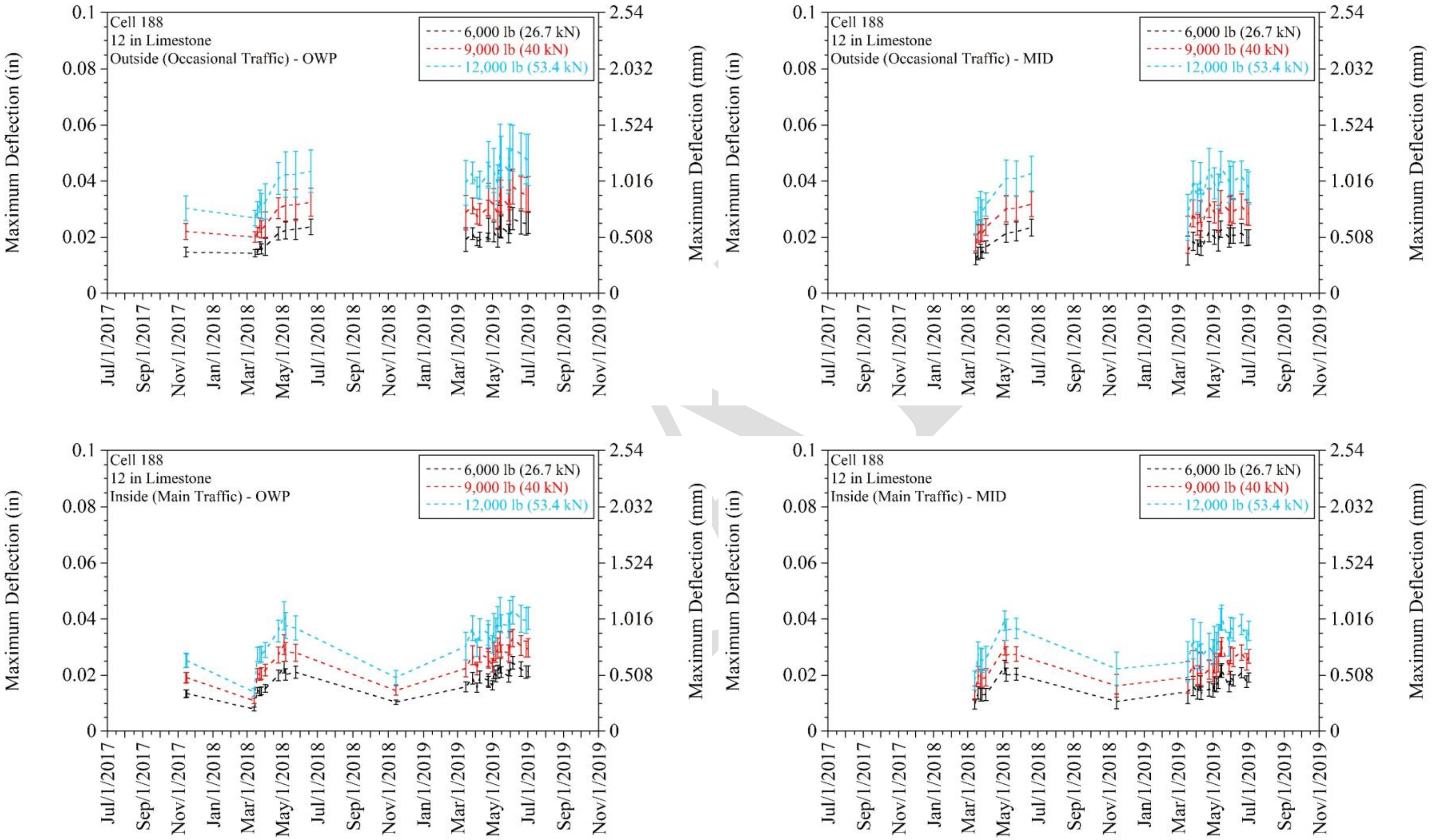

Cell 189 (12 in RCA+RAP) – maximum deflection (error bars represent one standard deviation of the data):

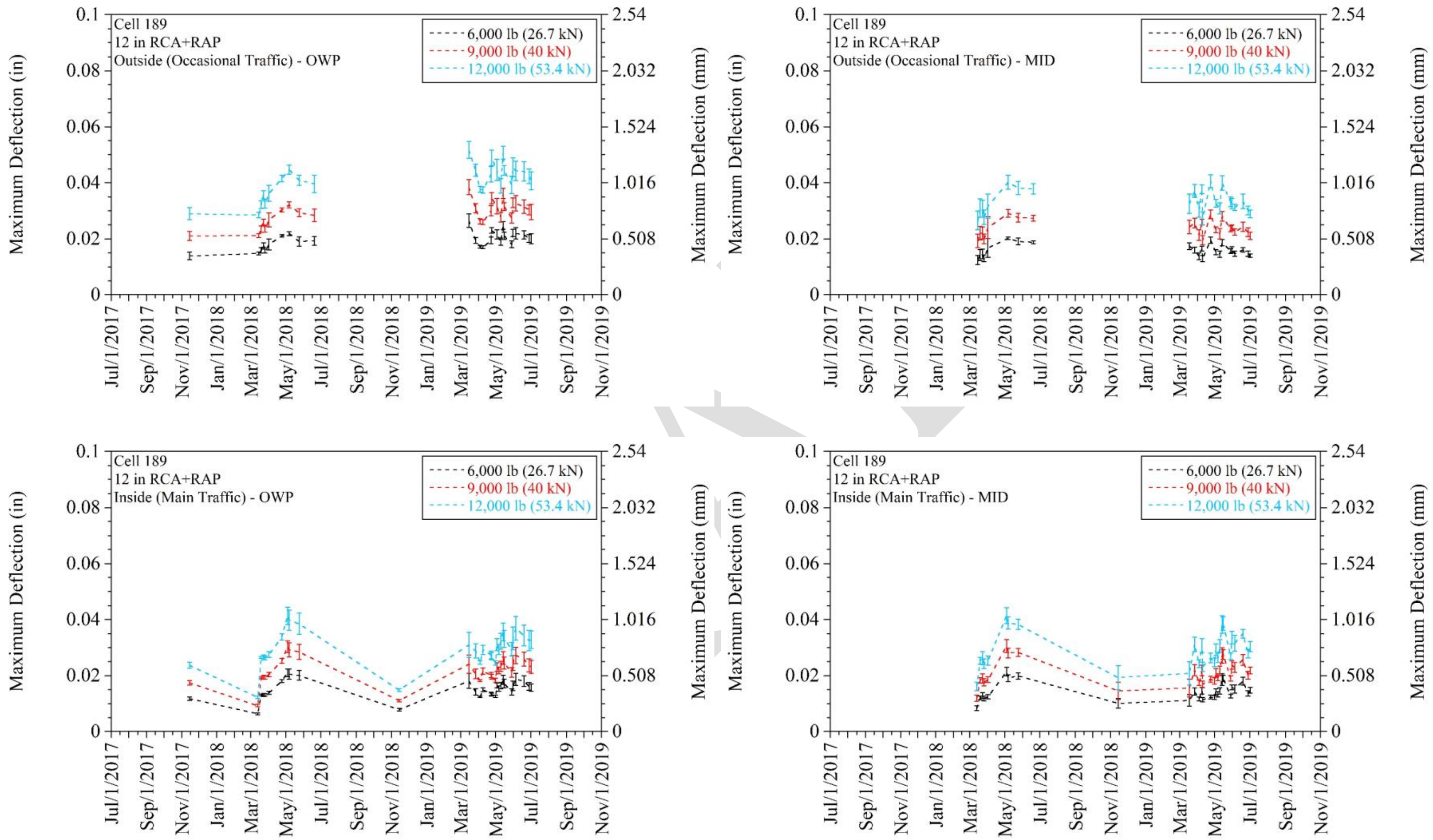

Cell 127 (18 in LSSB) – maximum deflection (error bars represent one standard deviation of the data):

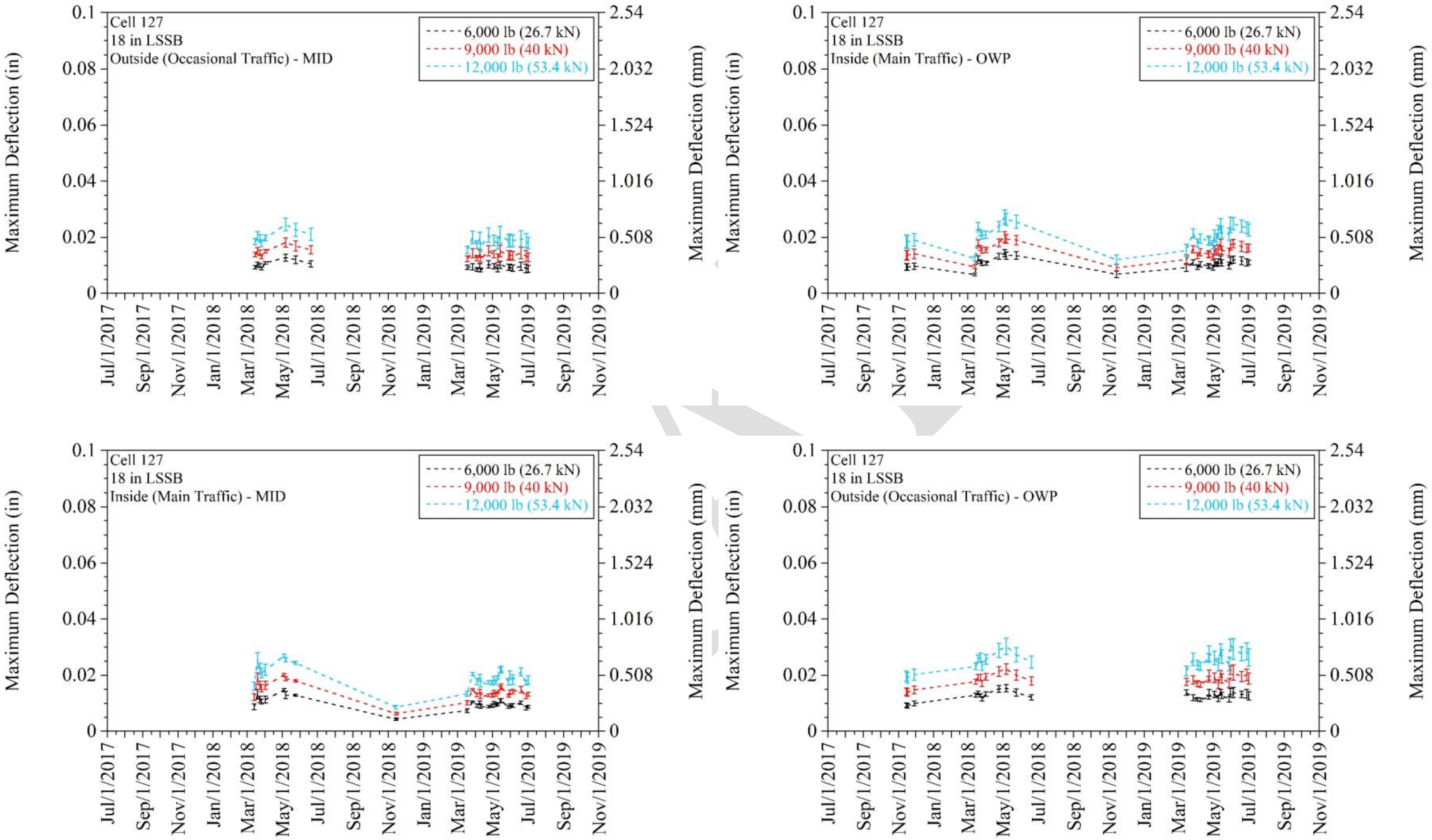

Cell 227 (18 in LSSB) – maximum deflection (error bars represent one standard deviation of the data):

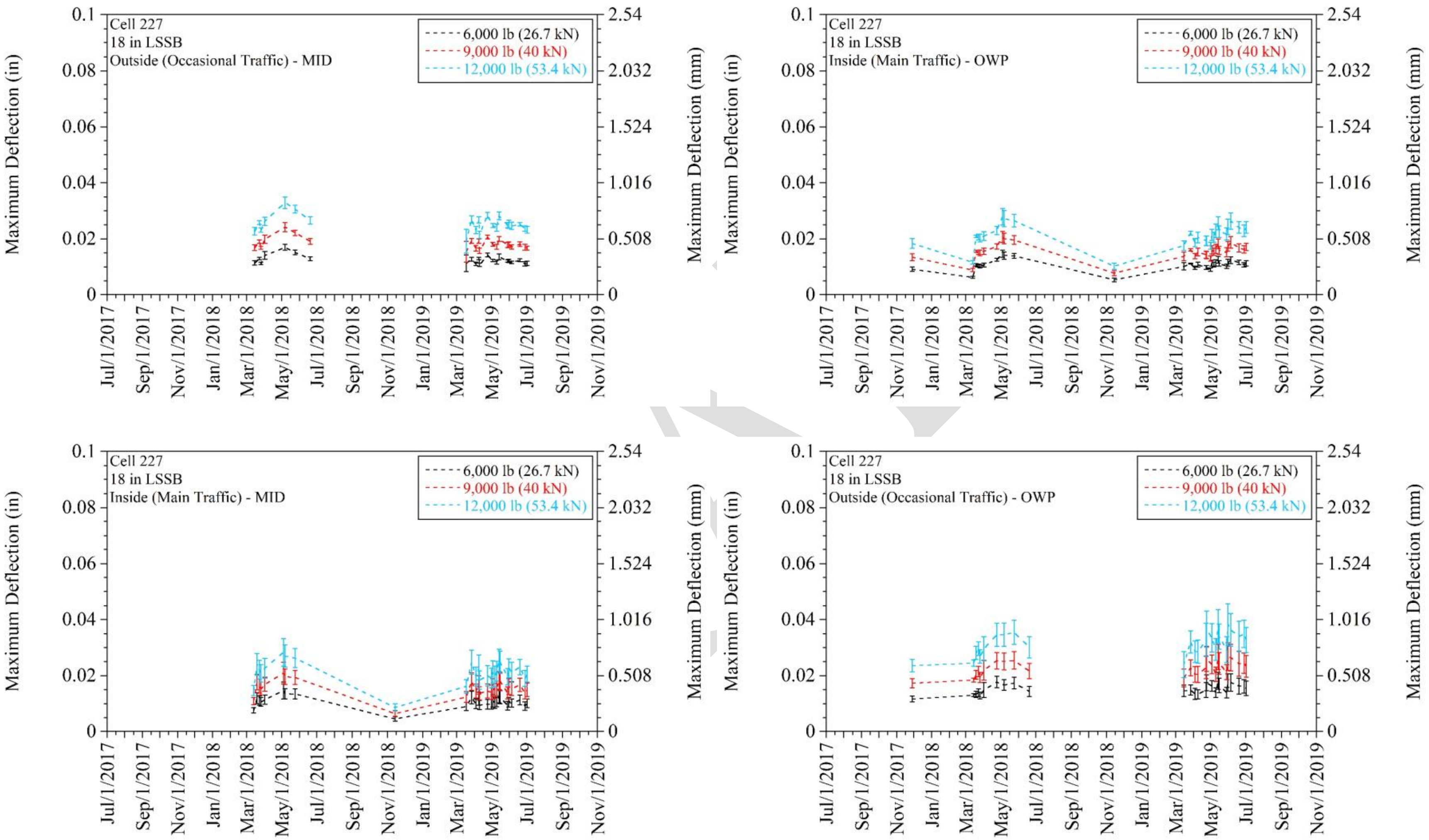

Cell 328 (9 in LSSB – TX) – maximum deflection (error bars represent one standard deviation of the data):

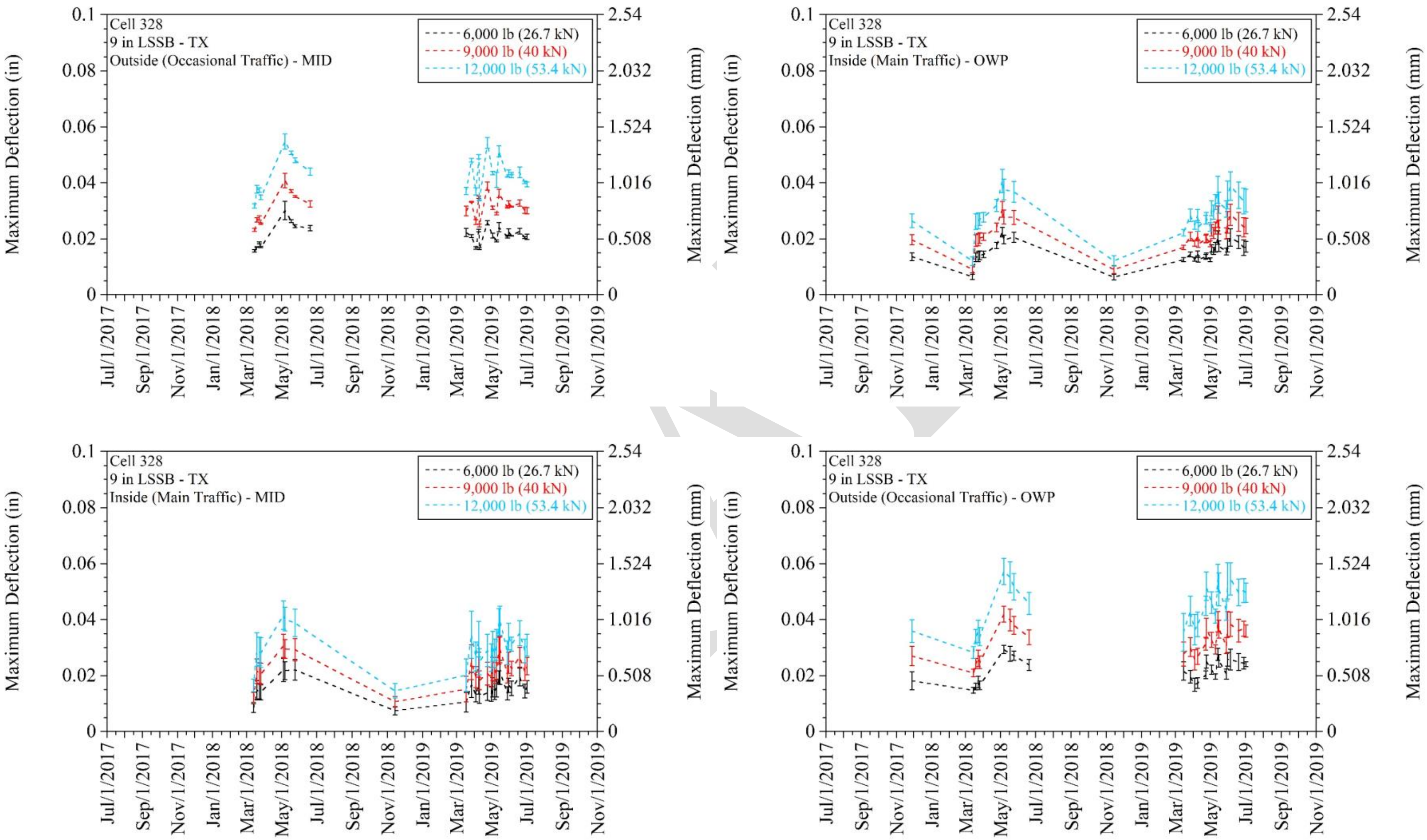

Cell 428 (9 in LSSB – TX+GT) – maximum deflection (error bars represent one standard deviation of the data):

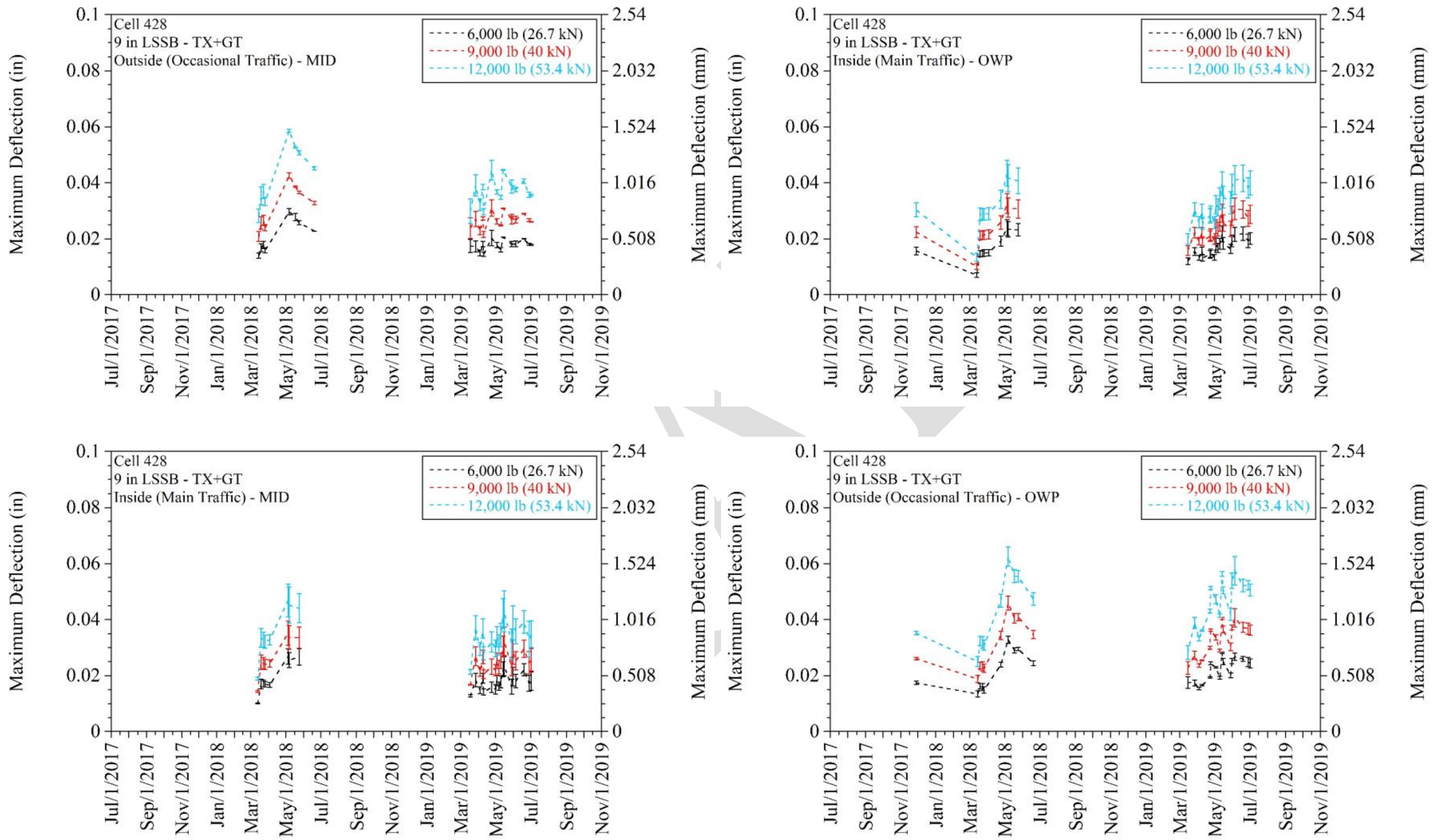

Cell 528 (9 in LSSB – BX+GT) – maximum deflection (error bars represent one standard deviation of the data):

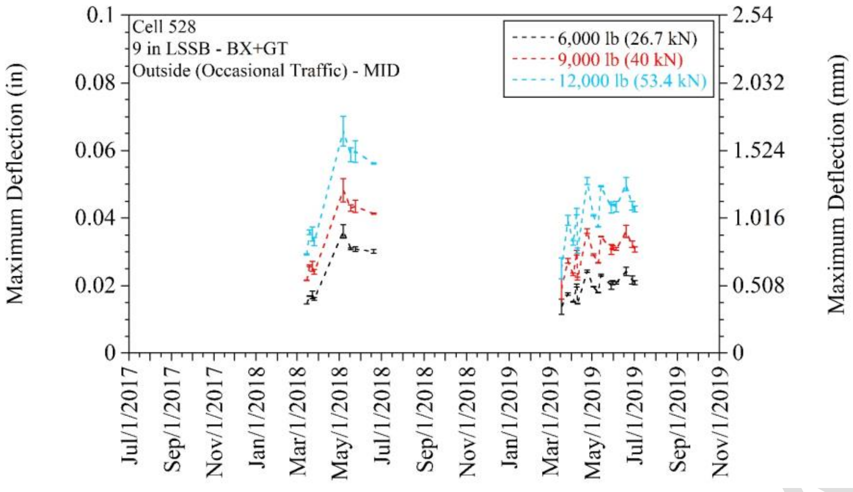

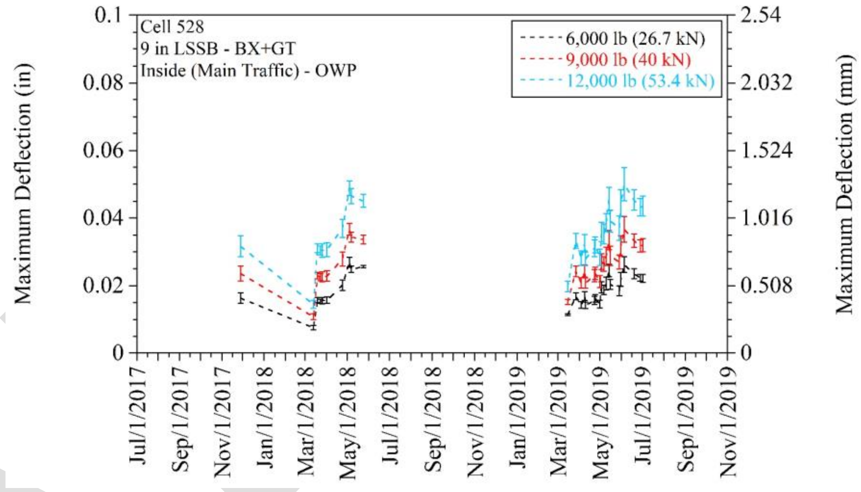

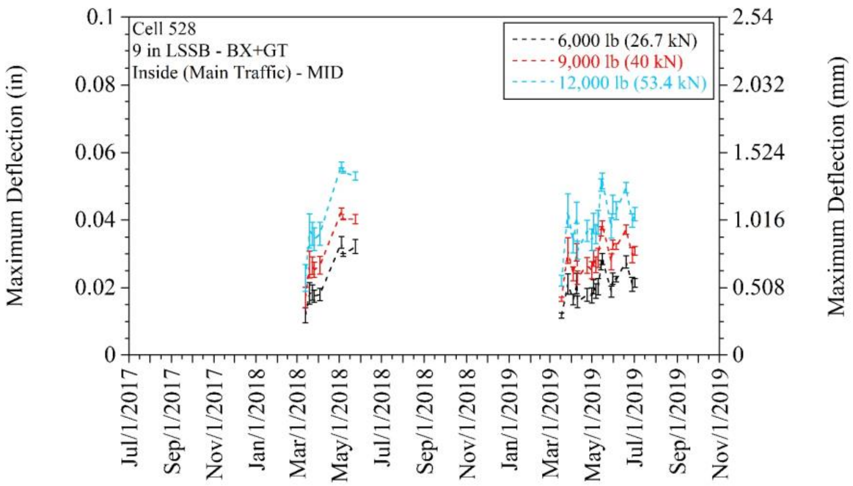

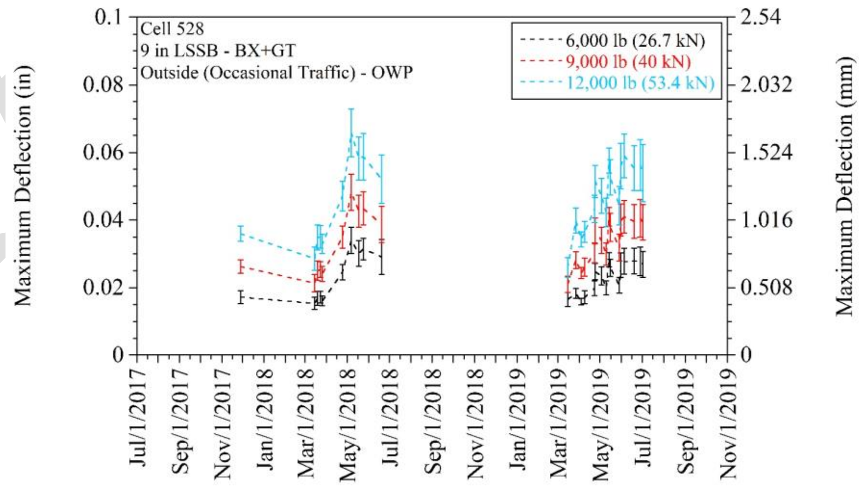

Cell 628 (9 in LSSB – BX) – maximum deflection (error bars represent one standard deviation of the data):

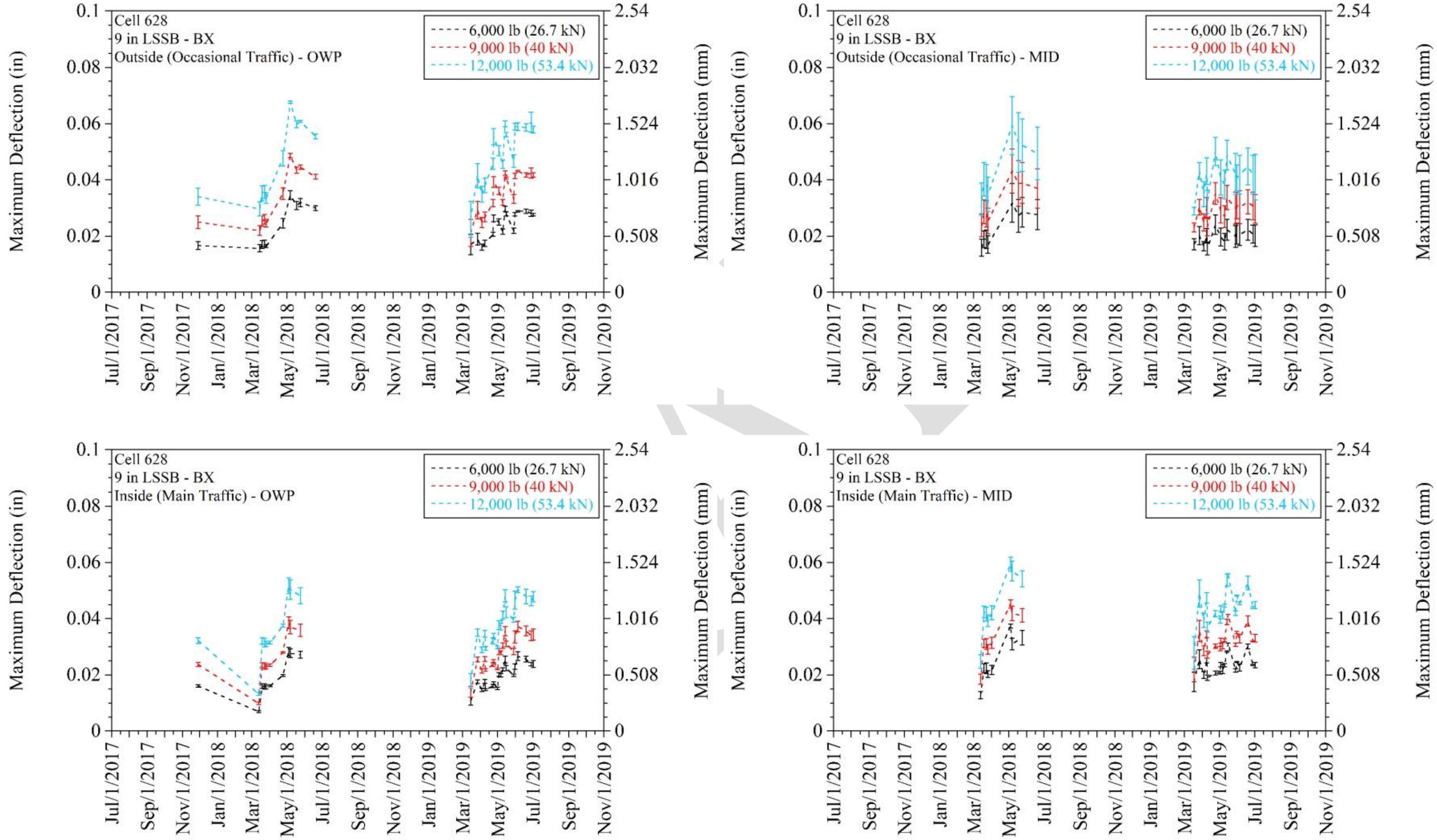

Cell 728 (9 in LSSB) – maximum deflection (error bars represent one standard deviation of the data):

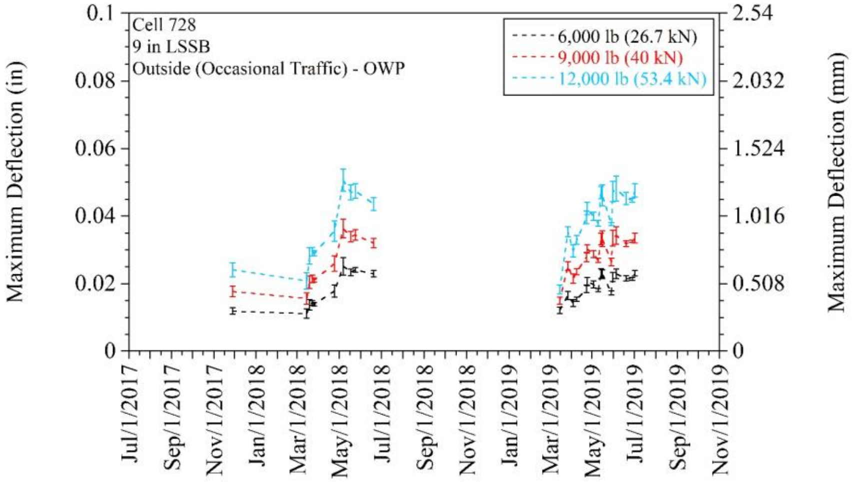

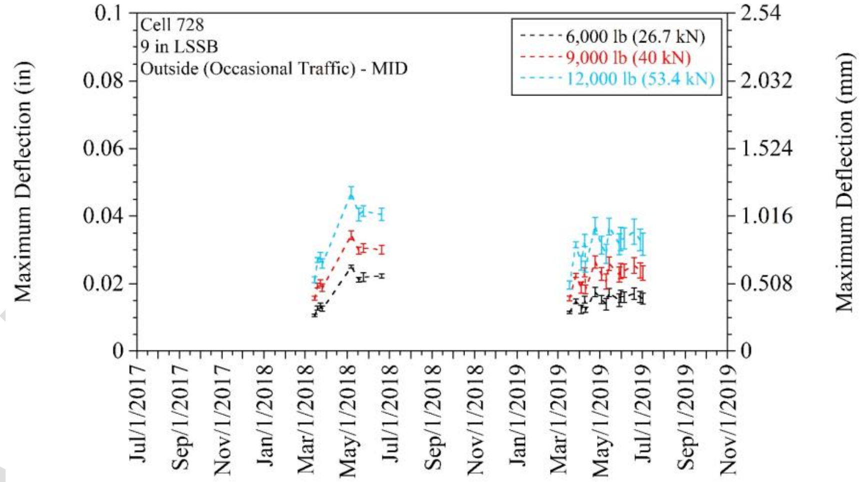

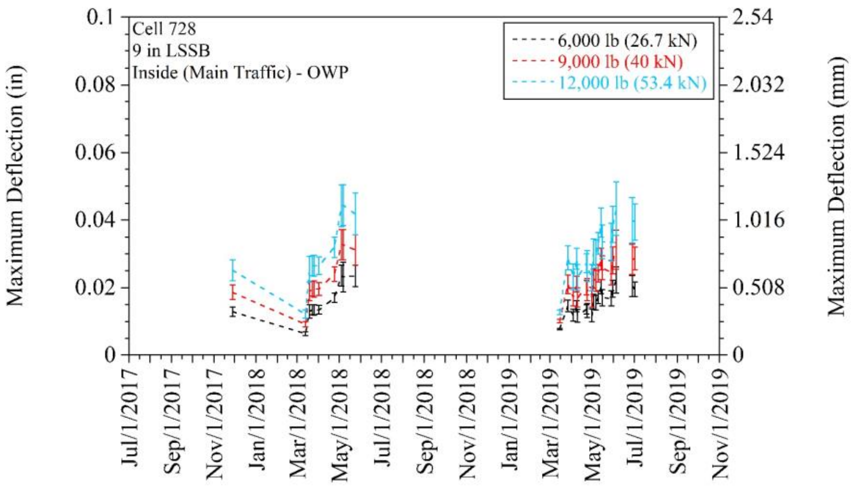

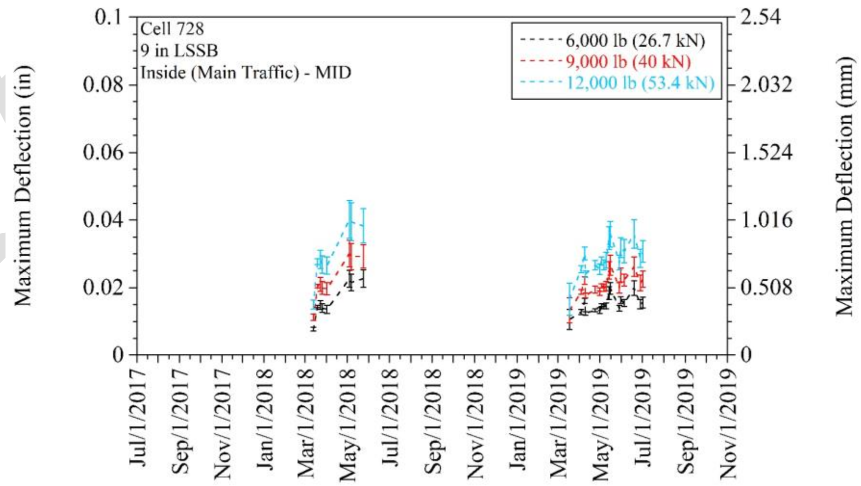

APPENDIX F. COMPOSITE E_{FWD} VALUES AT 6,000 LB (26.7 KN), 9,000 LB (40 KN), AND 12,000 LB (53.4 KN) FOR EACH CELL

Cell 185 (12 in coarse RCA) – composite E_{FWD} (error bars represent one standard deviation of the data):

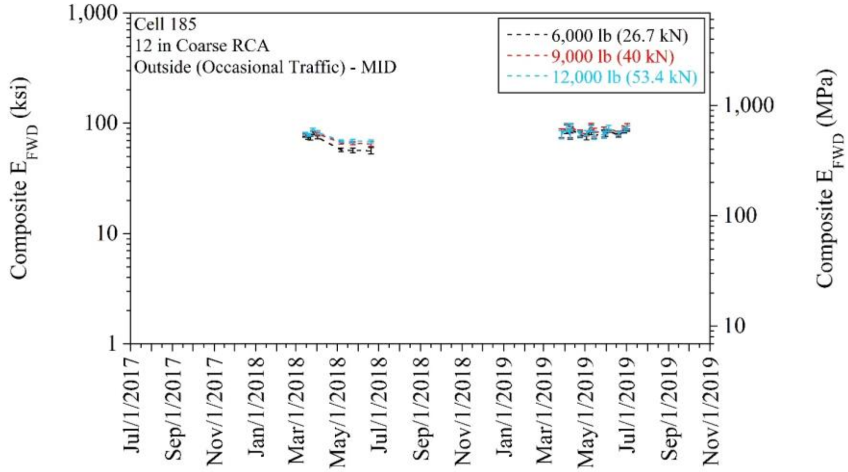

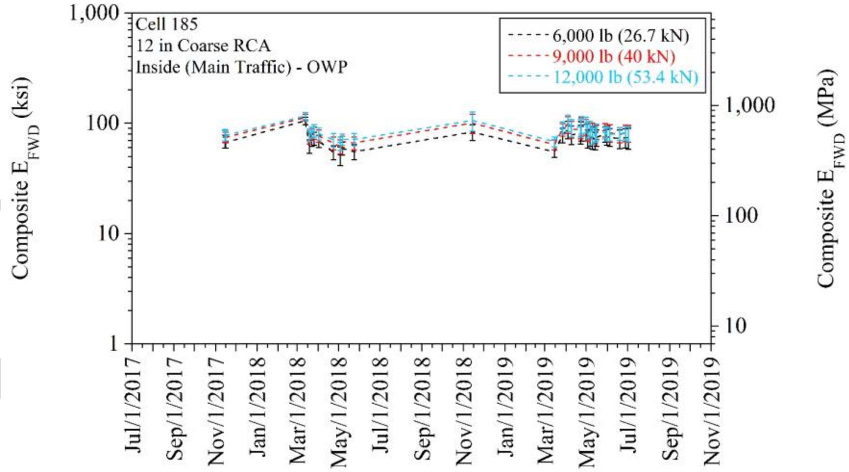

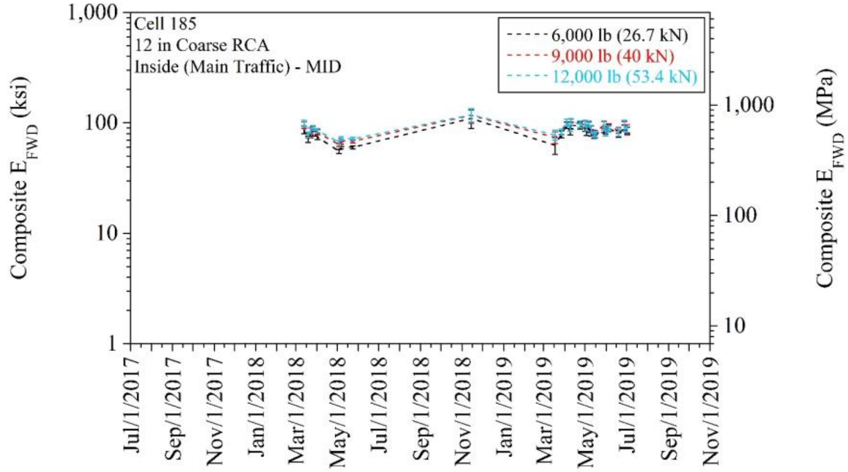

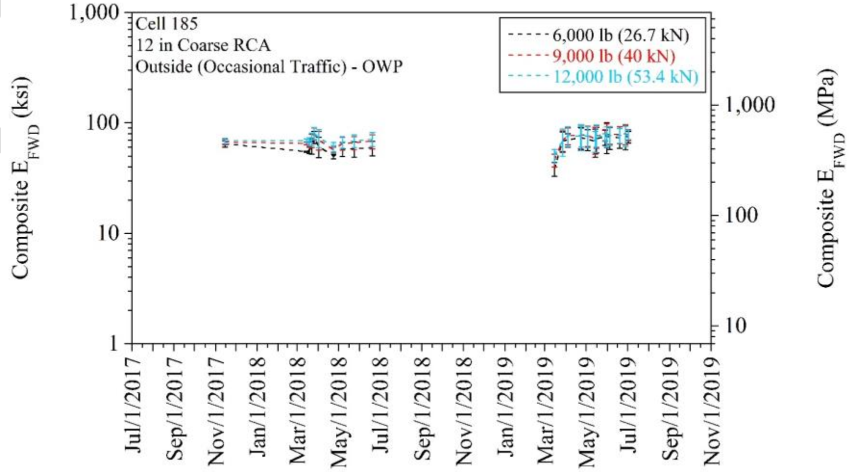

Cell 186 (12 in fine RCA) – composite E_{FWD} (error bars represent one standard deviation of the data):

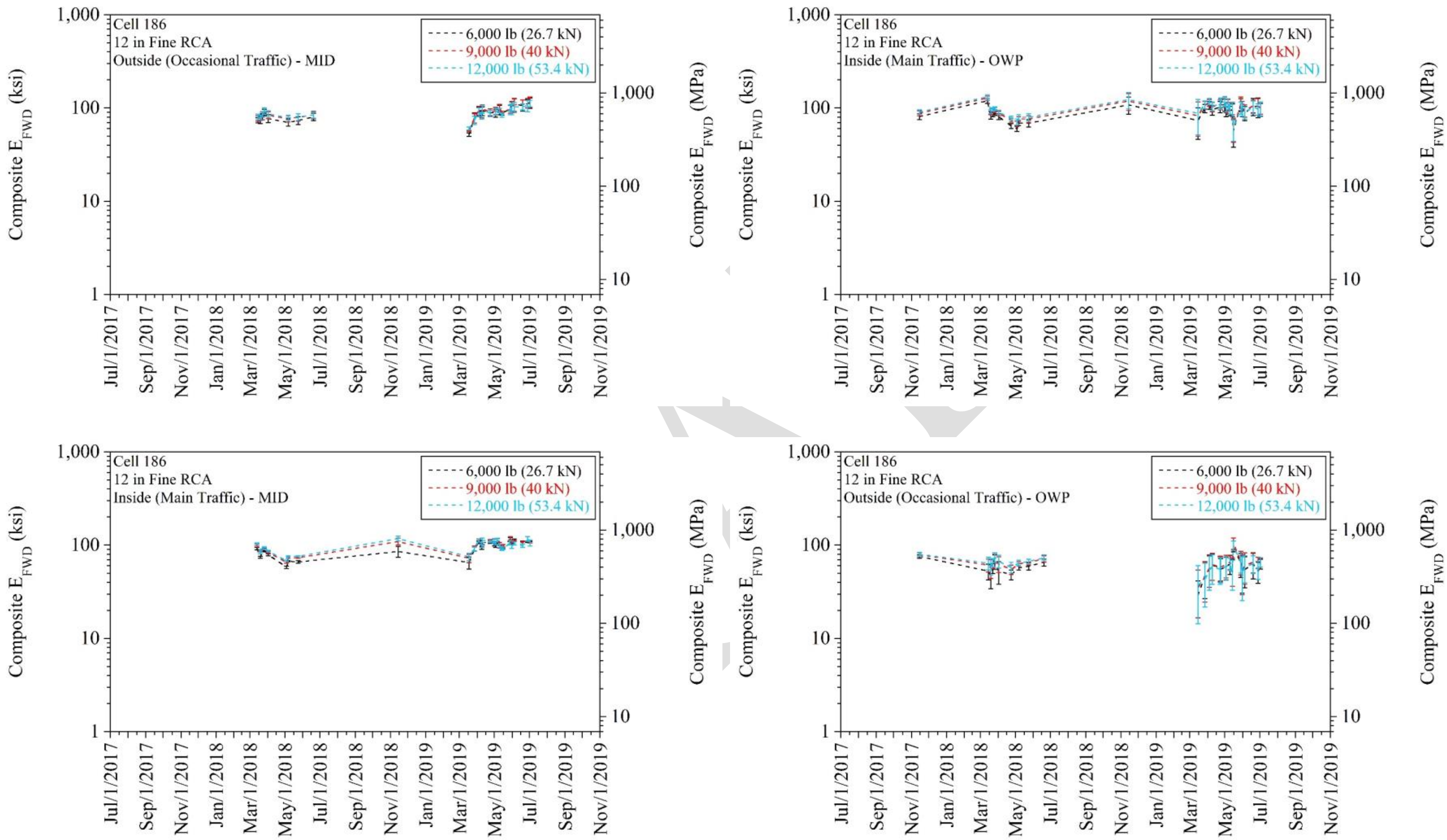

Cell 188 (12 in limestone) – composite E_{FWD} (error bars represent one standard deviation of the data):

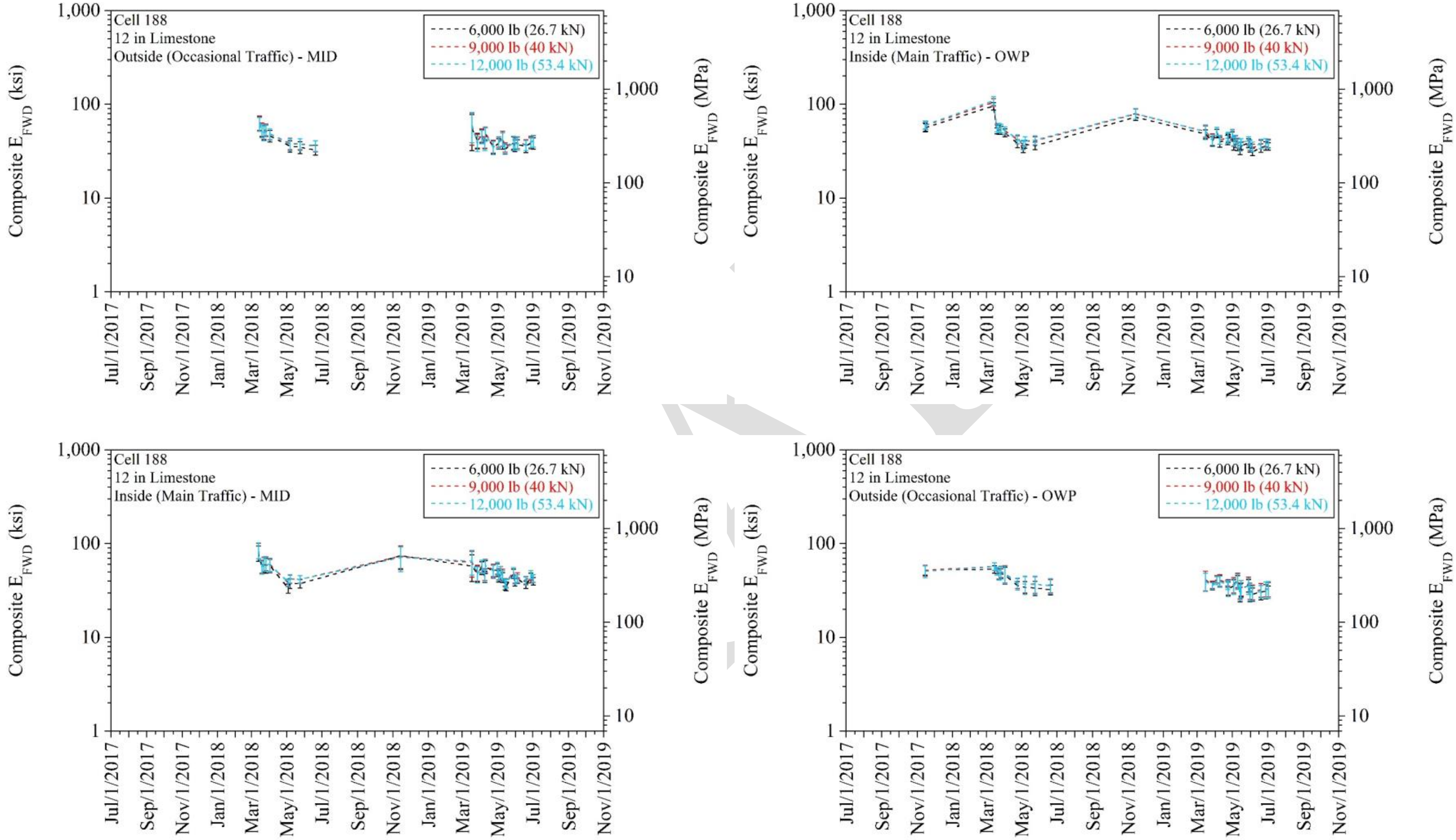

Cell 189 (12 in RCA+RAP) – composite E_{FWD} (error bars represent one standard deviation of the data):

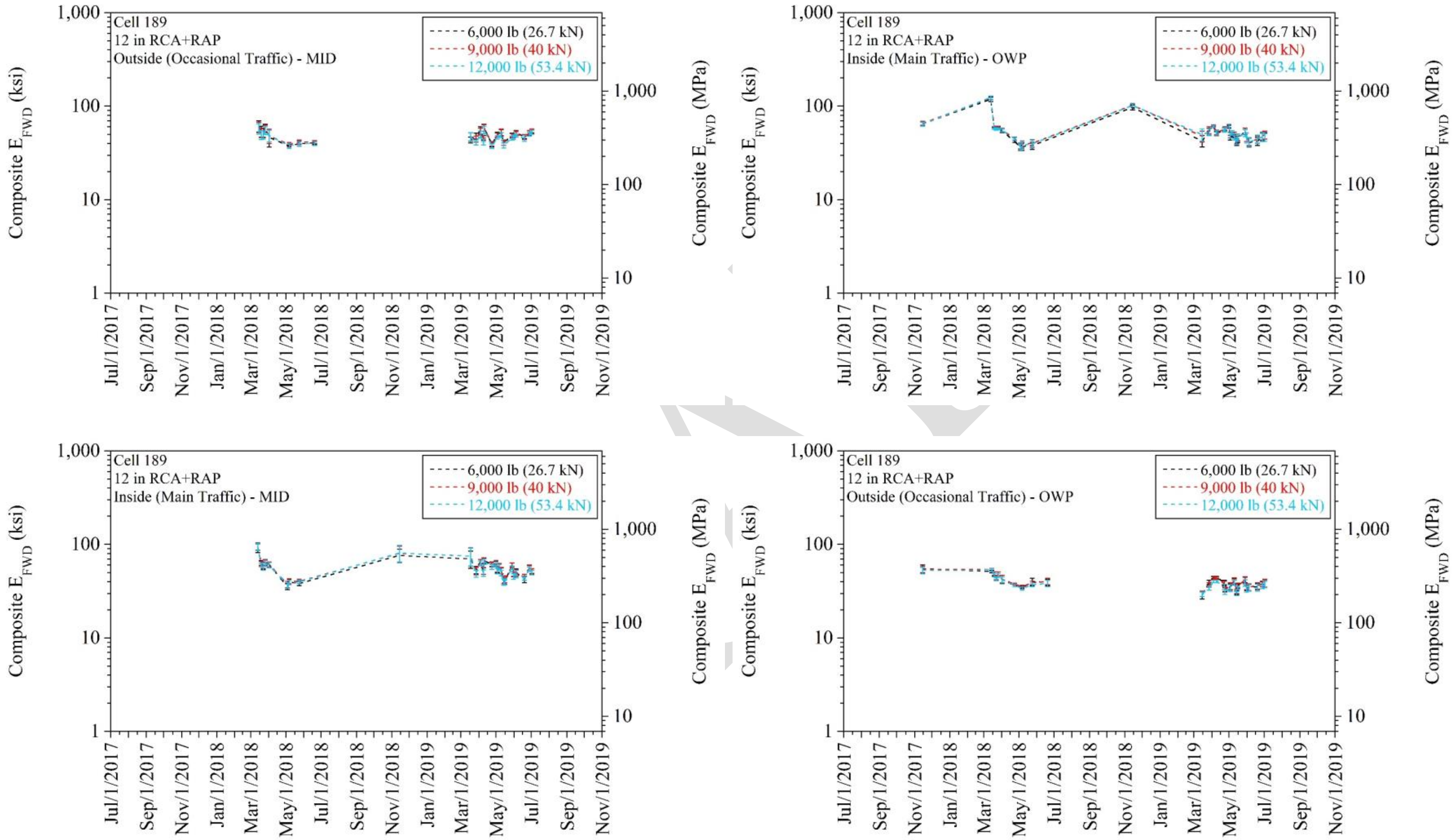

Cell 127 (18 in LSSB) – composite E_{FWD} (error bars represent one standard deviation of the data):

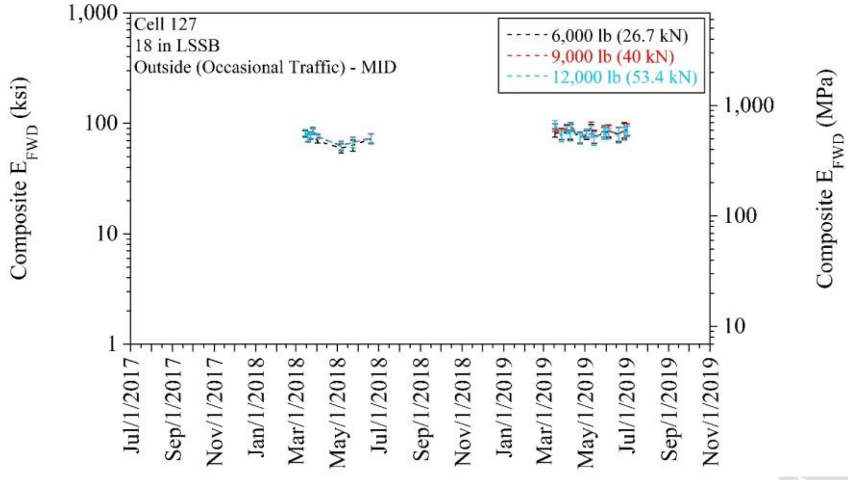

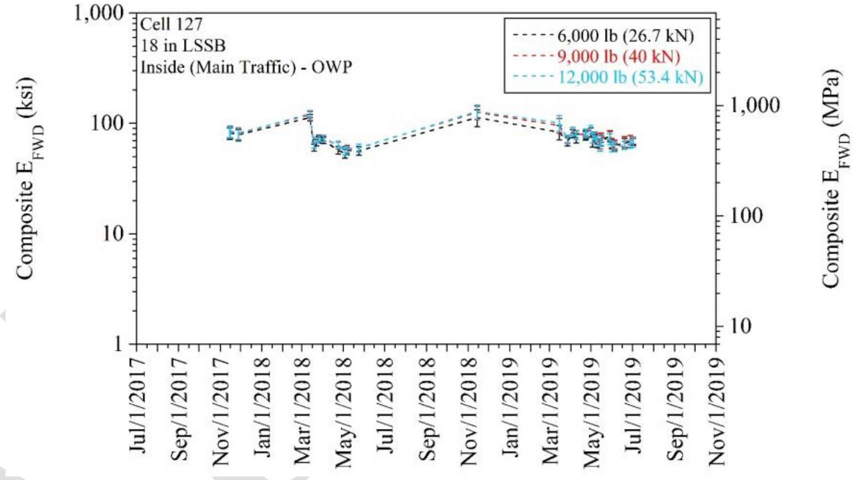

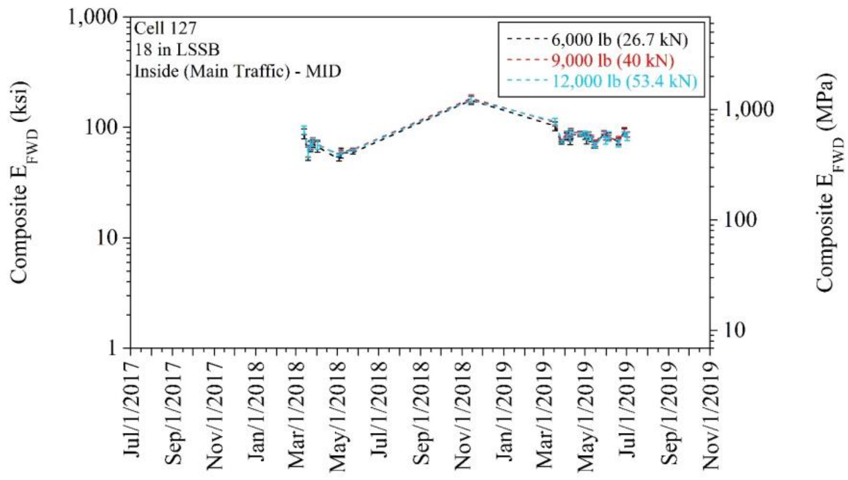

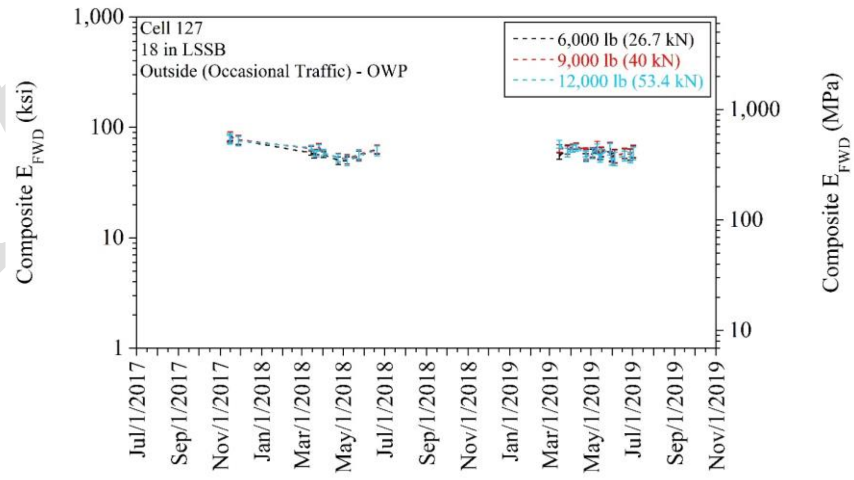

Cell 227 (18 in LSSB) – composite E_{FWD} (error bars represent one standard deviation of the data):

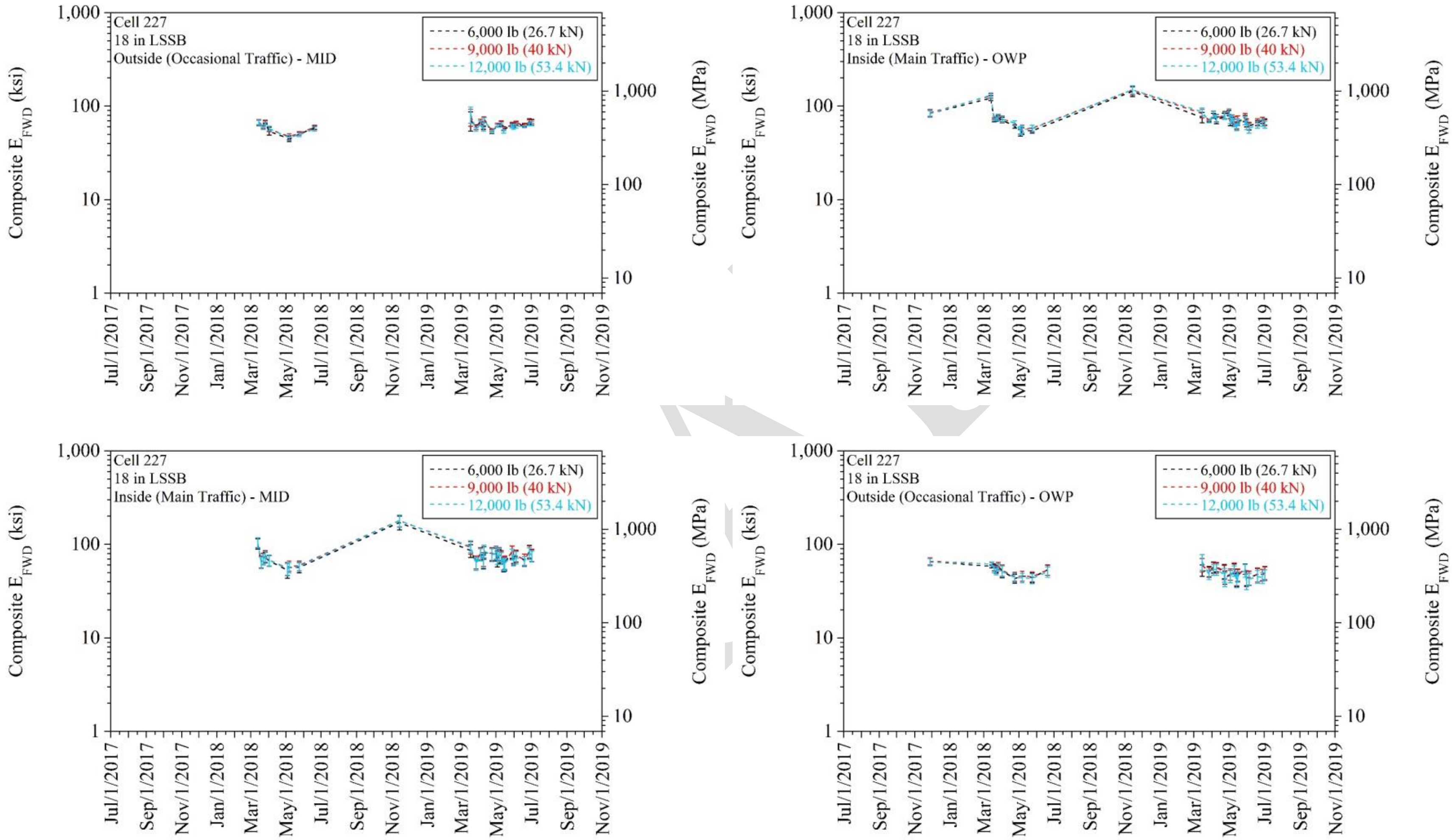

Cell 328 (9 in LSSB – TX) – composite E_{FWD} (error bars represent one standard deviation of the data):

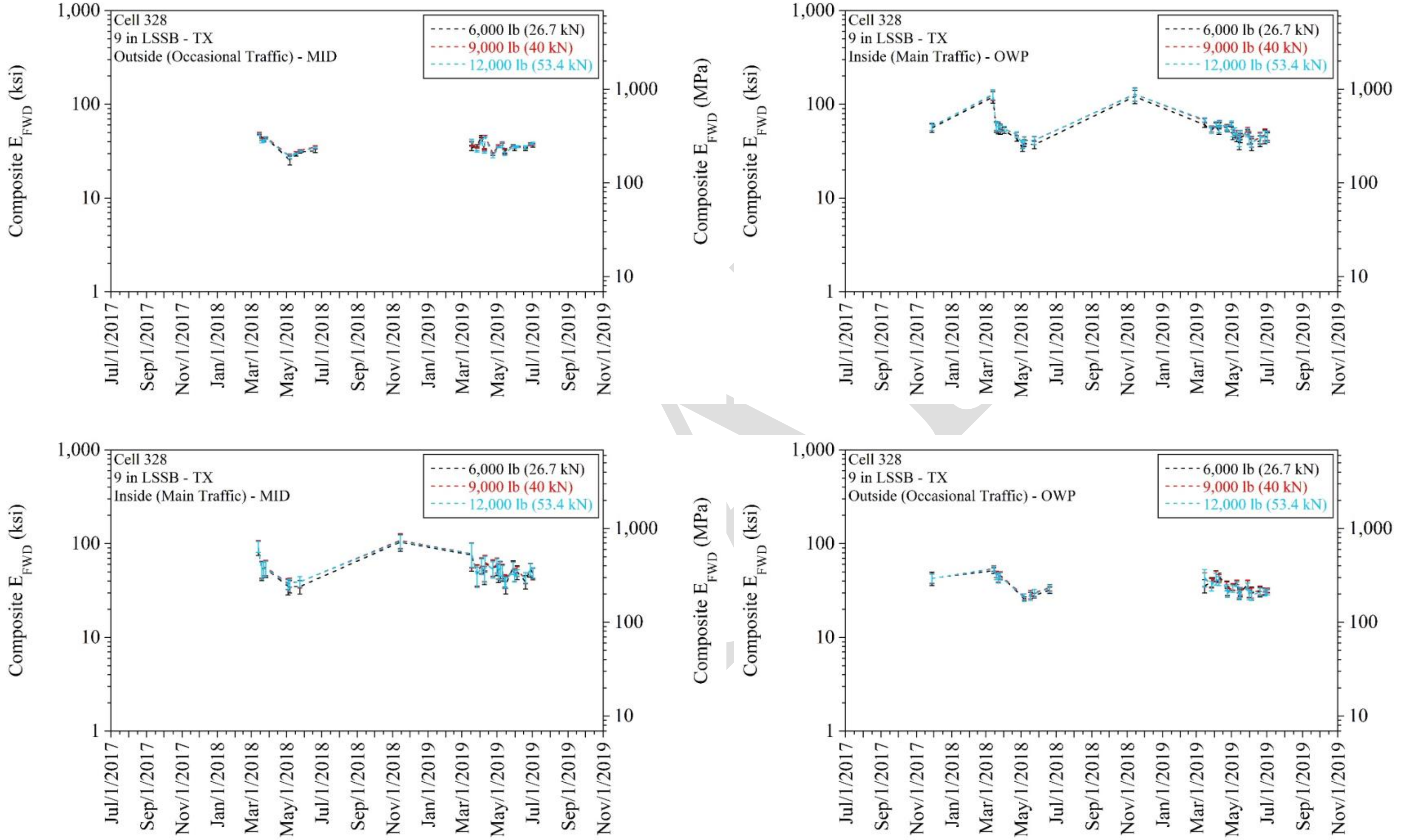

Cell 428 (9 in LSSB – TX+GT) – composite E_{FWD} (error bars represent one standard deviation of the data):

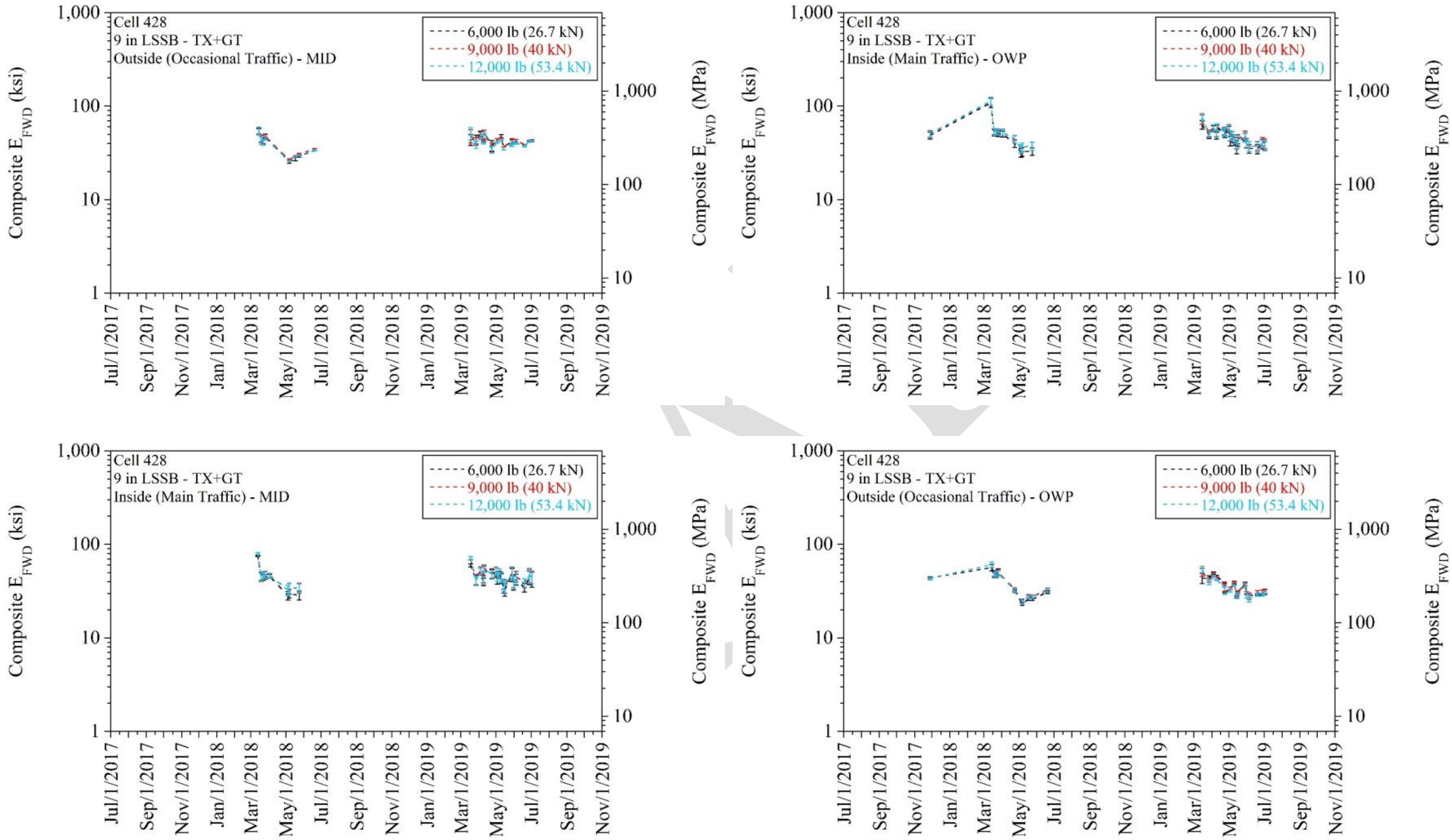

Cell 528 (9 in LSSB – BX+GT) – composite E_{FWD} (error bars represent one standard deviation of the data):

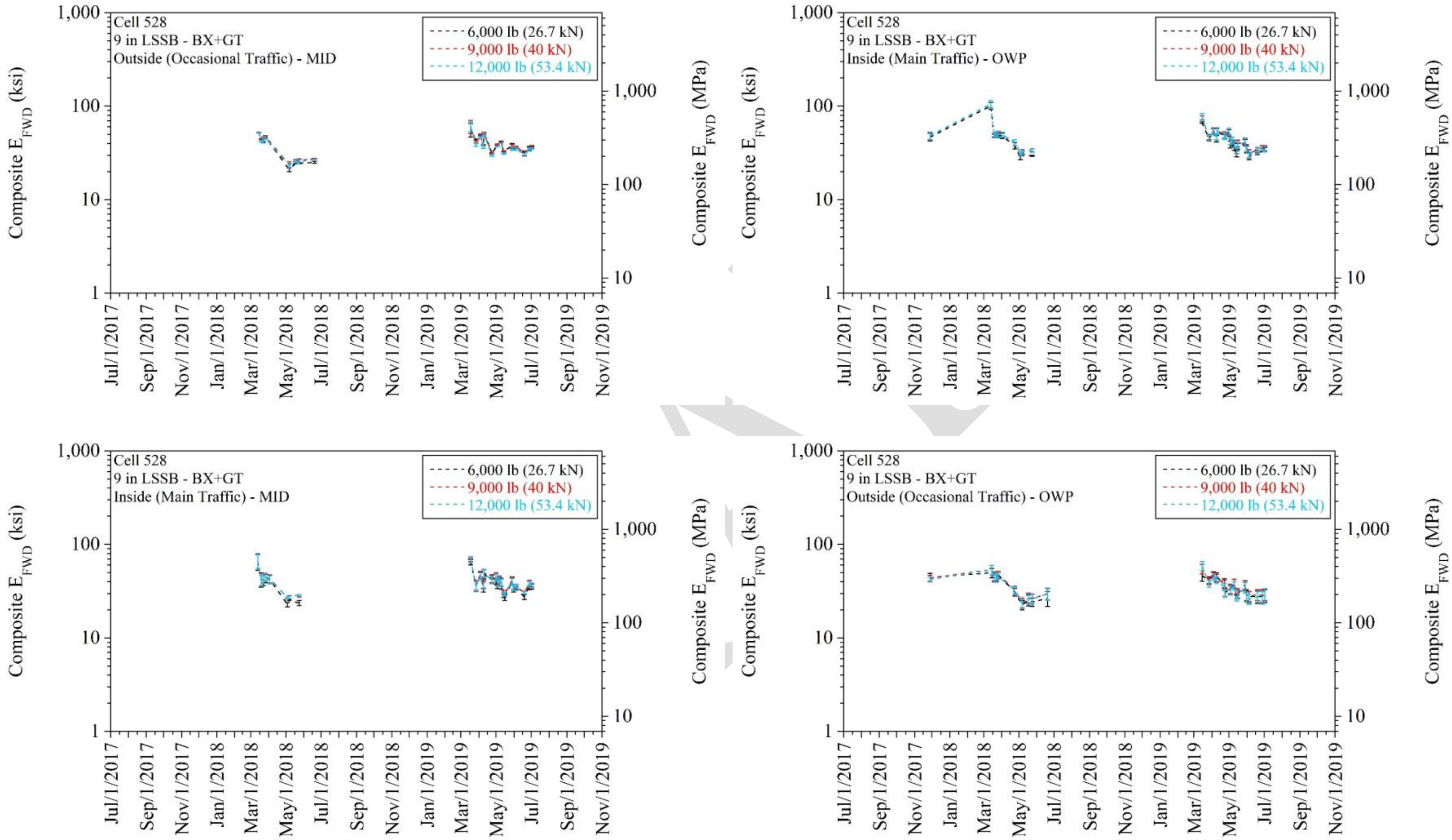

Cell 628 (9 in LSSB – BX) – composite E_{FWD} (error bars represent one standard deviation of the data):

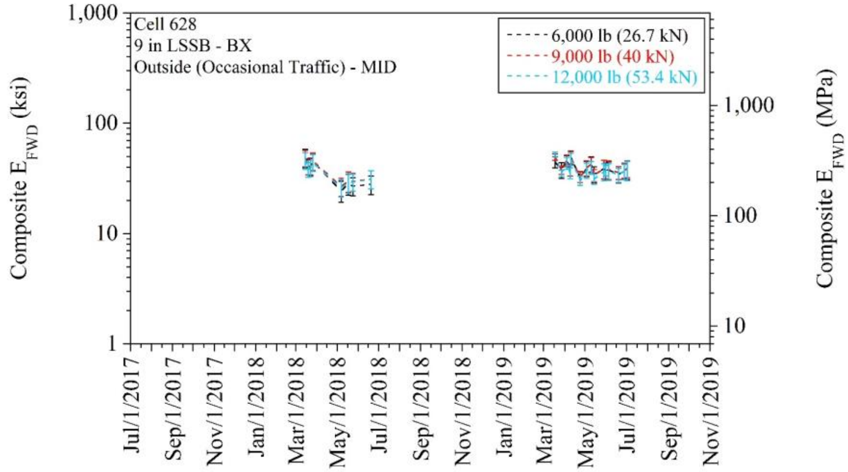

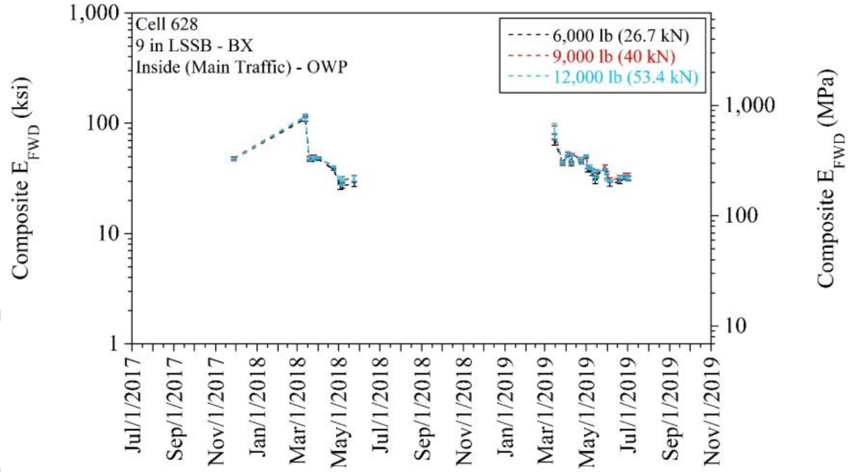

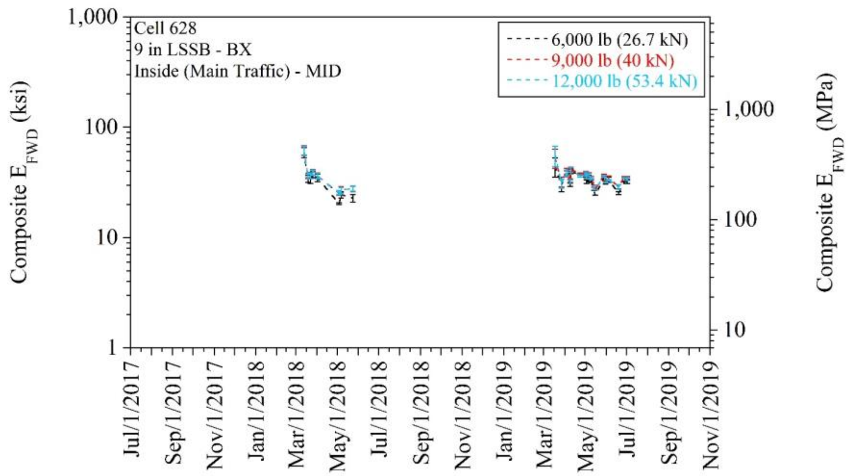

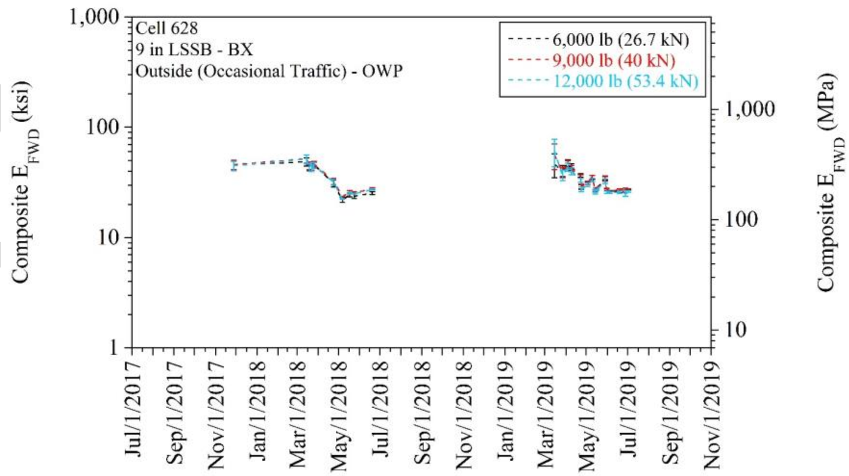

Cell 728 (9 in LSSB) – composite E_{FWD} (error bars represent one standard deviation of the data):

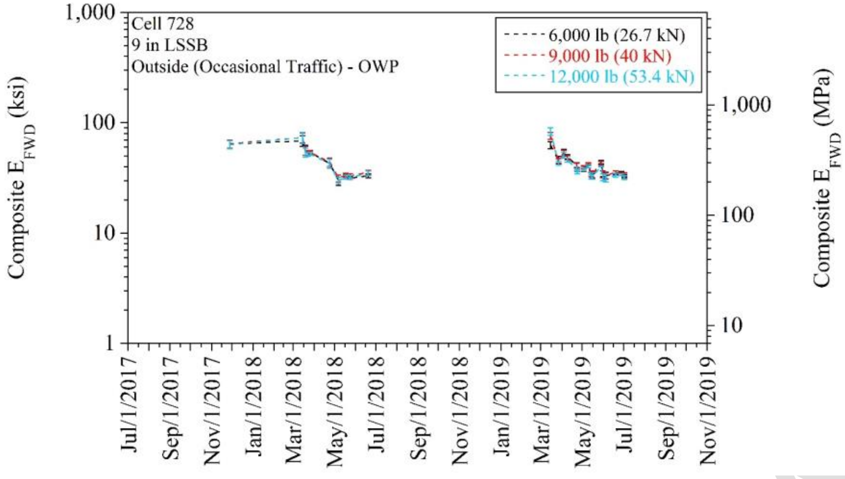

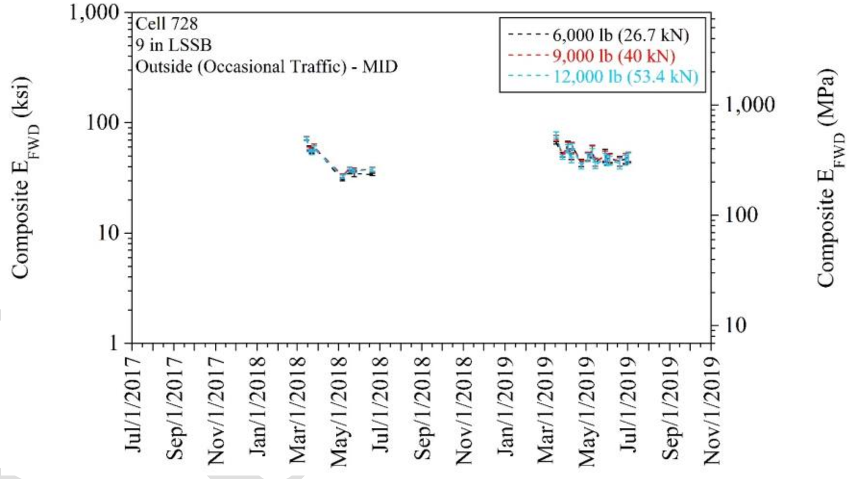

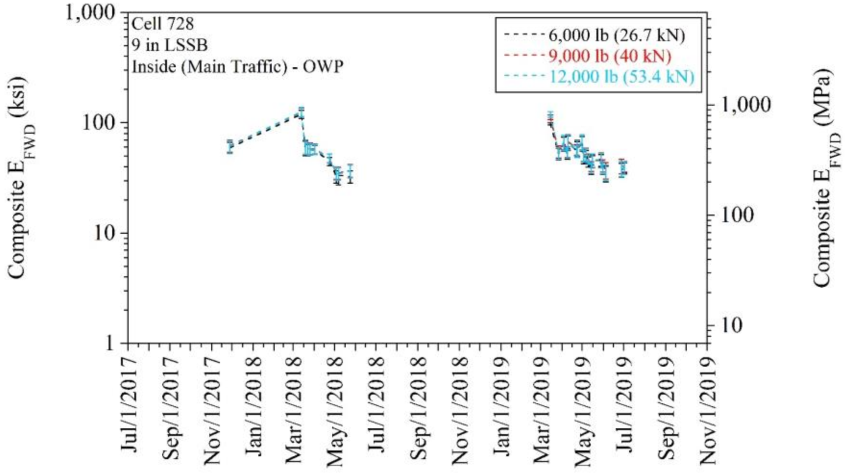

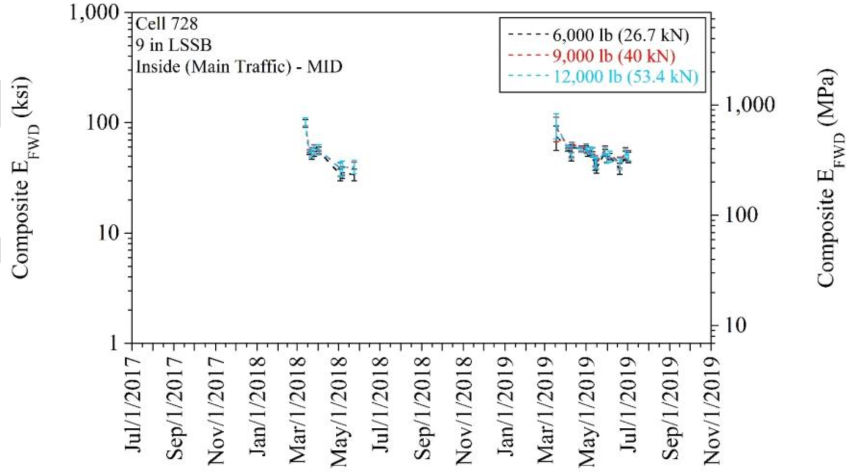

APPENDIX G. ASPHALT E_{FWD} VALUES AT 6,000 LB (26.7 KN), 9,000 LB (40 KN), AND 12,000 LB (53.4 KN) FOR EACH CELL

Cell 185 (12 in coarse RCA) – asphalt E_{FWD} (error bars represent one standard deviation of the data):

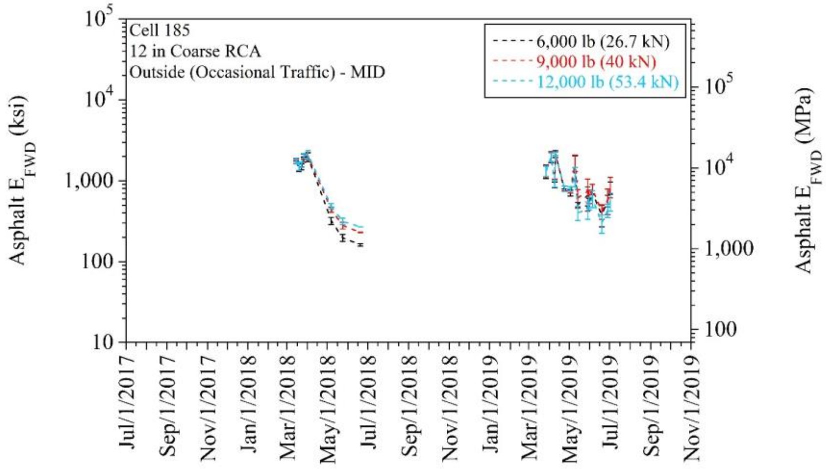

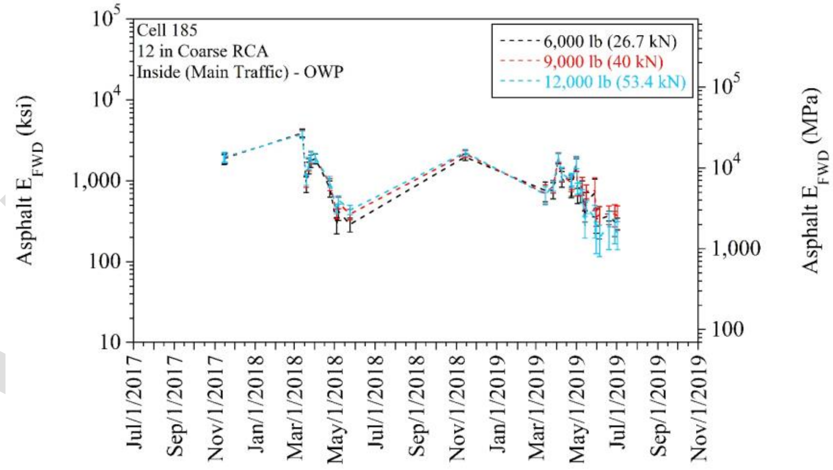

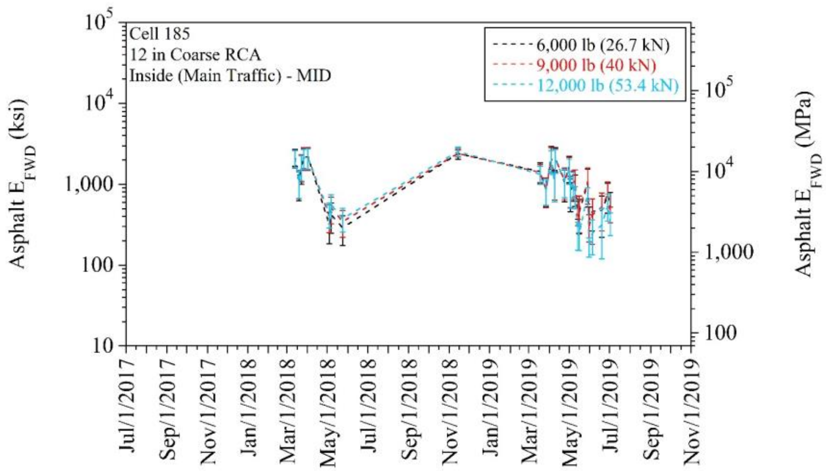

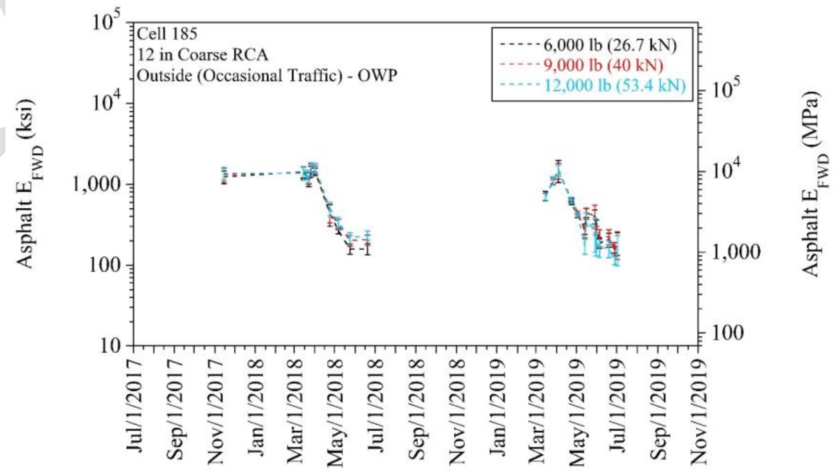

Cell 186 (12 in fine RCA) – asphalt E_{FWD} (error bars represent one standard deviation of the data):

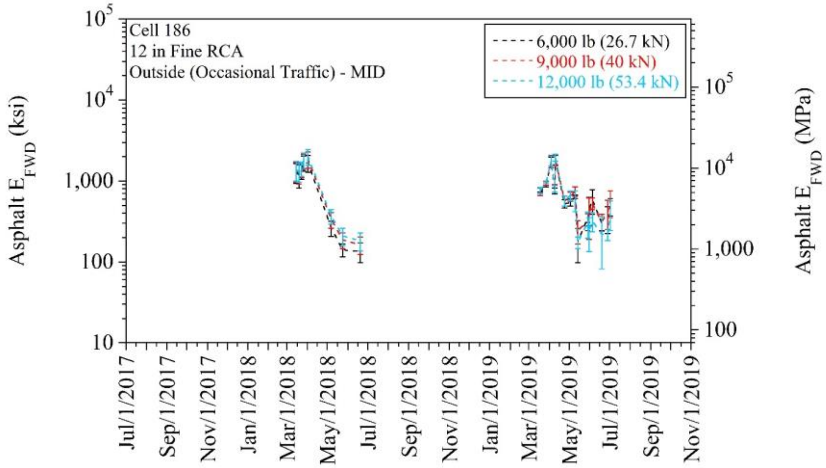

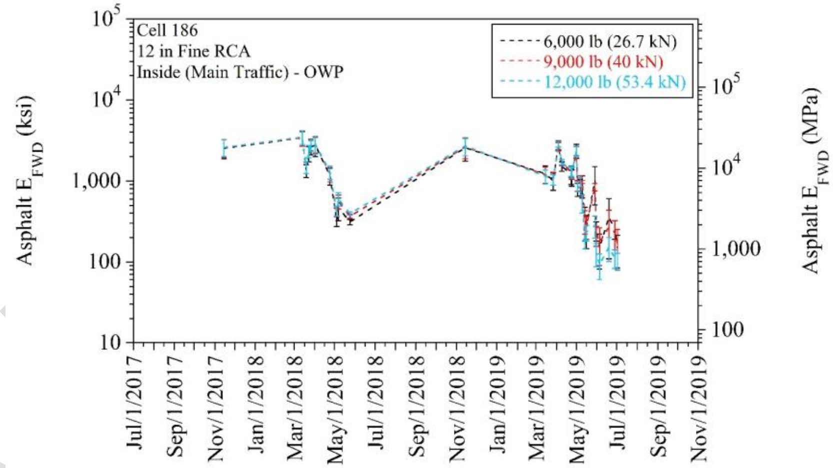

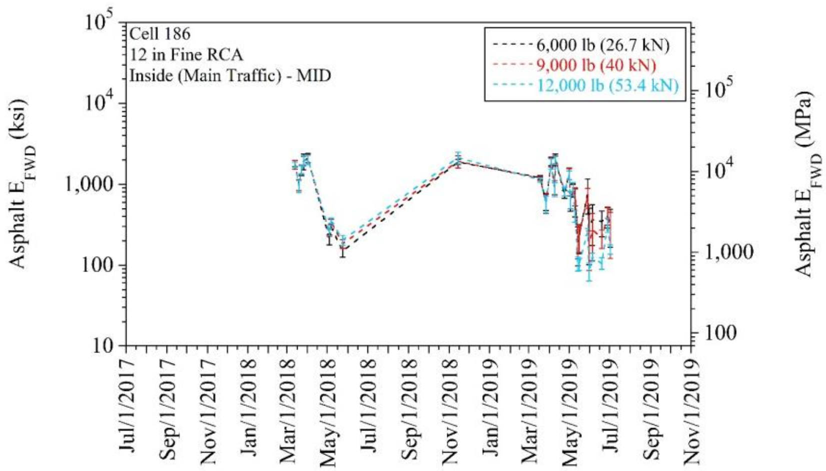

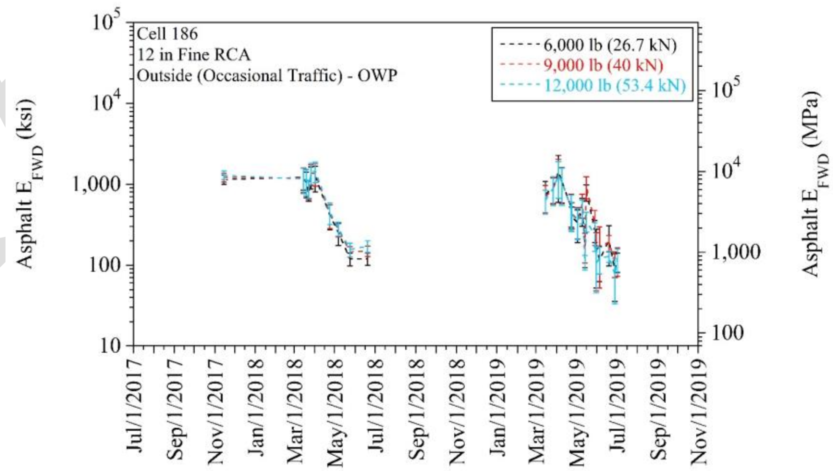

Cell 188 (12 in limestone) – asphalt E_{FWD} (error bars represent one standard deviation of the data):

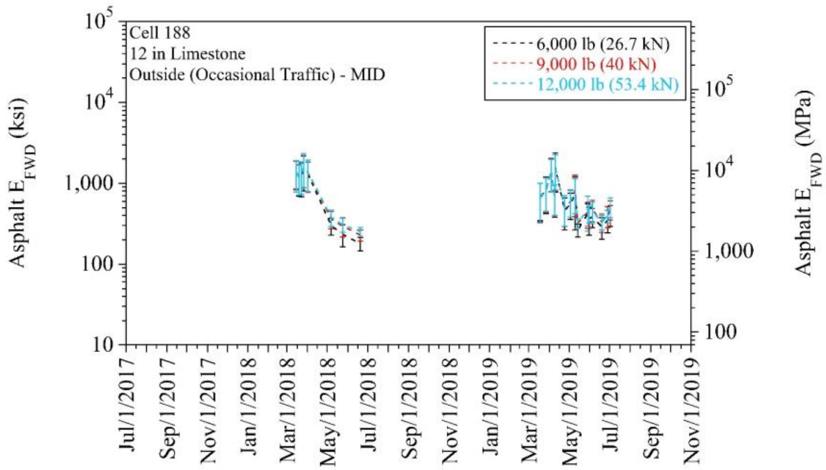

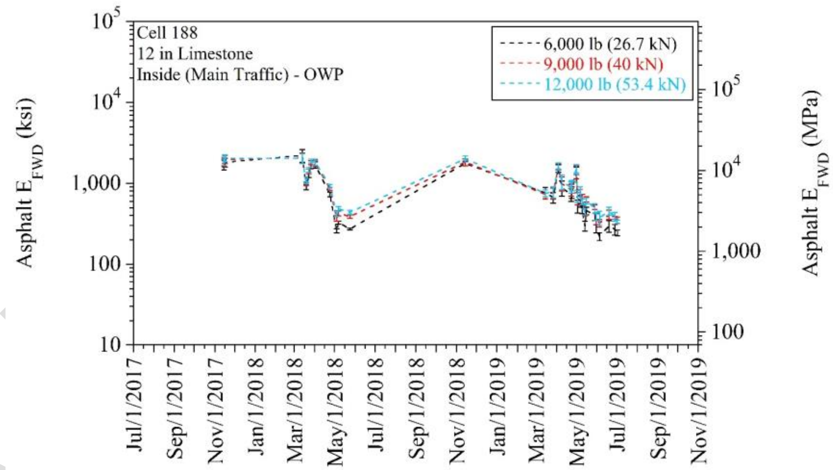

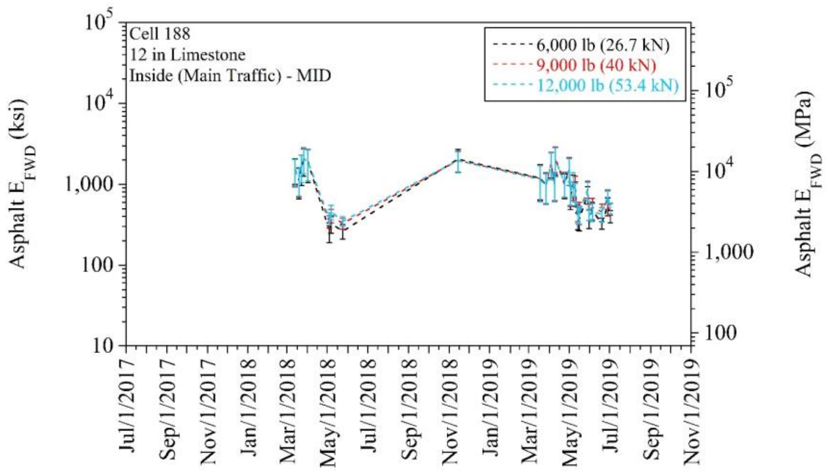

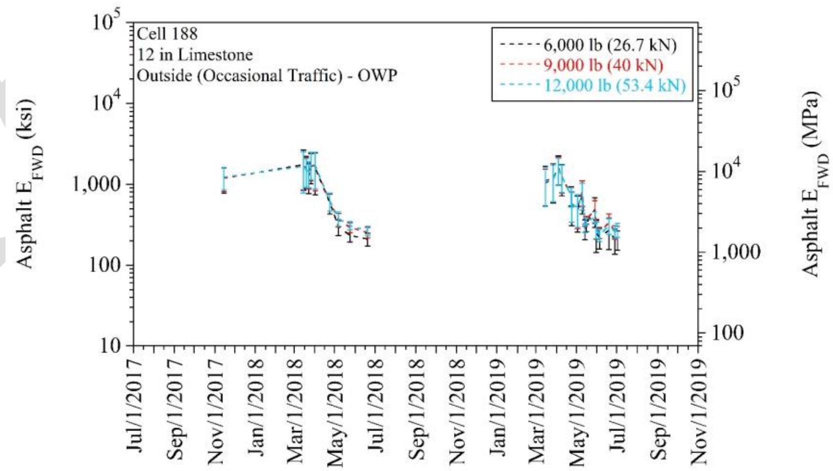

Cell 189 (12 in RCA+RAP) – asphalt E_{FWD} (error bars represent one standard deviation of the data):

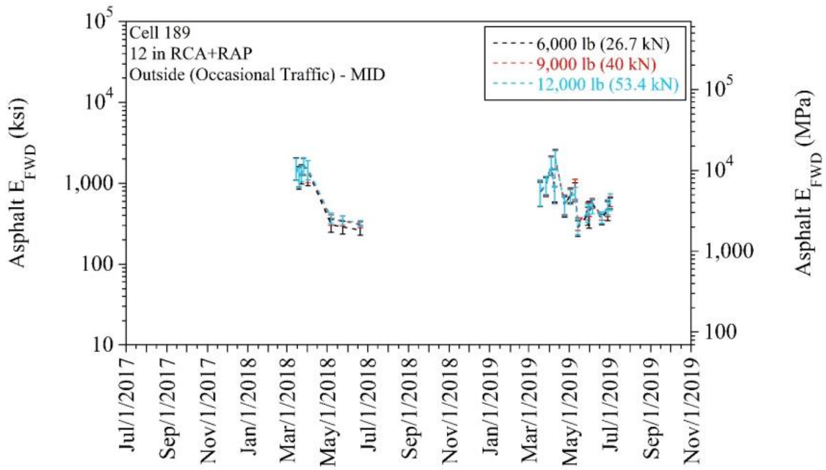

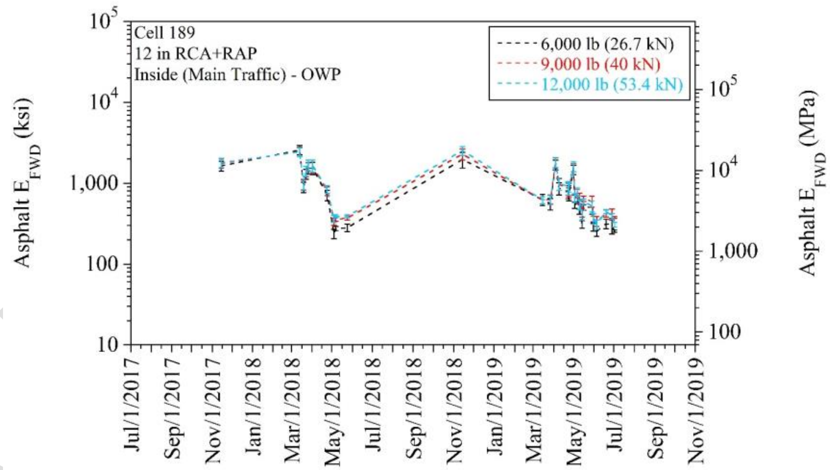

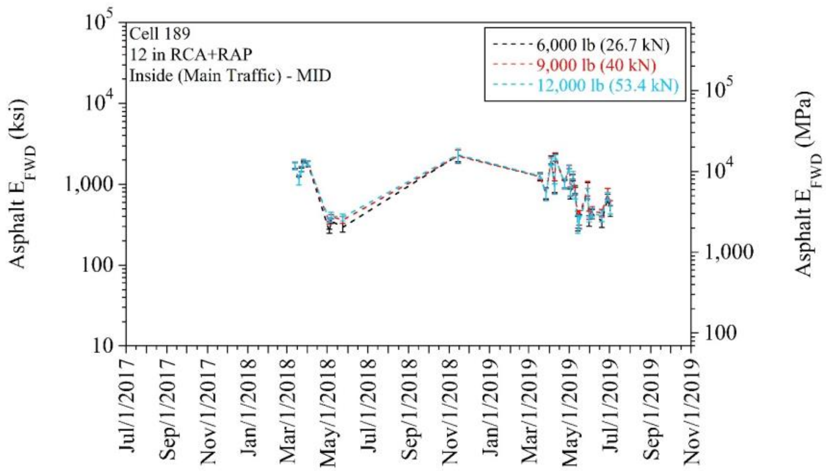

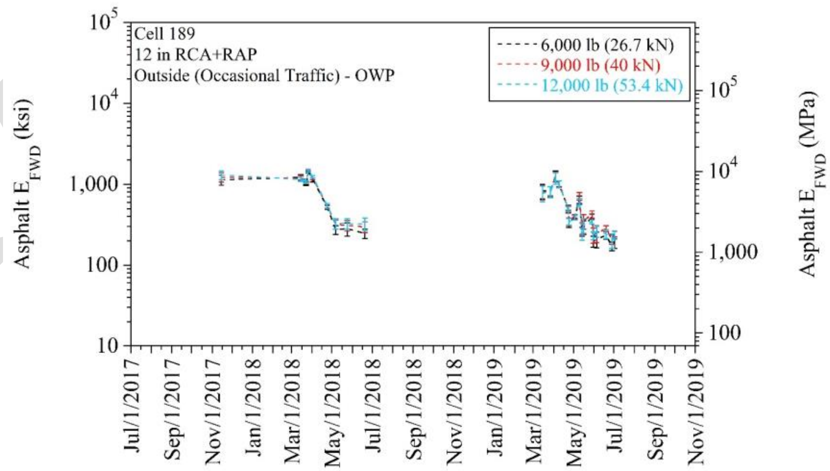

Cell 127 (18 in LSSB) – asphalt E_{FWD} (error bars represent one standard deviation of the data):

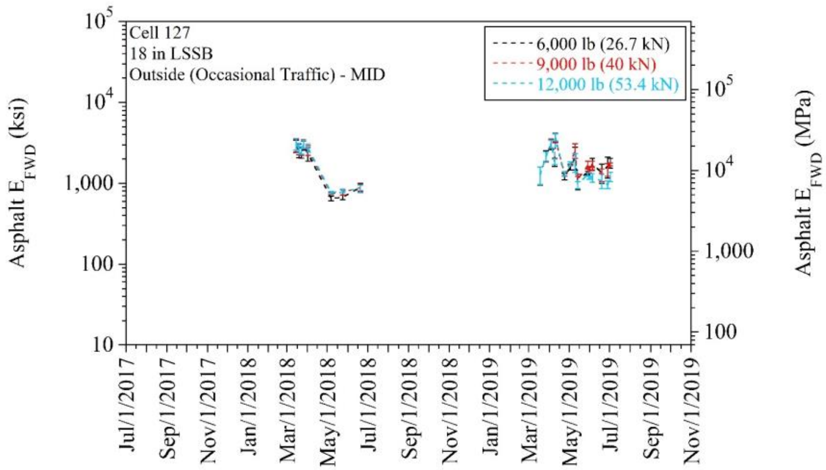

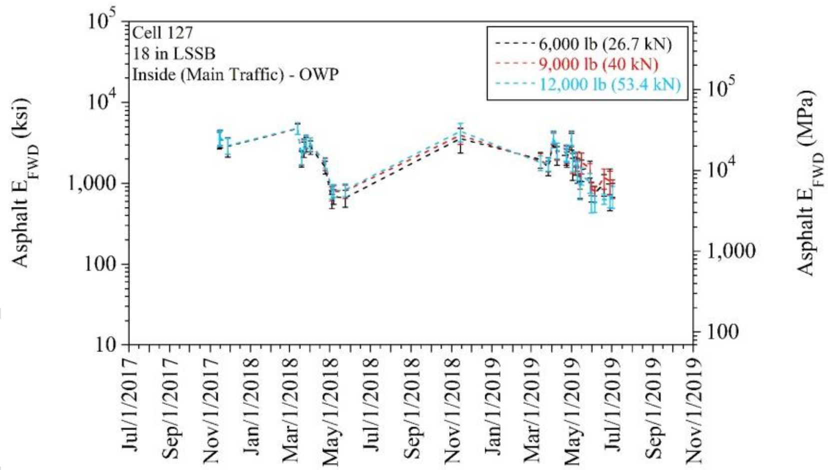

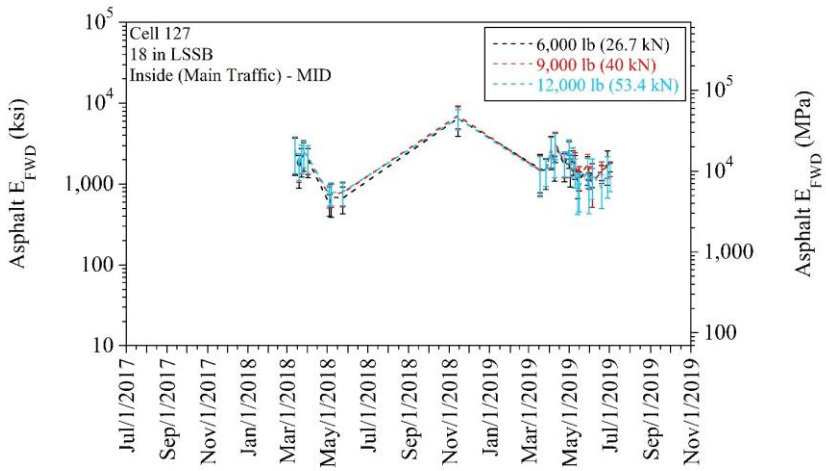

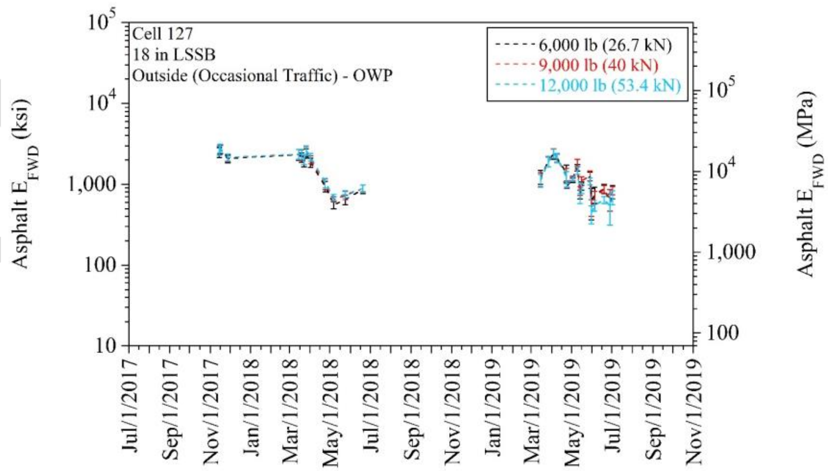

Cell 227 (18 in LSSB) – asphalt E_{FWD} (error bars represent one standard deviation of the data):

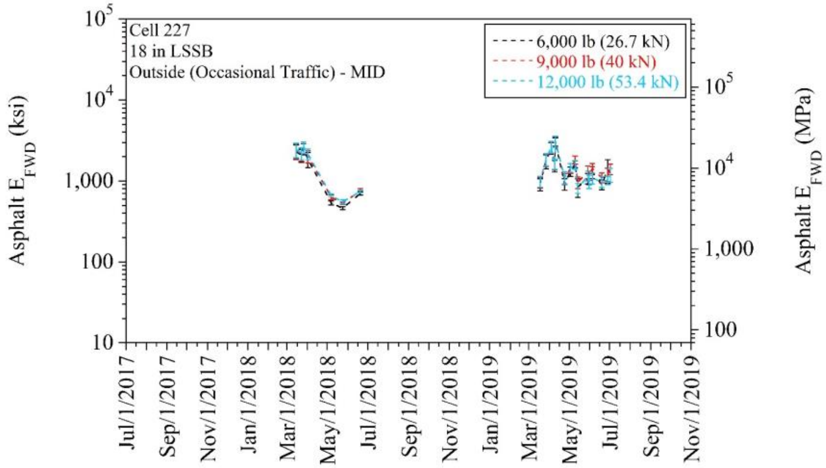

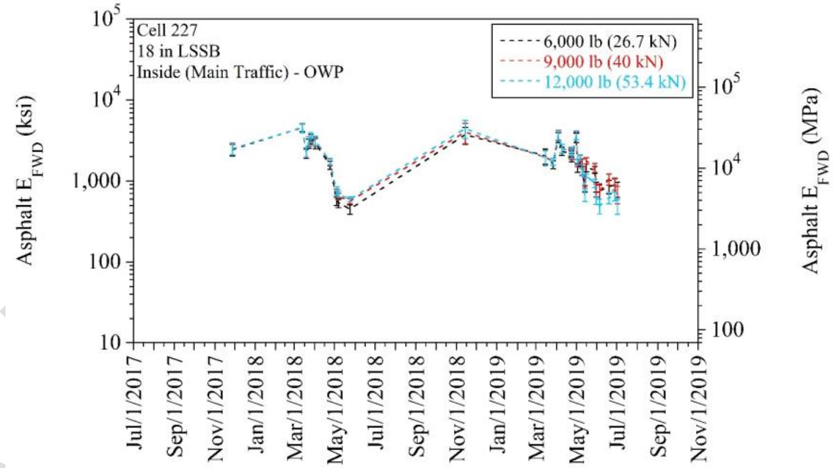

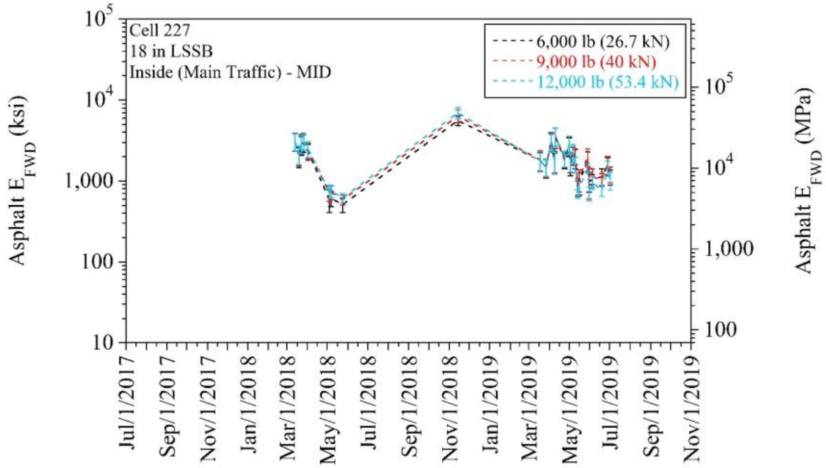

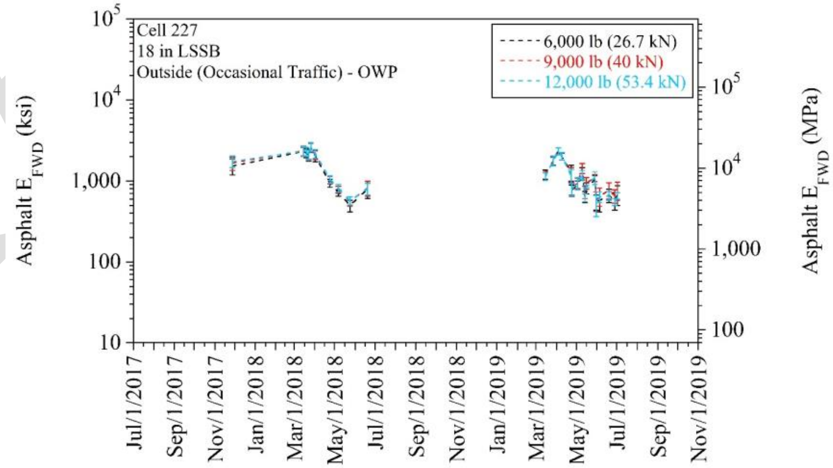

Cell 328 (9 in LSSB – TX) – asphalt E_{FWD} (error bars represent one standard deviation of the data):

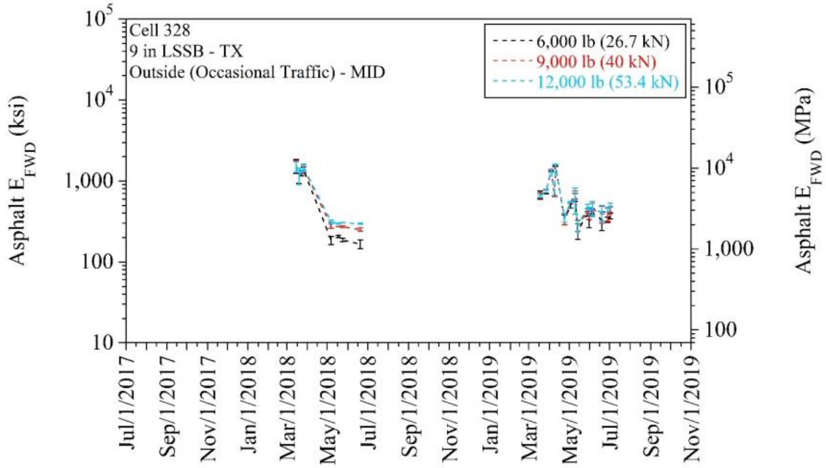

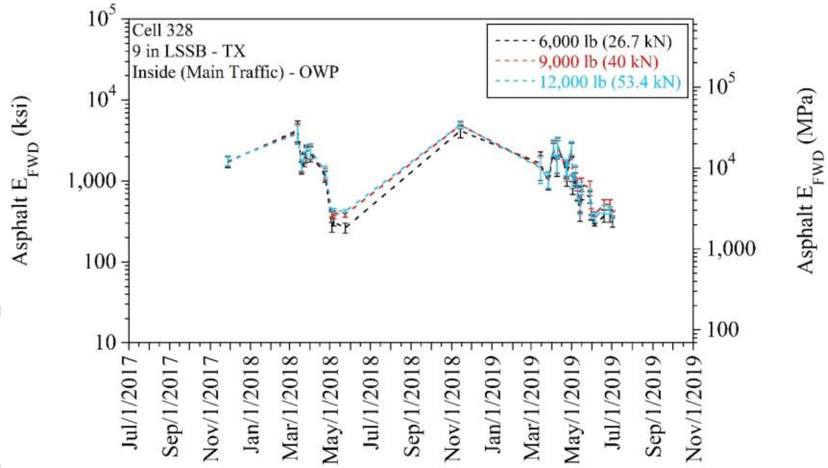

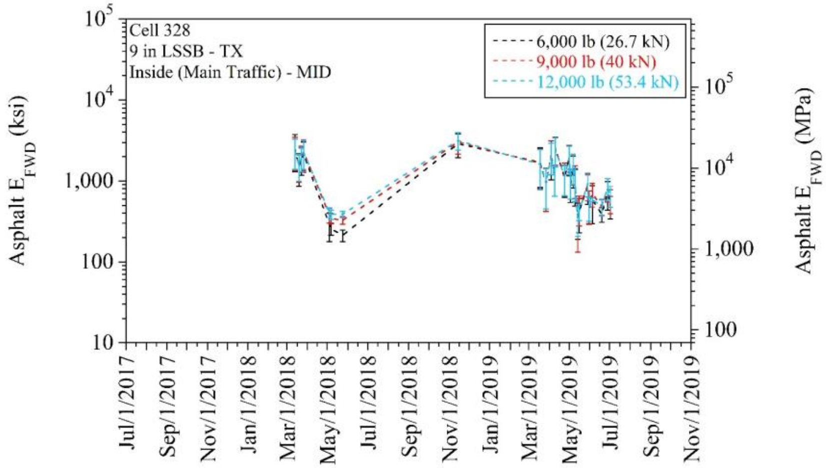

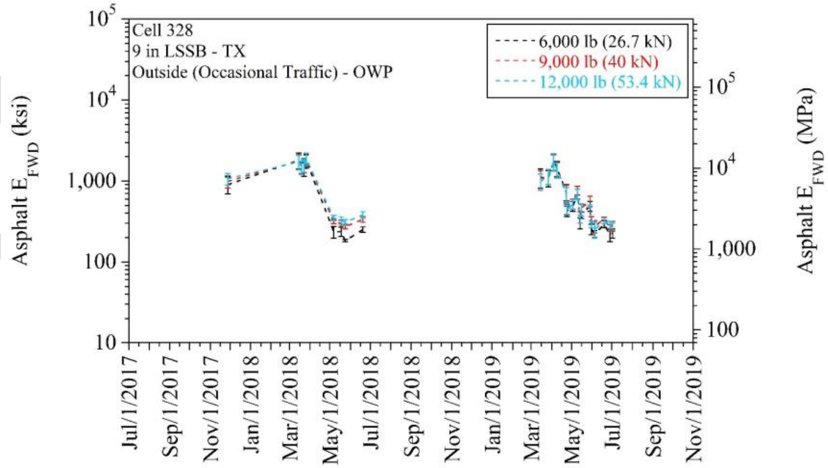

Cell 428 (9 in LSSB – TX+GT) – asphalt E_{FWD} (error bars represent one standard deviation of the data):

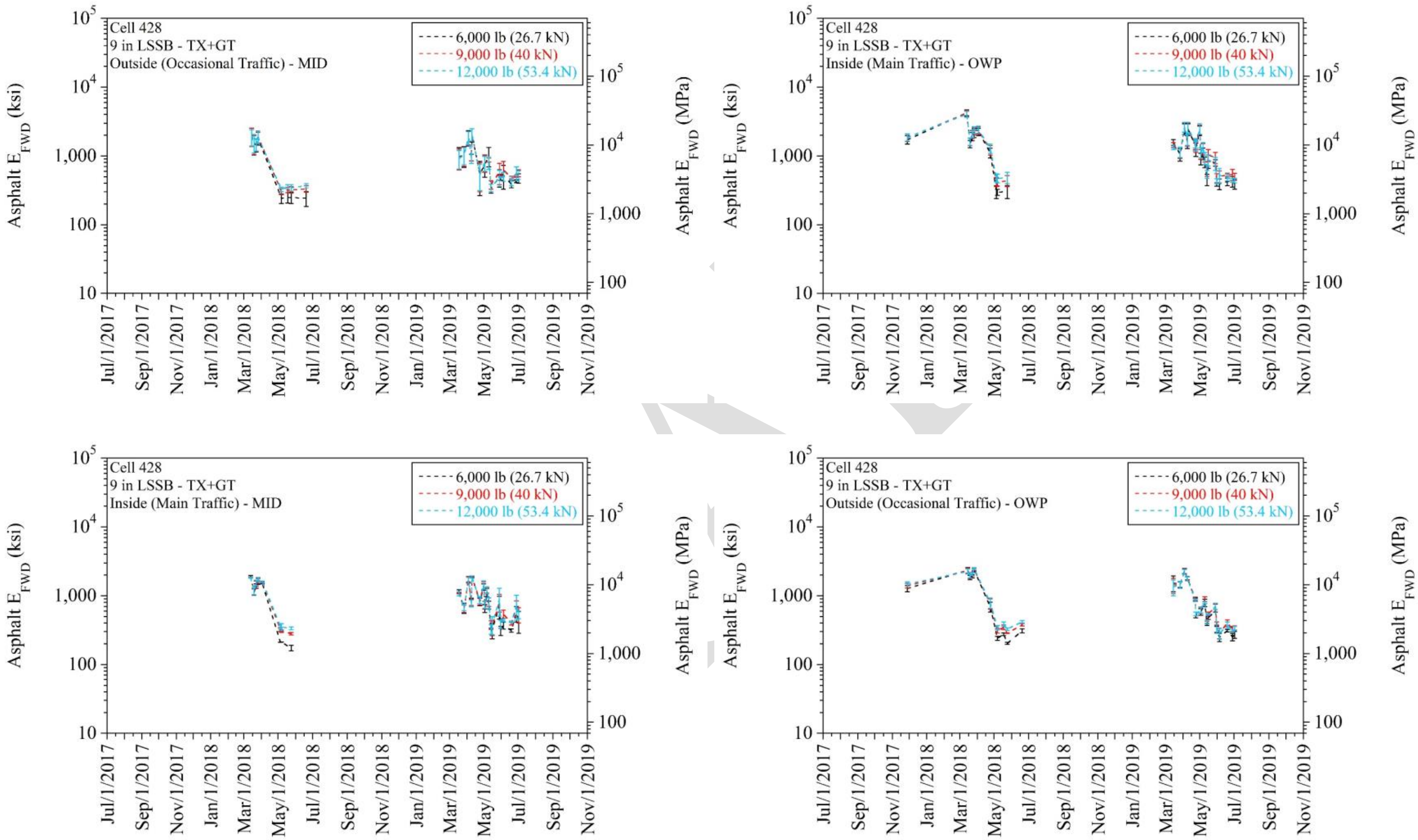

Cell 528 (9 in LSSB – BX+GT) – asphalt E_{FWD} (error bars represent one standard deviation of the data):

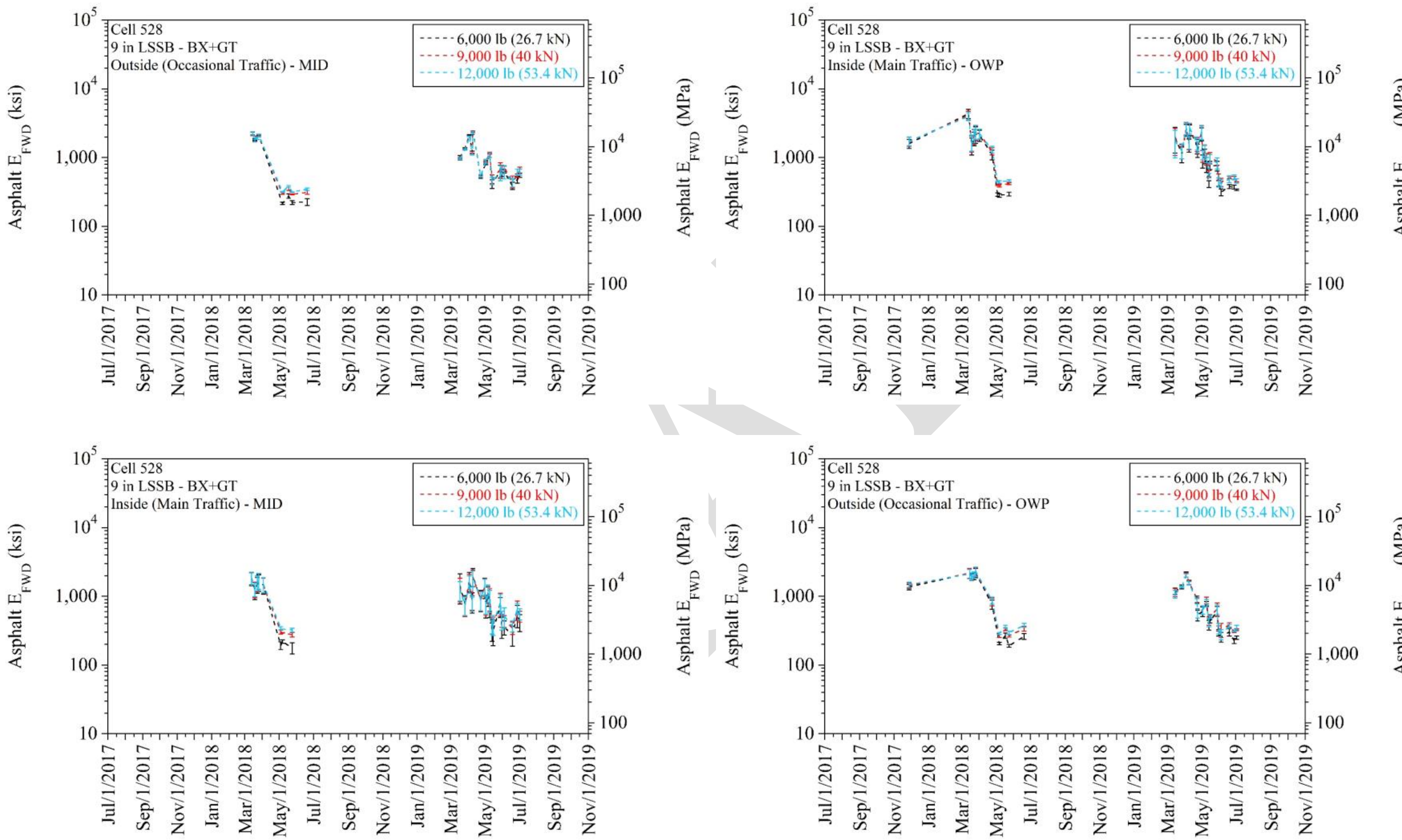

Cell 628 (9 in LSSB – BX) – asphalt E_{FWD} (error bars represent one standard deviation of the data):

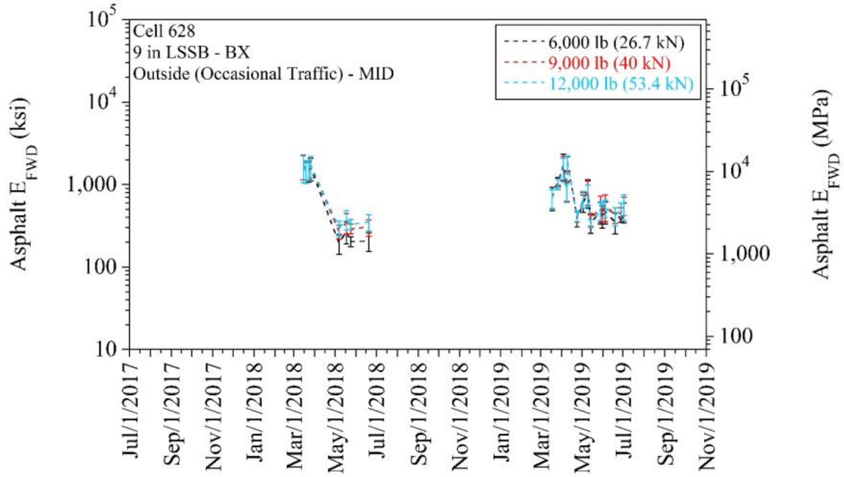

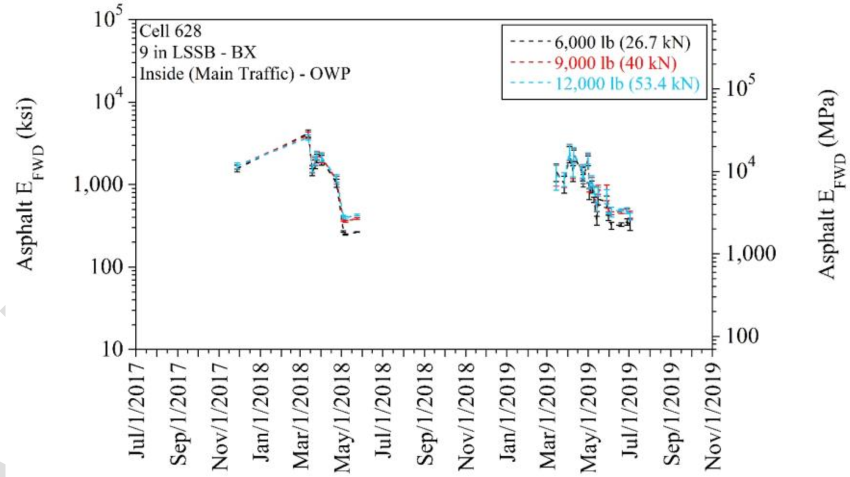

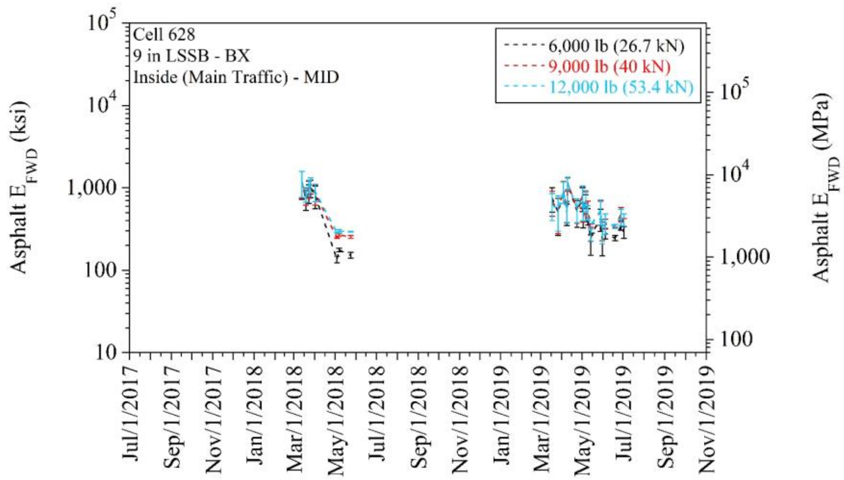

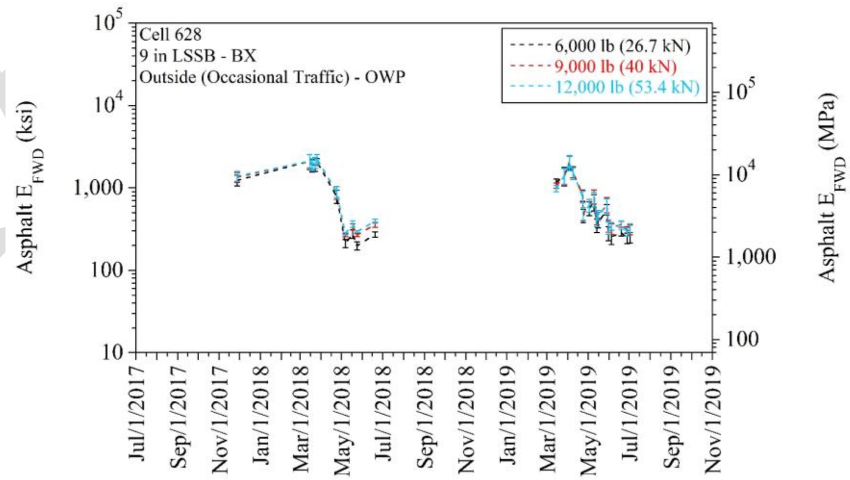

Cell 728 (9 in LSSB) – asphalt E_{FWD} (error bars represent one standard deviation of the data):

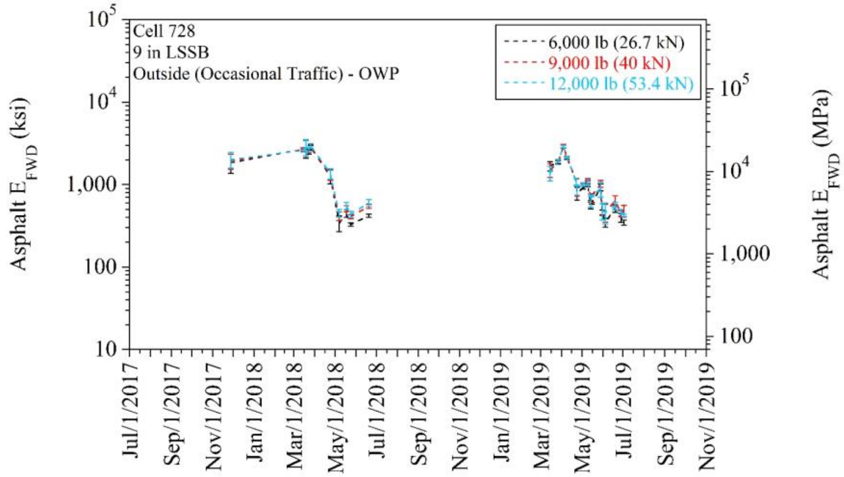

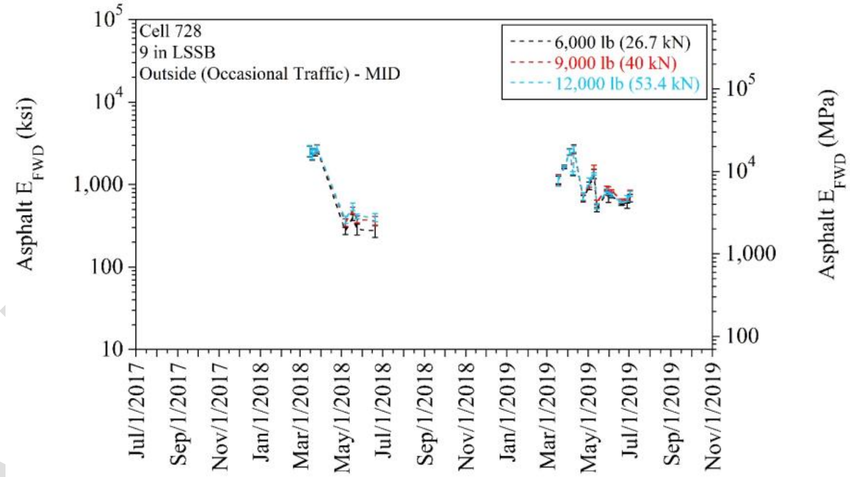

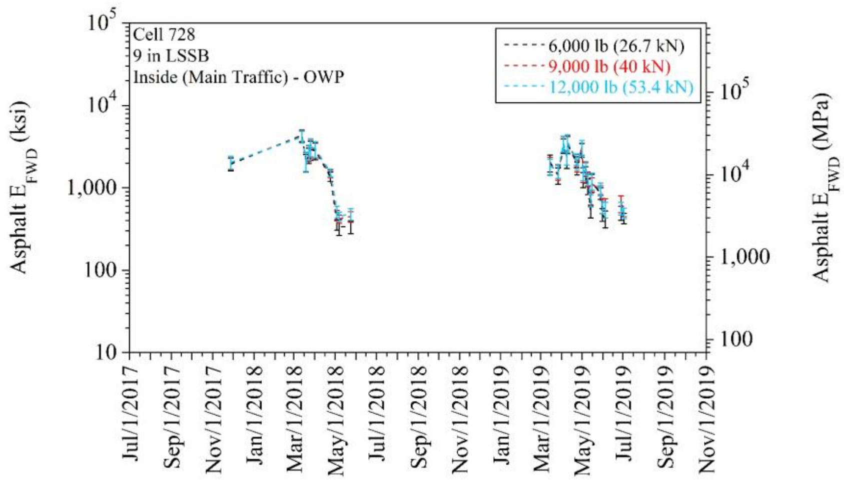

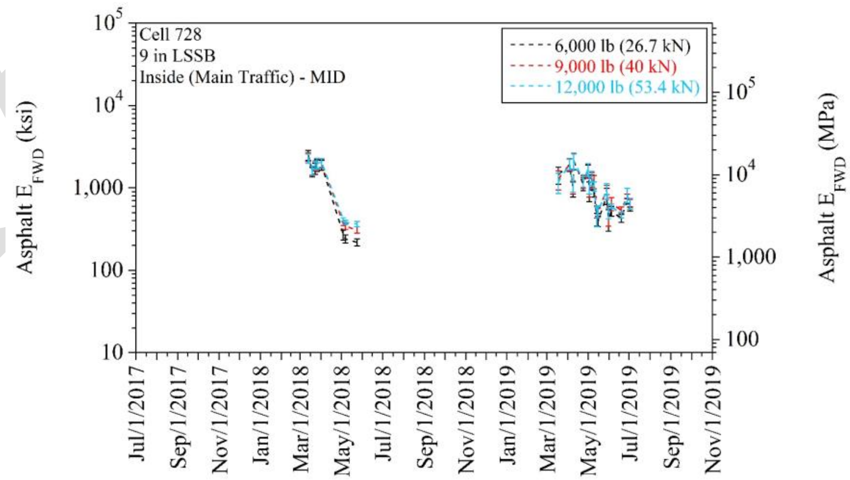

APPENDIX H. BASE+SUBBASE E$_{FWD}$ VALUES AT 6,000 LB (26.7 KN), 9,000 LB (40 KN), AND 12,000 LB (53.4 KN) FOR EACH CELL

Cell 185 (12 in coarse RCA) – base+subbase E_{FWD} (error bars represent one standard deviation of the data):

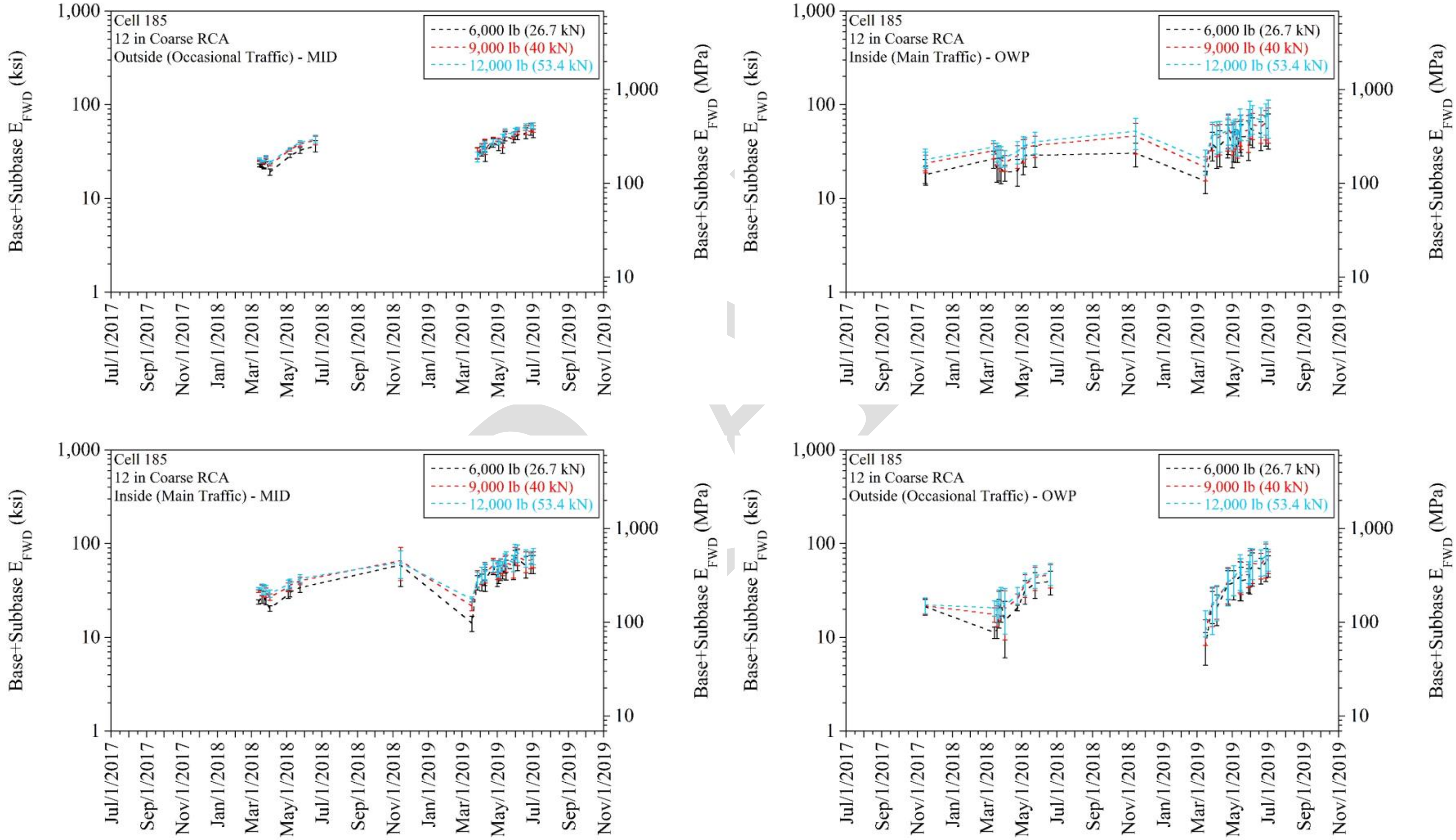

Cell 186 (12 in fine RCA) – base+subbase E_{FWD} (error bars represent one standard deviation of the data):

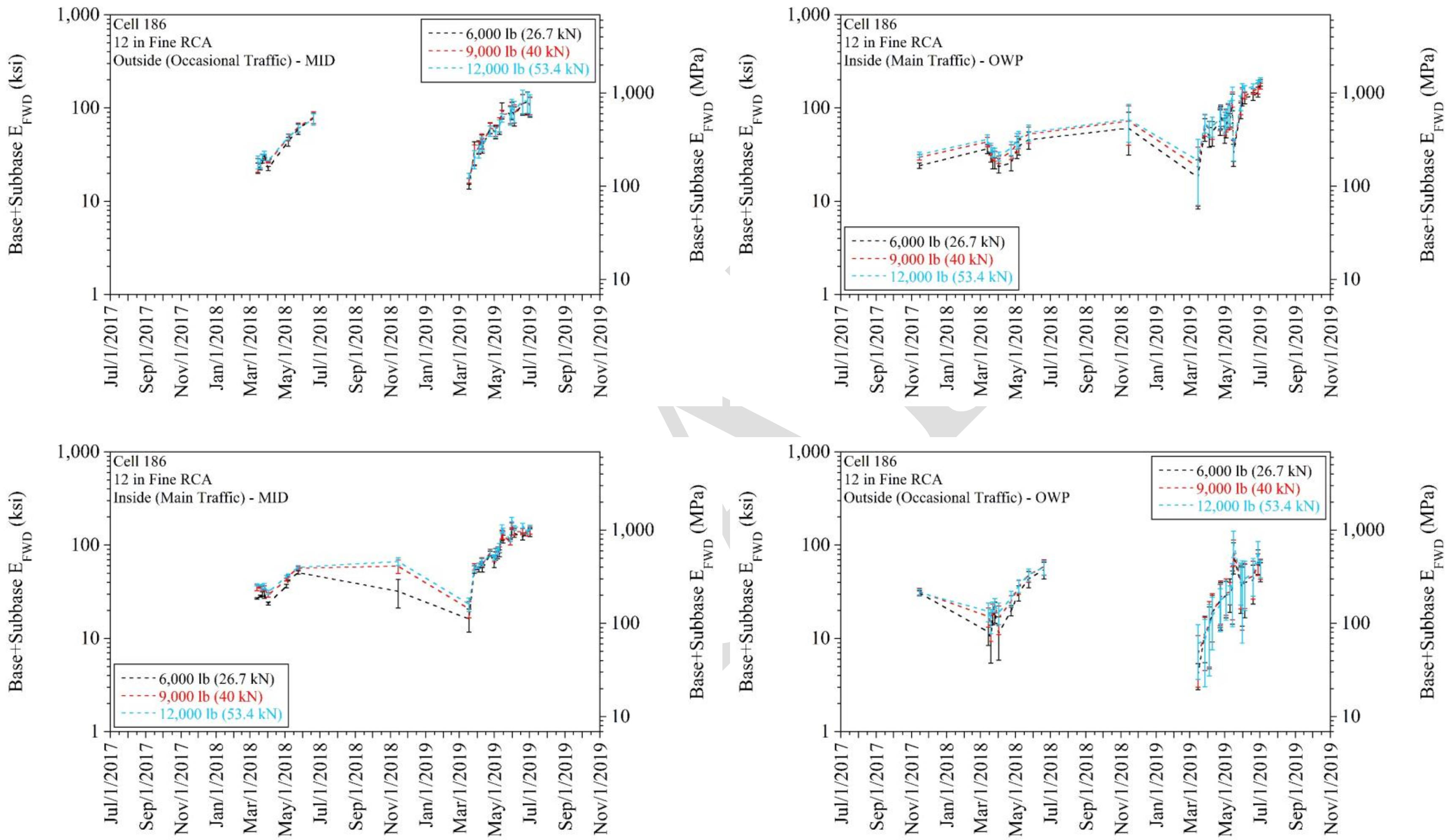

Cell 188 (12 in limestone) – base+subbase E_{FWD} (error bars represent one standard deviation of the data):

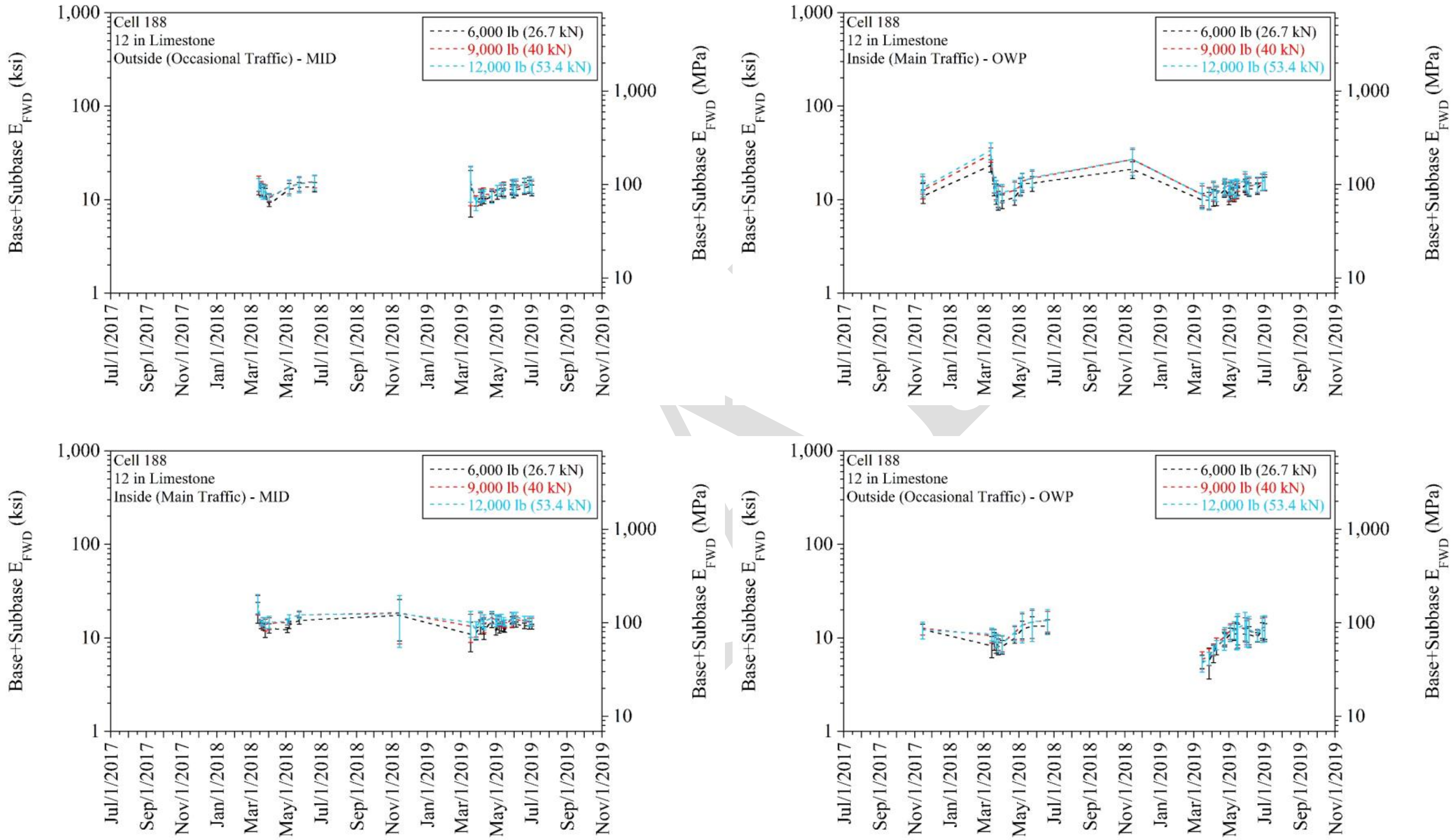

Cell 189 (12 in RCA+RAP) – base+subbase E_{FWD} (error bars represent one standard deviation of the data):

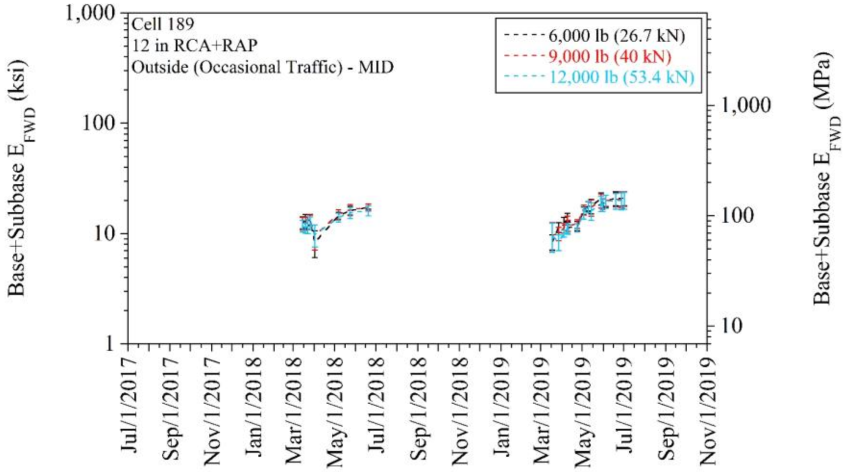

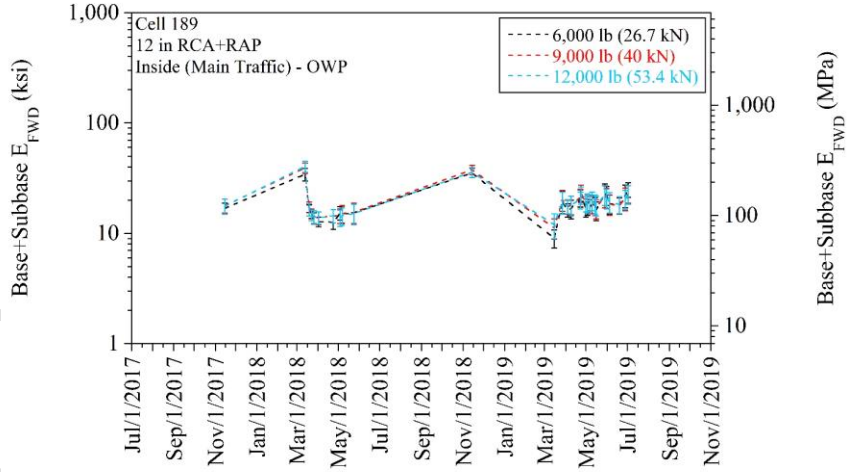

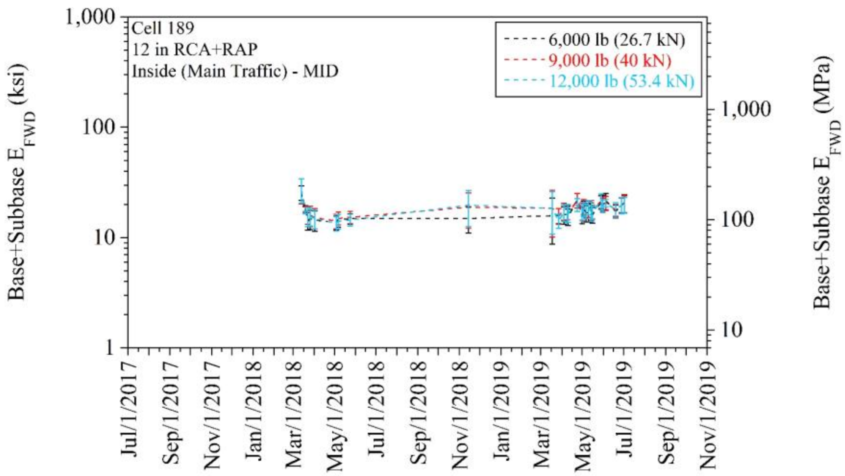

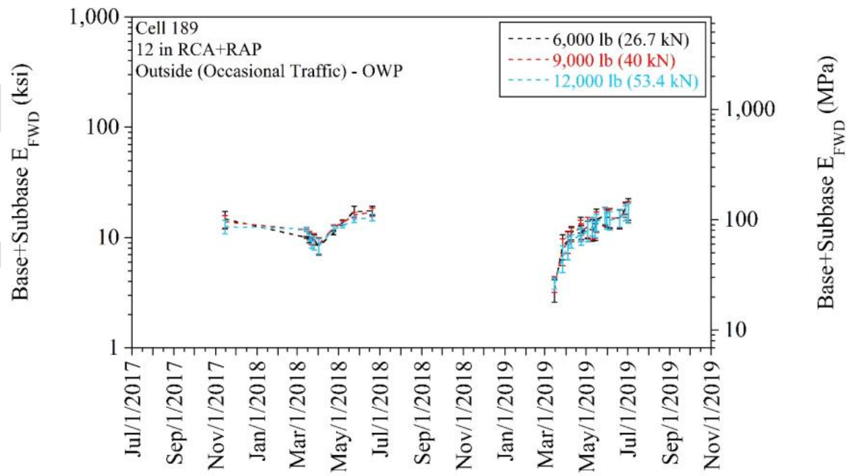

Cell 127 (18 in LSSB) – base+subbase E_{FWD} (error bars represent one standard deviation of the data):

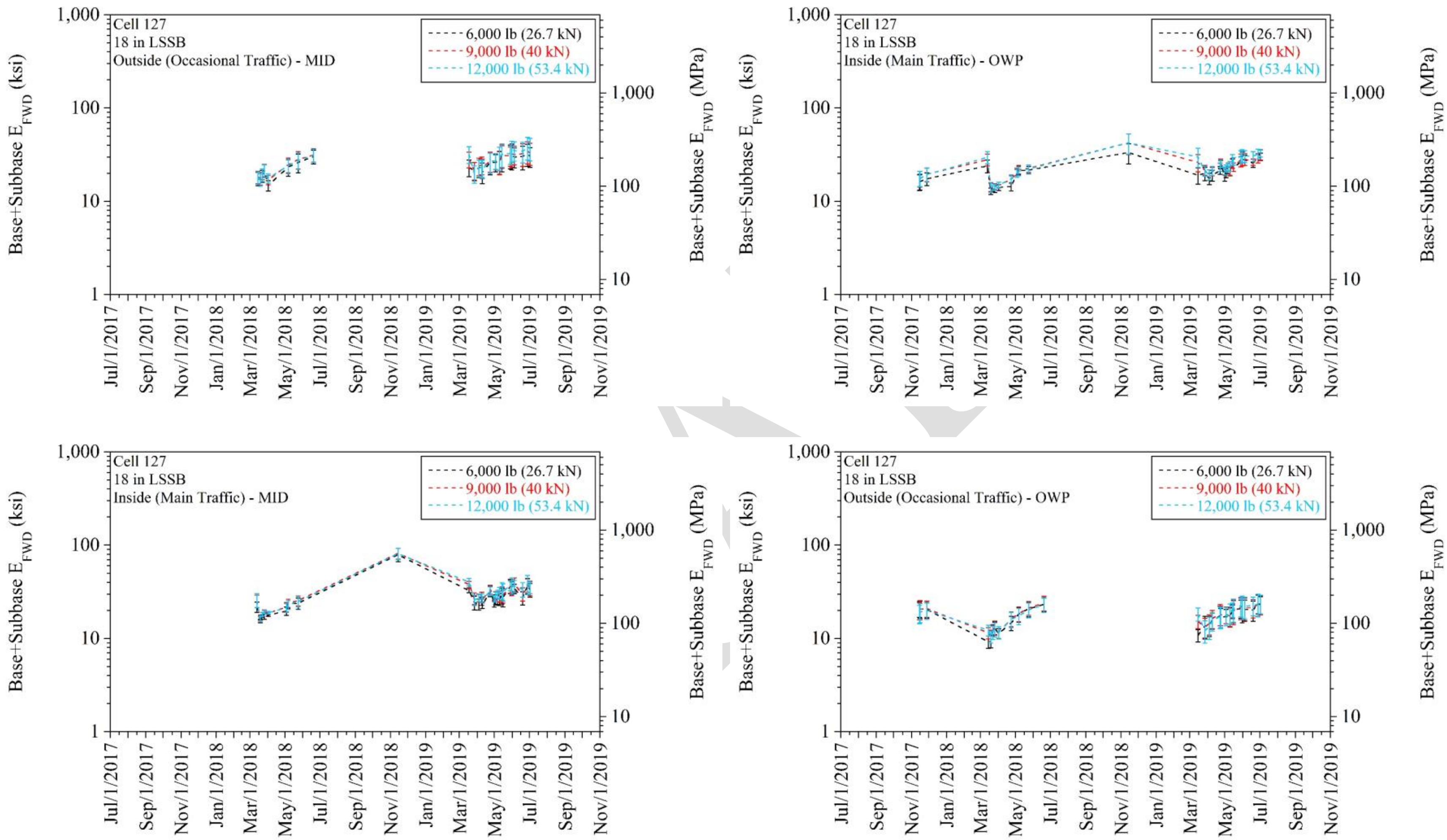

Cell 227 (18 in LSSB) – base+subbase E_{FWD} (error bars represent one standard deviation of the data):

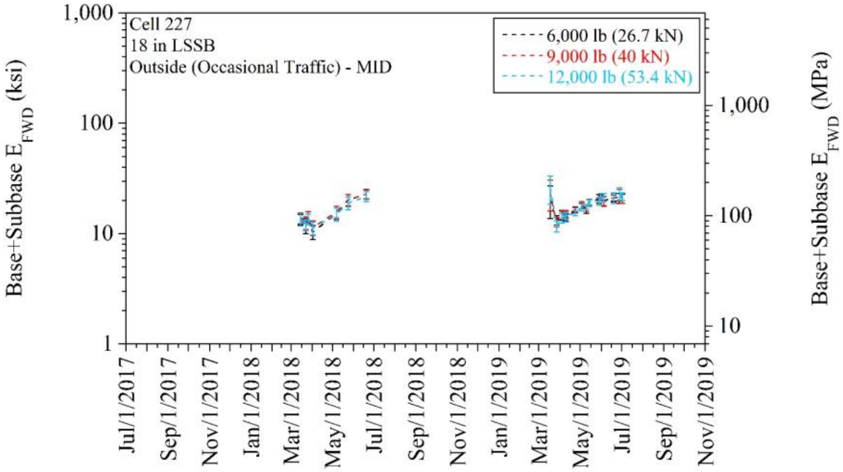

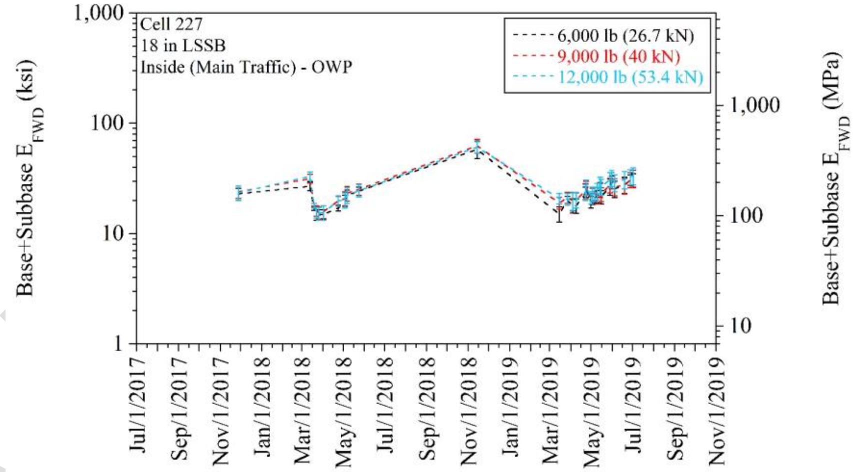

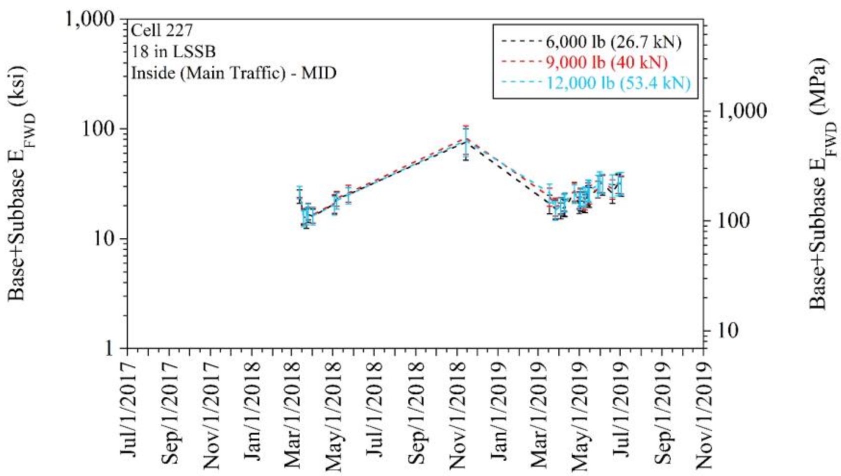

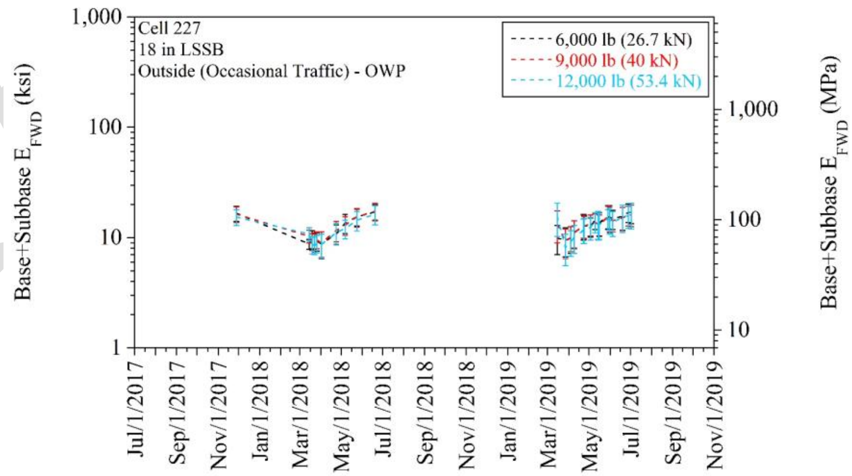

Cell 328 (9 in LSSB – TX) – base+subbase E_{FWD} (error bars represent one standard deviation of the data):

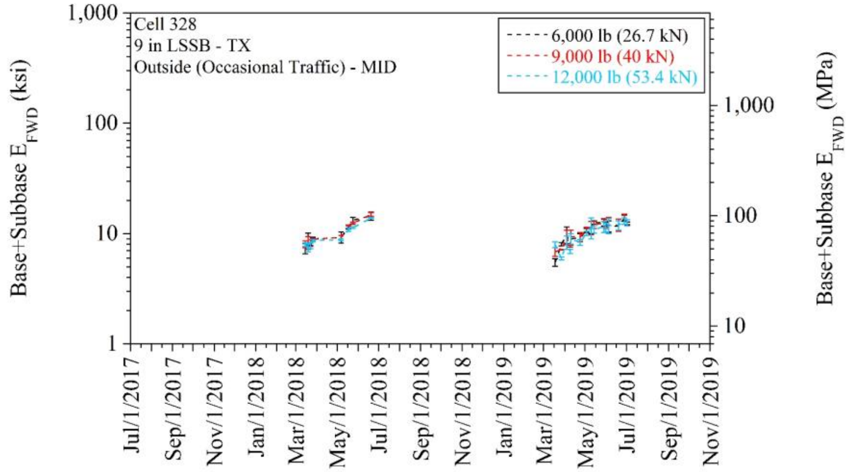

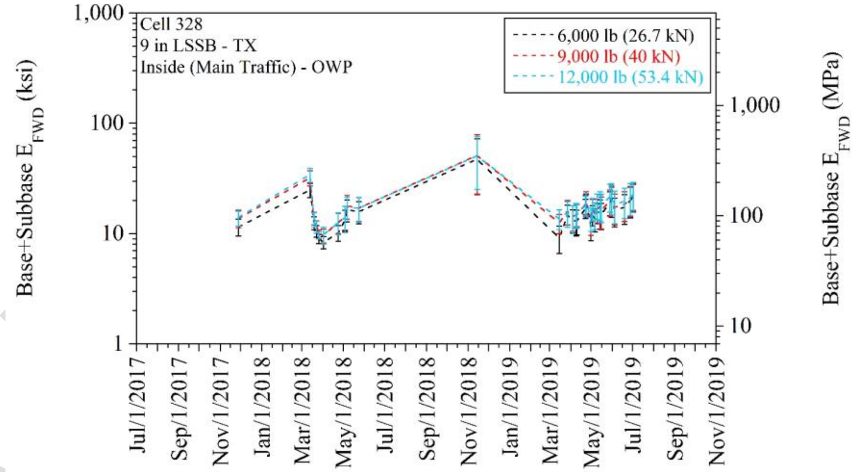

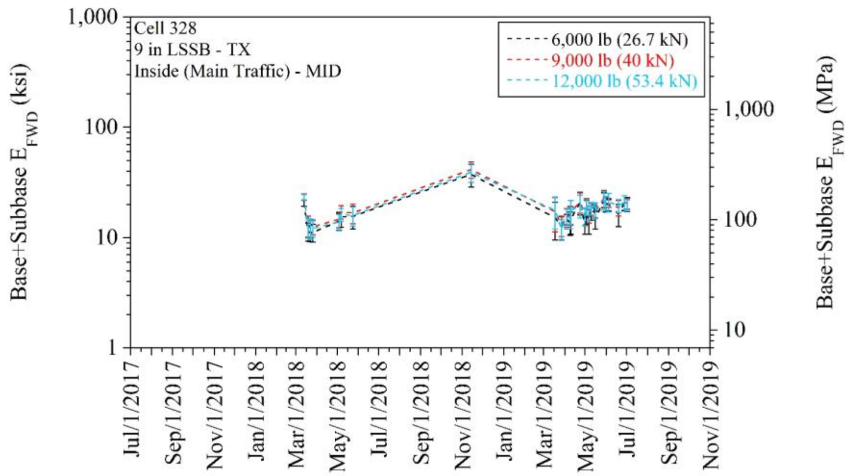

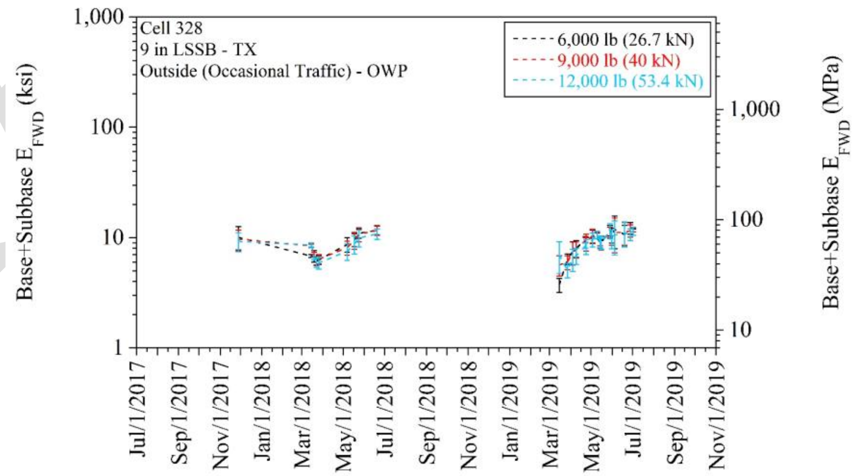

Cell 428 (9 in LSSB – TX+GT) – base+subbase E_{FWD} (error bars represent one standard deviation of the data):

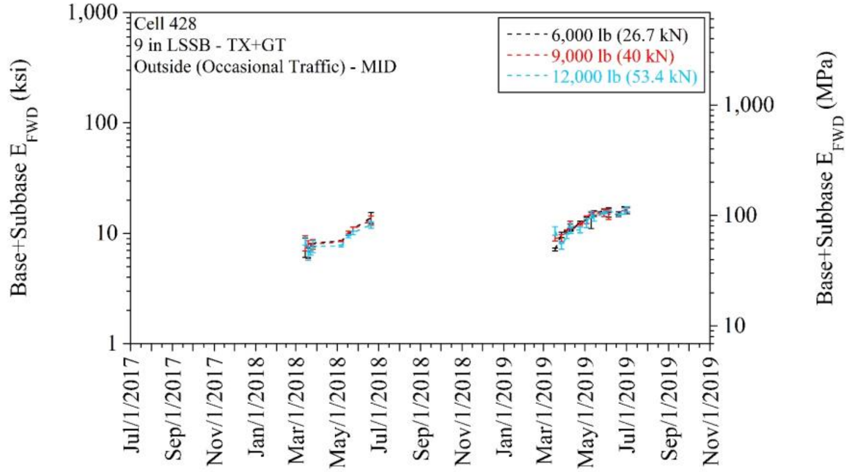

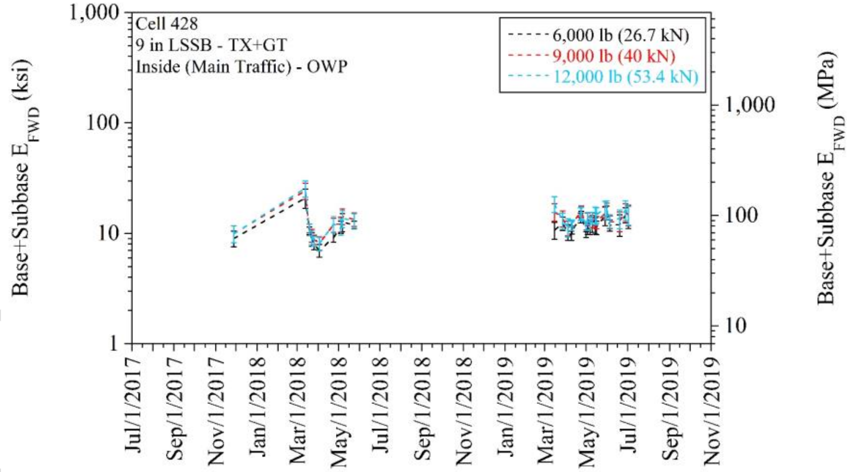

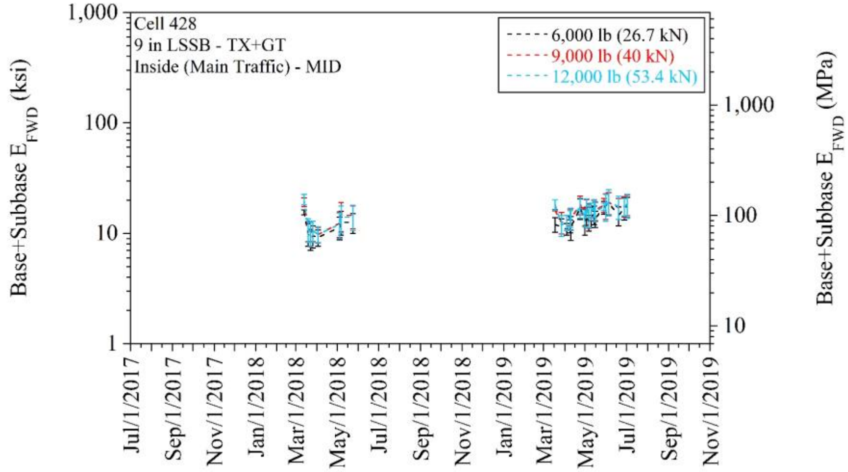

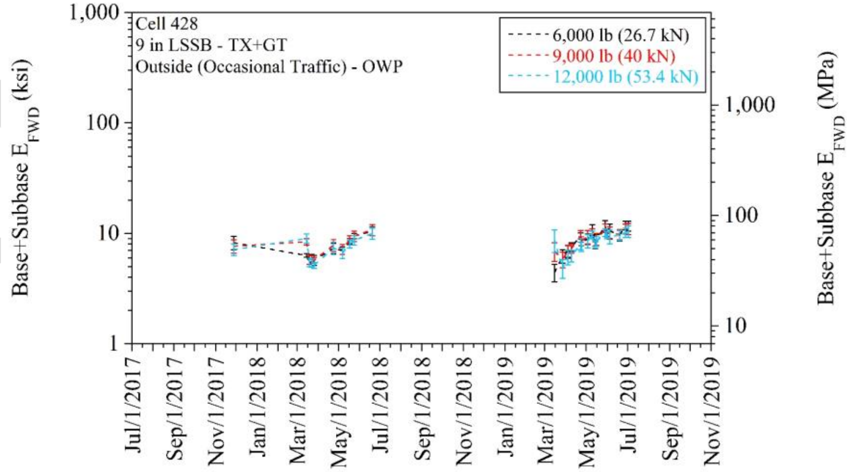

Cell 528 (9 in LSSB – BX+GT) – base+subbase E_{FWD} (error bars represent one standard deviation of the data):

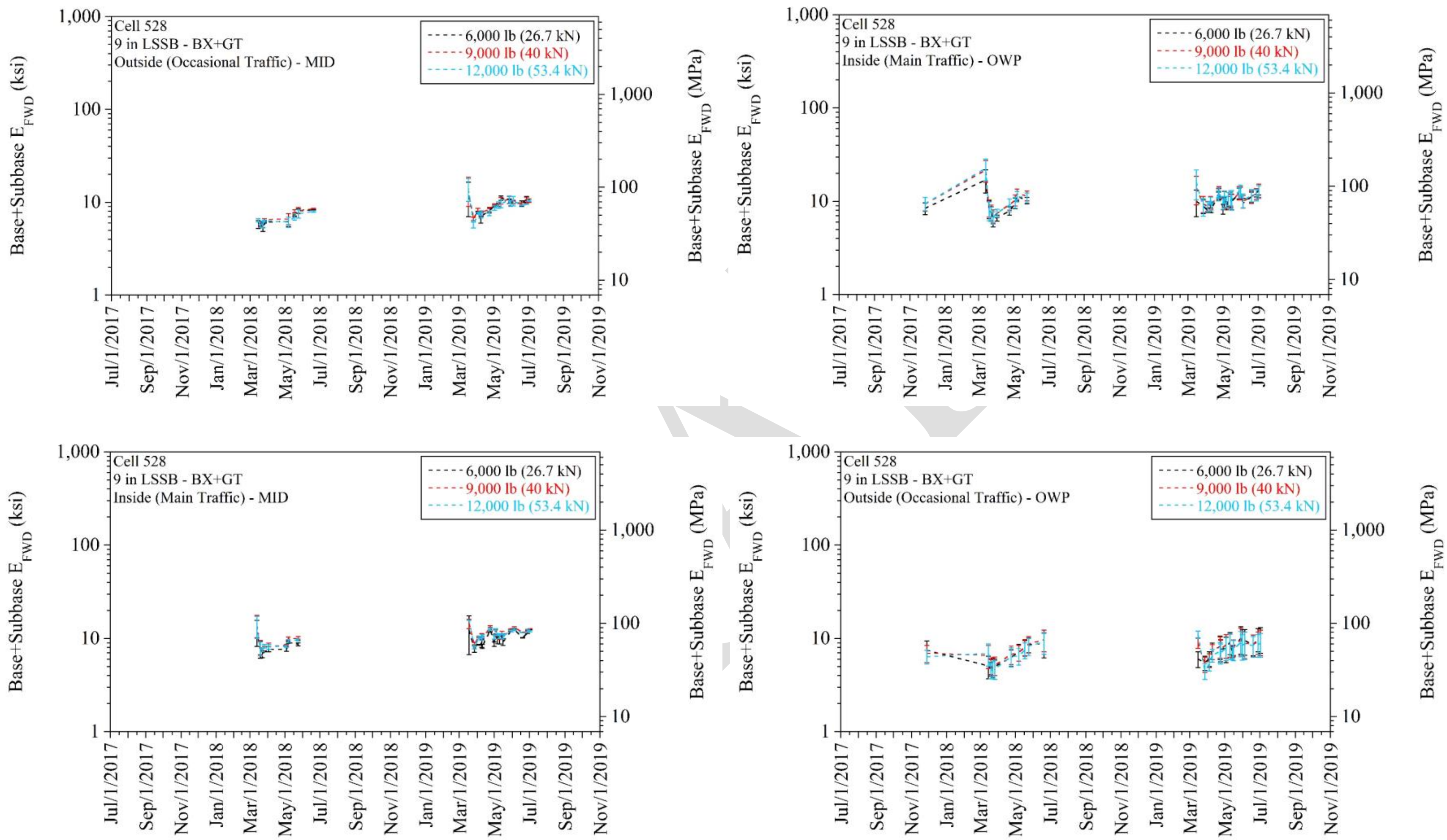

Cell 628 (9 in LSSB – BX) – base+subbase E_{FWD} (error bars represent one standard deviation of the data):

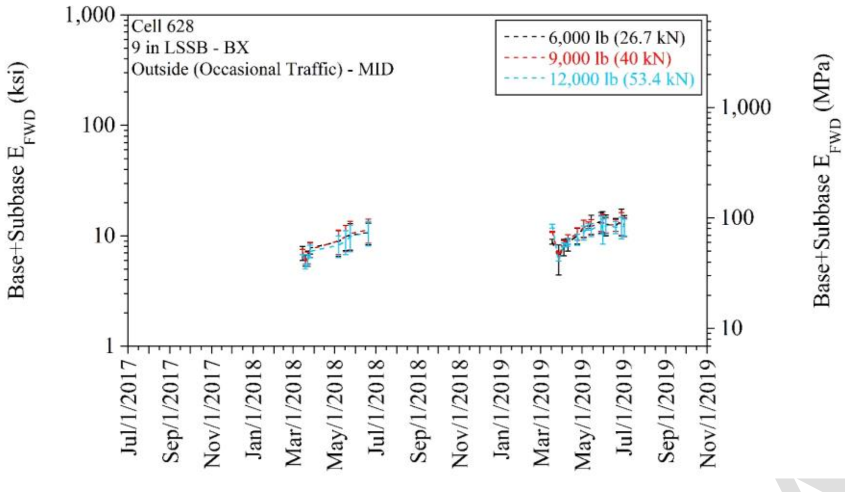

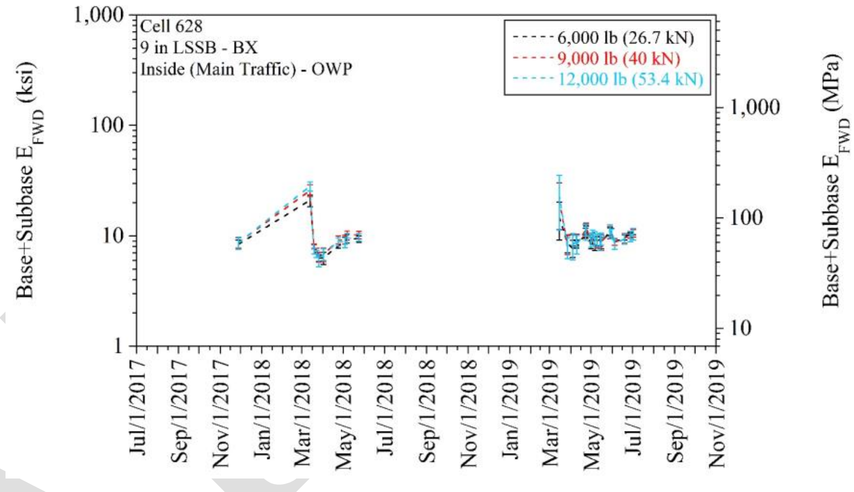

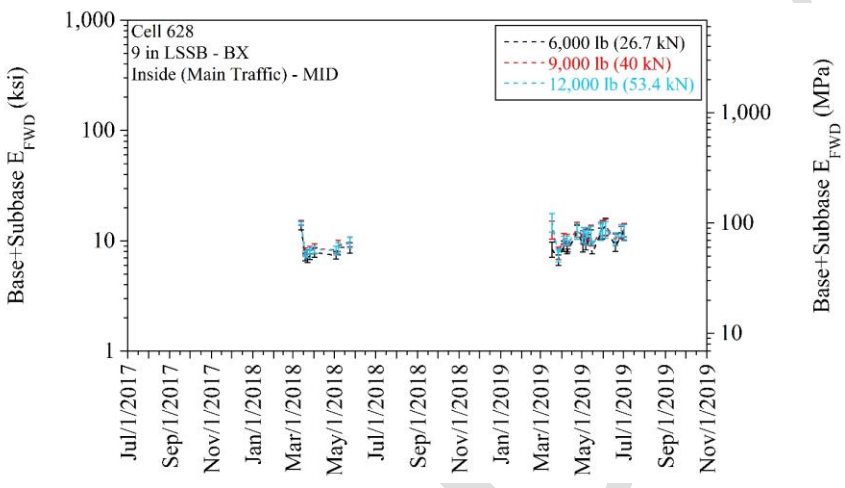

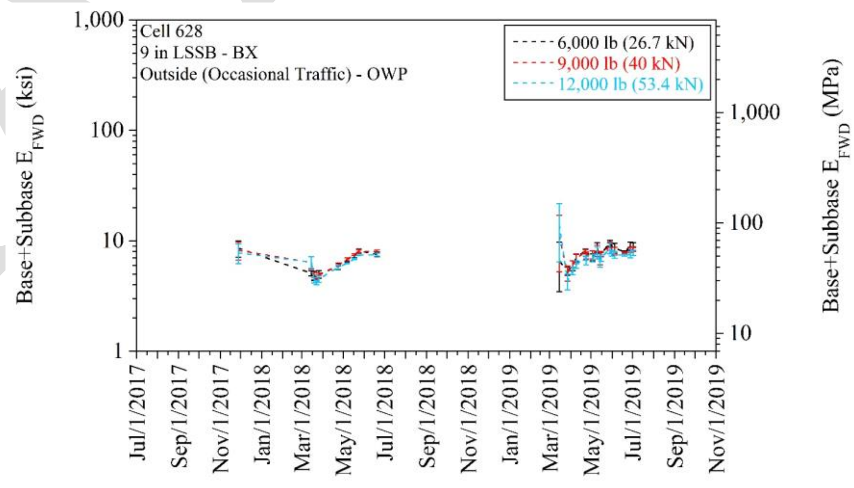

Cell 728 (9 in LSSB) – base+subbase E_{FWD} (error bars represent one standard deviation of the data):

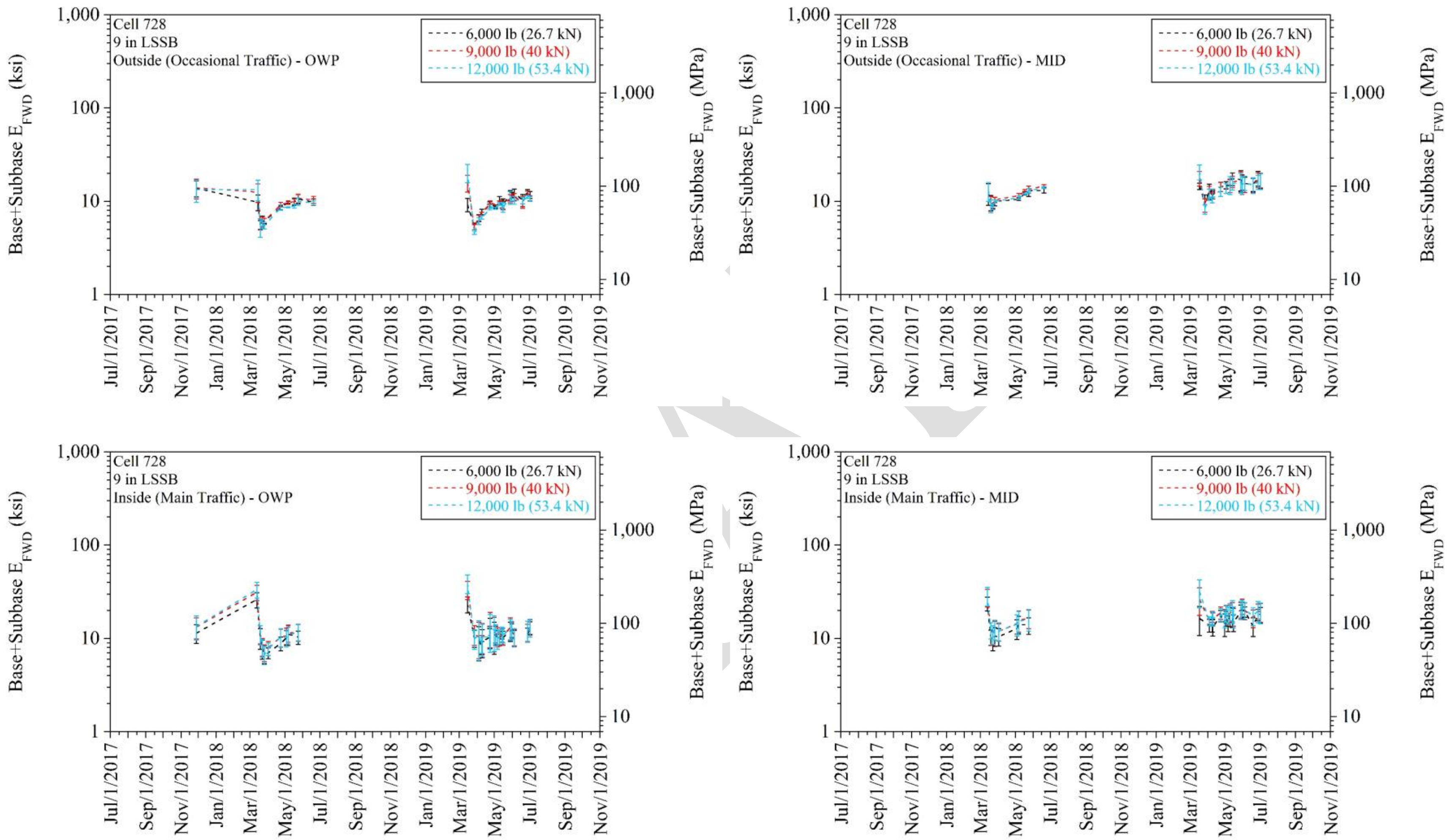

APPENDIX I. SUBGRADE E_{FWD} VALUES AT 6,000 LB (26.7 KN), 9,000 LB (40 KN), AND 12,000 LB (53.4 KN) FOR EACH CELL

Cell 185 (12 in coarse RCA) – subgrade E_{FWD} (error bars represent one standard deviation of the data):

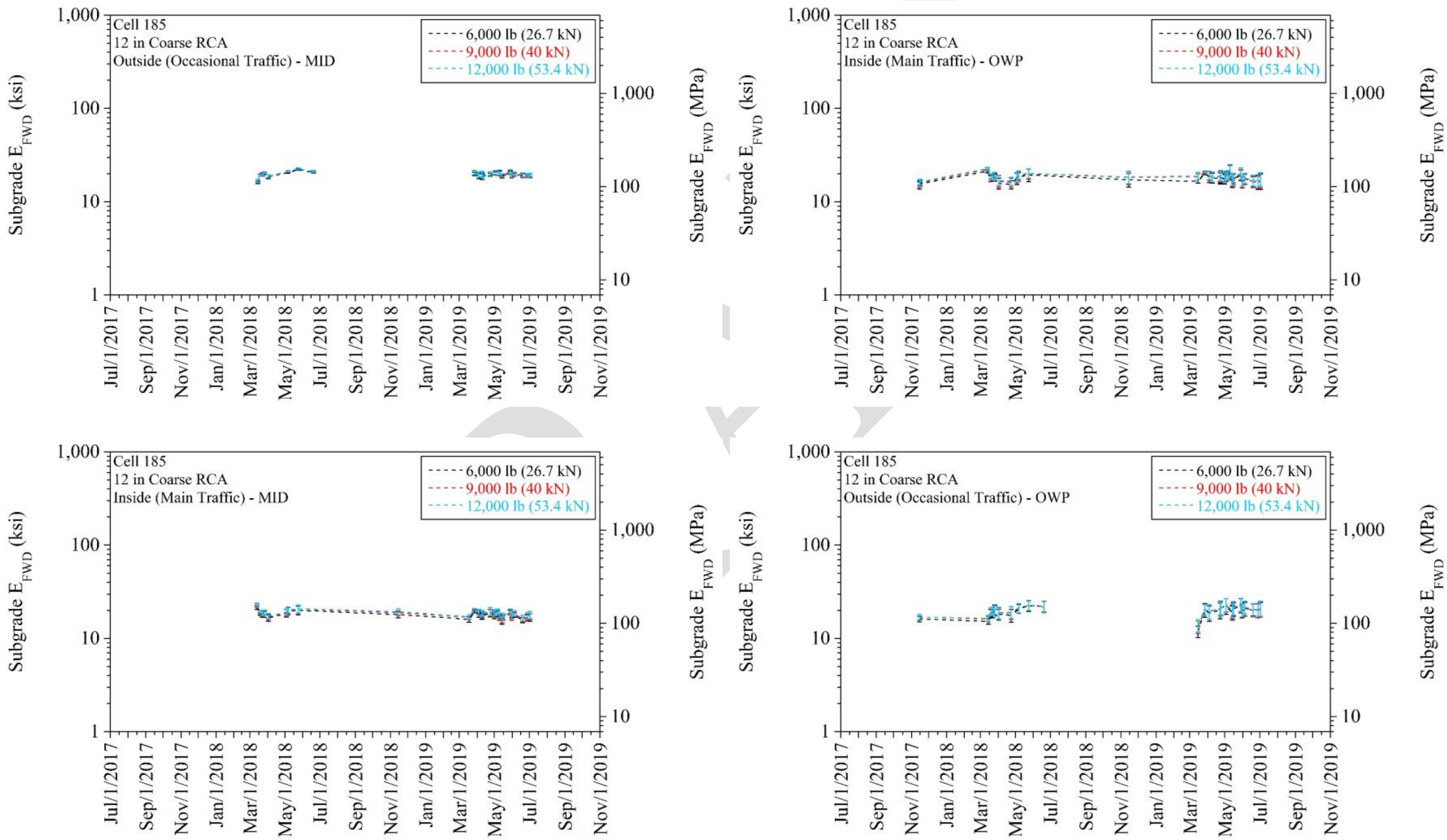

Cell 186 (12 in fine RCA) – subgrade E_{FWD} (error bars represent one standard deviation of the data):

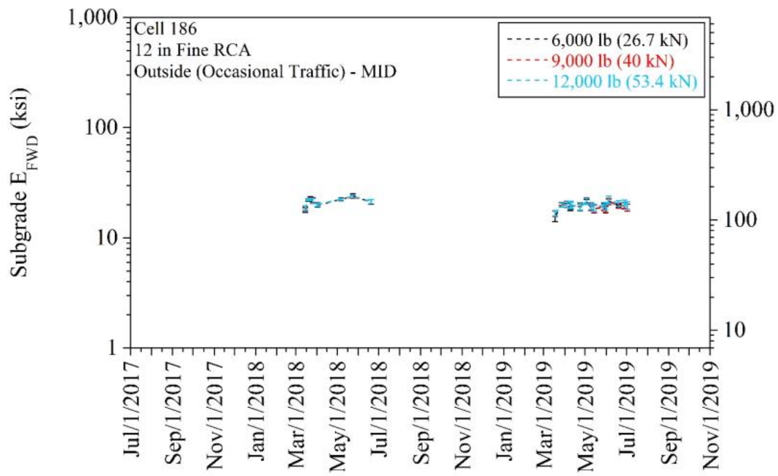

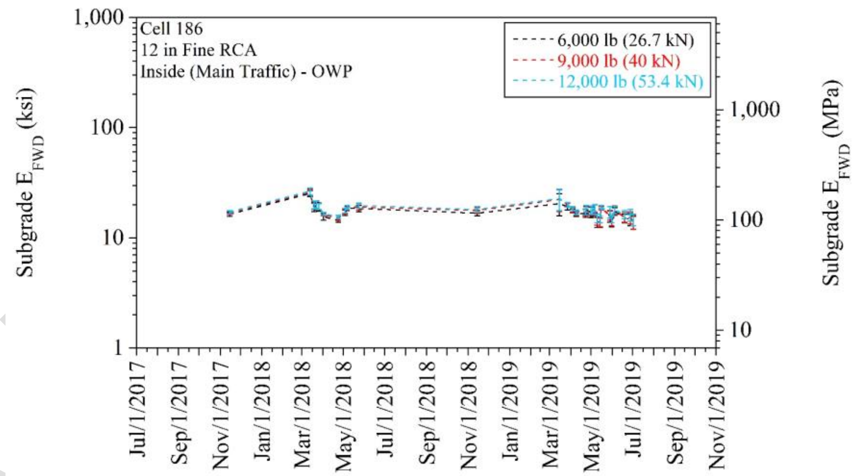

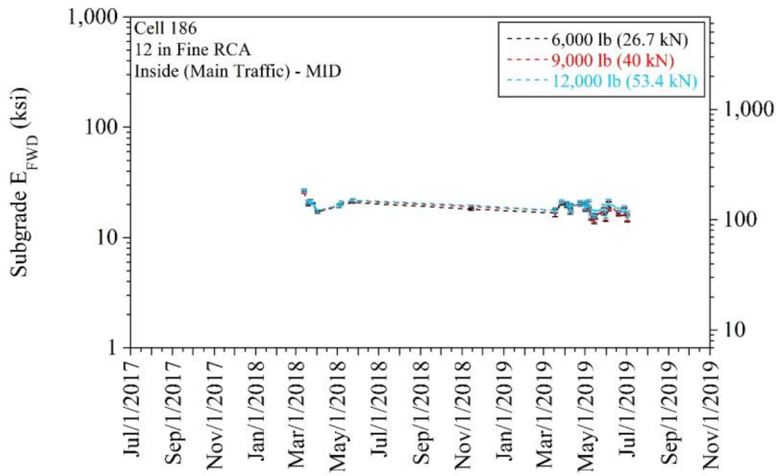

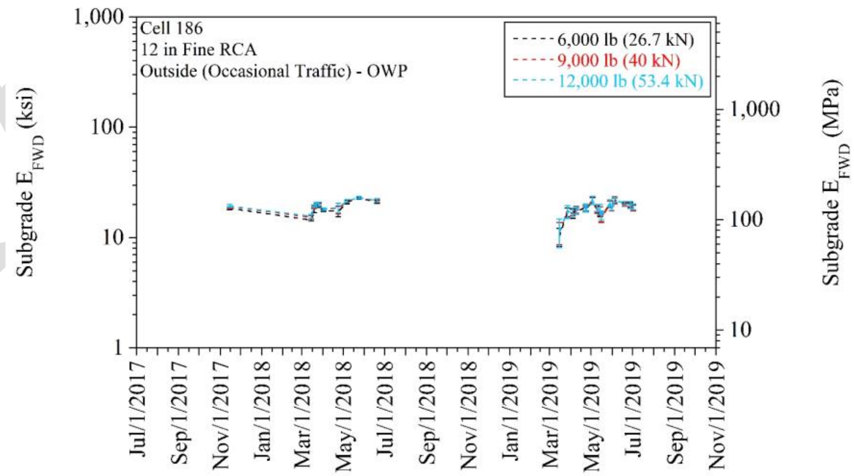

Cell 188 (12 in limestone) – subgrade E_{FWD} (error bars represent one standard deviation of the data):

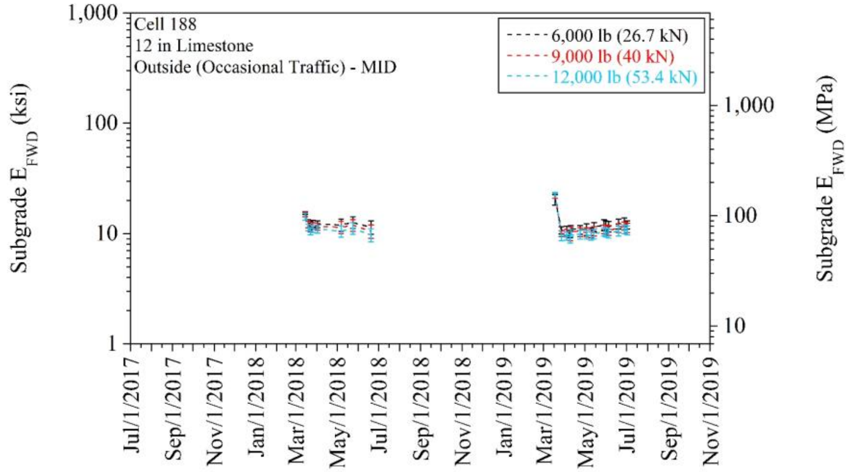

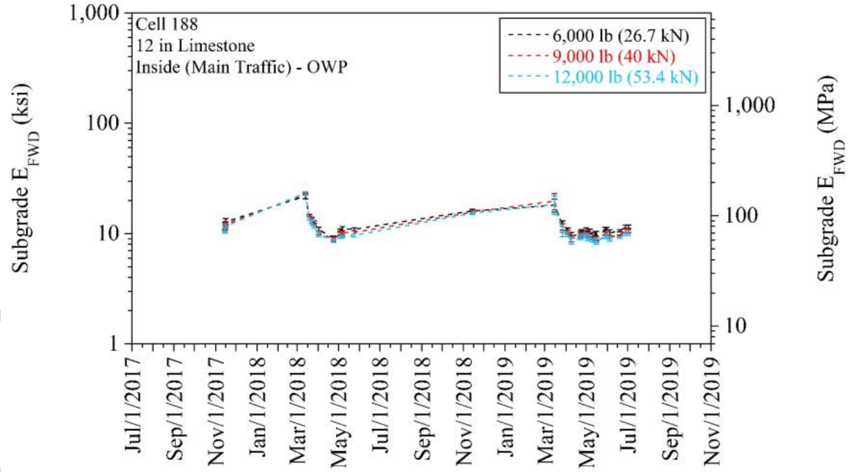

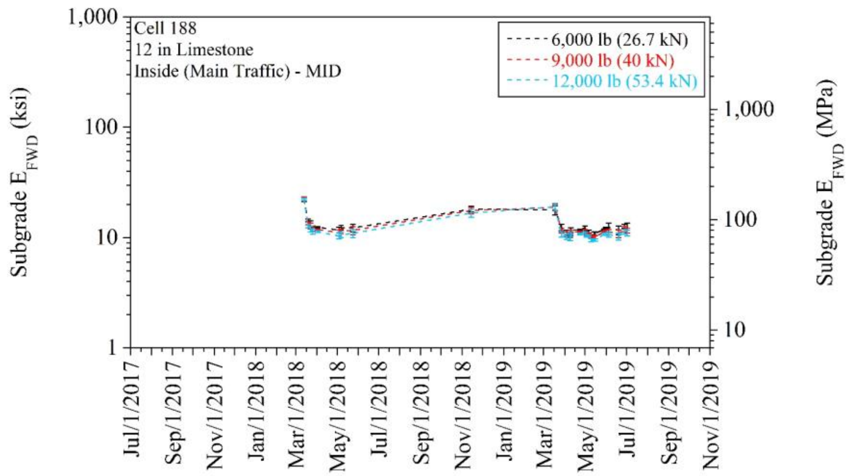

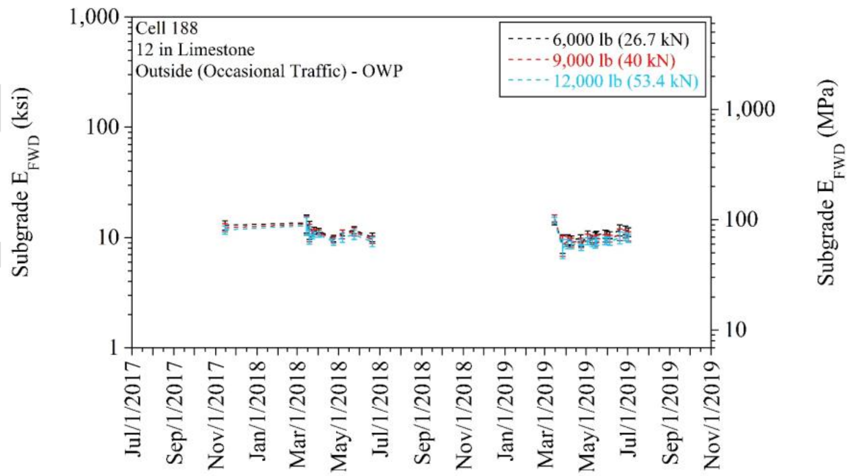

Cell 189 (12 in RCA+RAP) – subgrade E_{FWD} (error bars represent one standard deviation of the data):

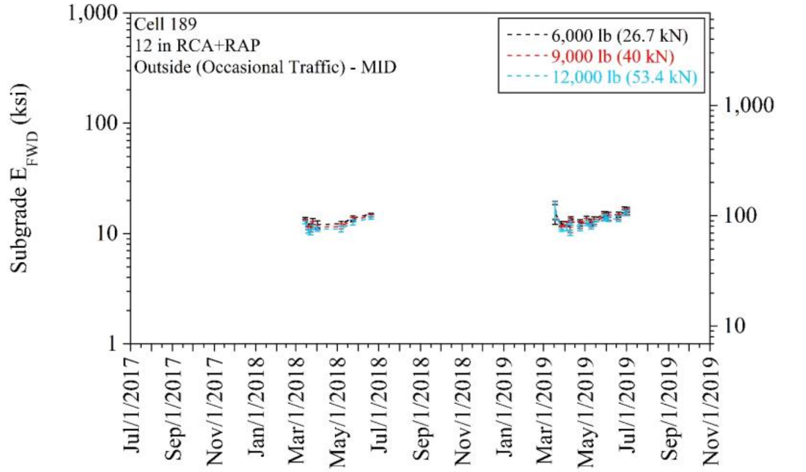

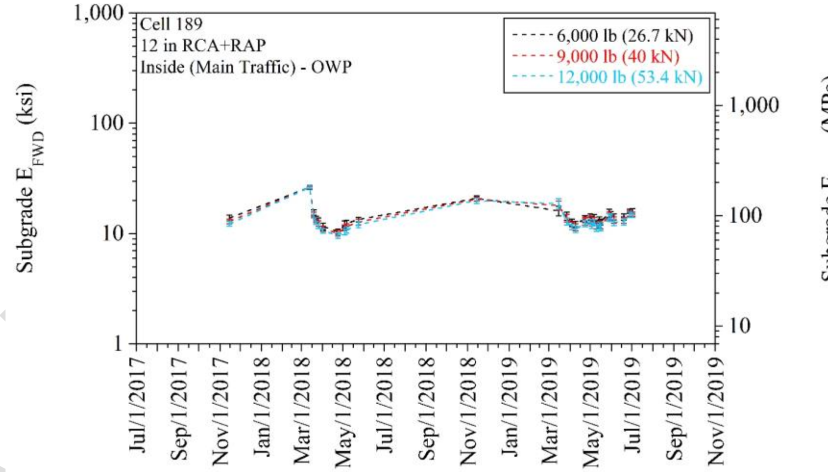

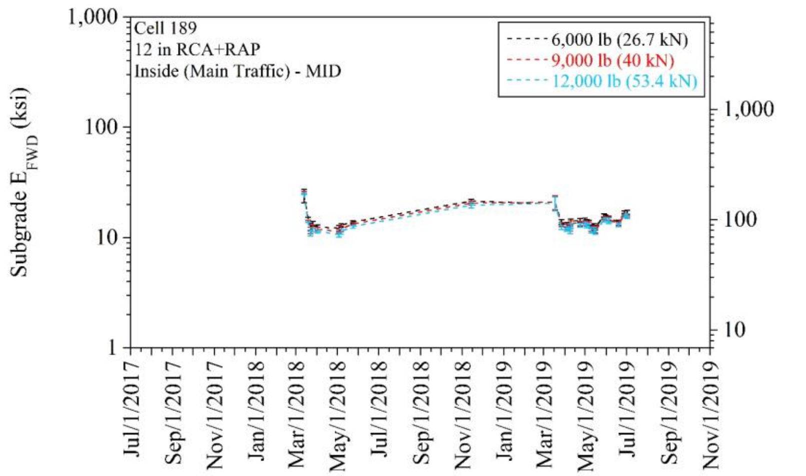

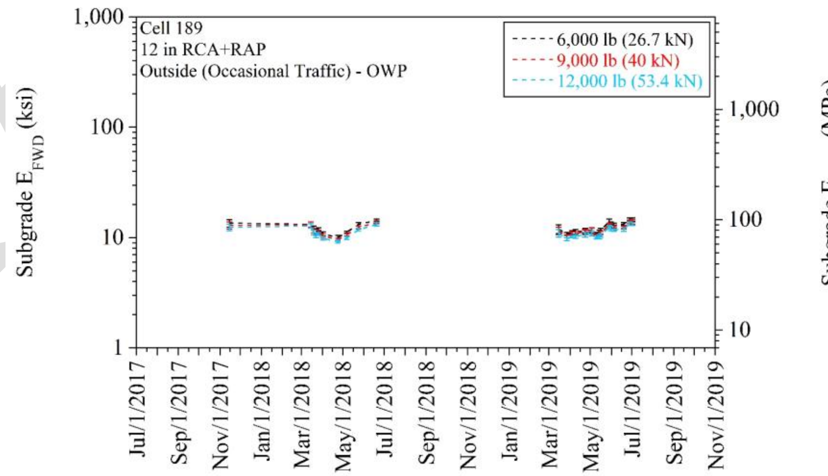

Cell 127 (18 in LSSB) – subgrade E_{FWD} (error bars represent one standard deviation of the data):

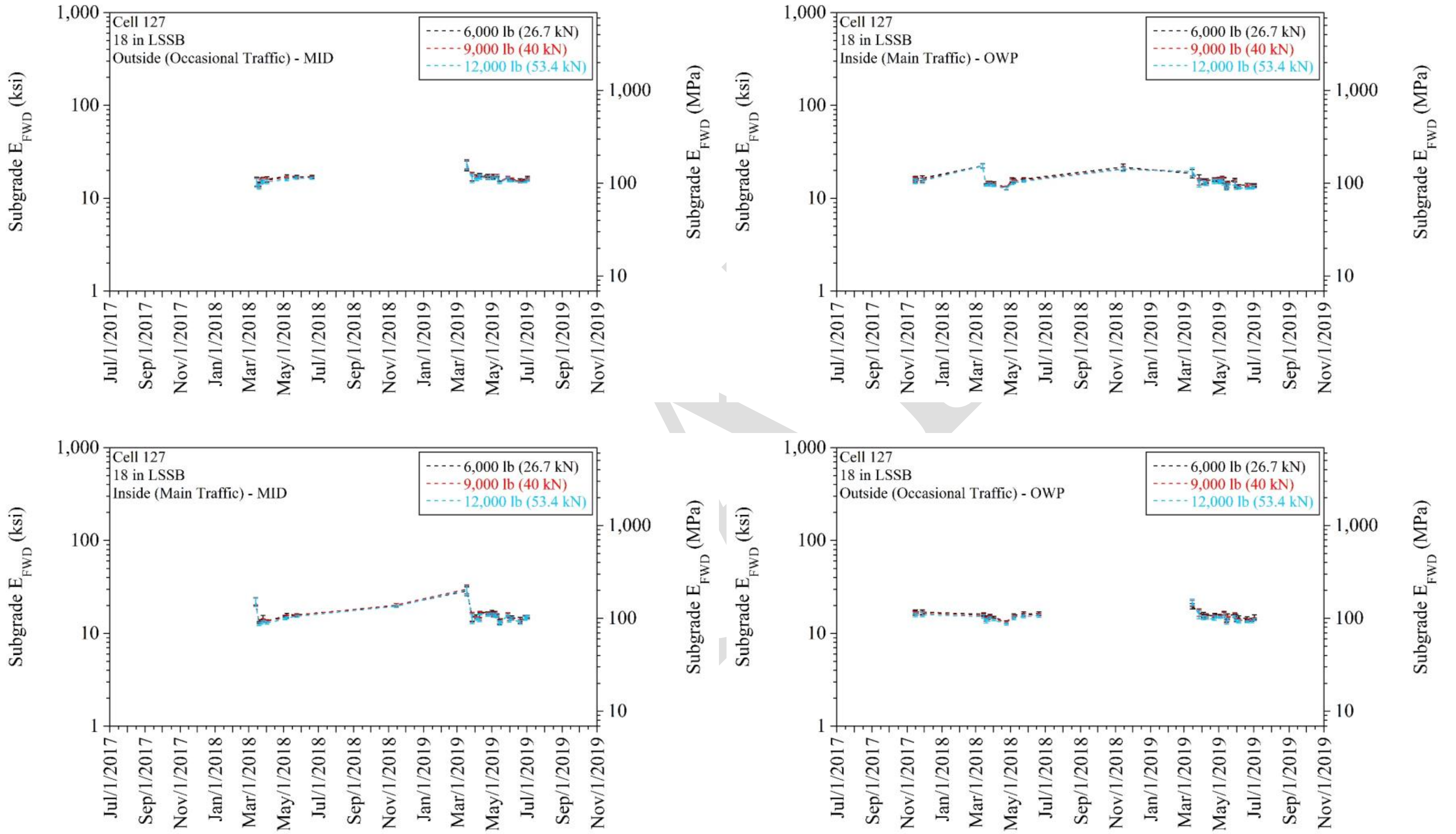

Cell 227 (18 in LSSB) – subgrade E_{FWD} (error bars represent one standard deviation of the data):

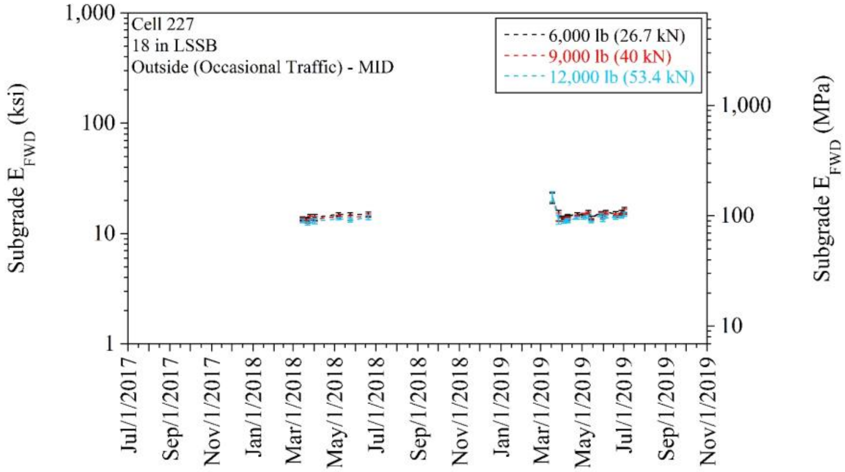

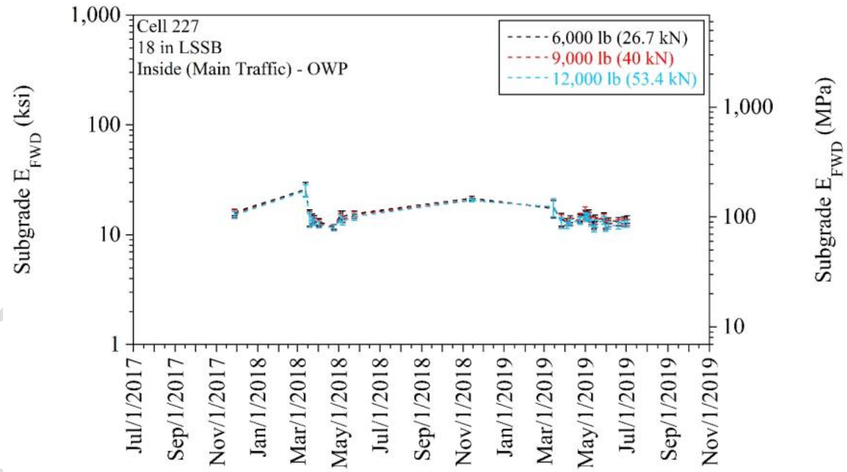

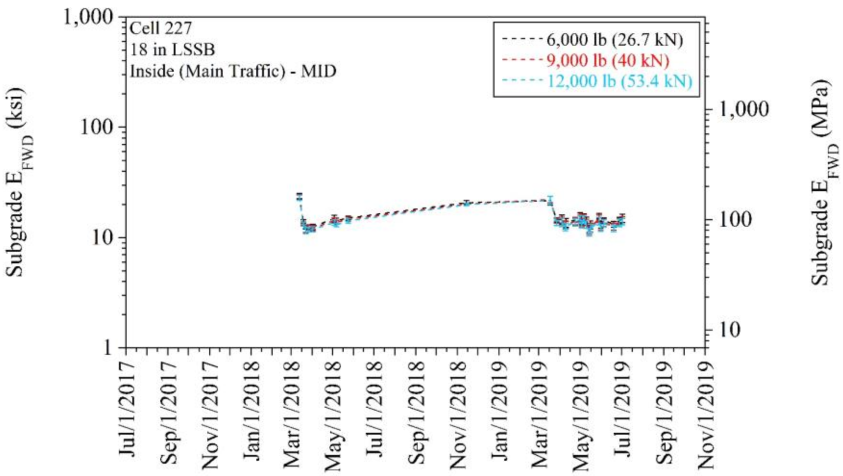

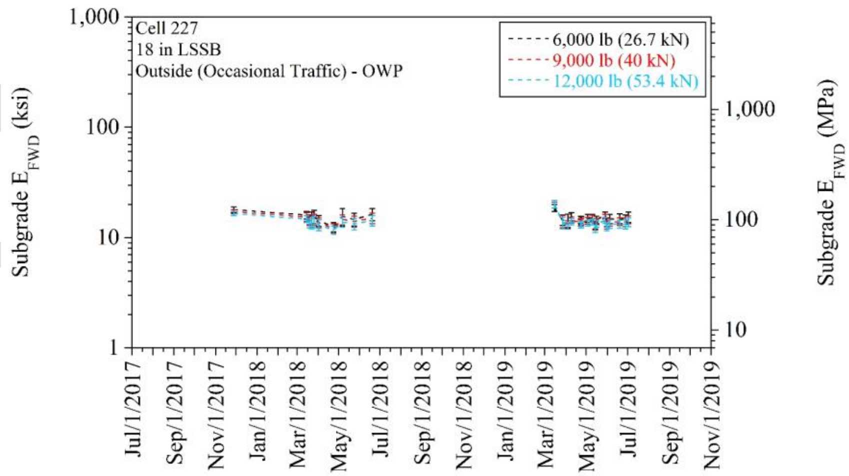

Cell 328 (9 in LSSB – TX) – subgrade E_{FWD} (error bars represent one standard deviation of the data):

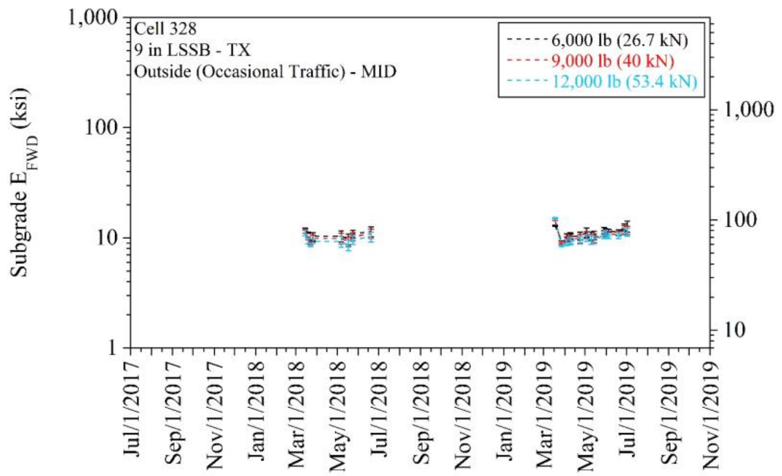

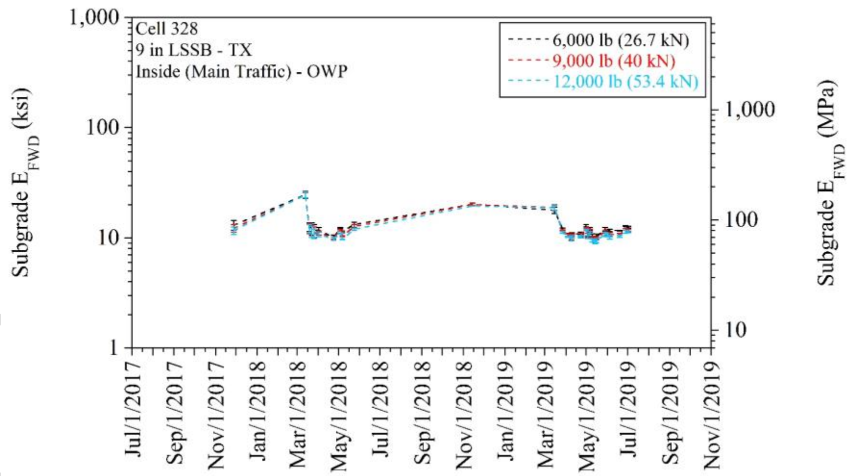

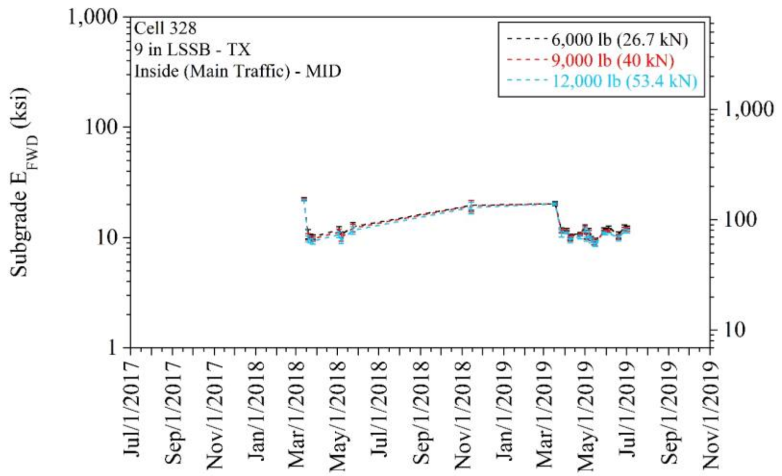

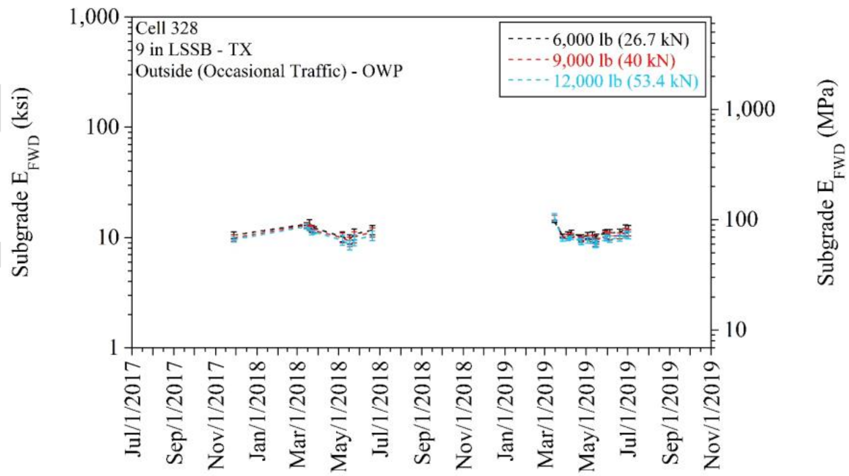

Cell 428 (9 in LSSB – TX+GT) – subgrade E_{FWD} (error bars represent one standard deviation of the data):

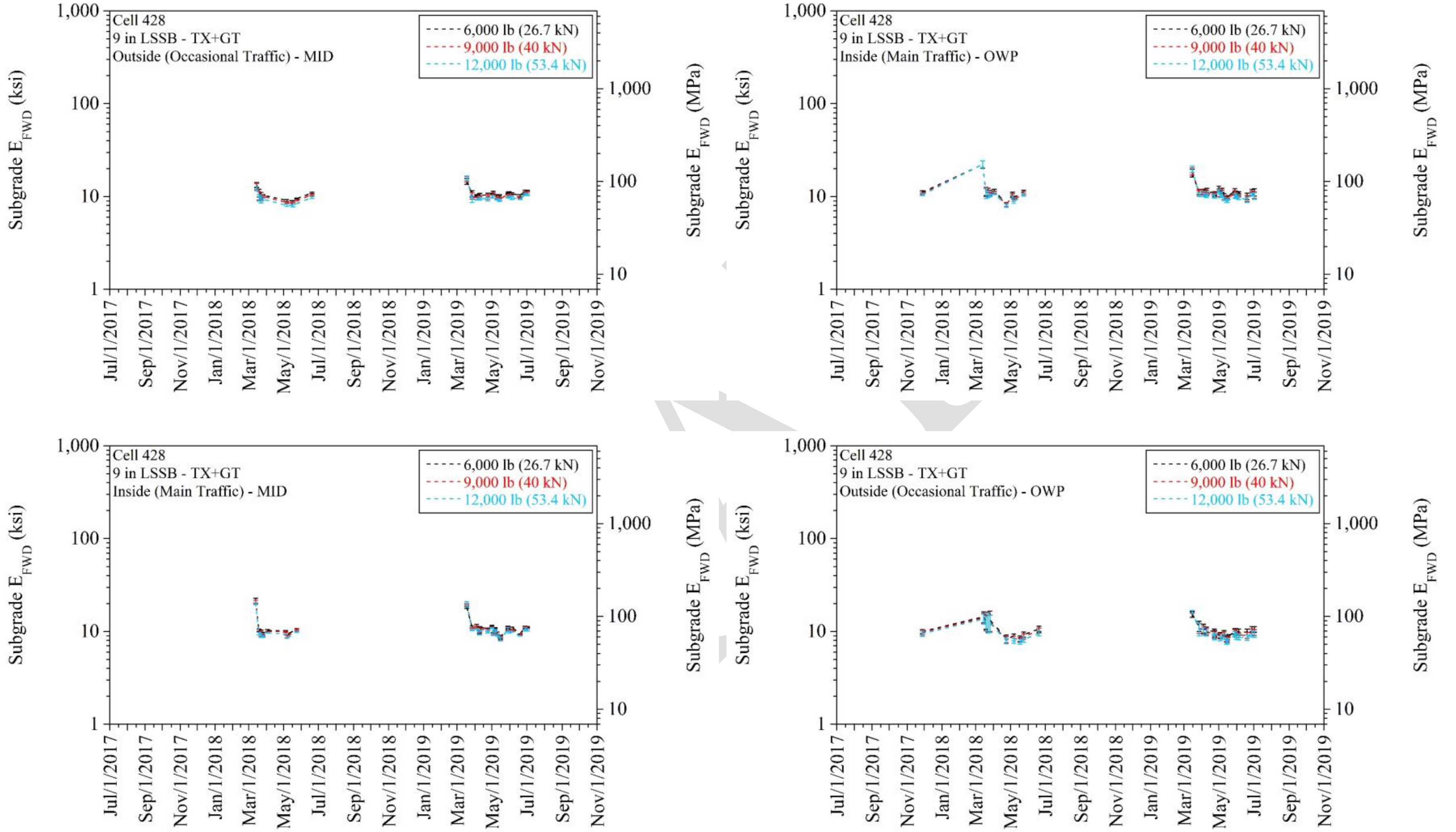

Cell 528 (9 in LSSB – BX+GT) – subgrade E_{FWD} (error bars represent one standard deviation of the data):

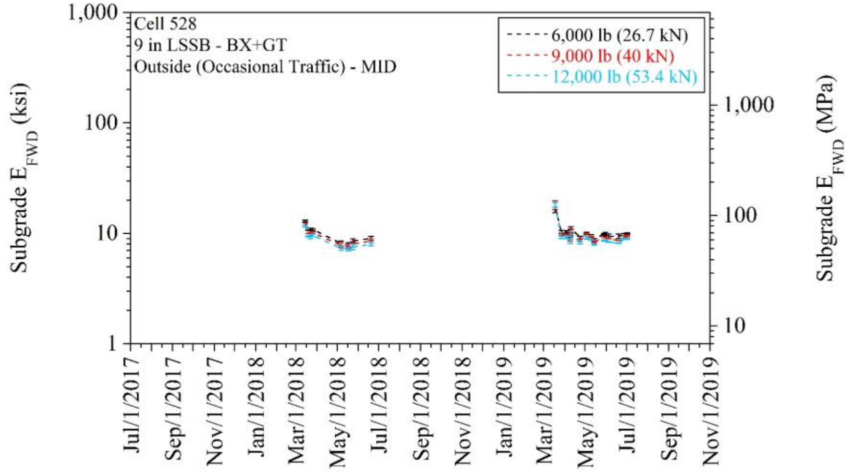

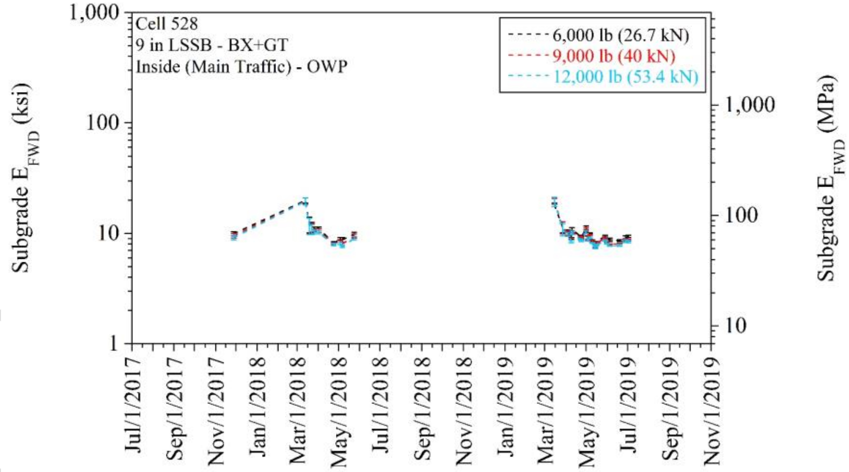

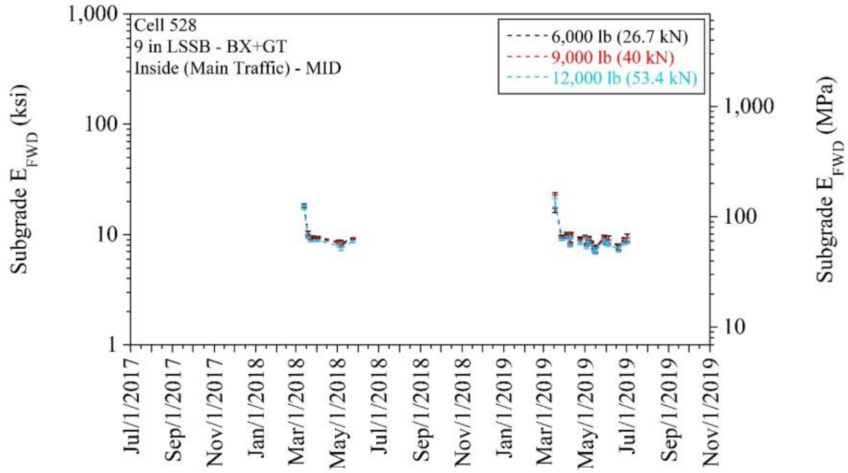

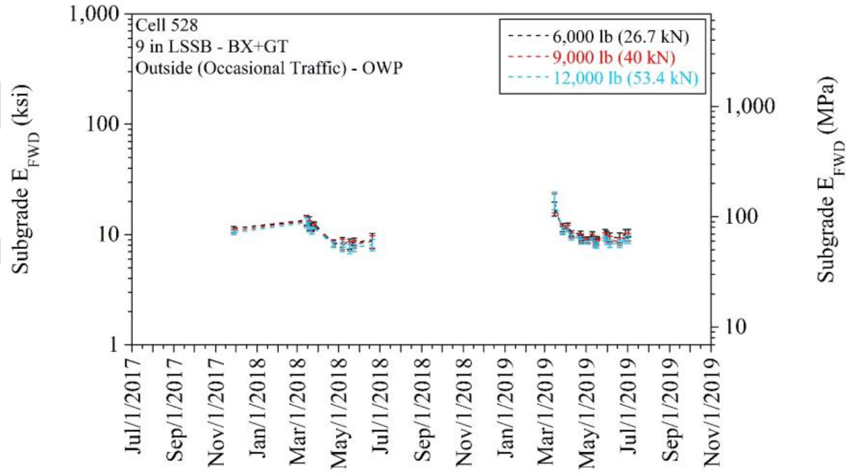

Cell 628 (9 in LSSB – BX) – subgrade E_{FWD} (error bars represent one standard deviation of the data):

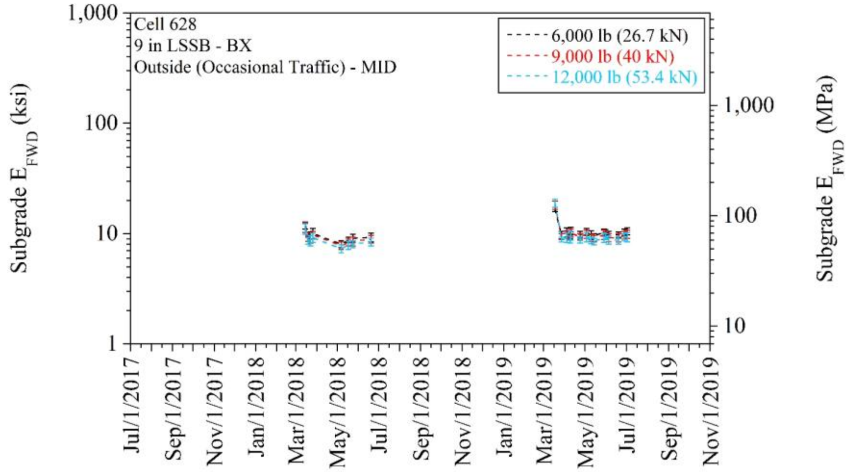

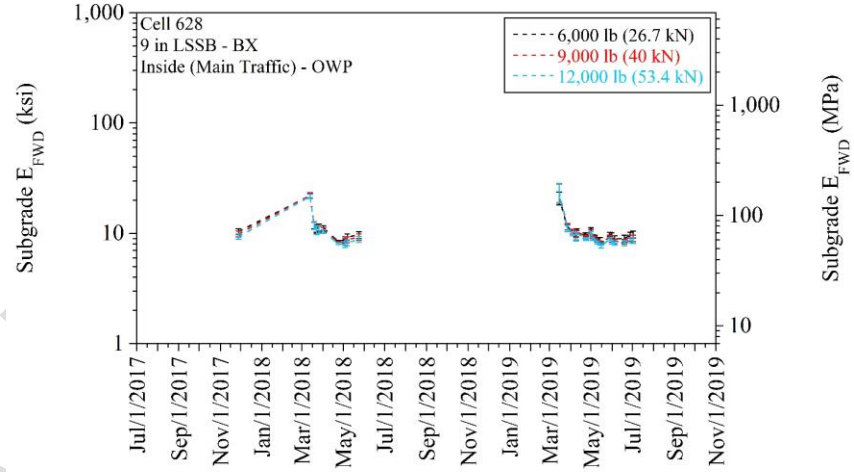

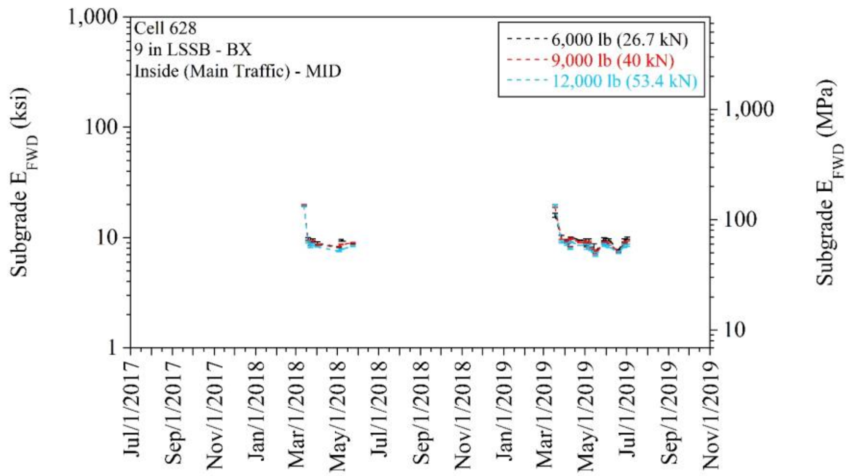

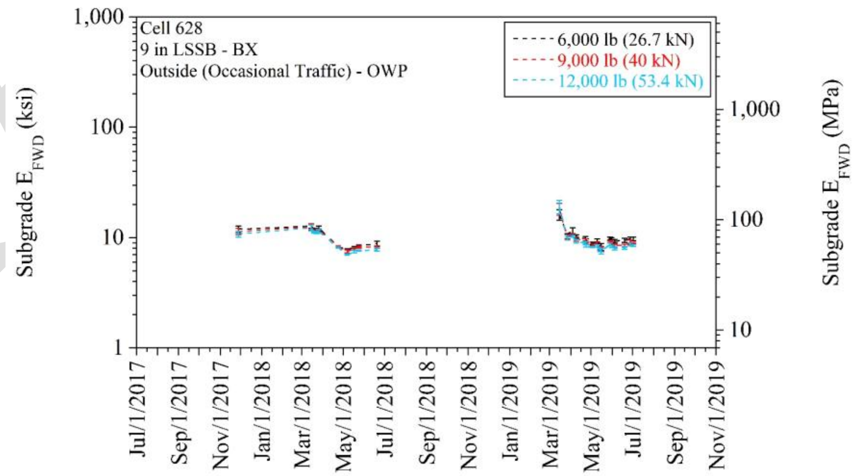

Cell 728 (9 in LSSB) – subgrade E_{FWD} (error bars represent one standard deviation of the data):

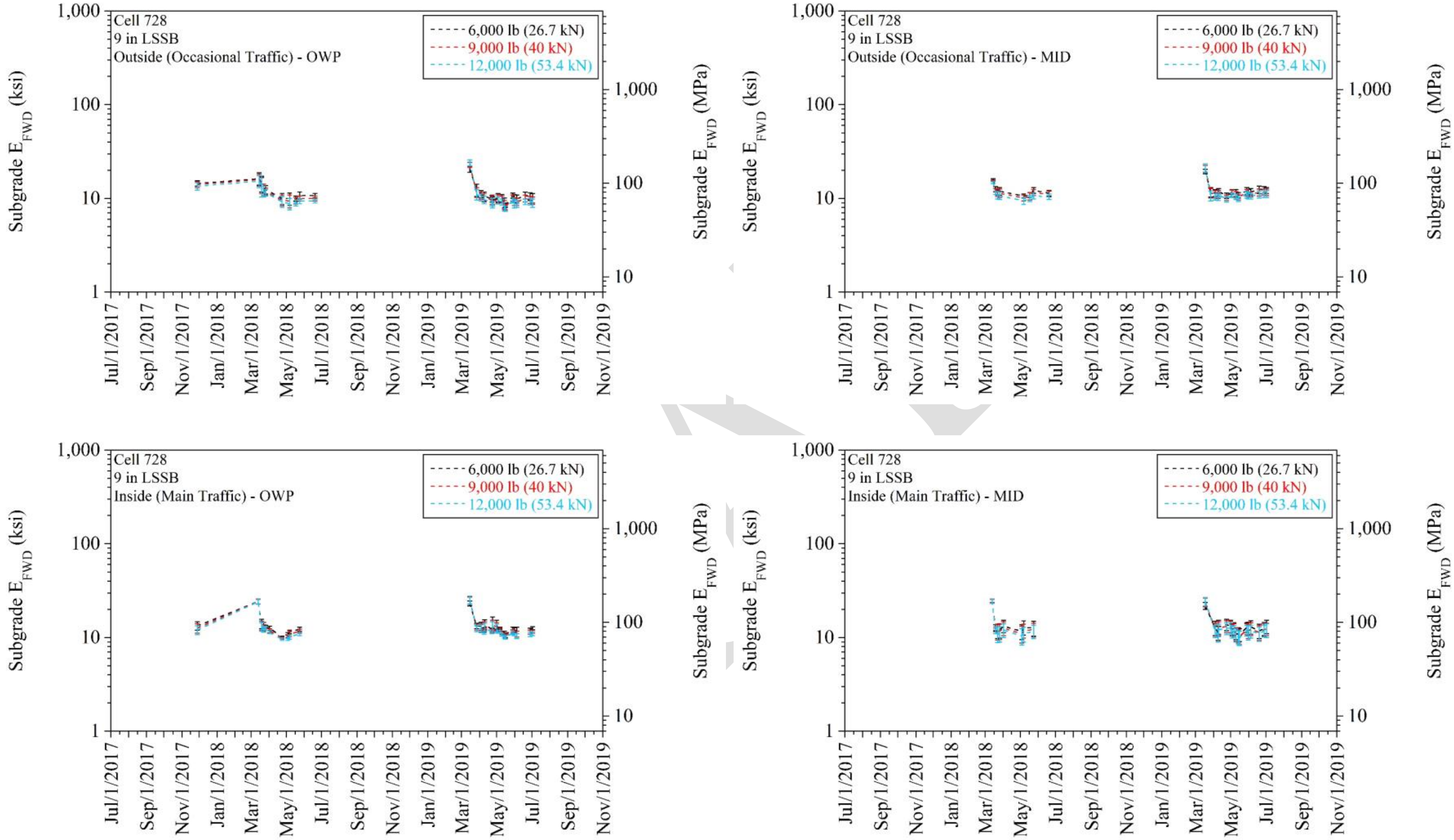

APPENDIX J. MAXIMUM DEFLECTIONS FOR DIFFERENT TEST LOCATIONS AT 9,000 LB (40 KN) FOR EACH CELL

(error bars represent one standard deviation of the data)

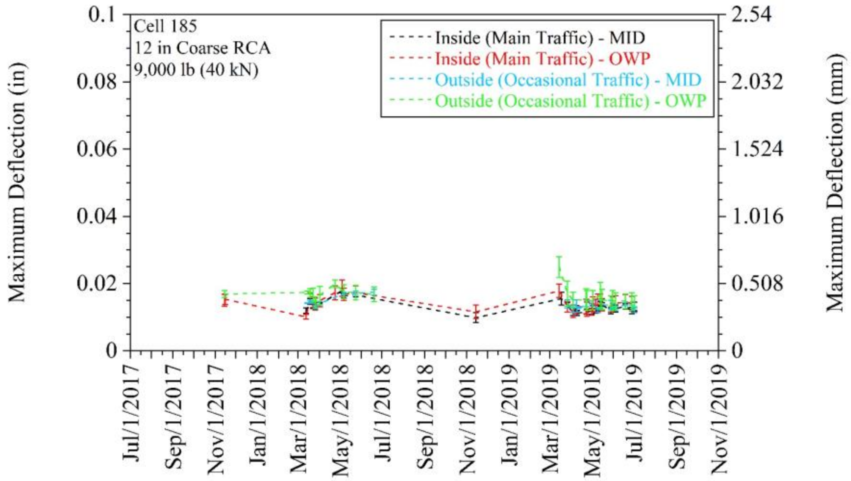

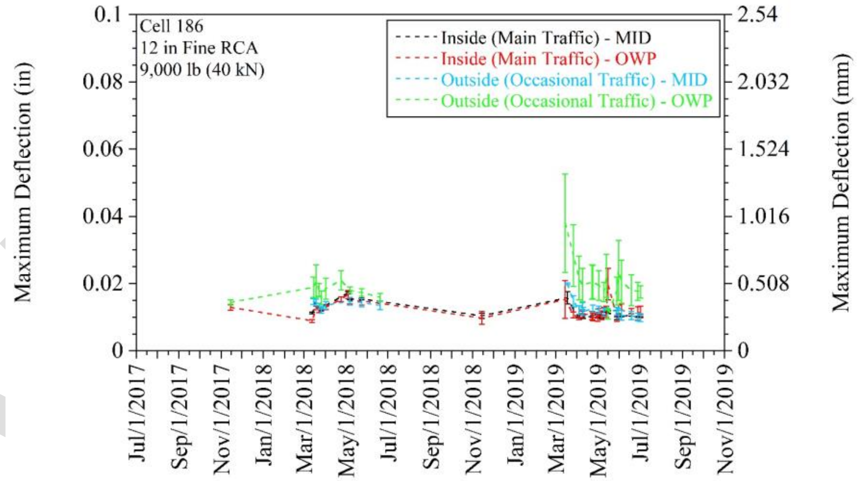

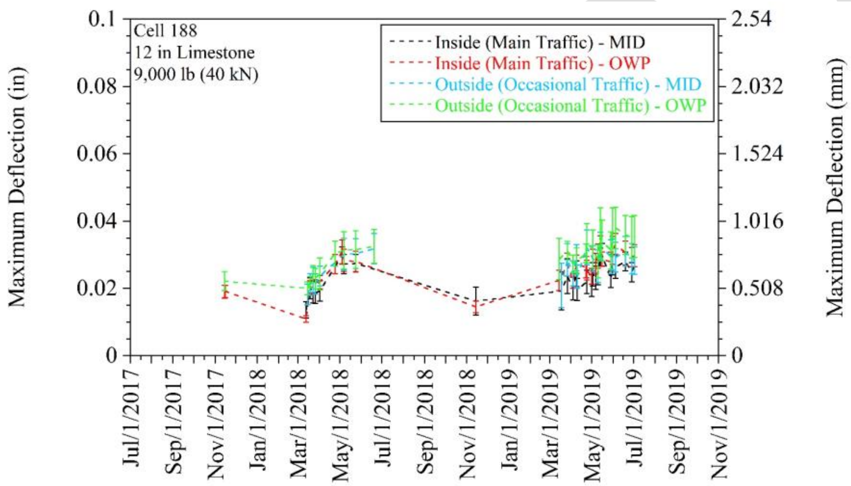

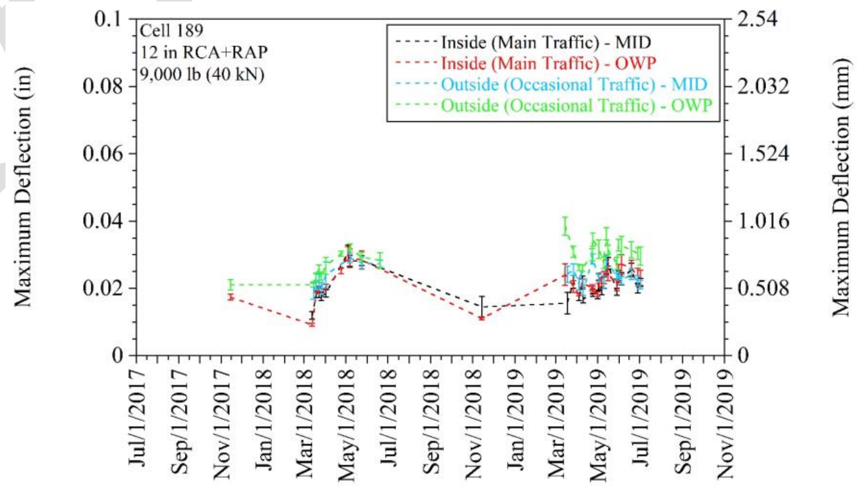

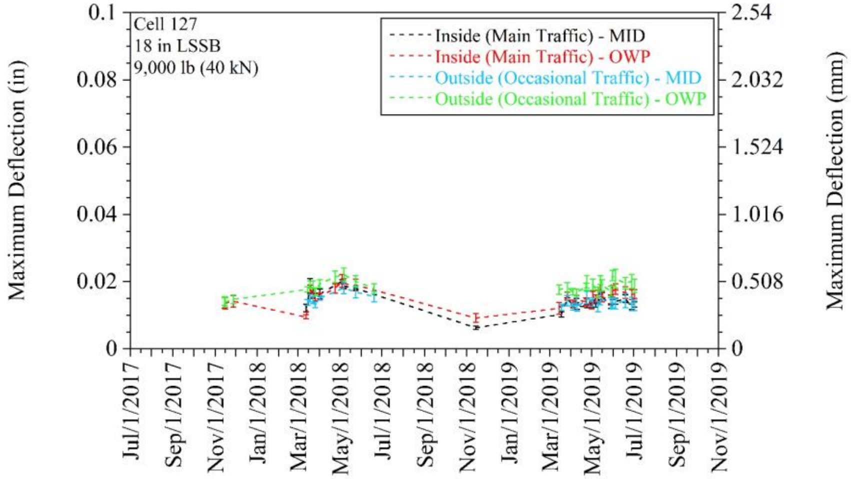
Cell 127
18 in LSSB
9,000 lb (40 kN)
Inside (Main Traffic) - MID
Inside (Main Traffic) - OWP
Outside (Occasional Traffic) - MID
Outside (Occasional Traffic) - OWP
Maximum Deflection (in)
Maximum Deflection (mm)
0.1
0.08
0.06
0.04
0.02
0
2.54
2.032
1.524
1.016
0.508
0
Jul/1/2017
Sep/1/2017
Nov/1/2017
Jan/1/2018
Mar/1/2018
May/1/2018
Jul/1/2018
Sep/1/2018
Nov/1/2018
Jan/1/2019
Mar/1/2019
May/1/2019
Jul/1/2019
Sep/1/2019
Nov/1/2019

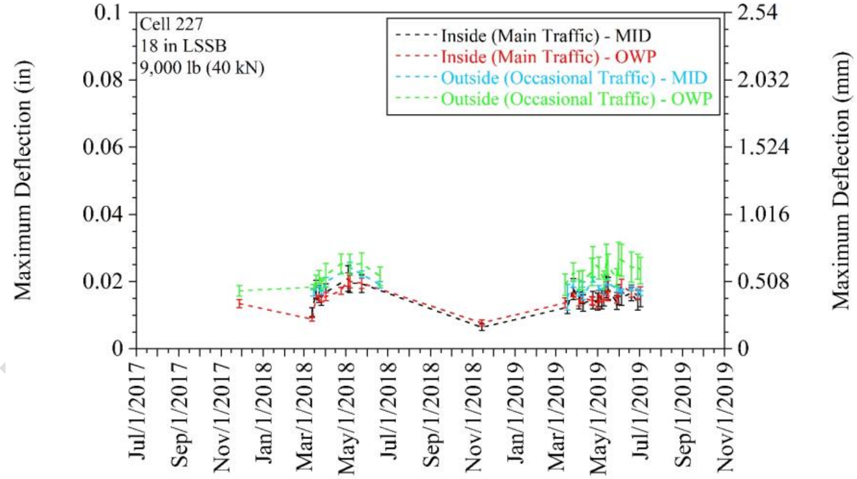
Cell 227
18 in LSSB
9,000 lb (40 kN)
Inside (Main Traffic) - MID
Inside (Main Traffic) - OWP
Outside (Occasional Traffic) - MID
Outside (Occasional Traffic) - OWP
Maximum Deflection (in)
Maximum Deflection (mm)
0.1
0.08
0.06
0.04
0.02
0
2.54
2.032
1.524
1.016
0.508
0
Jul/1/2017
Sep/1/2017
Nov/1/2017
Jan/1/2018
Mar/1/2018
May/1/2018
Jul/1/2018
Sep/1/2018
Nov/1/2018
Jan/1/2019
Mar/1/2019
May/1/2019
Jul/1/2019
Sep/1/2019
Nov/1/2019

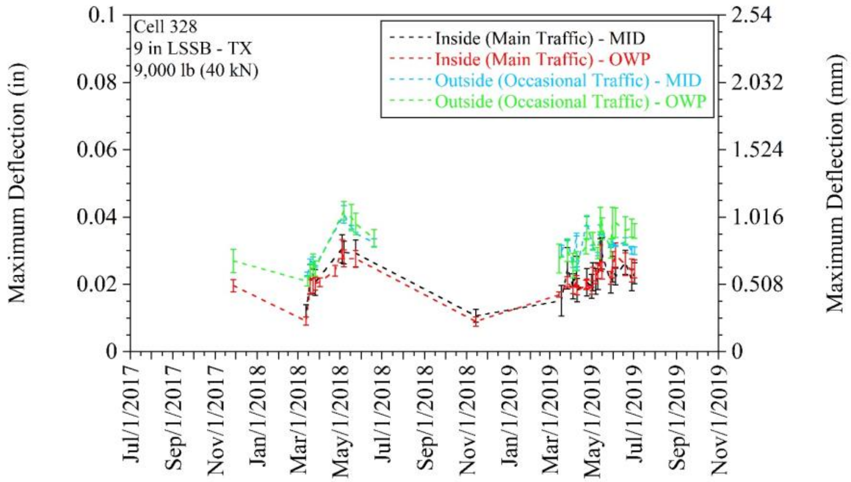
Cell 328
9 in LSSB - TX
9,000 lb (40 kN)
Inside (Main Traffic) - MID
Inside (Main Traffic) - OWP
Outside (Occasional Traffic) - MID
Outside (Occasional Traffic) - OWP
Maximum Deflection (in)
Maximum Deflection (mm)
0.1
0.08
0.06
0.04
0.02
0
2.54
2.032
1.524
1.016
0.508
0
Jul/1/2017
Sep/1/2017
Nov/1/2017
Jan/1/2018
Mar/1/2018
May/1/2018
Jul/1/2018
Sep/1/2018
Nov/1/2018
Jan/1/2019
Mar/1/2019
May/1/2019
Jul/1/2019
Sep/1/2019
Nov/1/2019

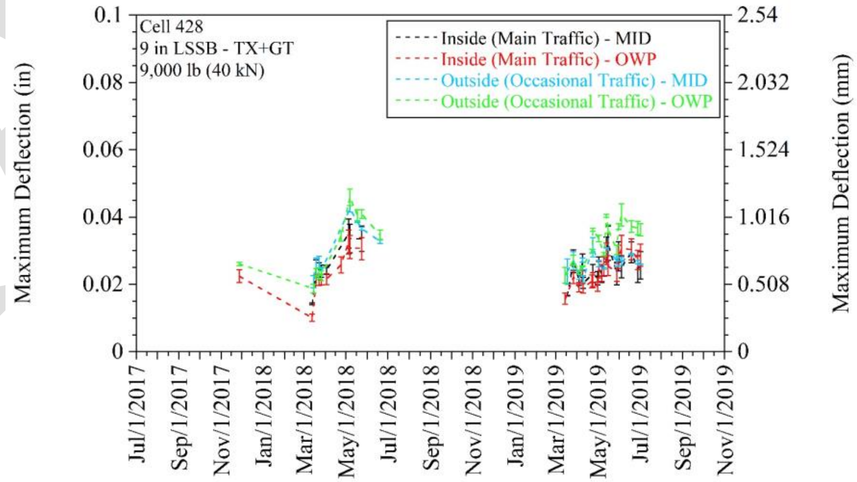
Cell 428
9 in LSSB - TX+GT
9,000 lb (40 kN)
Inside (Main Traffic) - MID
Inside (Main Traffic) - OWP
Outside (Occasional Traffic) - MID
Outside (Occasional Traffic) - OWP
Maximum Deflection (in)
Maximum Deflection (mm)
0.1
0.08
0.06
0.04
0.02
0
2.54
2.032
1.524
1.016
0.508
0
Jul/1/2017
Sep/1/2017
Nov/1/2017
Jan/1/2018
Mar/1/2018
May/1/2018
Jul/1/2018
Sep/1/2018
Nov/1/2018
Jan/1/2019
Mar/1/2019
May/1/2019
Jul/1/2019
Sep/1/2019
Nov/1/2019

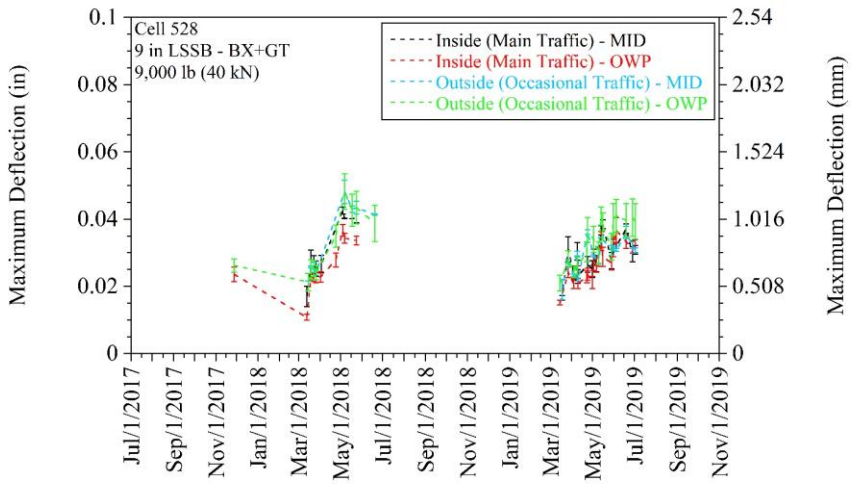
Cell 528
9 in LSSB - BX+GT
9,000 lb (40 kN)
Inside (Main Traffic) - MID
Inside (Main Traffic) - OWP
Outside (Occasional Traffic) - MID
Outside (Occasional Traffic) - OWP
Maximum Deflection (in)
Maximum Deflection (mm)

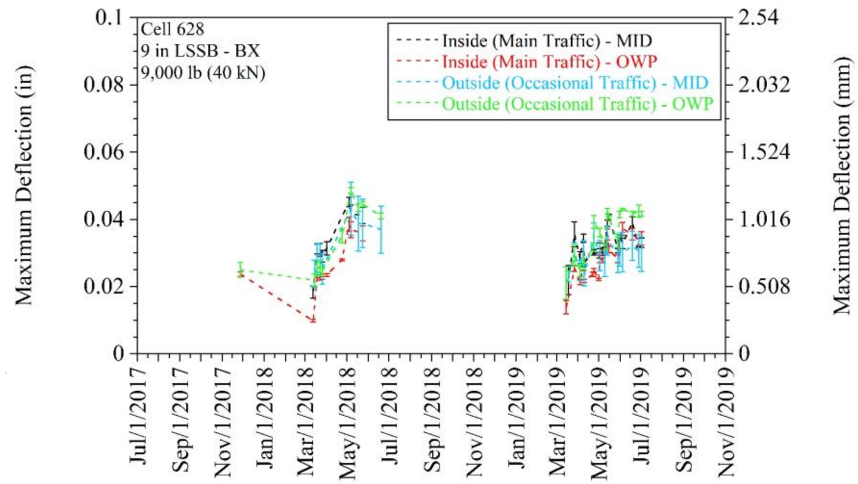
Cell 628
9 in LSSB - BX
9,000 lb (40 kN)
Inside (Main Traffic) - MID
Inside (Main Traffic) - OWP
Outside (Occasional Traffic) - MID
Outside (Occasional Traffic) - OWP
Maximum Deflection (in)
Maximum Deflection (mm)

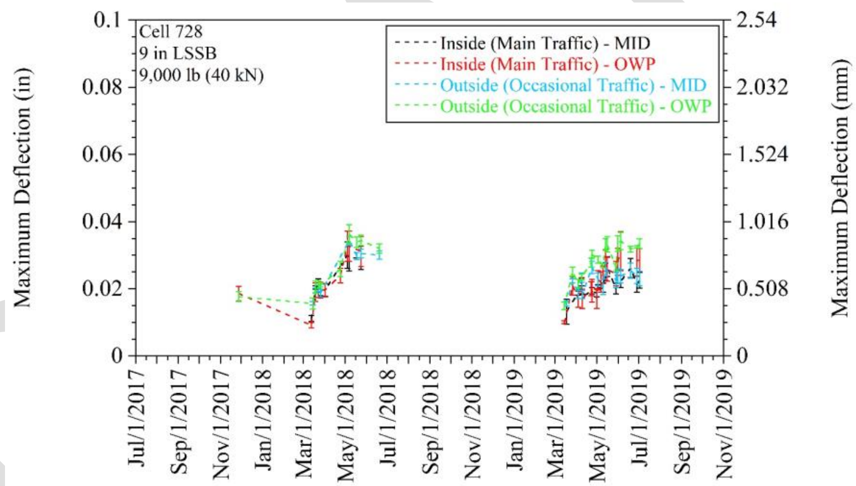
Cell 728
9 in LSSB
9,000 lb (40 kN)
Inside (Main Traffic) - MID
Inside (Main Traffic) - OWP
Outside (Occasional Traffic) - MID
Outside (Occasional Traffic) - OWP
Maximum Deflection (in)
Maximum Deflection (mm)

APPENDIX K. COMPOSITE E_{FWD} FOR DIFFERENT TEST LOCATIONS AT 9,000 LB (40 KN) FOR EACH CELL

(error bars represent one standard deviation of the data)

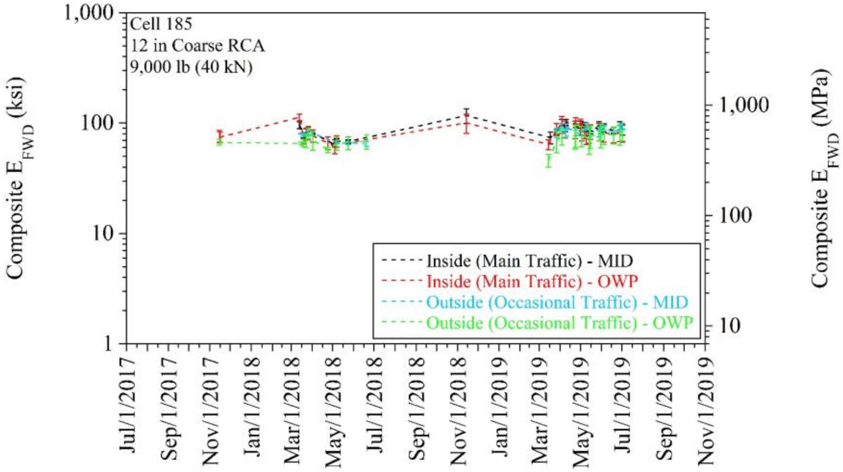

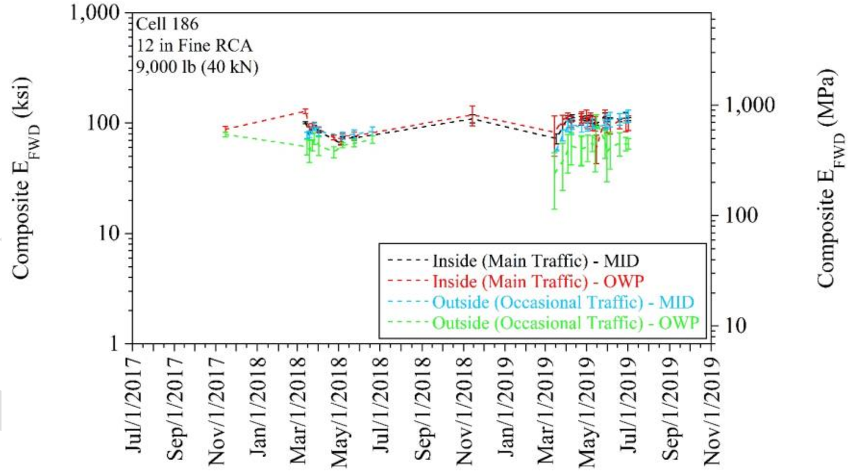

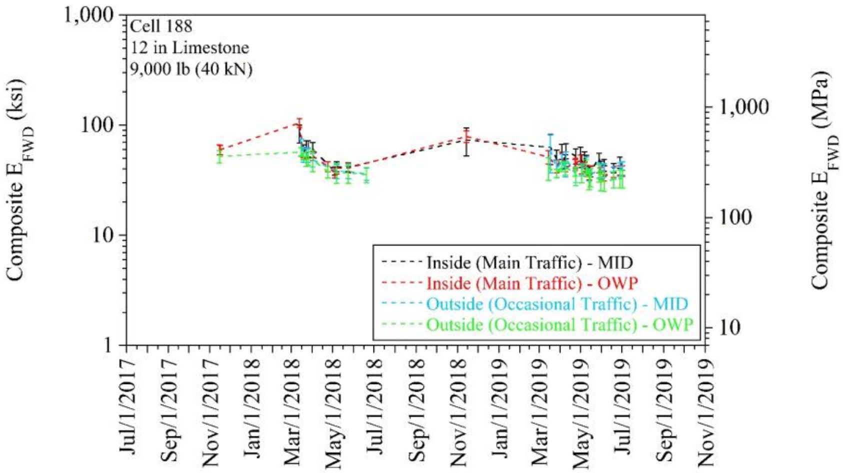

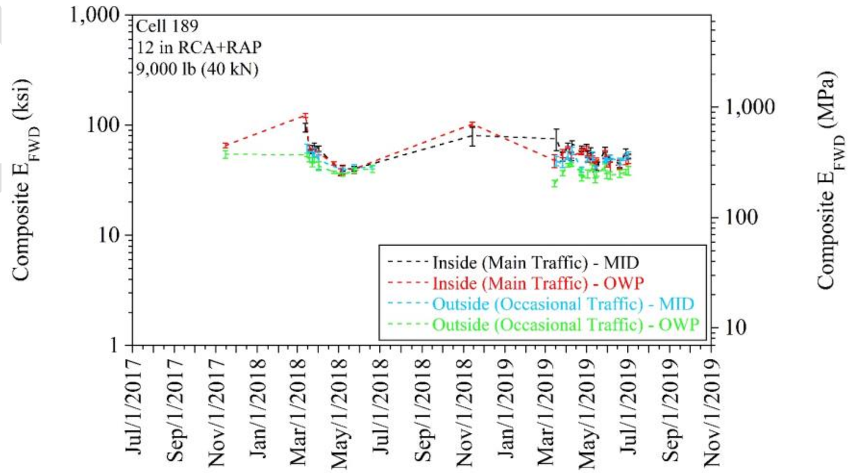

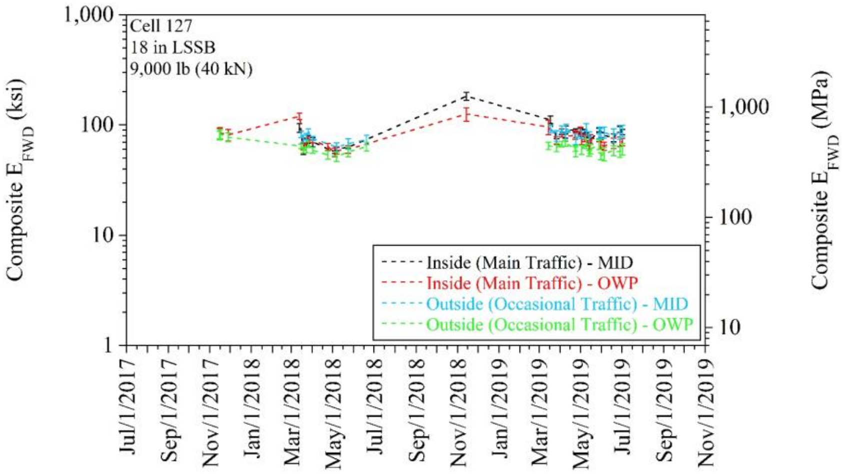
Cell 127
18 in LSSB
9,000 lb (40 kN)
Composite E_{FWD} (ksi)
Composite E_{FWD} (MPa)
Inside (Main Traffic) - MID
Inside (Main Traffic) - OWP
Outside (Occasional Traffic) - MID
Outside (Occasional Traffic) - OWP

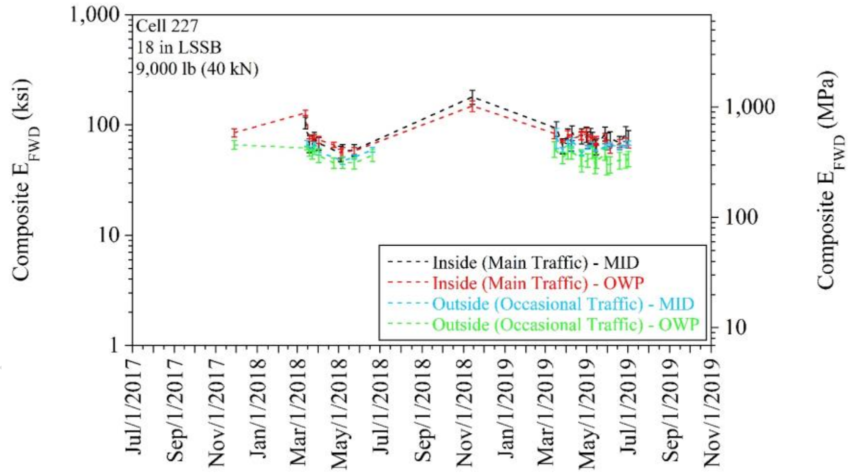
Cell 227
18 in LSSB
9,000 lb (40 kN)
Composite E_{FWD} (ksi)
Composite E_{FWD} (MPa)
Inside (Main Traffic) - MID
Inside (Main Traffic) - OWP
Outside (Occasional Traffic) - MID
Outside (Occasional Traffic) - OWP

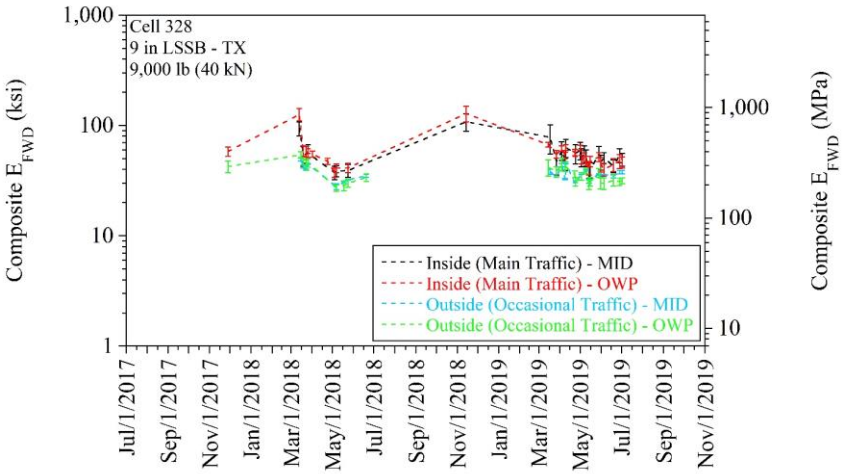
Cell 328
9 in LSSB - TX
9,000 lb (40 kN)
Composite E_{FWD} (ksi)
Composite E_{FWD} (MPa)
Inside (Main Traffic) - MID
Inside (Main Traffic) - OWP
Outside (Occasional Traffic) - MID
Outside (Occasional Traffic) - OWP

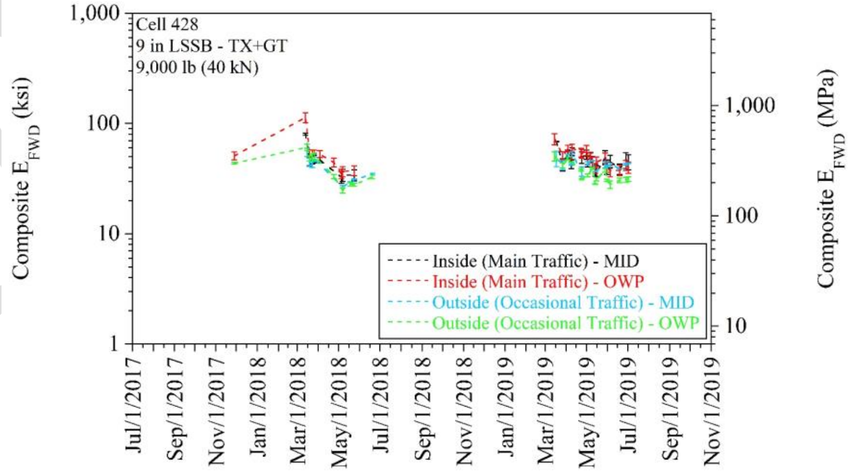
Cell 428
9 in LSSB - TX+GT
9,000 lb (40 kN)
Composite E_{FWD} (ksi)
Composite E_{FWD} (MPa)
Inside (Main Traffic) - MID
Inside (Main Traffic) - OWP
Outside (Occasional Traffic) - MID
Outside (Occasional Traffic) - OWP

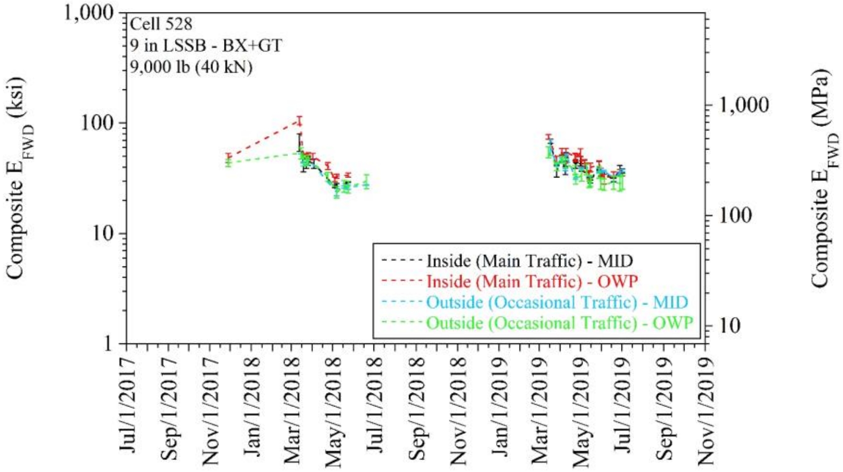

Cell 528
9 in LSSB - BX+GT
9,000 lb (40 kN)
Composite E_{FWD} (ksi)
Composite E_{FWD} (MPa)
Inside (Main Traffic) - MID
Inside (Main Traffic) - OWP
Outside (Occasional Traffic) - MID
Outside (Occasional Traffic) - OWP

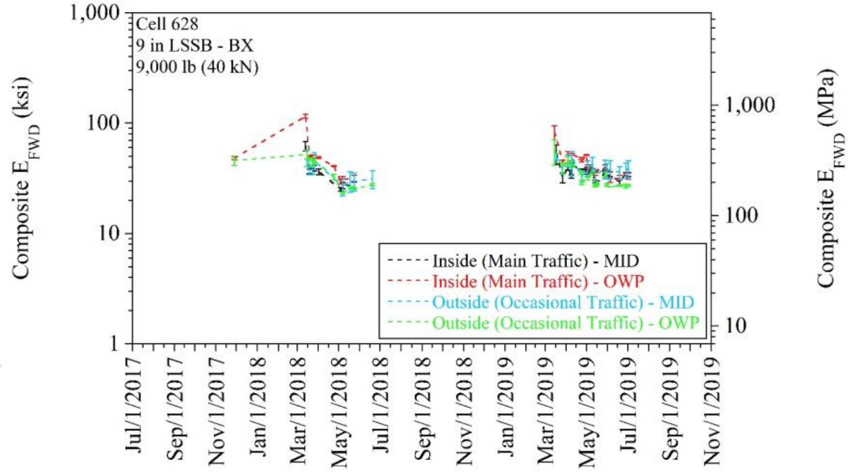

Cell 628
9 in LSSB - BX
9,000 lb (40 kN)
Composite E_{FWD} (ksi)
Composite E_{FWD} (MPa)
Inside (Main Traffic) - MID
Inside (Main Traffic) - OWP
Outside (Occasional Traffic) - MID
Outside (Occasional Traffic) - OWP

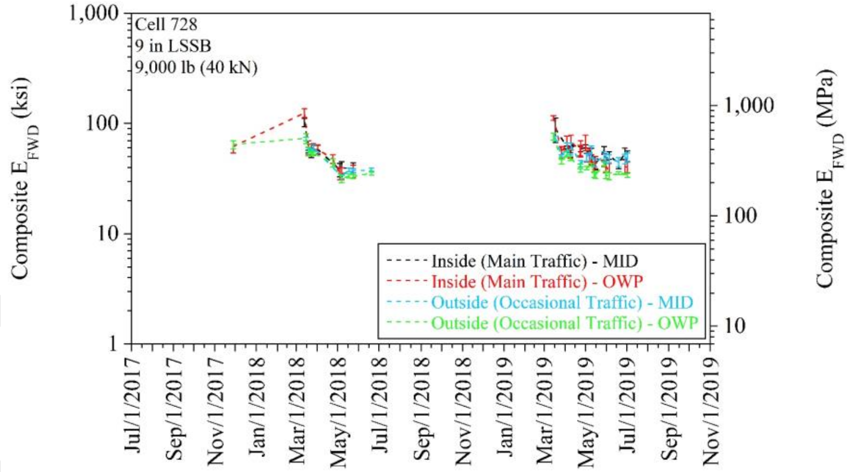

Cell 728
9 in LSSB
9,000 lb (40 kN)
Composite E_{FWD} (ksi)
Composite E_{FWD} (MPa)
Inside (Main Traffic) - MID
Inside (Main Traffic) - OWP
Outside (Occasional Traffic) - MID
Outside (Occasional Traffic) - OWP

APPENDIX L. ASPHALT E_{FWD} FOR DIFFERENT TEST LOCATIONS AT 9,000 LB (40 KN) FOR EACH CELL

(error bars represent one standard deviation of the data)

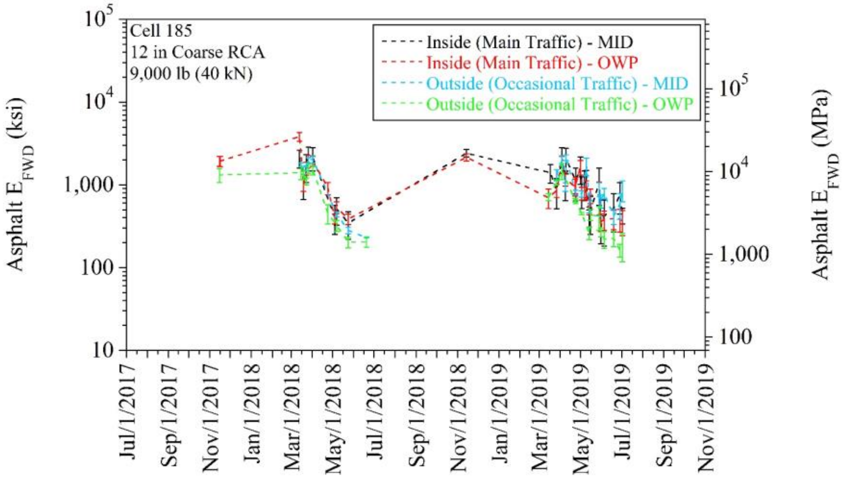

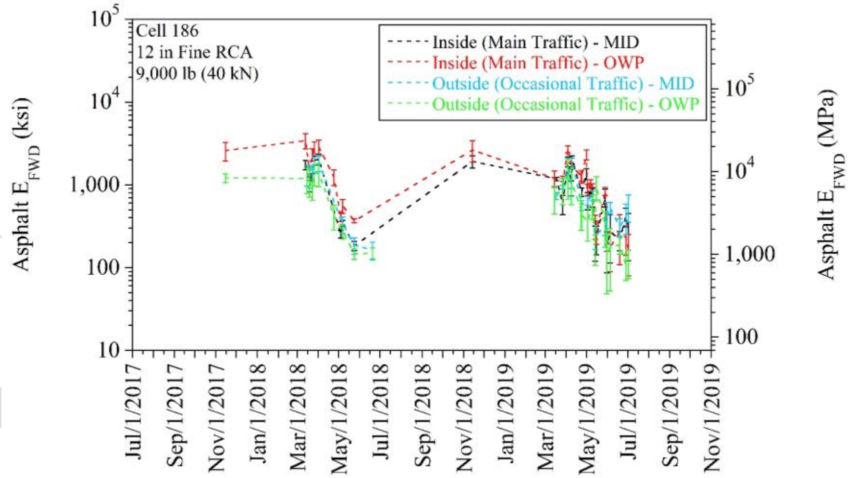

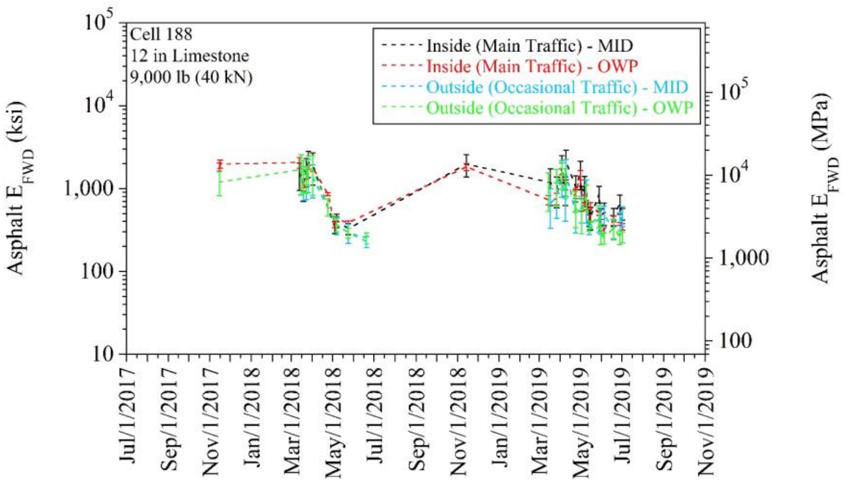

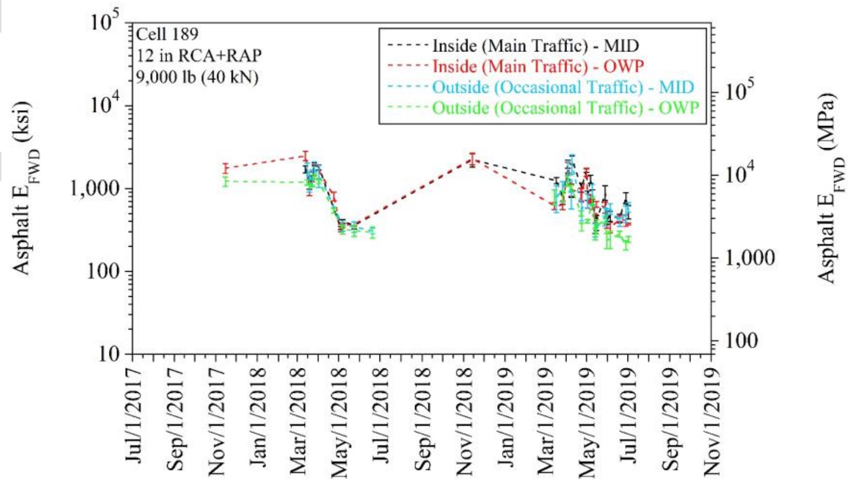

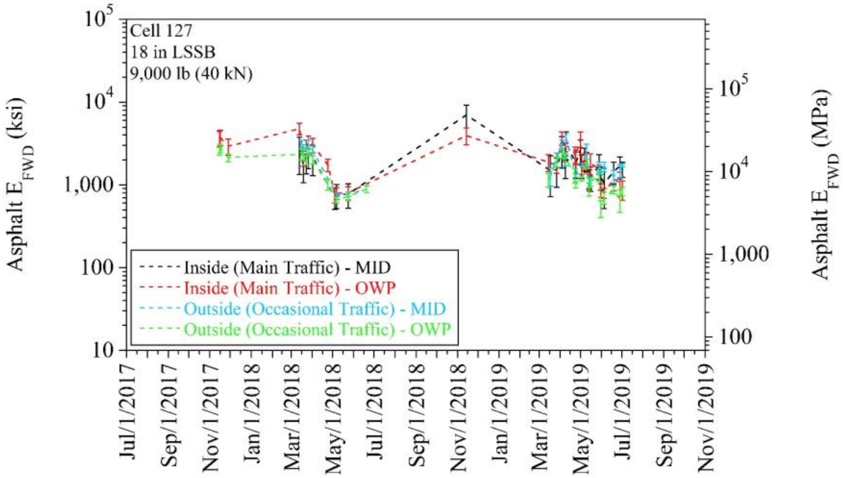
Cell 127
18 in LSSB
9,000 lb (40 kN)
Inside (Main Traffic) - MID
Inside (Main Traffic) - OWP
Outside (Occasional Traffic) - MID
Outside (Occasional Traffic) - OWP
Asphalt E_FWD (ksi)
Asphalt E_FWD (MPa)
10^5
10^4
1,000
100
10
Jul/1/2017
Sep/1/2017
Nov/1/2017
Jan/1/2018
Mar/1/2018
May/1/2018
Jul/1/2018
Sep/1/2018
Nov/1/2018
Jan/1/2019
Mar/1/2019
May/1/2019
Jul/1/2019
Sep/1/2019
Nov/1/2019

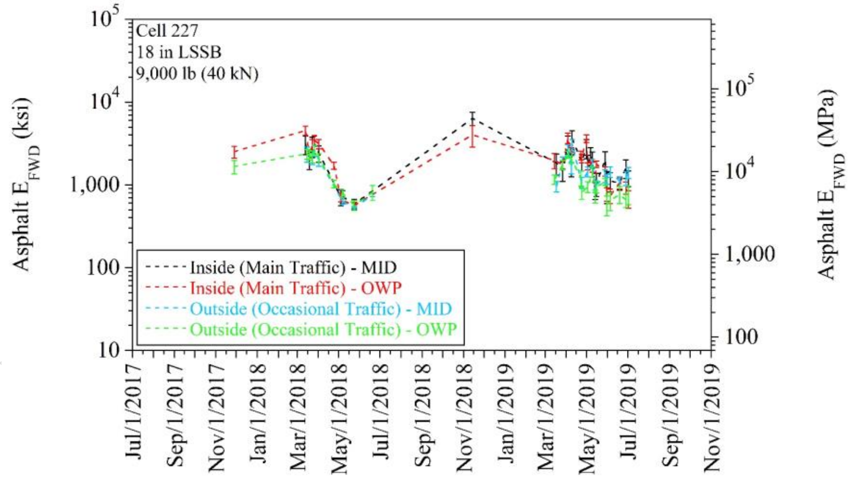
Cell 227
18 in LSSB
9,000 lb (40 kN)
Inside (Main Traffic) - MID
Inside (Main Traffic) - OWP
Outside (Occasional Traffic) - MID
Outside (Occasional Traffic) - OWP
Asphalt E_FWD (ksi)
Asphalt E_FWD (MPa)
Jul/1/2017
Sep/1/2017
Nov/1/2017
Jan/1/2018
Mar/1/2018
May/1/2018
Jul/1/2018
Sep/1/2018
Nov/1/2018
Jan/1/2019
Mar/1/2019
May/1/2019
Jul/1/2019
Sep/1/2019
Nov/1/2019

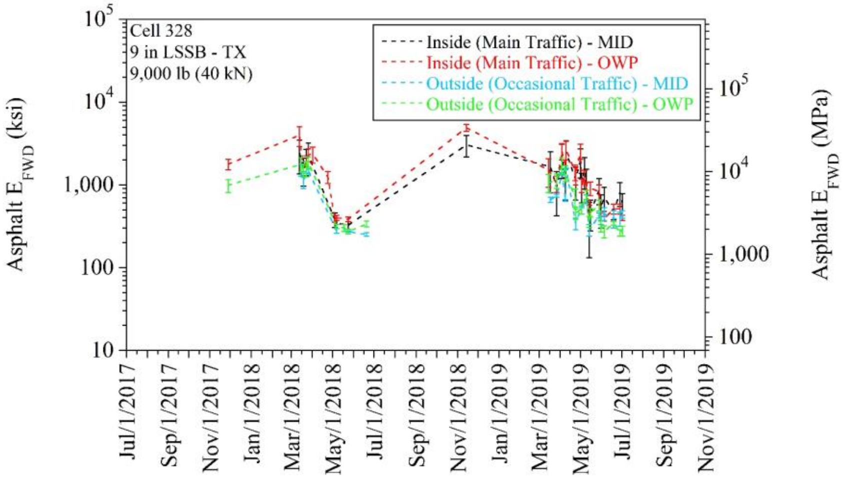
Cell 328
9 in LSSB - TX
9,000 lb (40 kN)
Inside (Main Traffic) - MID
Inside (Main Traffic) - OWP
Outside (Occasional Traffic) - MID
Outside (Occasional Traffic) - OWP
Asphalt E_FWD (ksi)
Asphalt E_FWD (MPa)
Jul/1/2017
Sep/1/2017
Nov/1/2017
Jan/1/2018
Mar/1/2018
May/1/2018
Jul/1/2018
Sep/1/2018
Nov/1/2018
Jan/1/2019
Mar/1/2019
May/1/2019
Jul/1/2019
Sep/1/2019
Nov/1/2019

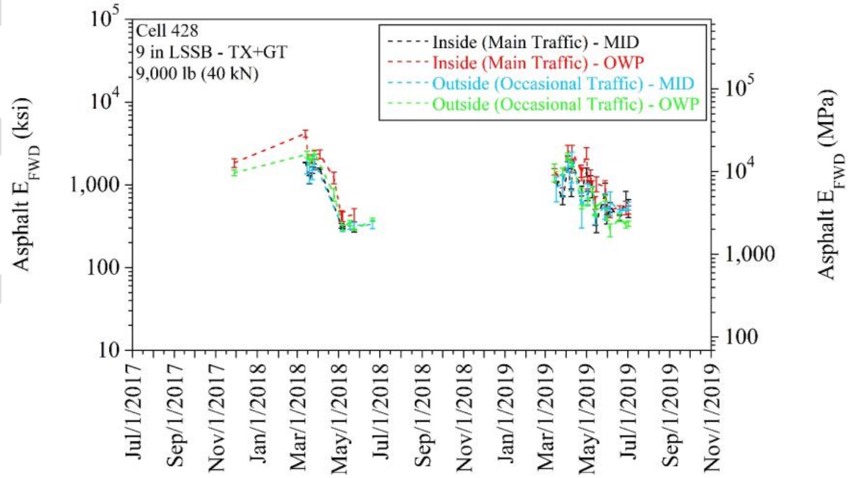
Cell 428
9 in LSSB - TX+GT
9,000 lb (40 kN)
Inside (Main Traffic) - MID
Inside (Main Traffic) - OWP
Outside (Occasional Traffic) - MID
Outside (Occasional Traffic) - OWP
Asphalt E_FWD (ksi)
Asphalt E_FWD (MPa)
Jul/1/2017
Sep/1/2017
Nov/1/2017
Jan/1/2018
Mar/1/2018
May/1/2018
Jul/1/2018
Sep/1/2018
Nov/1/2018
Jan/1/2019
Mar/1/2019
May/1/2019
Jul/1/2019
Sep/1/2019
Nov/1/2019

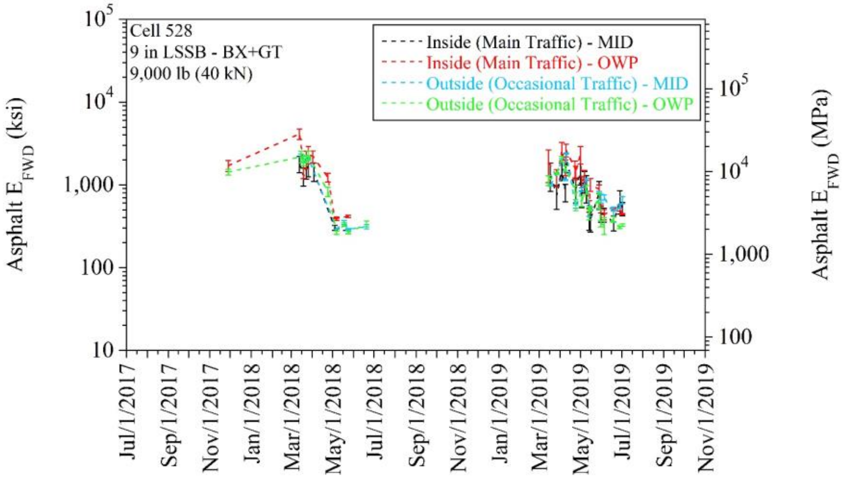
Cell 528
9 in LSSB - BX+GT
9,000 lb (40 kN)
Inside (Main Traffic) - MID
Inside (Main Traffic) - OWP
Outside (Occasional Traffic) - MID
Outside (Occasional Traffic) - OWP
Asphalt E_{FWD} (ksi)
Asphalt E_{FWD} (MPa)
10^5
10^4
1,000
100
10
10^5
10^4
1,000
100
Jul/1/2017
Sep/1/2017
Nov/1/2017
Jan/1/2018
Mar/1/2018
May/1/2018
Jul/1/2018
Sep/1/2018
Nov/1/2018
Jan/1/2019
Mar/1/2019
May/1/2019
Jul/1/2019
Sep/1/2019
Nov/1/2019

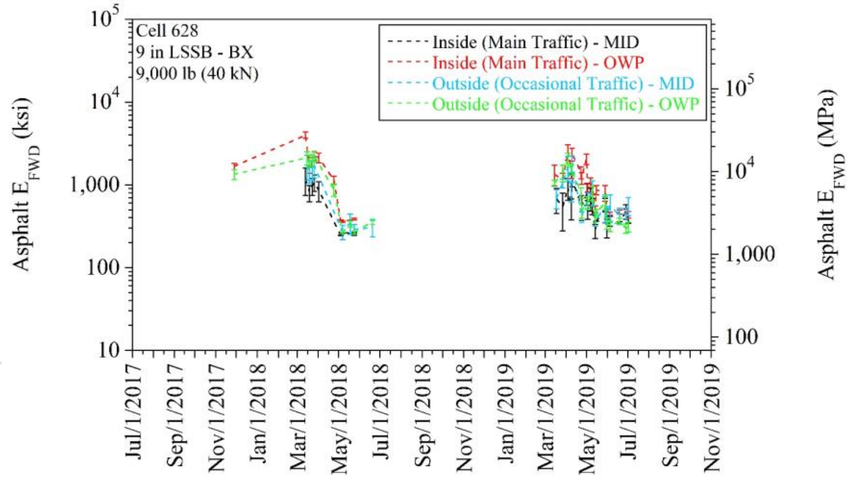
Cell 628
9 in LSSB - BX
9,000 lb (40 kN)
Inside (Main Traffic) - MID
Inside (Main Traffic) - OWP
Outside (Occasional Traffic) - MID
Outside (Occasional Traffic) - OWP
Asphalt E_{FWD} (ksi)
Asphalt E_{FWD} (MPa)
10^5
10^4
1,000
100
10
10^5
10^4
1,000
100
Jul/1/2017
Sep/1/2017
Nov/1/2017
Jan/1/2018
Mar/1/2018
May/1/2018
Jul/1/2018
Sep/1/2018
Nov/1/2018
Jan/1/2019
Mar/1/2019
May/1/2019
Jul/1/2019
Sep/1/2019
Nov/1/2019

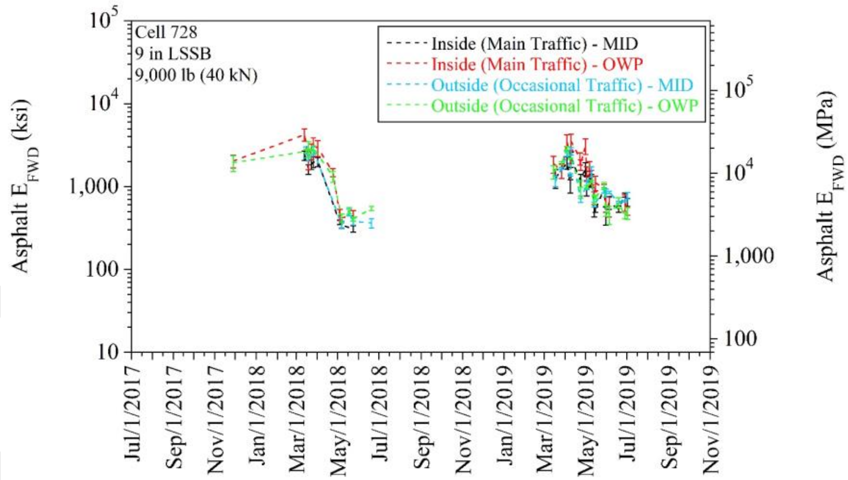
Cell 728
9 in LSSB
9,000 lb (40 kN)
Inside (Main Traffic) - MID
Inside (Main Traffic) - OWP
Outside (Occasional Traffic) - MID
Outside (Occasional Traffic) - OWP
Asphalt E_{FWD} (ksi)
Asphalt E_{FWD} (MPa)
10^5
10^4
1,000
100
10
10^5
10^4
1,000
100
Jul/1/2017
Sep/1/2017
Nov/1/2017
Jan/1/2018
Mar/1/2018
May/1/2018
Jul/1/2018
Sep/1/2018
Nov/1/2018
Jan/1/2019
Mar/1/2019
May/1/2019
Jul/1/2019
Sep/1/2019
Nov/1/2019

APPENDIX M. BASE+SUBBASE E_{FWD} FOR DIFFERENT TEST LOCATIONS AT 9,000 LB (40 KN) FOR EACH CELL

(error bars represent one standard deviation of the data)

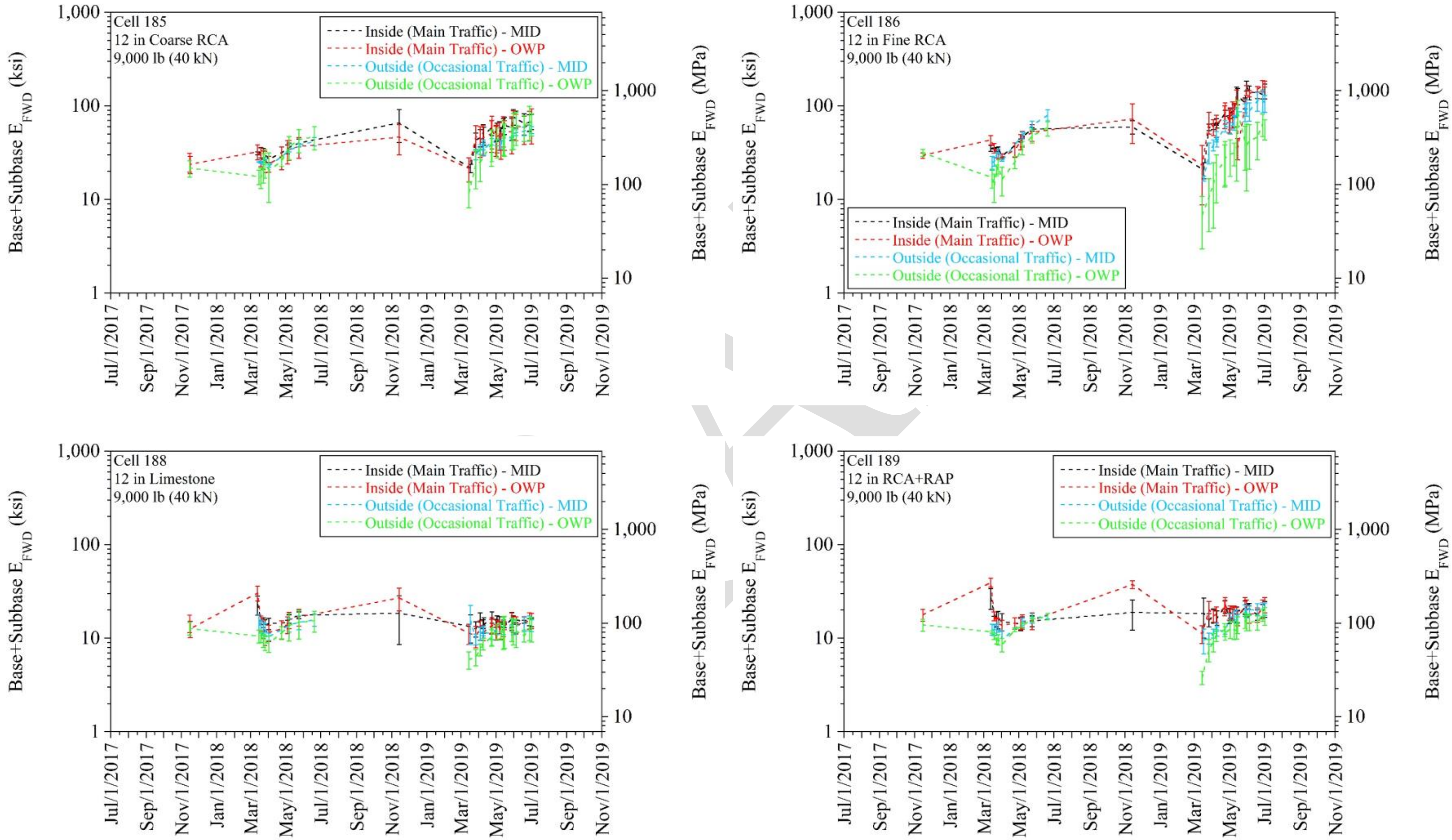

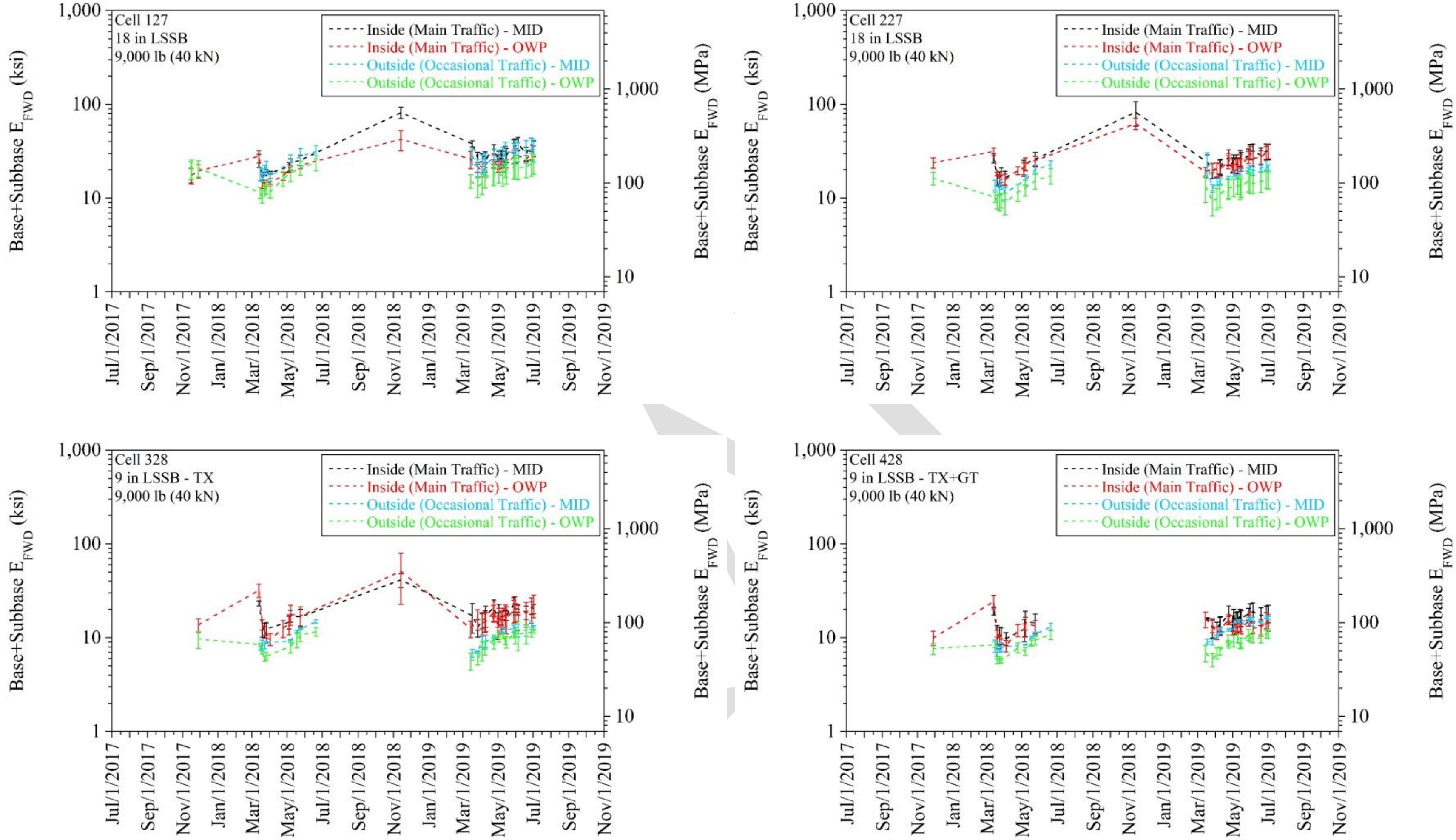

Cell 127
18 in LSSB
9,000 lb (40 kN)
Cell 227
18 in LSSB
9,000 lb (40 kN)
Cell 328
9 in LSSB - TX
9,000 lb (40 kN)
Cell 428
9 in LSSB - TX+GT
9,000 lb (40 kN)
Inside (Main Traffic) - MID
Inside (Main Traffic) - OWP
Outside (Occasional Traffic) - MID
Outside (Occasional Traffic) - OWP
Base+Subbase E_{FWD} (ksi)
Base+Subbase E_{FWD} (MPa)

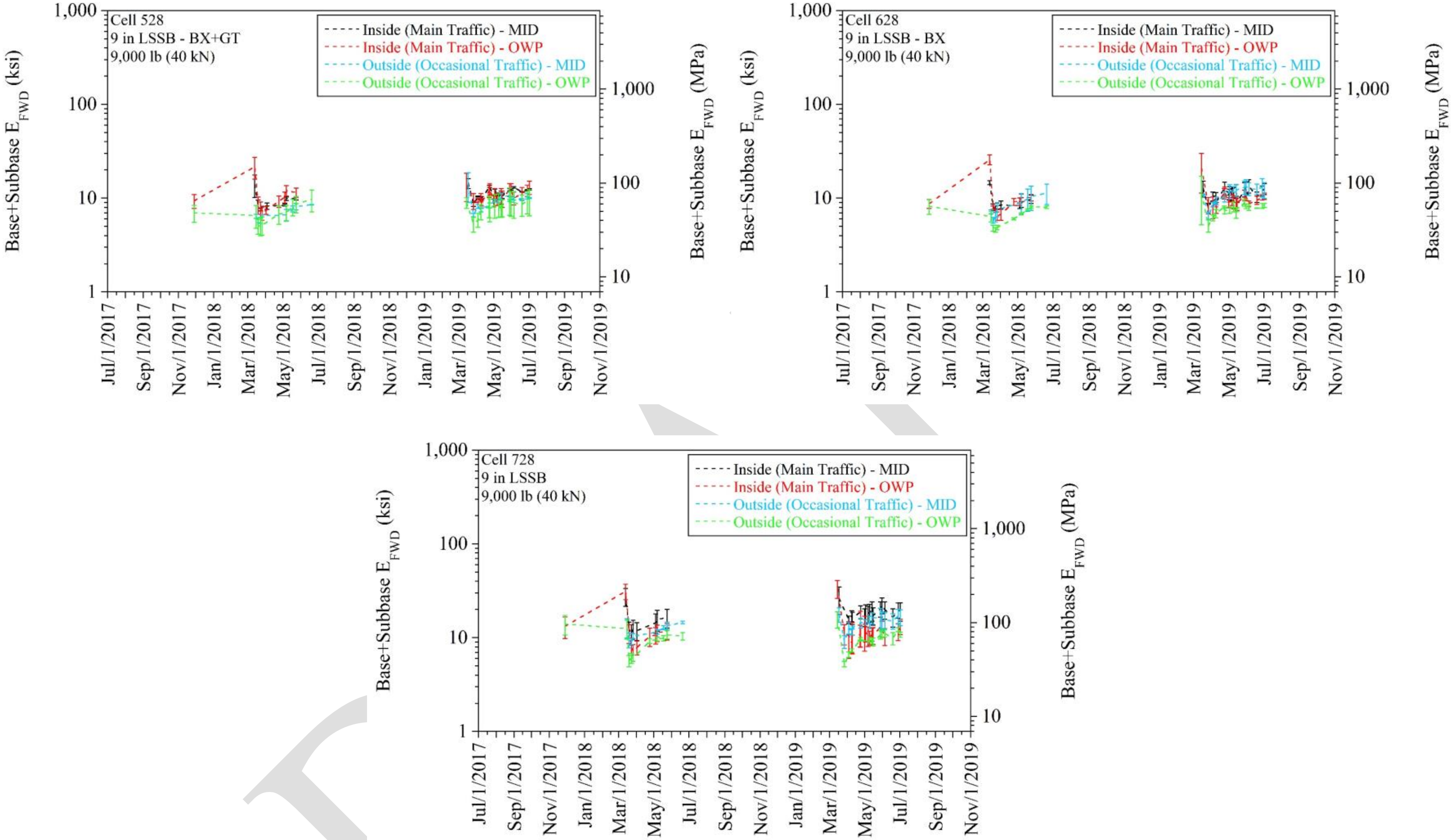
Cell 528
9 in LSSB - BX+GT
9,000 lb (40 kN)
Inside (Main Traffic) - MID
Inside (Main Traffic) - OWP
Outside (Occasional Traffic) - MID
Outside (Occasional Traffic) - OWP
Base+Subbase E_{FWD} (ksi)
Base+Subbase E_{FWD} (MPa)
1,000
100
10
1
10
100
1,000
Jul/1/2017
Sep/1/2017
Nov/1/2017
Jan/1/2018
Mar/1/2018
May/1/2018
Jul/1/2018
Sep/1/2018
Nov/1/2018
Jan/1/2019
Mar/1/2019
May/1/2019
Jul/1/2019
Sep/1/2019
Nov/1/2019
Cell 628
9 in LSSB - BX
9,000 lb (40 kN)
Inside (Main Traffic) - MID
Inside (Main Traffic) - OWP
Outside (Occasional Traffic) - MID
Outside (Occasional Traffic) - OWP
Base+Subbase E_{FWD} (ksi)
Base+Subbase E_{FWD} (MPa)
Cell 728
9 in LSSB
9,000 lb (40 kN)
Inside (Main Traffic) - MID
Inside (Main Traffic) - OWP
Outside (Occasional Traffic) - MID
Outside (Occasional Traffic) - OWP
Base+Subbase E_{FWD} (ksi)
Base+Subbase E_{FWD} (MPa)

APPENDIX N. SUBGRADE E_{FWD} FOR DIFFERENT TEST LOCATIONS AT 9,000 LB (40 KN) FOR EACH CELL

(error bars represent one standard deviation of the data)

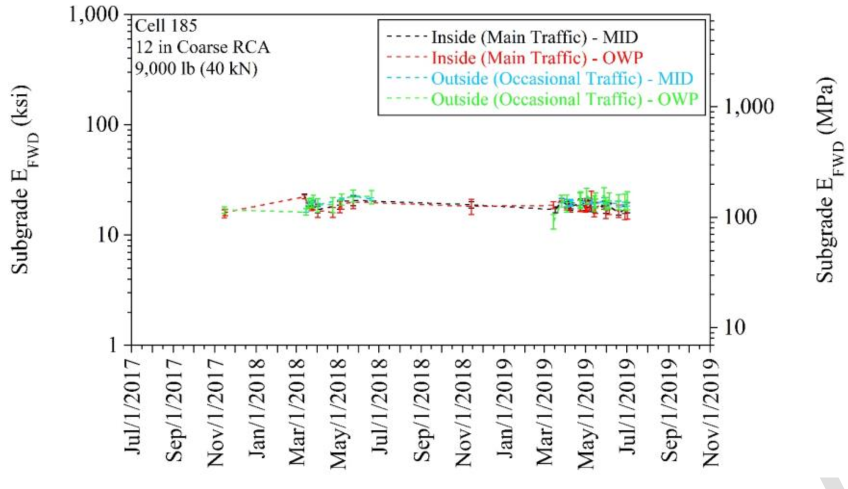

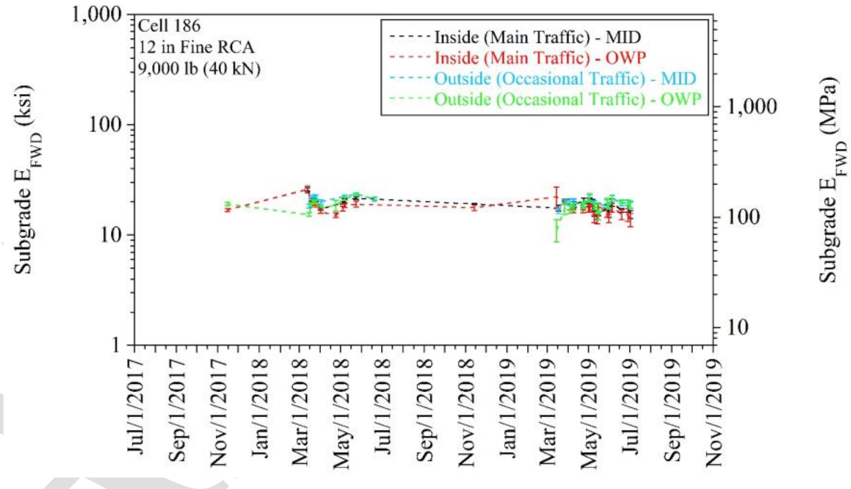

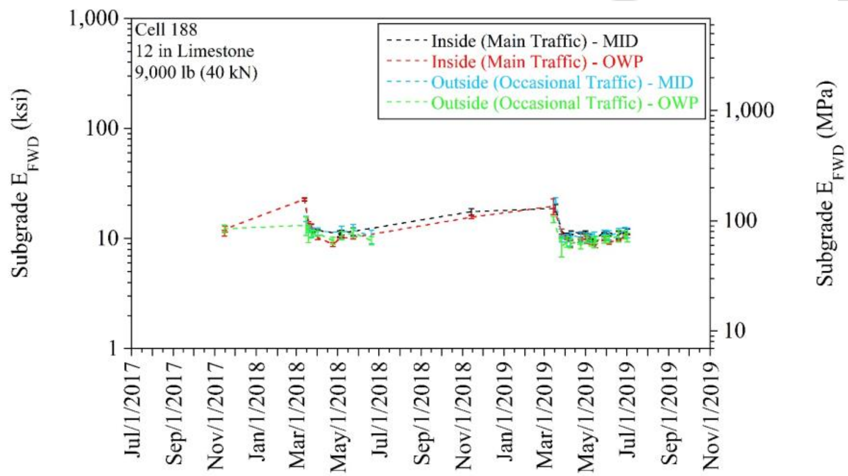

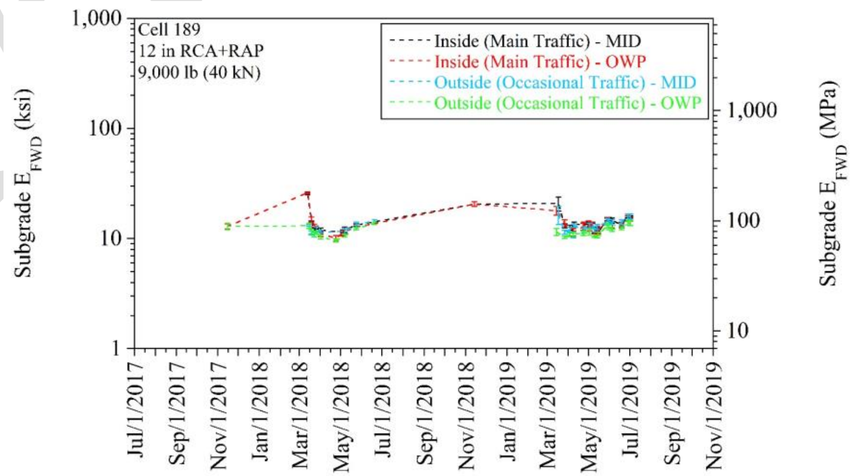

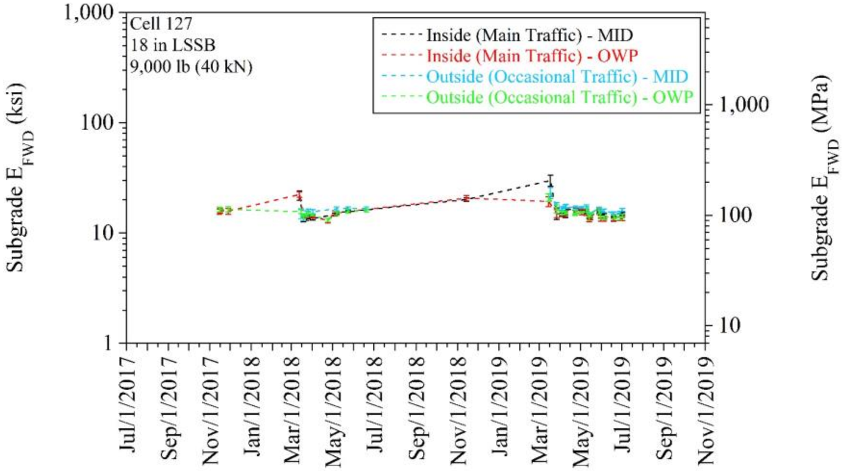
Cell 127
18 in LSSB
9,000 lb (40 kN)
Inside (Main Traffic) - MID
Inside (Main Traffic) - OWP
Outside (Occasional Traffic) - MID
Outside (Occasional Traffic) - OWP
Subgrade E_{FWD} (ksi)
Subgrade E_{FWD} (MPa)

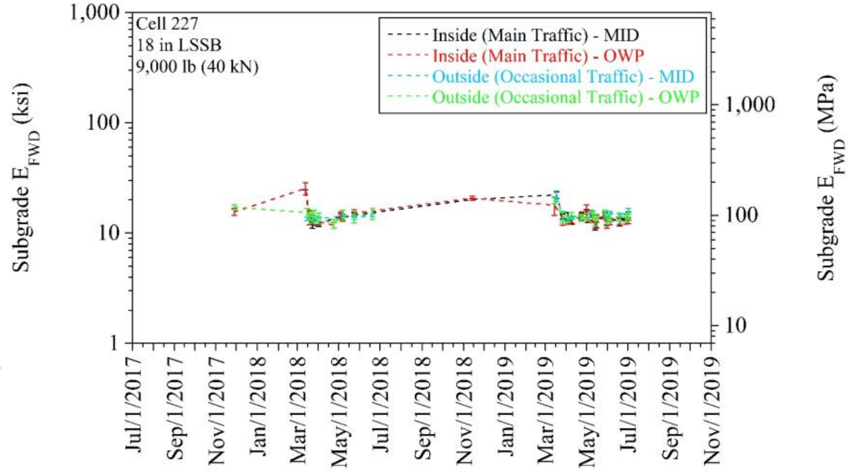
Cell 227
18 in LSSB
9,000 lb (40 kN)
Inside (Main Traffic) - MID
Inside (Main Traffic) - OWP
Outside (Occasional Traffic) - MID
Outside (Occasional Traffic) - OWP
Subgrade E_{FWD} (ksi)
Subgrade E_{FWD} (MPa)

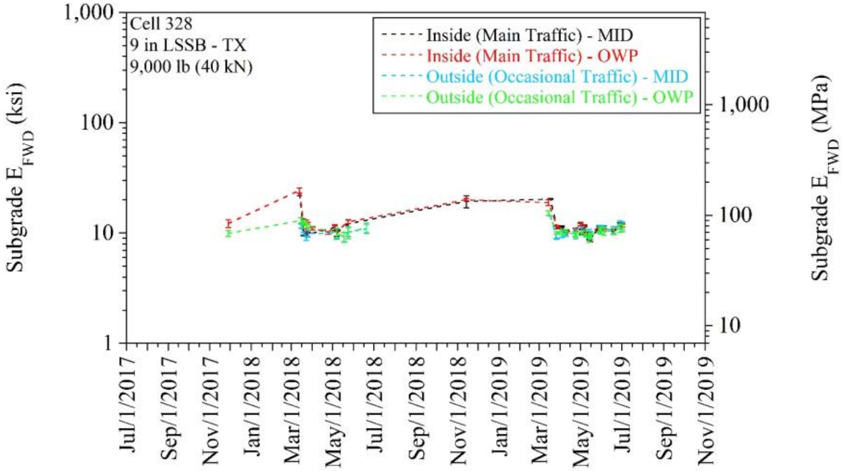
Cell 328
9 in LSSB - TX
9,000 lb (40 kN)
Inside (Main Traffic) - MID
Inside (Main Traffic) - OWP
Outside (Occasional Traffic) - MID
Outside (Occasional Traffic) - OWP
Subgrade E_{FWD} (ksi)
Subgrade E_{FWD} (MPa)

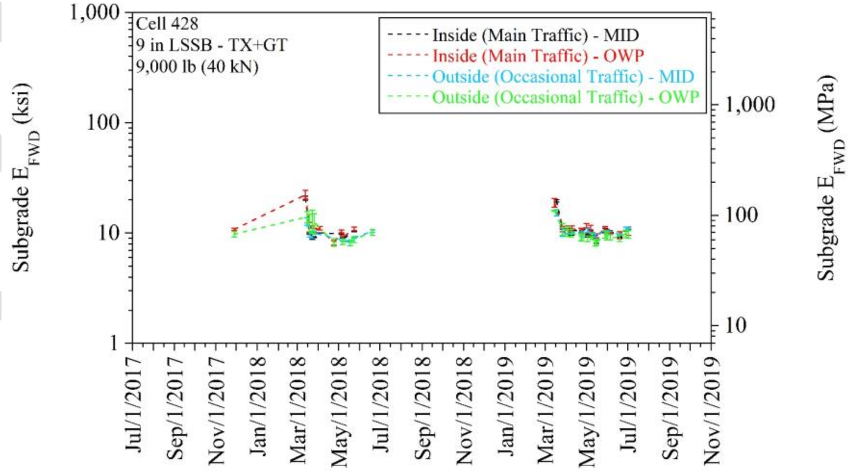
Cell 428
9 in LSSB - TX+GT
9,000 lb (40 kN)
Inside (Main Traffic) - MID
Inside (Main Traffic) - OWP
Outside (Occasional Traffic) - MID
Outside (Occasional Traffic) - OWP
Subgrade E_{FWD} (ksi)
Subgrade E_{FWD} (MPa)

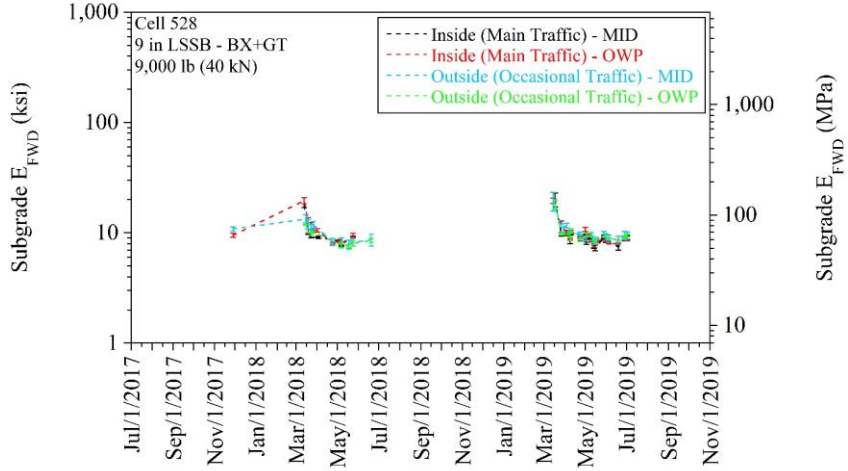
Cell 528
9 in LSSB - BX+GT
9,000 lb (40 kN)
Inside (Main Traffic) - MID
Inside (Main Traffic) - OWP
Outside (Occasional Traffic) - MID
Outside (Occasional Traffic) - OWP
Subgrade E_FWD (ksi)
Subgrade E_FWD (MPa)
1,000
100
10
1
1,000
100
10
Jul/1/2017
Sep/1/2017
Nov/1/2017
Jan/1/2018
Mar/1/2018
May/1/2018
Jul/1/2018
Sep/1/2018
Nov/1/2018
Jan/1/2019
Mar/1/2019
May/1/2019
Jul/1/2019
Sep/1/2019
Nov/1/2019

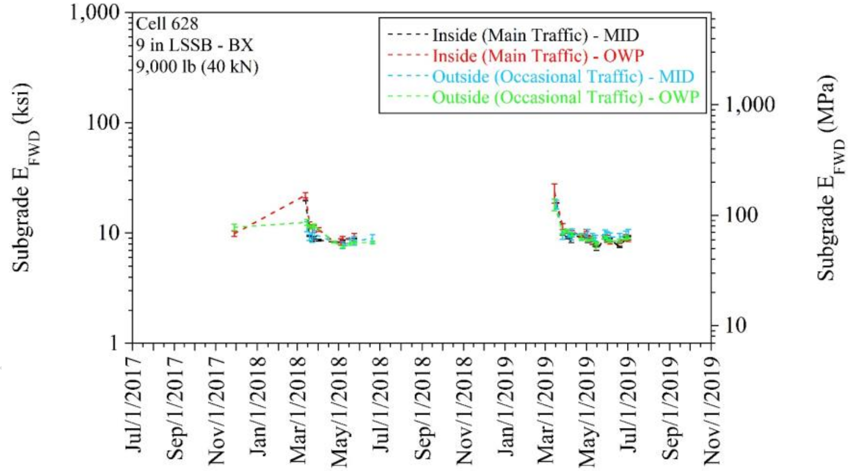
Cell 628
9 in LSSB - BX
9,000 lb (40 kN)
Inside (Main Traffic) - MID
Inside (Main Traffic) - OWP
Outside (Occasional Traffic) - MID
Outside (Occasional Traffic) - OWP
Subgrade E_FWD (ksi)
Subgrade E_FWD (MPa)
1,000
100
10
1
1,000
100
10
Jul/1/2017
Sep/1/2017
Nov/1/2017
Jan/1/2018
Mar/1/2018
May/1/2018
Jul/1/2018
Sep/1/2018
Nov/1/2018
Jan/1/2019
Mar/1/2019
May/1/2019
Jul/1/2019
Sep/1/2019
Nov/1/2019

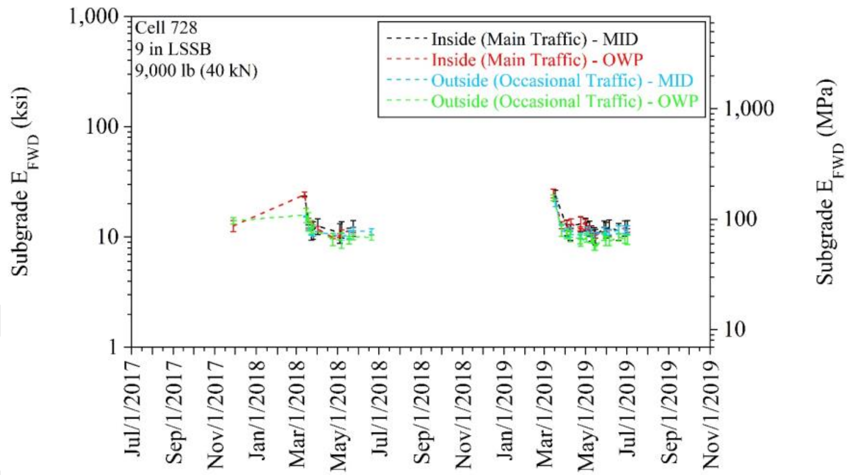
Cell 728
9 in LSSB
9,000 lb (40 kN)
Inside (Main Traffic) - MID
Inside (Main Traffic) - OWP
Outside (Occasional Traffic) - MID
Outside (Occasional Traffic) - OWP
Subgrade E_FWD (ksi)
Subgrade E_FWD (MPa)
1,000
100
10
1
1,000
100
10
Jul/1/2017
Sep/1/2017
Nov/1/2017
Jan/1/2018
Mar/1/2018
May/1/2018
Jul/1/2018
Sep/1/2018
Nov/1/2018
Jan/1/2019
Mar/1/2019
May/1/2019
Jul/1/2019
Sep/1/2019
Nov/1/2019

APPENDIX O. VOLUMETRIC WATER CONTENT (VWC) VALUES DETERMINED FOR THE SECOND THAWING PERIOD

The thawing period in 2019 was evaluated in three stages: (1) frozen (average VWC for one day in fully-frozen condition – right before the thawing starts), (2) during thawing (the peak VWC between fully-frozen and thawed conditions), and (3) after thawing (average VWC for one day after the peak VWC during thawing).

Cell	Depth (in)	Material	VWC - Thawing Period in 2019		
			Frozen	During Thawing	After Thawing
185	5	Coarse RCA	NA	NA	NA
	14	Coarse RCA	NA	NA	NA
	17	Select Granular Borrow	NA	NA	NA
	20.5	Sand Subgrade	NA	NA	NA
186	5	Fine RCA	0.0616	0.2107	0.1147
	14	Fine RCA	NA	NA	NA
	17	Select Granular Borrow	NA	NA	NA
	20.5	Sand Subgrade	NA	NA	NA
188	5	Limestone	0.0056	0.2126	0.0842
	14	Limestone	-0.011	0.416	0.0788
	17	Select Granular Borrow	0.0207	0.3042	0.2872
	20.5	Clay Loam Subgrade	0.0681	0.1719	0.1632
189	5	RCA+RAP	0.0206	0.2954	0.1196
	14	RCA+RAP	NA	0.3026	0.065
	17	Select Granular Borrow	0.0347	0.2467	0.2117
	20.5	Clay Loam Subgrade	0.1092	0.2553	0.2589
127	6.5	Class 6 Aggregate	0.017	0.3698	0.1094
	29	Clay Loam Subgrade	0.1272	0.2874	0.2778
	36	Clay Loam Subgrade	0.1398	0.2583	0.2634
728	8.5	Class 5Q Aggregate	0.0853	0.2146	0.1726
	19.5	Clay Loam Subgrade	0.1191	0.285	0.2631
	24	Clay Loam Subgrade	0.1305	0.2886	0.2865
	36	Clay Loam Subgrade	0.1425	0.3375	0.324

APPENDIX P. ELEVATION PROFILES FOR EACH TEST CELL

Cell 185 (12 in coarse RCA):

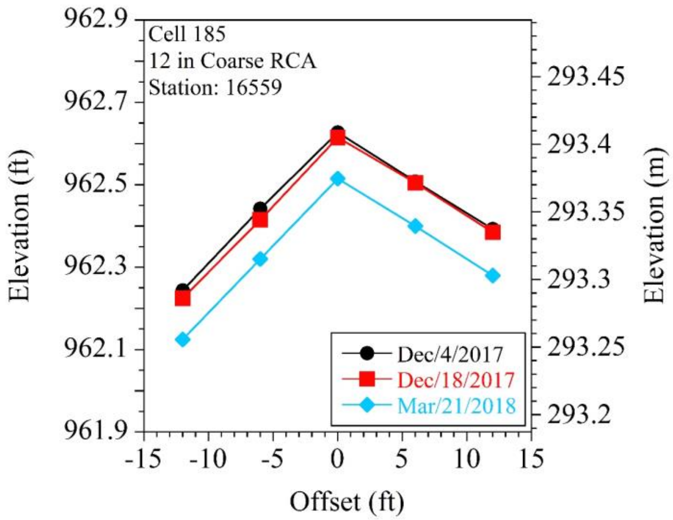

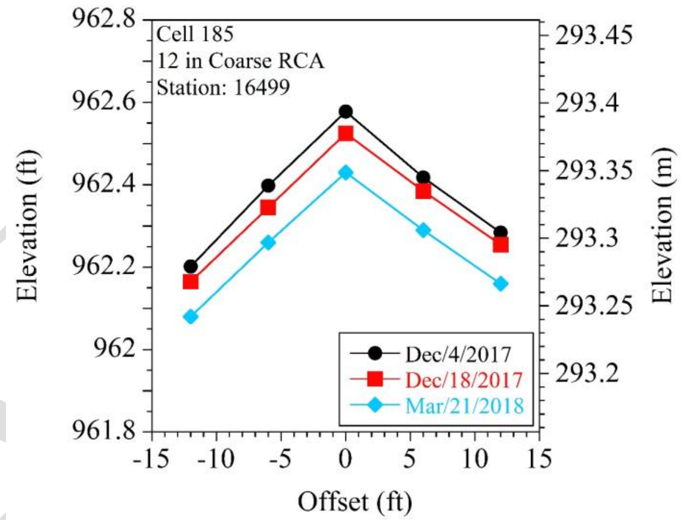

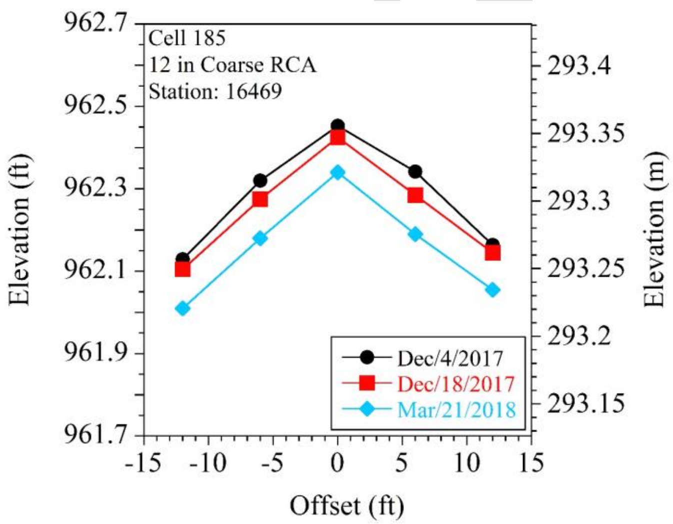

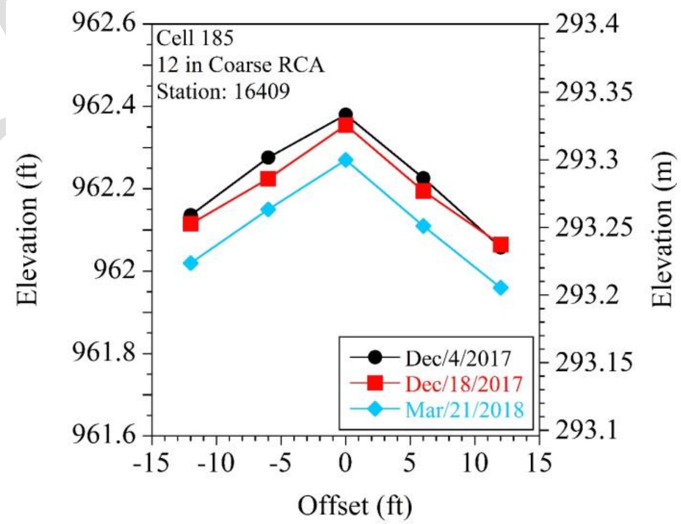

Cell 186 (12 in fine RCA):

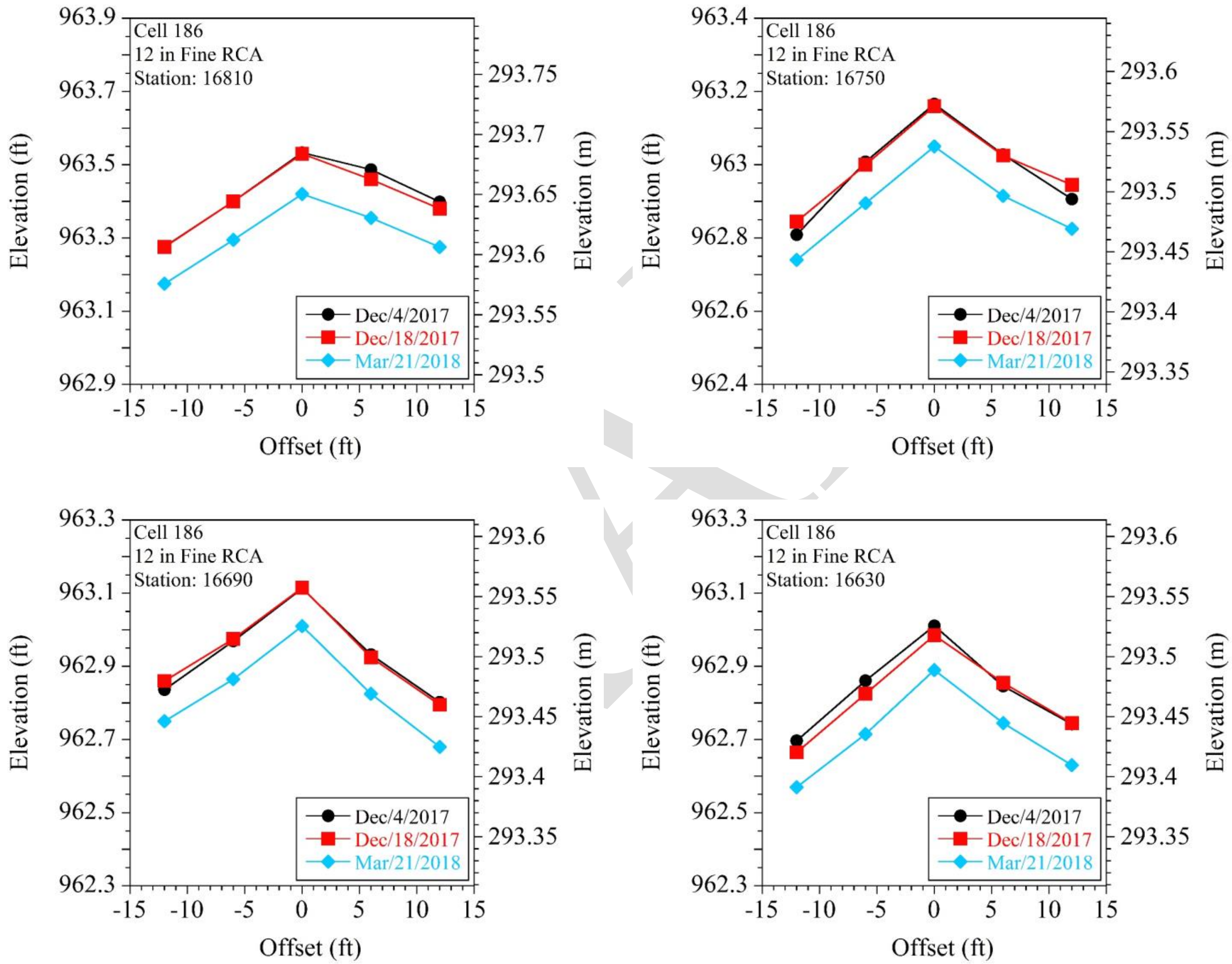

Cell 188 (12 in limestone):

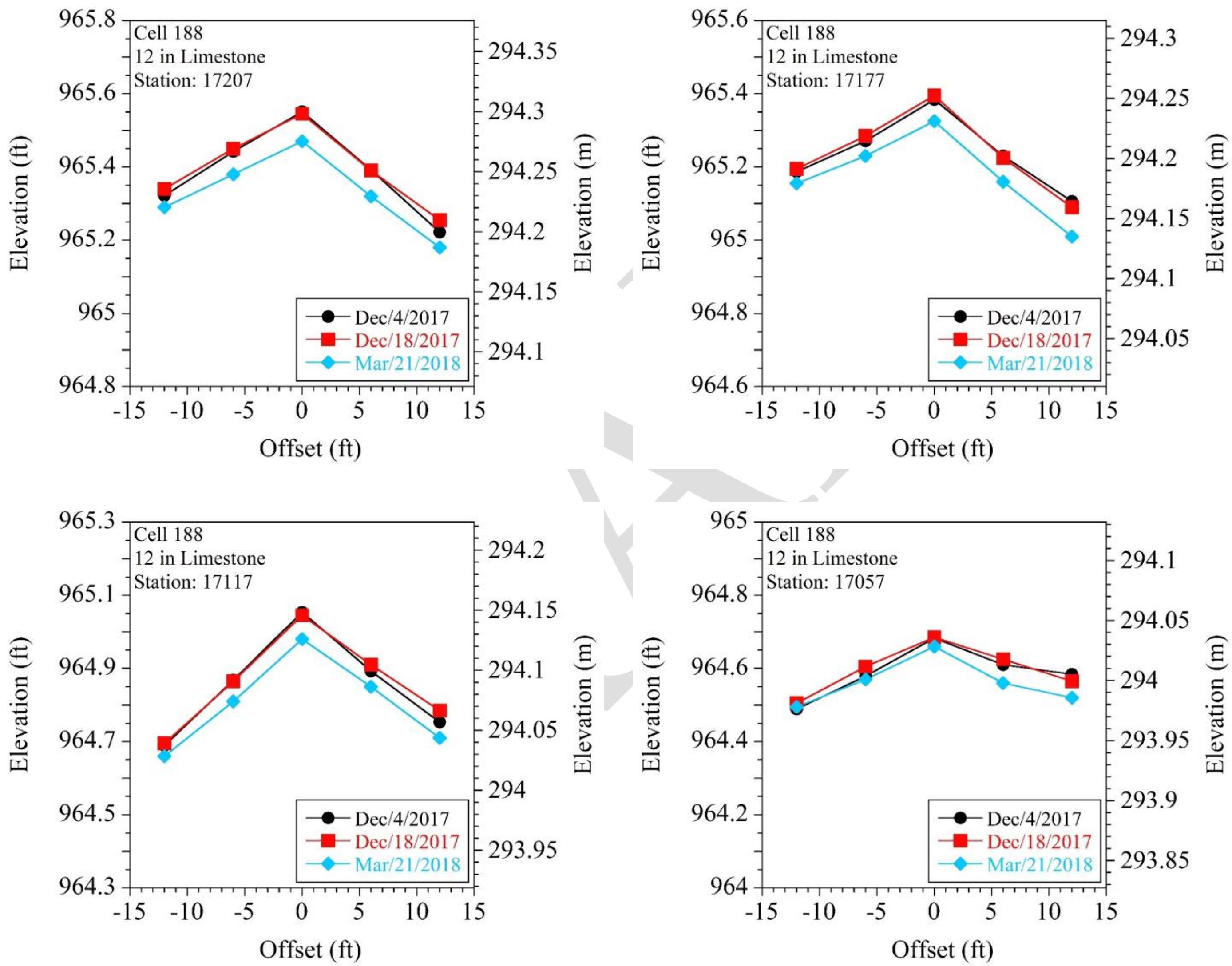

Cell 189 (12 in RCA+RAP):

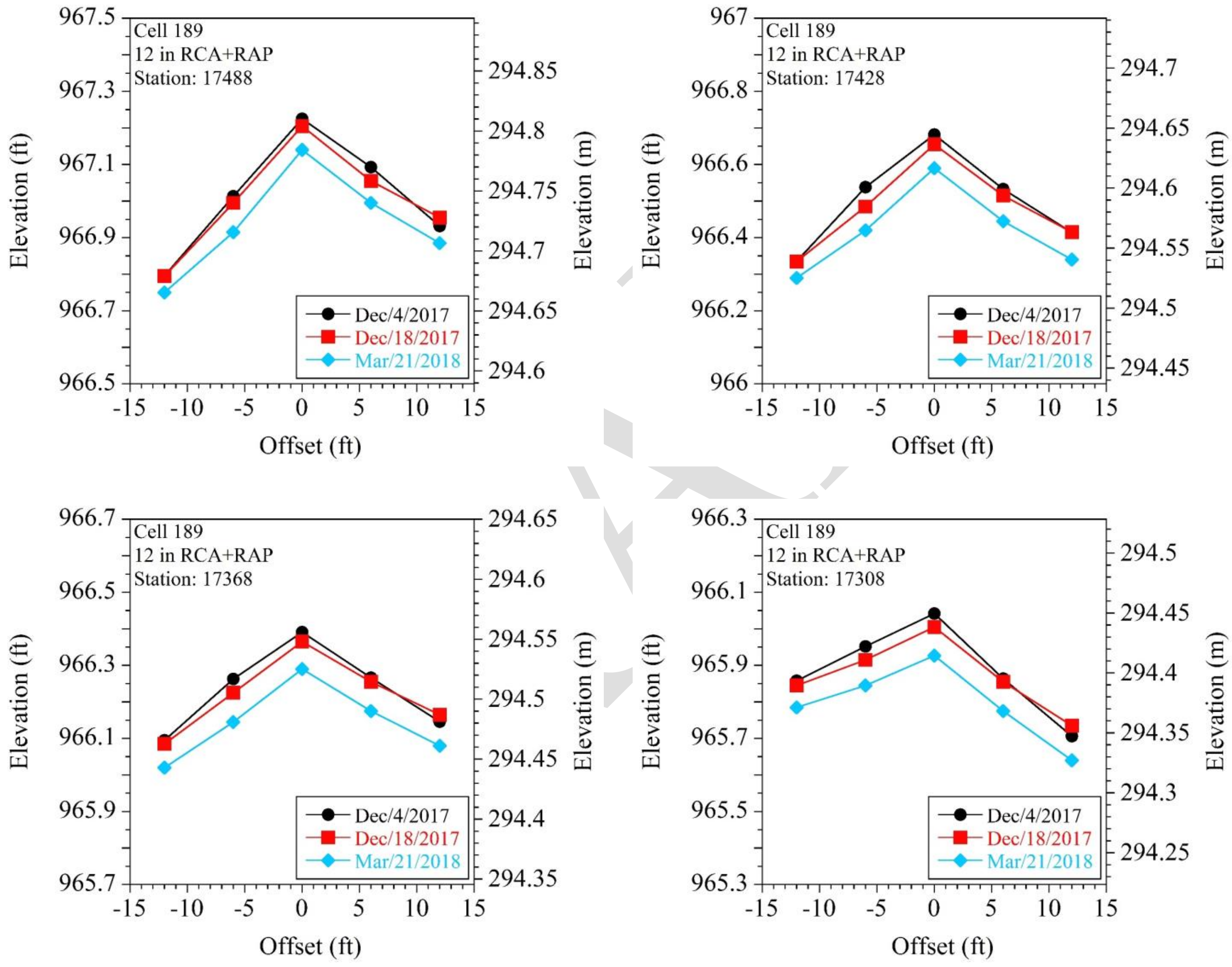

Cell 127 (18 in LSSB):

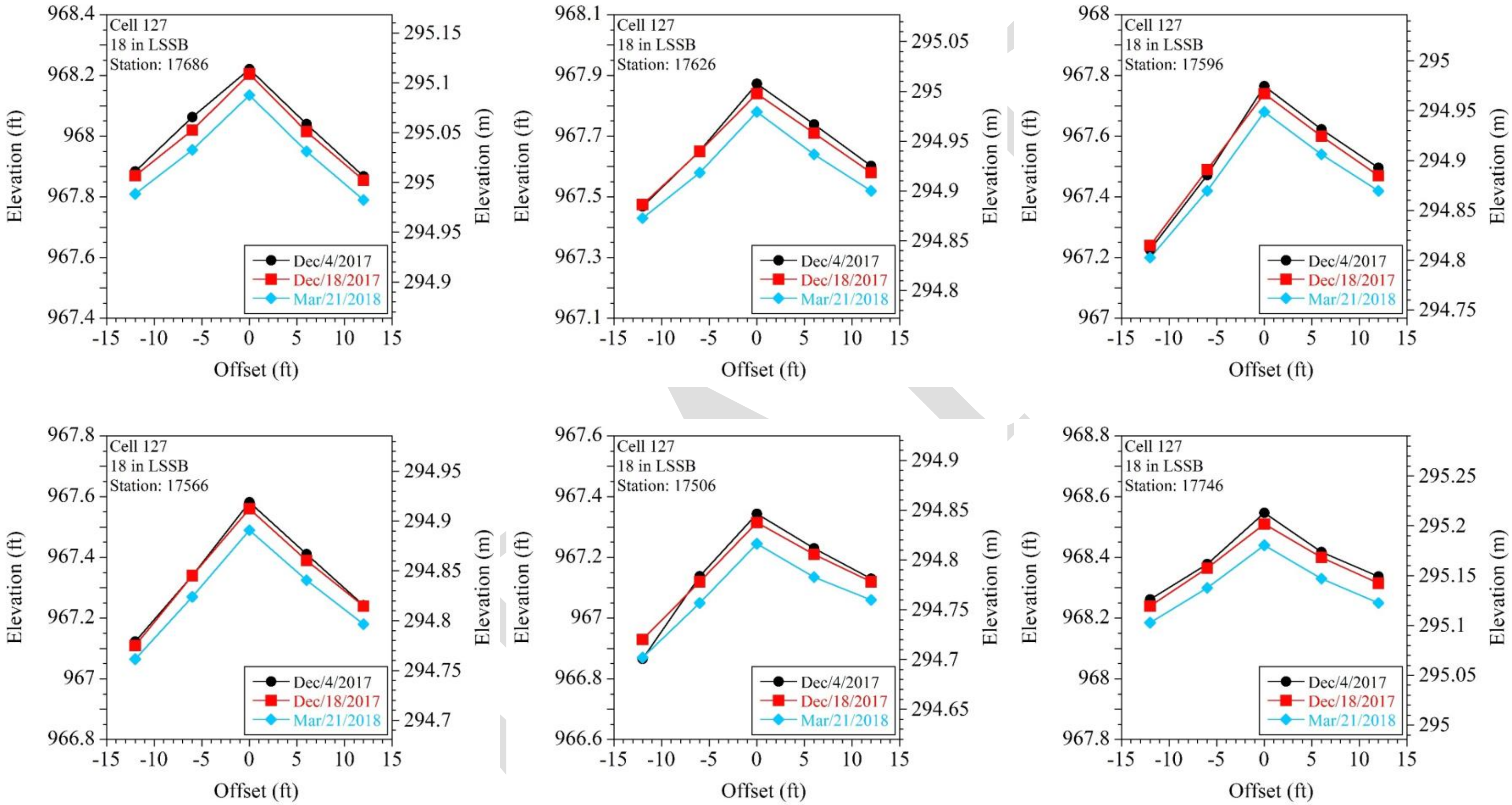

Cell 227 (18 in LSSB):

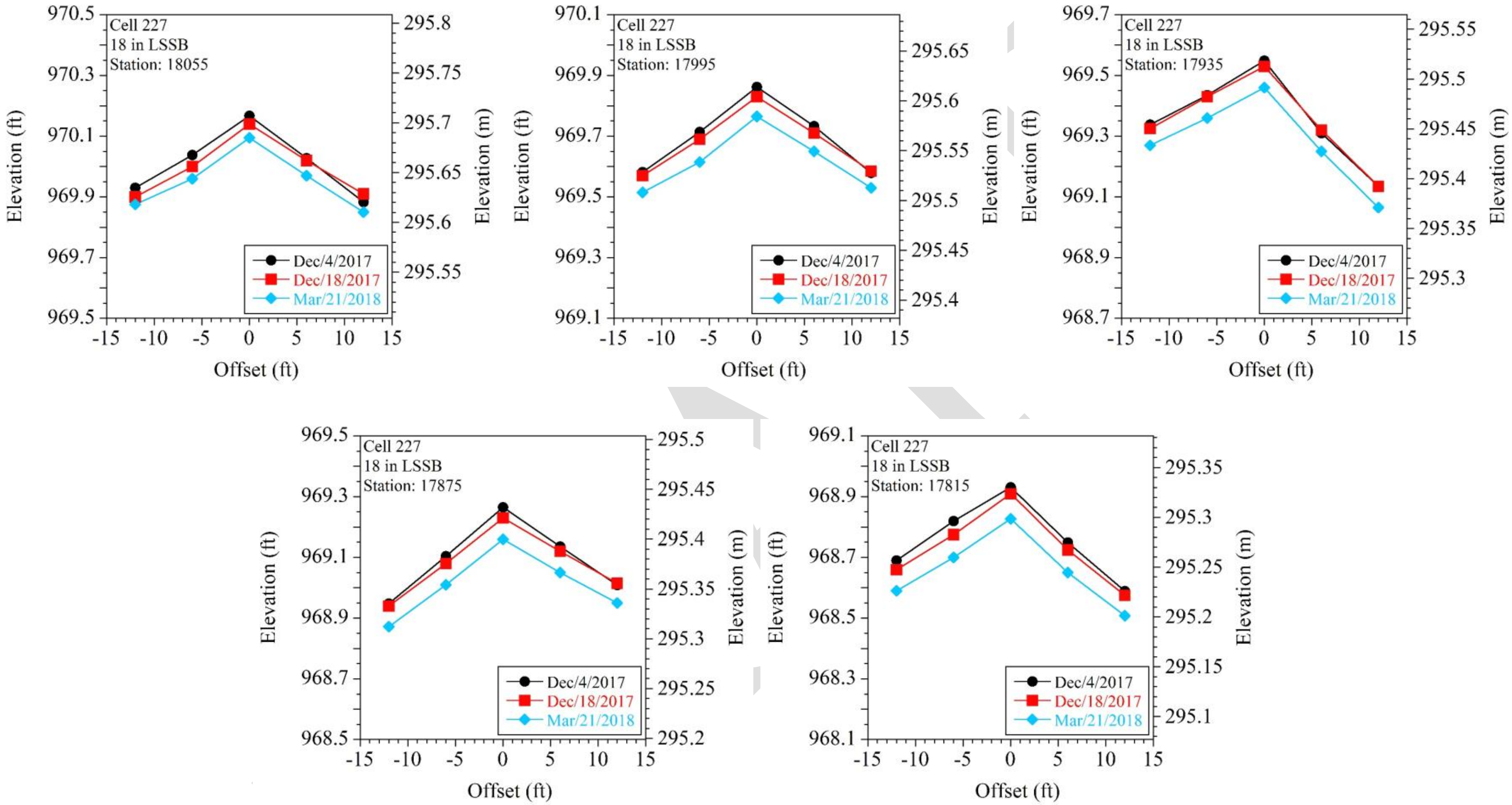

__Cell 328 (9 in LSSB – TX):__

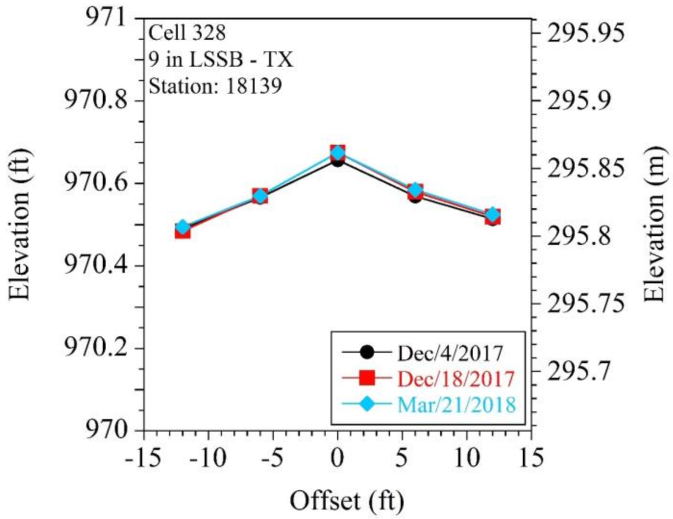

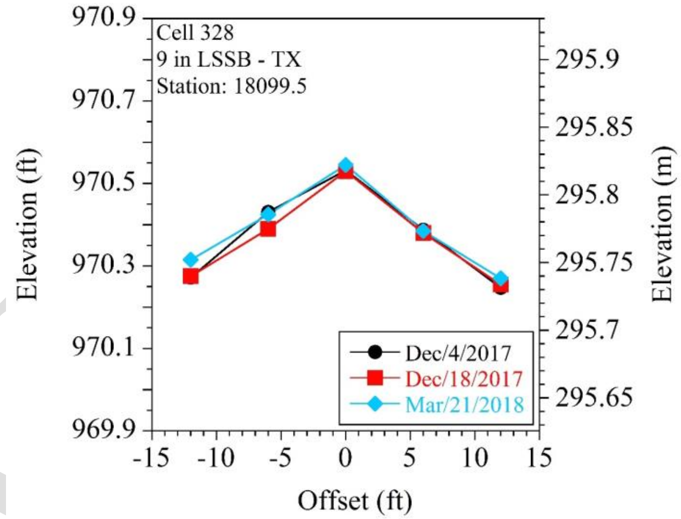

__Cell 428 (9 in LSSB – TX+GT):__

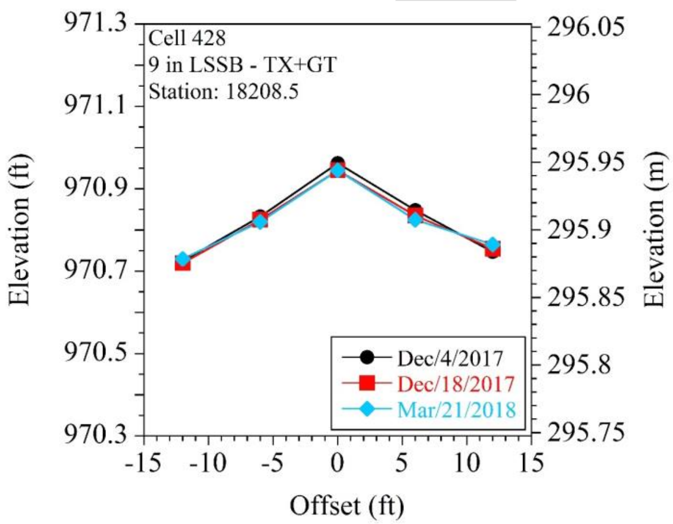

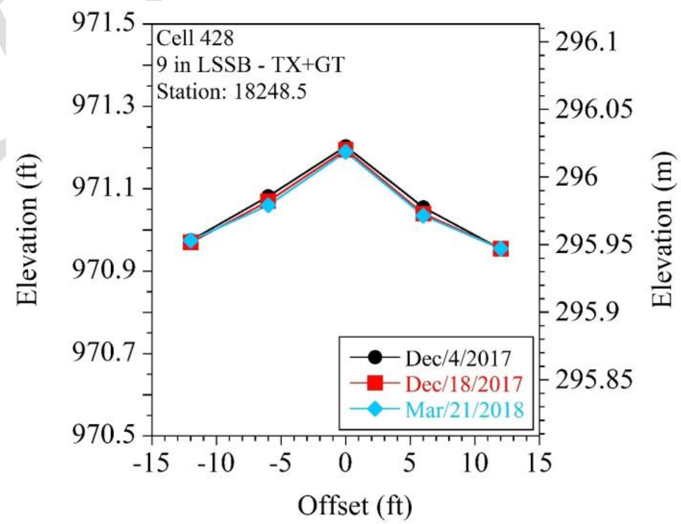

Cell 528 (9 in LSSB – BX+GT):

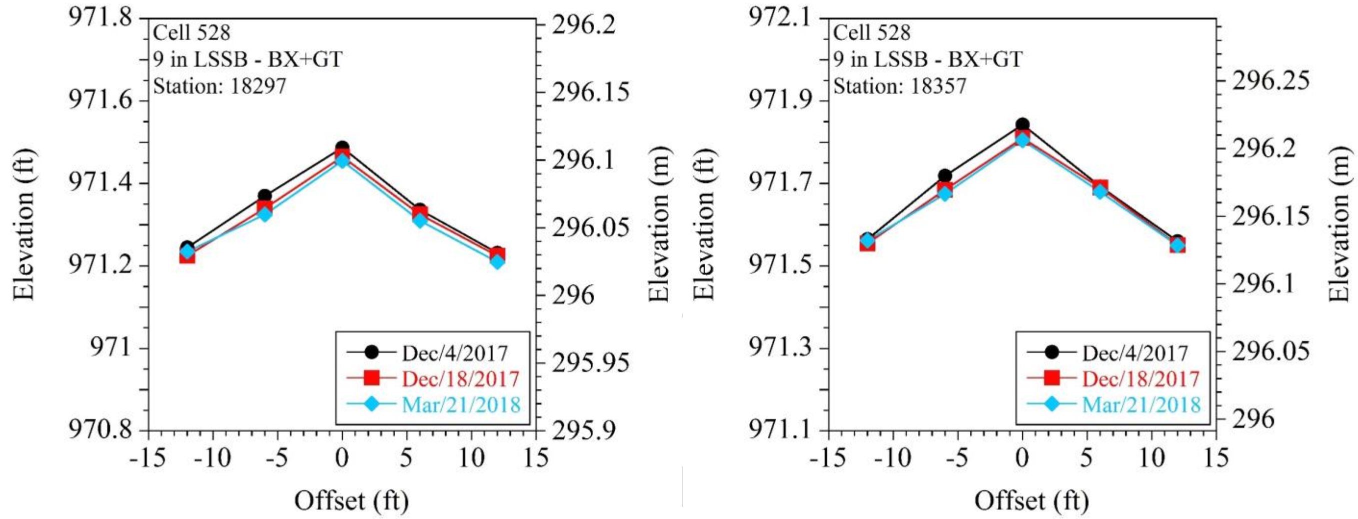

Cell 628 (9 in LSSB – BX):

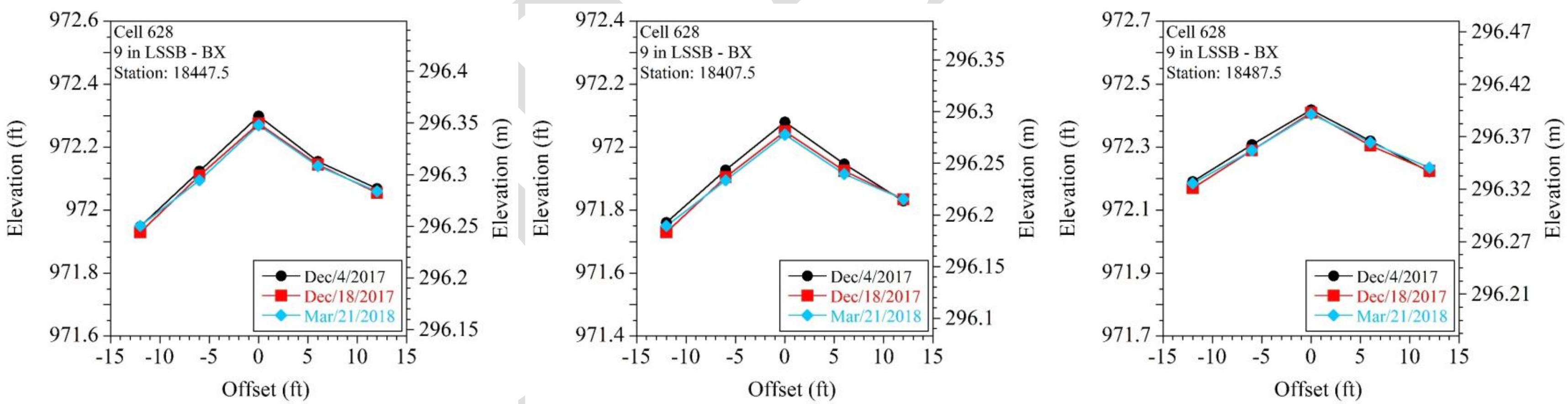

Cell 728 (9 in LSSB):

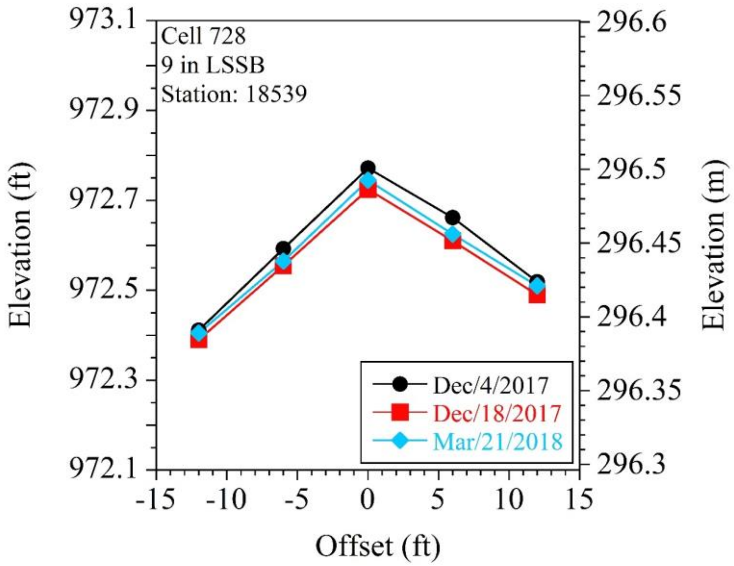

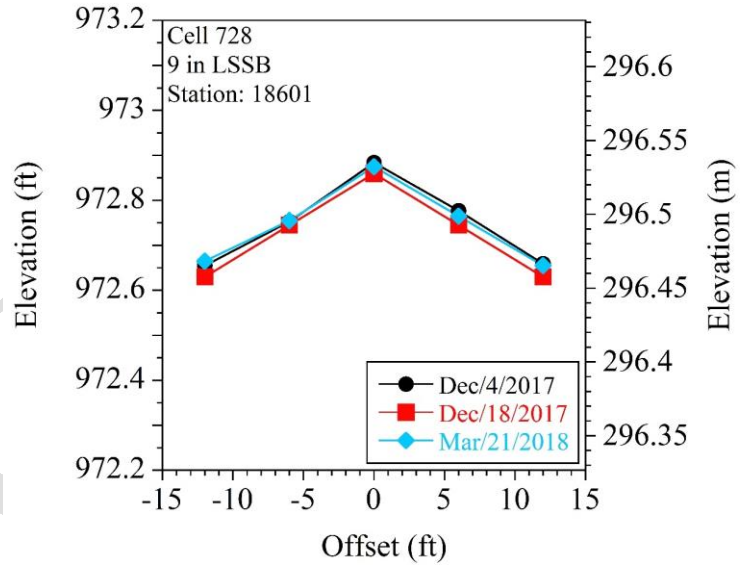

APPENDIX R. RUT DEPTH MEASUREMENTS FOR EACH CELL

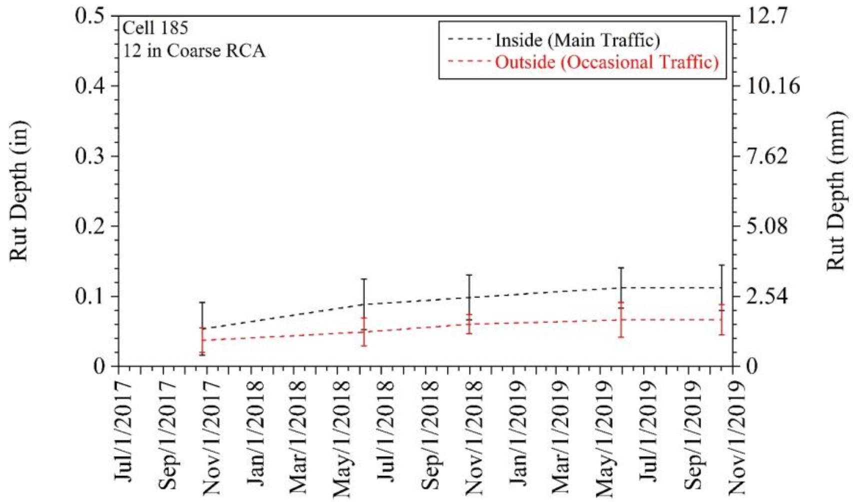

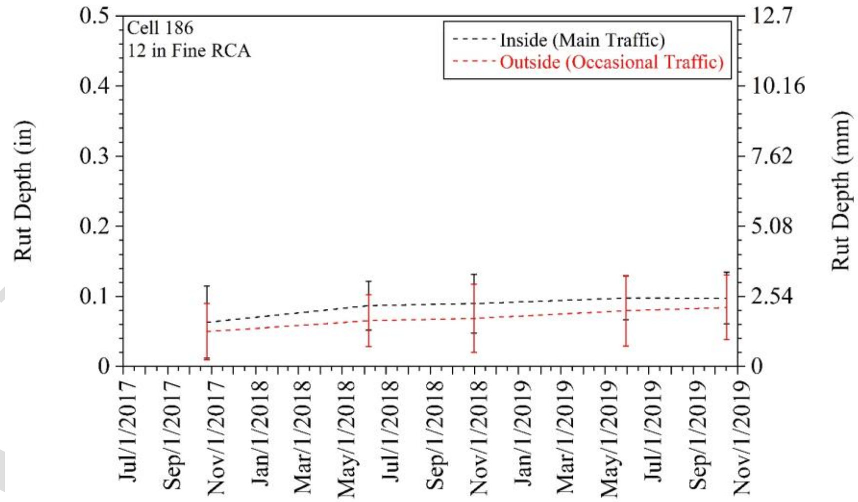

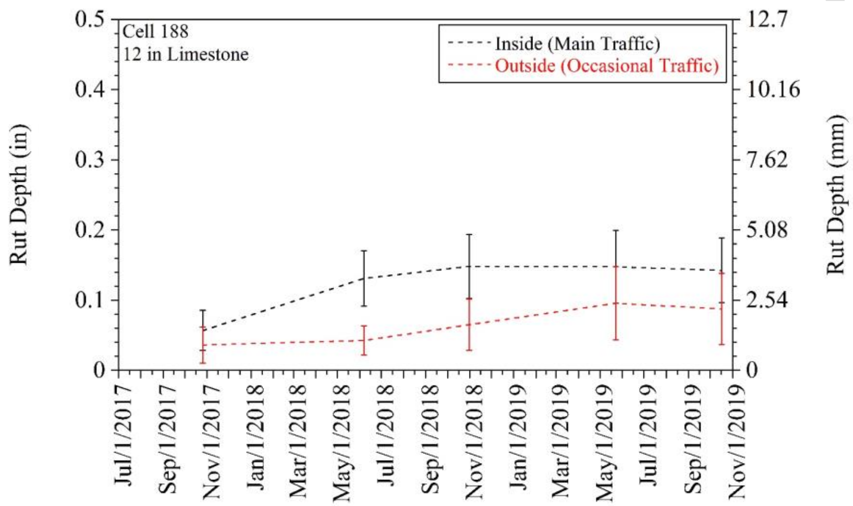

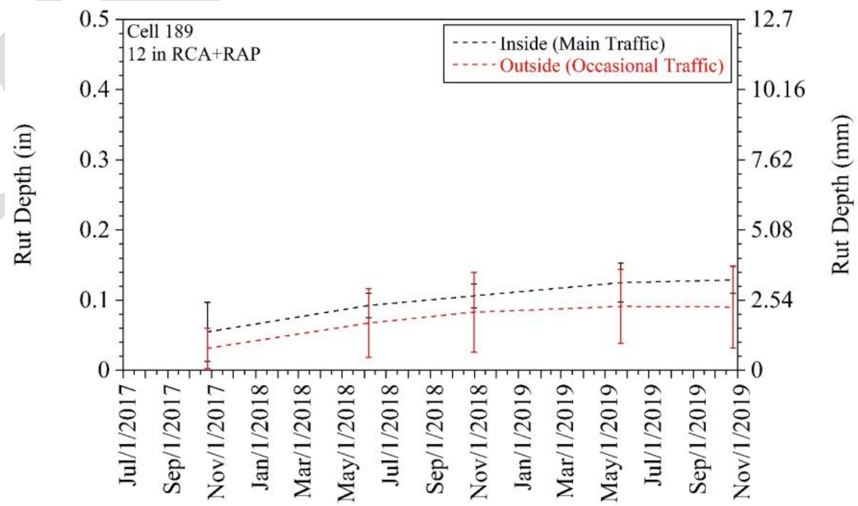

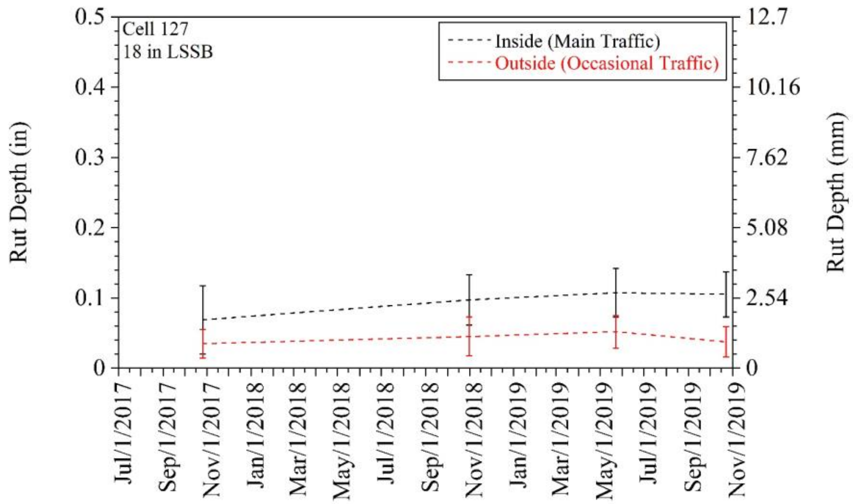
Cell 127
18 in LSSB
Inside (Main Traffic)
Outside (Occasional Traffic)
Rut Depth (in)
Rut Depth (mm)
0.5
0.4
0.3
0.2
0.1
0
12.7
10.16
7.62
5.08
2.54
0
Jul/1/2017
Sep/1/2017
Nov/1/2017
Jan/1/2018
Mar/1/2018
May/1/2018
Jul/1/2018
Sep/1/2018
Nov/1/2018
Jan/1/2019
Mar/1/2019
May/1/2019
Jul/1/2019
Sep/1/2019
Nov/1/2019

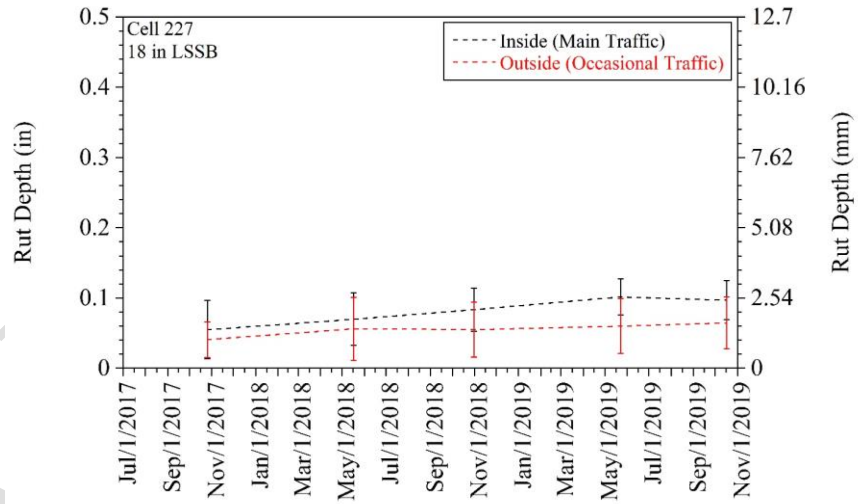
Cell 227
18 in LSSB
Inside (Main Traffic)
Outside (Occasional Traffic)
Rut Depth (in)
Rut Depth (mm)
0.5
0.4
0.3
0.2
0.1
0
12.7
10.16
7.62
5.08
2.54
0
Jul/1/2017
Sep/1/2017
Nov/1/2017
Jan/1/2018
Mar/1/2018
May/1/2018
Jul/1/2018
Sep/1/2018
Nov/1/2018
Jan/1/2019
Mar/1/2019
May/1/2019
Jul/1/2019
Sep/1/2019
Nov/1/2019

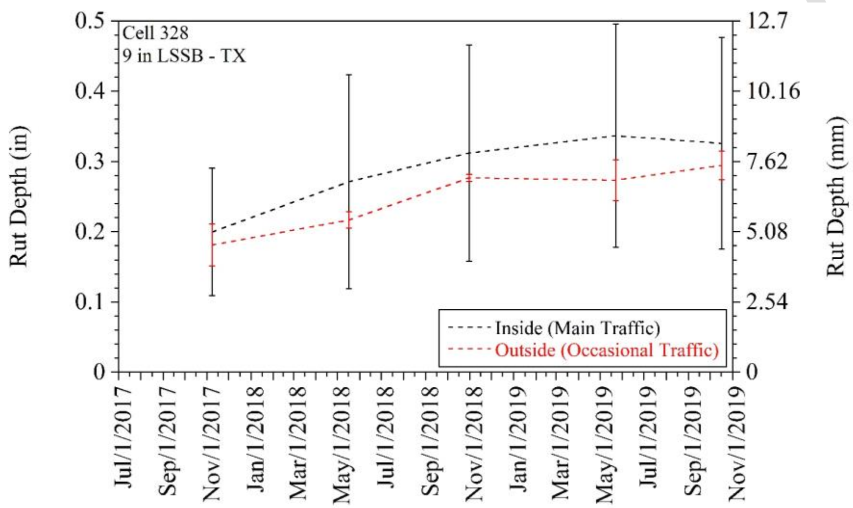
Cell 328
9 in LSSB - TX
Inside (Main Traffic)
Outside (Occasional Traffic)
Rut Depth (in)
Rut Depth (mm)
0.5
0.4
0.3
0.2
0.1
0
12.7
10.16
7.62
5.08
2.54
0
Jul/1/2017
Sep/1/2017
Nov/1/2017
Jan/1/2018
Mar/1/2018
May/1/2018
Jul/1/2018
Sep/1/2018
Nov/1/2018
Jan/1/2019
Mar/1/2019
May/1/2019
Jul/1/2019
Sep/1/2019
Nov/1/2019

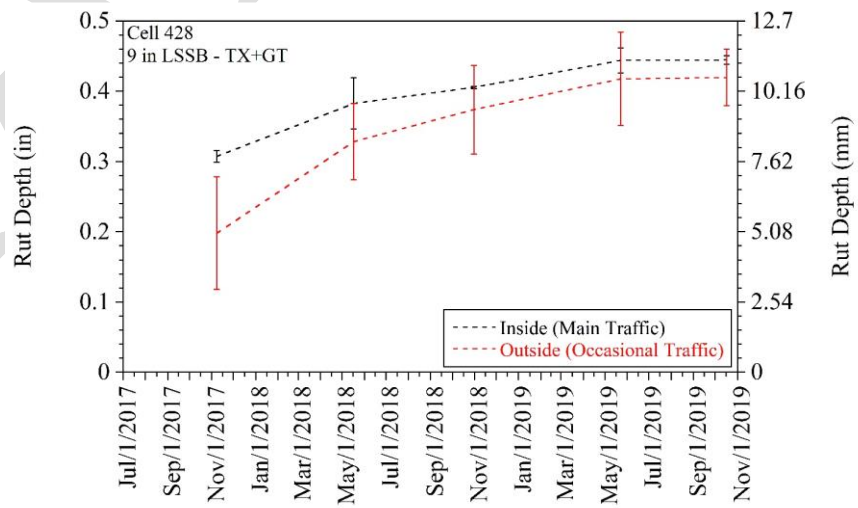
Cell 428
9 in LSSB - TX+GT
Inside (Main Traffic)
Outside (Occasional Traffic)
Rut Depth (in)
Rut Depth (mm)
0.5
0.4
0.3
0.2
0.1
0
12.7
10.16
7.62
5.08
2.54
0
Jul/1/2017
Sep/1/2017
Nov/1/2017
Jan/1/2018
Mar/1/2018
May/1/2018
Jul/1/2018
Sep/1/2018
Nov/1/2018
Jan/1/2019
Mar/1/2019
May/1/2019
Jul/1/2019
Sep/1/2019
Nov/1/2019

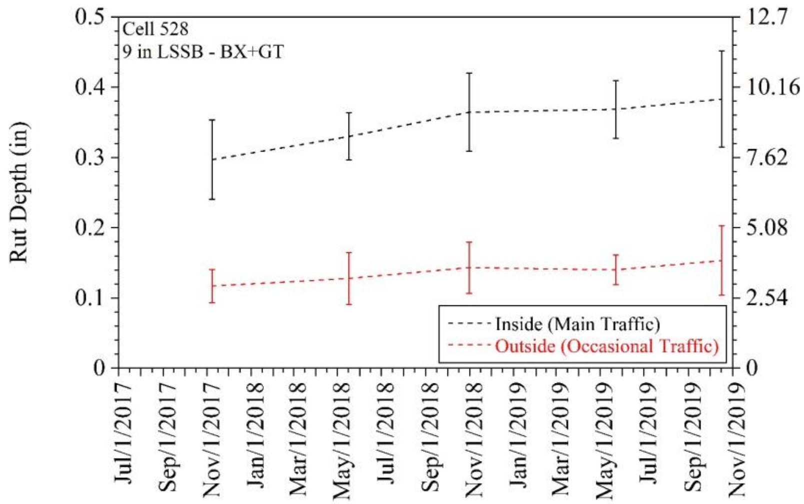
Cell 528
9 in LSSB - BX+GT
Rut Depth (in)
Rut Depth (mm)
Inside (Main Traffic)
Outside (Occasional Traffic)
0.5
0.4
0.3
0.2
0.1
0
12.7
10.16
7.62
5.08
2.54
0
Jul/1/2017
Sep/1/2017
Nov/1/2017
Jan/1/2018
Mar/1/2018
May/1/2018
Jul/1/2018
Sep/1/2018
Nov/1/2018
Jan/1/2019
Mar/1/2019
May/1/2019
Jul/1/2019
Sep/1/2019
Nov/1/2019

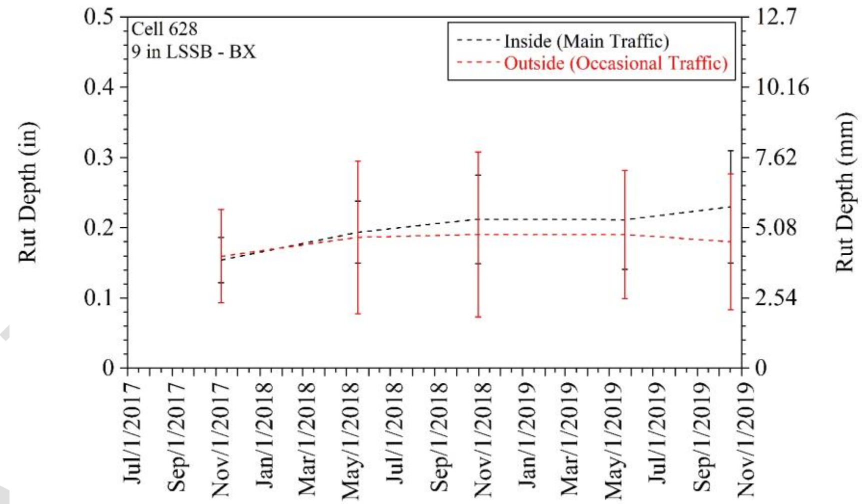
Cell 628
9 in LSSB - BX
Rut Depth (in)
Rut Depth (mm)
Inside (Main Traffic)
Outside (Occasional Traffic)
0.5
0.4
0.3
0.2
0.1
0
12.7
10.16
7.62
5.08
2.54
0
Jul/1/2017
Sep/1/2017
Nov/1/2017
Jan/1/2018
Mar/1/2018
May/1/2018
Jul/1/2018
Sep/1/2018
Nov/1/2018
Jan/1/2019
Mar/1/2019
May/1/2019
Jul/1/2019
Sep/1/2019
Nov/1/2019

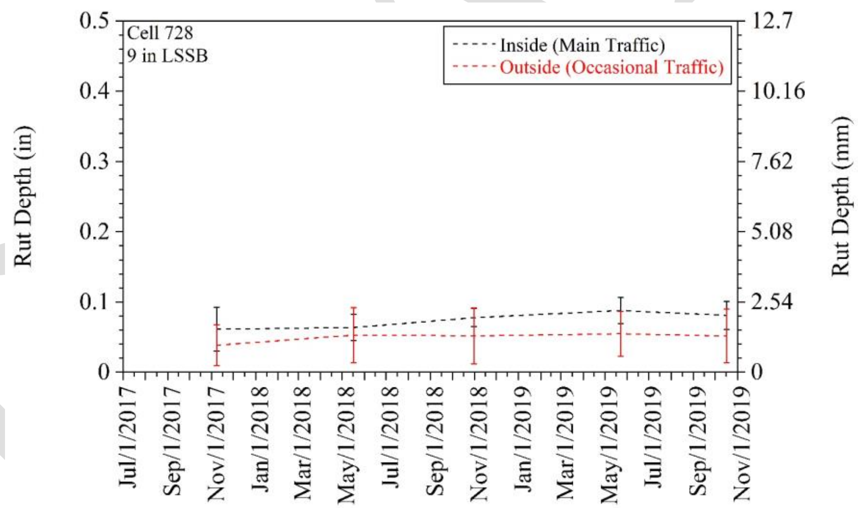
Cell 728
9 in LSSB
Rut Depth (in)
Rut Depth (mm)
Inside (Main Traffic)
Outside (Occasional Traffic)
0.5
0.4
0.3
0.2
0.1
0
12.7
10.16
7.62
5.08
2.54
0
Jul/1/2017
Sep/1/2017
Nov/1/2017
Jan/1/2018
Mar/1/2018
May/1/2018
Jul/1/2018
Sep/1/2018
Nov/1/2018
Jan/1/2019
Mar/1/2019
May/1/2019
Jul/1/2019
Sep/1/2019
Nov/1/2019

APPENDIX S. INTERNATIONAL ROUGHNESS INDEX (IRI) TEST RESULTS FOR EACH CELL

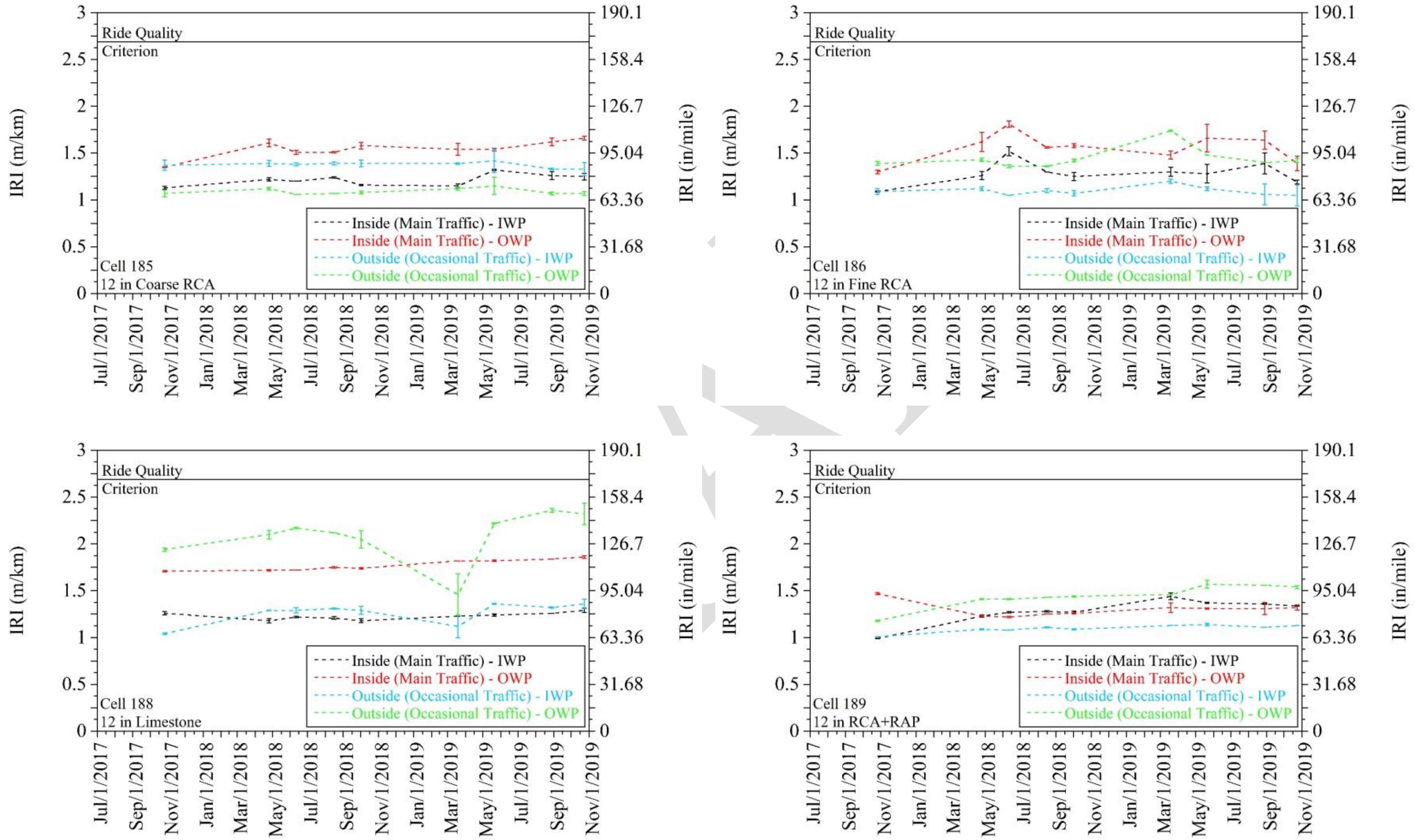

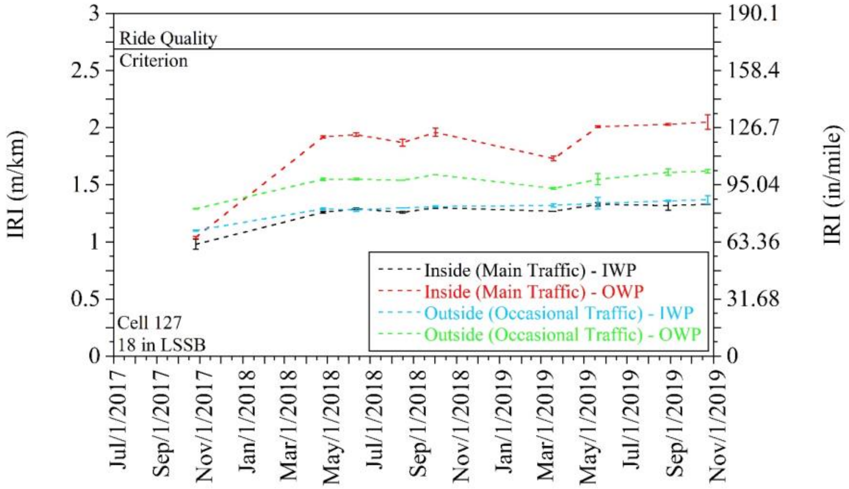
Ride Quality
Criterion
Cell 127
18 in LSSB
Inside (Main Traffic) - IWP
Inside (Main Traffic) - OWP
Outside (Occasional Traffic) - IWP
Outside (Occasional Traffic) - OWP
IRI (m/km)
IRI (in/mile)

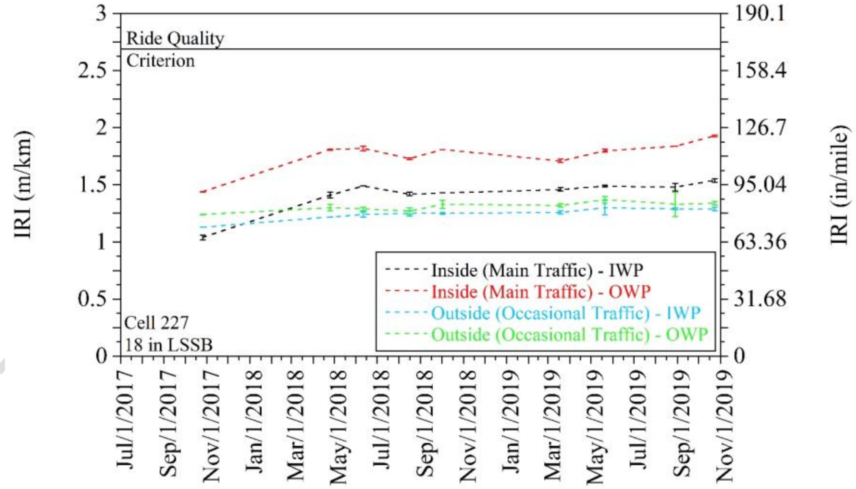
Ride Quality
Criterion
Cell 227
18 in LSSB
Inside (Main Traffic) - IWP
Inside (Main Traffic) - OWP
Outside (Occasional Traffic) - IWP
Outside (Occasional Traffic) - OWP
IRI (m/km)
IRI (in/mile)

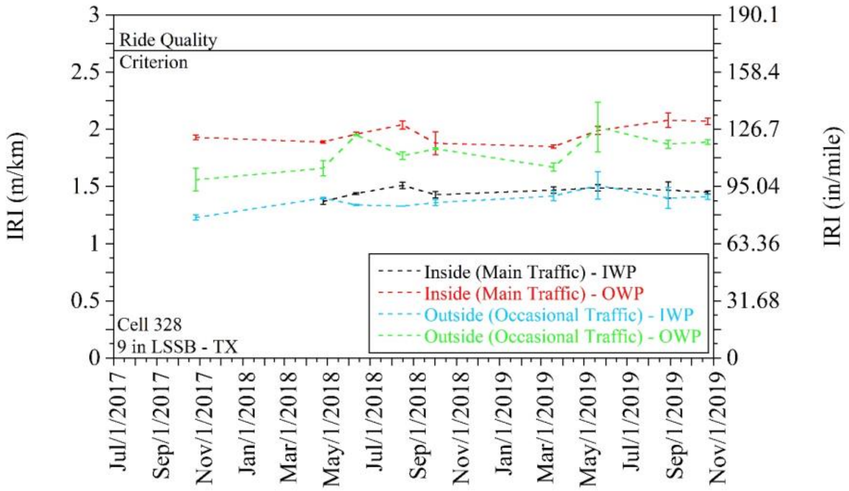
Ride Quality
Criterion
Cell 328
9 in LSSB - TX
Inside (Main Traffic) - IWP
Inside (Main Traffic) - OWP
Outside (Occasional Traffic) - IWP
Outside (Occasional Traffic) - OWP
IRI (m/km)
IRI (in/mile)

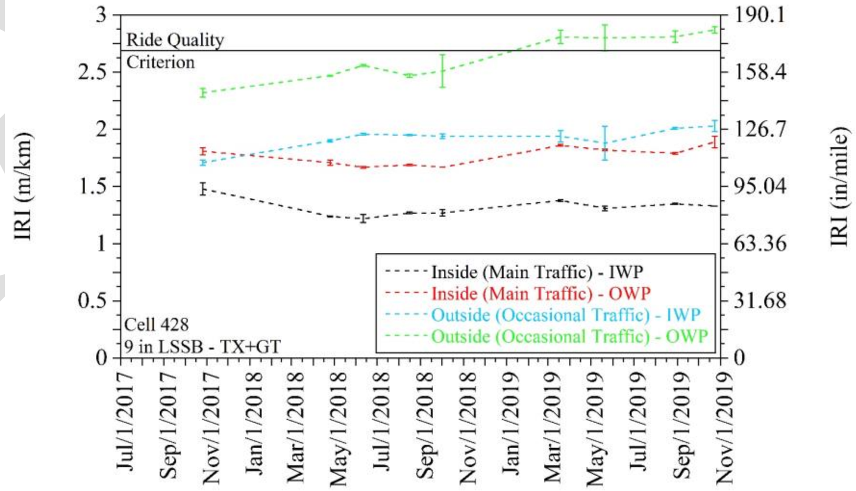
Ride Quality
Criterion
Cell 428
9 in LSSB - TX+GT
Inside (Main Traffic) - IWP
Inside (Main Traffic) - OWP
Outside (Occasional Traffic) - IWP
Outside (Occasional Traffic) - OWP
IRI (m/km)
IRI (in/mile)

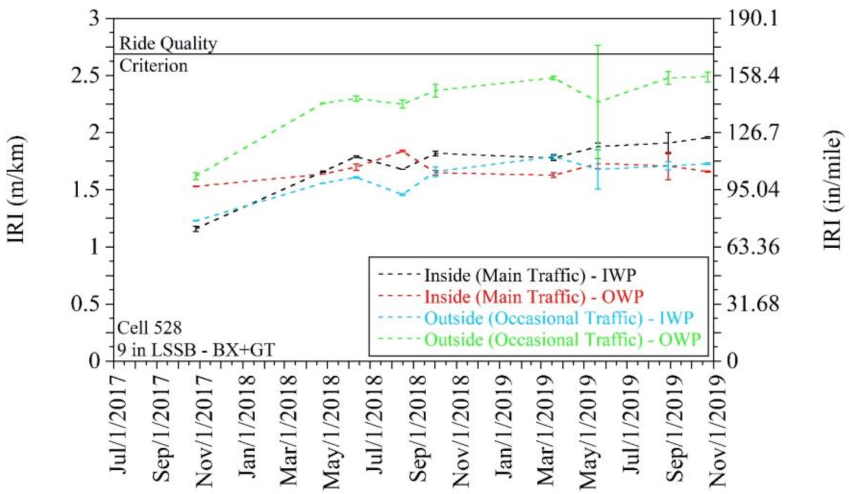
Ride Quality
Criterion
Cell 528
9 in LSSB - BX+GT
Inside (Main Traffic) - IWP
Inside (Main Traffic) - OWP
Outside (Occasional Traffic) - IWP
Outside (Occasional Traffic) - OWP
IRI (m/km)
IRI (in/mile)

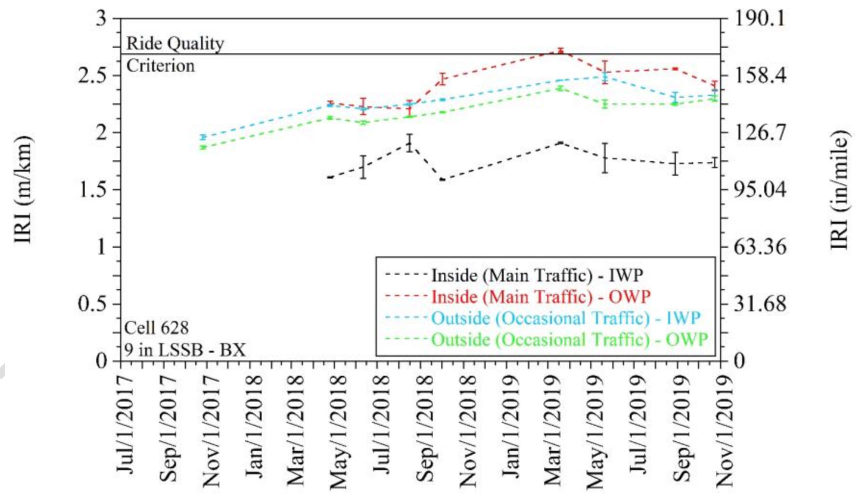
Ride Quality
Criterion
Cell 628
9 in LSSB - BX
Inside (Main Traffic) - IWP
Inside (Main Traffic) - OWP
Outside (Occasional Traffic) - IWP
Outside (Occasional Traffic) - OWP
IRI (m/km)
IRI (in/mile)

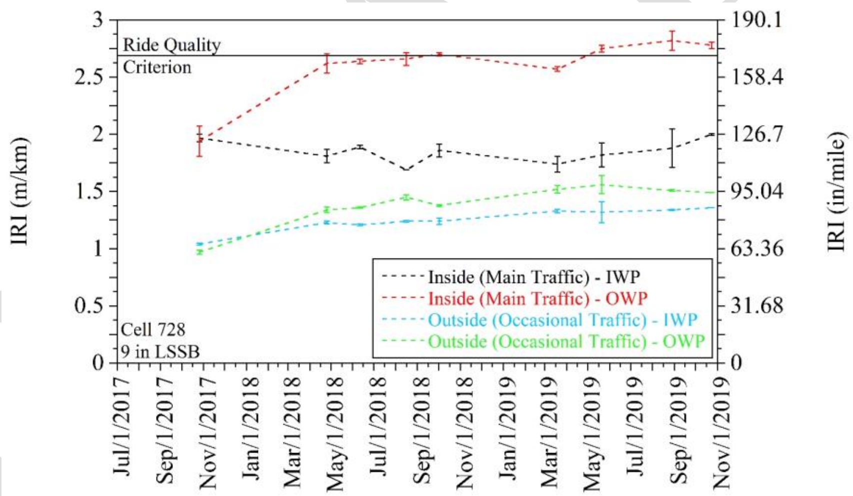
Ride Quality
Criterion
Cell 728
9 in LSSB
Inside (Main Traffic) - IWP
Inside (Main Traffic) - OWP
Outside (Occasional Traffic) - IWP
Outside (Occasional Traffic) - OWP
IRI (m/km)
IRI (in/mile)

APPENDIX T. INTERNATIONAL ROUGHNESS INDEX (IRI) IN THE INSIDE LANE (MAIN TRAFFIC) – IWP OF THE TEST CELLS

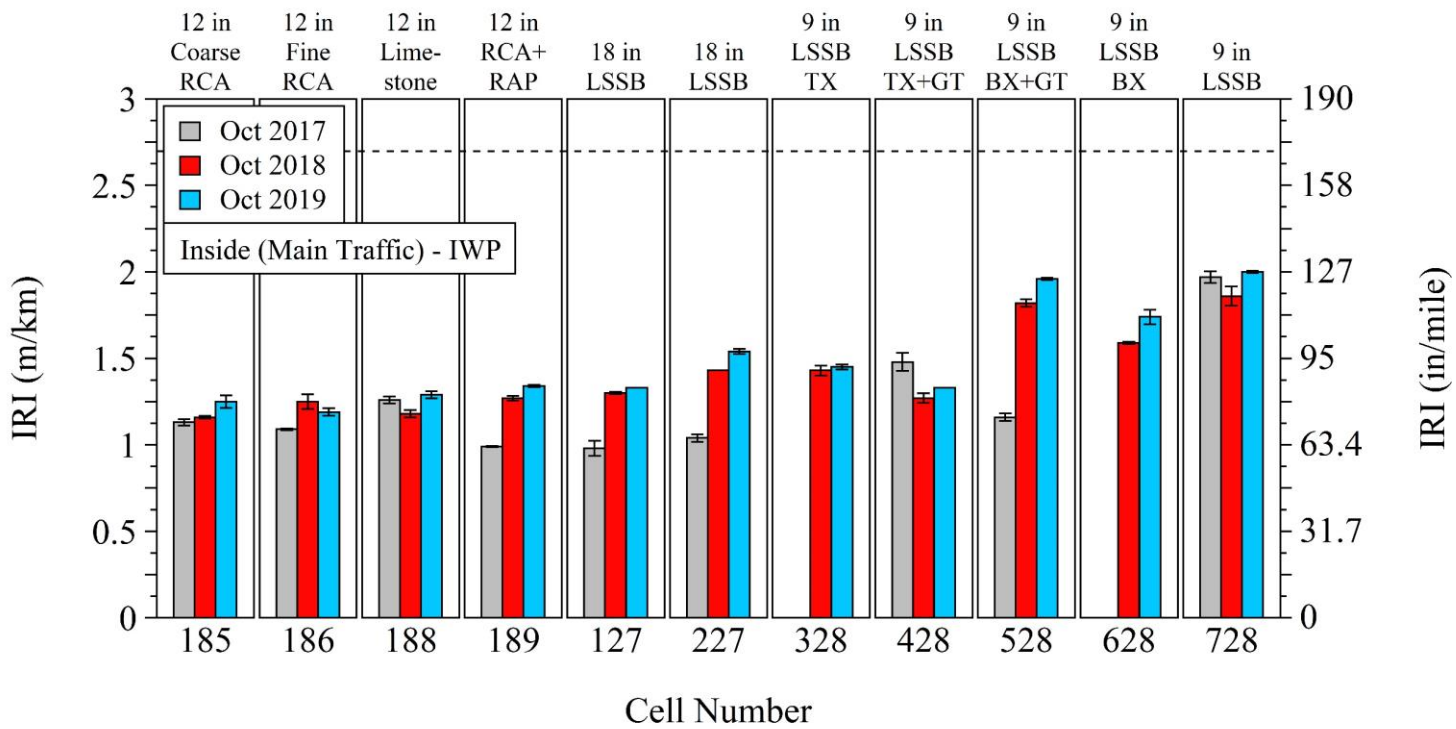

APPENDIX U. RAVELING IN THE TEST CELLS

Raveling pictures taken from the distress identification manual for the LTTP (Miller and Bellinger 2014):

Loss of fine aggregate

Loss of fine and some coarse aggregate

Loss of coarse aggregate

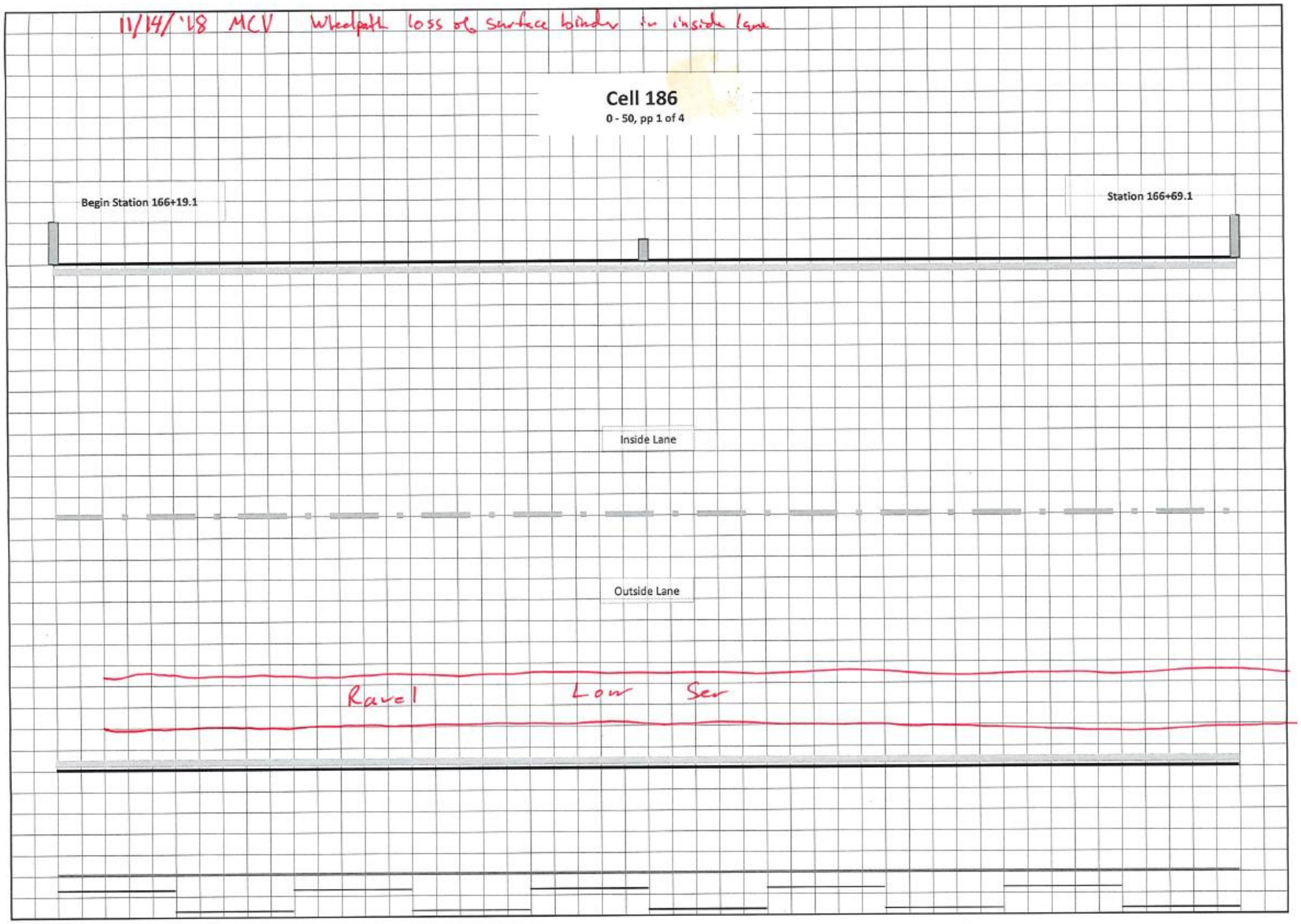

Illustration of raveling on the distress survey maps

Cell Number	Cell Description	Lane	Date	Raveling – Low Severity (Area)	Raveling – Moderate Severity (Area)
185	12 in Coarse RCA	Inside	11/14/2018	0	6
			3/26/2019	0	6
			12/4/2019	0	6
186	12 in Fine RCA	Inside	11/14/2018	0	0
			3/26/2019	0	0
			12/4/2019	0	0
188	12 in Limestone	Inside	11/14/2018	44	0
			3/26/2019	44	0
			12/4/2019	44	0
189	12 in RCA+RAP	Inside	11/14/2018	5	0
			3/26/2019	5	0
			12/4/2019	5	0
127	18 in LSSB	Inside	11/14/2018	1	0
			3/26/2019	1	0
			12/4/2019	1	0
227	18 in LSSB	Inside	11/14/2018	123	0
			3/26/2019	123	0
			12/4/2019	123	0
328	9 in LSSB – TX	Inside	12/17/2018	0	0
			4/7/2019	0	0
			12/4/2019	0	0
428	9 in LSSB – TX+GT	Inside	12/17/2018	0	0
			4/7/2019	0	0
			12/4/2019	0	0
528	9 in LSSB – BX+GT	Inside	12/17/2018	0	0
			4/7/2019	0	0
			12/4/2019	0	0
628	9 in LSSB – BX	Inside	12/17/2018	0	0
			4/7/2019	0	0
			12/4/2019	0	0
728	9 in LSSB	Inside	12/17/2018	0	0
			4/7/2019	0	0
			12/4/2019	0	0

Cell Number	Cell Description	Lane	Date	Raveling – Low Severity (Area)	Raveling – Moderate Severity (Area)
185	12 in Coarse RCA	Outside	11/14/2018	0	12
			3/26/2019	0	12
			12/4/2019	0	12
186	12 in Fine RCA	Outside	11/14/2018	0	0
			3/26/2019	0	0
			12/4/2019	0	0
188	12 in Limestone	Outside	11/14/2018	30	0
			3/26/2019	30	0
			12/4/2019	30	0
189	12 in RCA+RAP	Outside	11/14/2018	0	0
			3/26/2019	0	0
			12/4/2019	0	0
127	18 in LSSB	Outside	11/14/2018	0	0
			3/26/2019	0	0
			12/4/2019	0	0
227	18 in LSSB	Outside	11/14/2018	27	0
			3/26/2019	30	0
			12/4/2019	30	0
328	9 in LSSB – TX	Outside	12/17/2018	0	0
			4/7/2019	0	0
			12/4/2019	0	0
428	9 in LSSB – TX+GT	Outside	12/17/2018	0	0
			4/7/2019	0	0
			12/4/2019	0	0
528	9 in LSSB – BX+GT	Outside	12/17/2018	0	0
			4/7/2019	0	0
			12/4/2019	0	0
628	9 in LSSB – BX	Outside	12/17/2018	0	0
			4/7/2019	0	0
			12/4/2019	0	0
728	9 in LSSB	Outside	12/17/2018	0	0
			4/7/2019	0	0
			12/4/2019	0	0